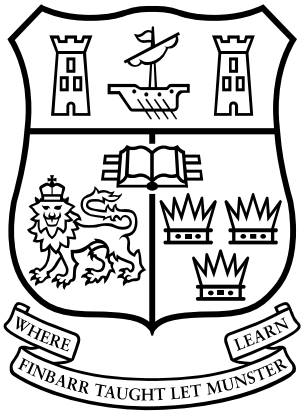
CORA Cork Open Research Archive
Cartlann Taighde Oscailte Chorcaí

| | |
|---|---|
| Title | Electromagnetic tracking and steering for catheter navigation |
| Authors | O'Donoghue, Kilian |
| Publication date | 2014 |
| Original Citation | O'Donoghue, K. 2014. Electromagnetic tracking and steering for catheter navigation. PhD Thesis, University College Cork. |
| Type of publication | Doctoral thesis |
| Rights | © 2014, Kilian O'Donoghue. - http://creativecommons.org/licenses/by-nc-nd/3.0/ |
| Download date | 2026-11-05 17:09:44 |
| Item downloaded from | https://hdl.handle.net/10468/2025 |



UCC
University College Cork, Ireland
Coláiste na hOllscoile Corcaigh




# Electromagnetic Tracking and Steering for Catheter Navigation

Kilian O'Donoghue

A thesis presented to the National University of Ireland for the degree of Doctor of Philosophy

October, 2014

Supervised by Dr. Pádraig Cantillon-Murphy

School of Engineering

University College Cork

Ireland

# Declaration

I hereby declare that I am the sole author of this thesis and all of the work undertaken in this thesis is original in content and was carried out by the author. Work carried out by others has been duly acknowledged in the thesis.

This is a true copy of the thesis, including any required final revisions, as accepted by my examiners. The work presented has not been accepted in any previous application for a degree.

Signed: _____

Date: _____

# Abstract

This thesis explores the use of electromagnetics for both steering and tracking of medical instruments in minimally invasive surgeries. The end application is virtual navigation of the lung for biopsy of early stage cancer nodules. Navigation to the peripheral regions of the lung is difficult due to physical dimensions of the bronchi and current methods have low successes rates for accurate diagnosis.

Firstly, the potential use of DC magnetic fields for the actuation of catheter devices with permanently magnetised distal attachments is investigated. Catheter models formed from various materials and magnetic tip formations are used to examine the usefulness of relatively low power and compact electromagnets. The force and torque that can be exerted on a small permanent magnet is shown to be extremely limited. Hence, after this initial investigation we turn our attention to electromagnetic tracking, in the development of a novel, low-cost implementation of a GPS-like system for navigating within a patient.

A planar magnetic transmitter, formed on a printed circuit board for a low-profile and low cost manufacture, is used to generate a low frequency magnetic field distribution which is detected by a small induction coil sensor. The field transmitter is controlled by a novel closed-loop system that ensures a highly stable magnetic field with reduced interference from one transmitter coil to another. Efficient demodulation schemes are presented which utilise synchronous detection of each magnetic field component experienced by the sensor. The overall tracking accuracy of the system is shown to be less than 2 mm with an orientation error less than 1°. A novel demodulation implementation using a unique undersampling approach allows the use of reduced sample rates to sample the signals of interest without loss of tracking accuracy. This is advantageous for embedded microcontroller implementations of EM tracking systems.

The EM tracking system is demonstrated in the pre-clinical environment of a breathing lung phantom. The airways of the phantom are successfully navigated using the system in combination with a 3D computer model rendered from CT data. Registration is achieved using both a landmark rigid registration method and a hybrid fiducial-free approach.

The design of a planar magnetic shield structure for blocking the effects of metallic distortion from below the transmitter is presented which successfully blocks the impact of large ferromagnetic objects such as operating tables. A variety of shielding material are analysed with MuMetal and ferrite both providing excellent shieling performance and an increased signal to noise ratio. Finally, the effect of conductive materials and human tissue on magnetic field measurements is presented. Error due to induced eddy currents and capacitive coupling is shown to severely affect EM tracking accuracy at higher frequencies.

# Acknowledgements

I wish to thank everyone who have helped and contributed to my work over the course of my PhD. This thesis would not have been possible without their support and guidance. Firstly, I thank my academic supervisor, Dr. Pádraig Cantillon-Murphy for his excellent guidance, support and encouragement over the past few years. I would also like to thank Dr. Gordon Lightbody and Professor Georg Rose for examining my thesis as well as Dr. Marcus Kennedy and Dr. Kashif Ali Khan from the Department of Pulmonology in Cork University Hospital for all their contributions.

I wish to thank all the staff of the Department of Electrical and Electronic Engineering at University College Cork. I extend a big thank you to Mick O'Shea and Tim Power in the Mechanical Workshop for all their help in constructing and designing the various mechanical components and test fixtures that feature so prominently in this thesis. I would especially like to thank James Griffiths for all his help and advice which made the design and success of my work possible.

Big thanks goes out to Adrian, Brendan, Diarmaid, Donal, Ed, Kevin, Pat and Yeny in the Power Electronics Lab and Alex, Conor, Joe and Pietro in the Bioelectromagnetics Group. Cheers for all the banter, craic and extensive tea break discussions, not to mention the endless card games and innumerable pints that helped make this such an enjoyable experience.

I must also, of course, thank my parents and family for all their support and encouragement, you've all been great!

Finally, I thank Teresa for sharing this journey with me, along with all the stress, long hours and everything else…I couldn't have done it without you!

# List of Publications

**Journal Papers:**

1. K. O'Donoghue and P. Cantillon-Murphy, "Planar magnetic shielding for use with electromagnetic tracking systems", *IEEE Transactions on Magnetics,* doi: 10.1109/TMAG.2014.2352344, Aug 2014.
2. K. O'Donoghue and P. Cantillon-Murphy, "Low cost super-Nyquist asynchronous demodulation for use in EM tracking systems", *IEEE Transactions on Instrumentation and Measurement,* doi: 10.1109/TIM.2014.2343431, Aug 2014.
3. K. O'Donoghue, D. Eustace, J. Griffiths, M. O'Shea, T. Power and P. Cantillon-Murphy, "Catheter position tracking system using planar magnetics and closed loop current control,", *IEEE Transactions on Magnetics*, 50(7), 1-9, July 2014.
4. K. O'Donoghue and P. Cantillon-Murphy, *Journal of Magnetism and Magnetic Materials*, "Deflection modeling of permanent magnet spherical chains in the presence of external magnetic fields", 343, 251-256, Oct 2013.

**Conference Papers:**

1. K. O'Donoghue, A. Corvó, P. Nardelli, C. O'Shea, K. A. Khan, M. Kennedy and P. Cantillon-Murphy, "Evaluation of a novel tracking system in a breathing lung model", *36th Annual International Conference of the IEEE Engineering in Medicine and Biology Society*, Chicago, Illinois, USA, August 26-30, 2014.
2. K. O'Donoghue, A. Corvó, P. Nardelli, C. O'Shea, K. A. Khan, M. Kennedy and P. Cantillon-Murphy, "Evaluation of a novel EM tracking system in a breathing lung model", *The Hamlyn Symposium on Medical Robotics*, London, United Kingdom, July 12-15, 2014.
3. K. O'Donoghue, and P. Cantillon-Murphy, "A low cost system for 3D position and orientation sensing," *The Hamlyn Symposium on Medical Robotics*, London, United Kingdom, June 22-25, 2013.
4. K. O'Donoghue, D. Hogan, M. Healy and P. Cantillon-Murphy, "Magnetic Catheter Guidance in a Human Lung Model: an initial feasibility study." *Joint Workshop on New Technologies for Computer/Robot Assisted Surgery*, Madrid, Spain, July 2012.
5. K. O'Donoghue and P. Cantillon-Murphy, "Can Permanent Magnets Aid in Minimally-Invasive Procedures," *Joint Workshop on New Technologies for Computer/Robot Assisted Surgery*, Graz, Austria, July 2011.

# Table of Contents

**Declaration** ..... III
**Abstract** ..... V
**Acknowledgements** ..... VI
**List of Publications** ..... VII
**Table of Contents** ..... VIII
**List of Figures** ..... XV
**List of Tables** ..... XXVIII
**List of Abbreviations** ..... XXX
**Chapter 1 Introduction** ..... 1
1.1. Overview ..... 1
1.2. Thesis Objectives ..... 2
1.3. Thesis Structure ..... 3
**Chapter 2 Preliminary Investigations of Magnetic Catheter Steering** ..... 4
2.1. Overview ..... 4
2.2. Literature Review ..... 5
2.2.1. Stereotaxis Niobe ..... 5
2.2.2. Magnetic Pills and Micro-robots ..... 5
2.2.3. Navigation within MRI ..... 6
2.3. Magnetic Actuation Theory ..... 6
2.4. Proposed Magnetic Catheter Design ..... 8
2.5. Deflection Testing For Magnetic Catheters ..... 9
2.5.1. Catheter Materials ..... 9
2.5.2. Test Setup ..... 9
2.5.3. Electromagnetic Coil Actuator ..... 10
2.5.4. Magnetic Catheter Tips ..... 12
2.5.5. Results ..... 13
2.5.6. Discussion ..... 16
2.6. Deflection Modelling of Spherical Chains of Permanent Magnets ..... 16
2.6.1. Introduction ..... 16
2.6.2. Spherical Permanent Magnets ..... 18
2.6.3. Magnetic Energy ..... 18
2.6.4. Two Sphere Case ..... 19
2.6.5. N Spheres ..... 20

2.6.6. Numerical Simulation ..... 21
2.6.7. Experimental Setup ..... 22
2.6.7.1. Magnets ..... 22
2.6.7.2. Helmholtz Coil ..... 22
2.6.7.3. Test Apparatus ..... 22
2.6.8. Results ..... 24
2.6.9. Conclusion ..... 28
2.7. EM Tracking and Steering ..... 29
2.7.1. Overview ..... 29
2.7.2. Magnetic Catheter and Tracking Sensor ..... 29
2.7.3. Test Setup ..... 30
2.7.4. Controller Design ..... 32
2.7.5. Open Loop Tests ..... 32
2.7.6. Closed Loop Results ..... 34
2.7.7. Discussion ..... 36
2.8. Summary ..... 36
**Chapter 3 EM Tracking: Design and Implementation** ..... 38
3.1. Overview ..... 38
3.2. Introduction ..... 38
3.3. Theory of EM Tracking ..... 41
3.3.1. Overview ..... 41
3.3.2. EM Tracking Topologies ..... 41
3.3.3. Formulation of Governing Equations ..... 42
3.3.4. EM Tracking Subsystems ..... 43
3.4. Commercial EM Tracking Systems ..... 46
3.4.1. NDI Aurora ..... 46
3.4.2. Ascension trakSTAR ..... 47
3.4.3. Calypso 4D ..... 47
3.4.4. Superdimension iLogic System ..... 48
3.4.5. Veran SPINDrive ..... 48
3.5. Overview of System Iterations ..... 49
3.6. EM Tracking Simulations ..... 51
3.6.1. Overview ..... 51
3.6.2. Transmitter Array Optimisation ..... 51
3.6.3. Testing Methodology ..... 52
3.6.4. Coil Formations ..... 52
3.6.5. Formations with 9 and 16 Coils ..... 53

3.7. Magnetic Field Transmitter Design ..... 55
3.7.1. Magnetic Field Modelling ..... 55
3.7.2. Filament models ..... 56
3.7.3. ICNIRP Exposure Limits ..... 57
3.7.4. Determination of Required Field Strength and Frequency ..... 58
3.7.5. PCB Design ..... 59
3.8. Magnetic Field Sensors ..... 63
3.8.1. Sensor Types ..... 63
3.8.2. Induction Coil Theory ..... 65
3.8.3. NDI Sensor analysis ..... 67
3.8.4. Sensor Calibrator ..... 67
3.8.5. Test Setup ..... 69
3.8.6. Sensor Frequency Response ..... 69
3.8.7. Sensor Equivalent Circuit Model ..... 70
3.8.8. Linearity with Magnetic Field Amplitude ..... 71
3.8.9. Induced Voltage versus Induced Current Measurements ..... 73
3.9. Demodulation Methods ..... 74
3.9.1. Introduction ..... 74
3.9.2. Synchronous Demodulation ..... 74
3.9.3. Digital Filtering ..... 77
3.9.4. Asynchronous Demodulation ..... 79
3.9.5. Double Demodulation ..... 80
3.9.6. Effect of Frequency Mismatch ..... 81
3.9.7. Comparing Synchronous and Asynchronous Demodulation ..... 82
3.9.8. Efficient Matrix Demodulation Implementation ..... 84
3.9.9. Choice of Window Functions ..... 89
3.10. Circuit Design and Construction ..... 91
3.10.1. Constant AC Current Driver ..... 91
3.10.2. Driver Circuit Design and Stability Analysis ..... 92
3.10.3. Power Amplifier Stage ..... 96
3.10.4. Coupled Transmitter Analysis ..... 98
3.10.5. Signal Generation ..... 101
3.10.6. Current Driver Testing ..... 101
3.10.7. Sensor Amplifier ..... 103
3.10.8. Cable Considerations ..... 106
3.10.9. Current Waveform Summing Amplifier ..... 108
3.11. Simulink Demodulator Implementation ..... 109

3.11.1. Overview ..... 109
3.11.2. Data Acquisition ..... 110
3.11.3. Phase Shifter ..... 111
3.11.4. S Functions ..... 111
3.11.5. Filtering ..... 112
3.12. Undersampling for EM Tracking ..... 112
3.13. Low Cost Microcontroller Implementation of the Demodulator ..... 115
3.13.1. Arduino Due ..... 115
3.13.2. Demodulator Implementation ..... 115
3.13.3. ADC and Analog Front-end ..... 117
3.13.4. Filtering ..... 118
3.13.5. PC Interface ..... 119
**Chapter 4 EM Tracking: Testing and Results** ..... 120
4.1. Overview ..... 120
4.2. Tracking Accuracy Experimental Setup ..... 121
4.2.1. Static Test Setup ..... 121
4.2.2. Scribble Test Setup ..... 123
4.2.3. Error Calculation ..... 124
4.3. Calibration Methods ..... 124
4.3.1. Overview ..... 124
4.3.2. Calibration Algorithm ..... 124
4.3.3. Weighting Functions ..... 125
4.3.4. Calibration Example ..... 126
4.4. Testing P&O Algorithm Parameters ..... 128
4.4.1. Overview ..... 128
4.4.2. Choice of Least Squares Solver ..... 130
4.4.3. Effect of Function and Step Size Tolerances ..... 130
4.4.4. Bounded or Unbounded Input Variables ..... 131
4.4.5. Analytical or Numerical Jacobian ..... 131
4.4.6. Levenberg-Marquardt Scaling ..... 132
4.4.7. Improved Algorithm ..... 132
4.4.8. Final Parameter Choice ..... 133
4.5. Magnetic Field Testing ..... 134
4.5.1. Single Coil Tests ..... 134
4.5.2. Transmitter Array Testing ..... 134
4.5.3. Magnetic Noise Measurements ..... 136
4.5.4. Safety Limits ..... 138

4.6. Position and Orientation Accuracy Testing ..... 139
4.6.1. Static Position Tests ..... 139
4.6.2. Scribble Tests ..... 142
4.6.3. Dynamic Performance ..... 143
4.6.4. Position and Orientation Noise ..... 146
4.7. System Noise Analysis ..... 147
4.8. Transmitter Current Driver Performance ..... 150
4.8.1. Current Source Stability ..... 150
4.8.2. Induced Crosstalk Reduction ..... 151
4.9. Microcontroller Implementation Results ..... 152
4.9.1. Undersampling Examples ..... 152
4.9.2. Asynchronous Demodulator Performance ..... 153
4.9.3. Effect of Frequency Mismatch ..... 155
4.9.4. Undersampling Noise Tests ..... 156
4.9.5. Scribble Tests ..... 156
4.9.6. Static Position Tests ..... 158
4.10. Effect of Coil Size and Field Gradient ..... 159
4.10.1. Experimental Tests ..... 159
4.10.2. Simulation Results ..... 163
4.11. Discussion: Phase 1 Implementation ..... 164
4.11.1. System Accuracy ..... 164
4.11.2. System Stability ..... 166
4.11.3. Crosstalk Reduction ..... 166
4.11.4. Dynamic Performance ..... 166
4.12. Discussion: Phase 2 Implementation ..... 167
4.12.1. Undersampling ..... 167
4.12.2. System Accuracy ..... 167
4.12.3. Benefit of External ADCs ..... 168
4.12.4. System Cost ..... 168
4.13. Summary ..... 168
**Chapter 5 Pre-clinical EM Tracking Evaluation** ..... 170
5.1. Overview ..... 170
5.2. Clinical Background ..... 170
5.3. Portable EM Tracking System ..... 172
5.4. Inflatable Lung Model ..... 174
5.5. 3D CT Lung Models ..... 175
5.6. Registration ..... 177

5.6.1. Overview ..... 177
5.6.2. Rigid Landmark Registration Method ..... 177
5.6.3. Landmark Registration Example ..... 178
5.6.4. Hybrid Registration Method ..... 179
5.6.5. Hybrid Method Example ..... 180
5.7. Experimental Setup ..... 181
5.7.1. Bronchoscope ..... 181
5.7.2. Real Time Display ..... 181
5.7.3. EM Tracker ..... 182
5.7.4. Breathing Lung Model ..... 182
5.8. Results ..... 183
5.8.1. Landmark Registration ..... 183
5.8.2. Navigation Accuracy ..... 183
5.8.3. Hybrid Algorithm Registration ..... 185
5.8.4. Reaching the Target ..... 185
5.8.5. Breathing Motion ..... 187
5.9. Discussion ..... 191
**Chapter 6 Planar Magnetic Shielding for use with EM Tracking Systems** ..... 192
6.1. Overview ..... 192
6.2. Introduction ..... 192
6.3. Background Theory ..... 193
6.3.1. Method of Images ..... 193
6.3.2. Eddy Current Distortion and Higher Frequency Effects ..... 195
6.4. Simulations ..... 195
6.4.1. Finite Element Modelling ..... 195
6.4.2. Shielding Performance ..... 196
6.5. Experimental Setup and Methods ..... 198
6.5.1. Magnetic Measurement Circuit ..... 198
6.5.2. Shielding Tests ..... 199
6.5.3. Shielding Materials ..... 200
6.5.4. Multi-Dipole Transmitter Board ..... 201
6.5.5. Single Axis Position Accuracy Tests ..... 202
6.5.6. 5-DOF Position Accuracy Tests ..... 202
6.6. Results ..... 202
6.6.1. Frequency Response of Shielding ..... 202
6.6.2. Shielding Performance with Distance ..... 205
6.6.3. Linearity of Shield Materials ..... 206

6.6.4. Method of Images ..... 207
6.6.5. Position Accuracy Performance ..... 207
6.7. Discussion ..... 211
6.7.1. Shielding Performance ..... 211
6.7.2. Positioning Accuracy ..... 211
6.7.3. Linearity ..... 212
6.8. Conclusion ..... 213
**Chapter 7 Frequency Effects in EM Tracking** ..... 214
7.1. Overview ..... 214
7.2. Frequency Response of Conductive Distorters ..... 214
7.2.1. Introduction ..... 214
7.2.2. Modelling ..... 215
7.2.3. Simulation ..... 217
7.2.4. Experimental Setup ..... 221
7.2.5. Results ..... 222
7.2.6. Discussion ..... 226
7.3. Frequency Response of Human Tissue ..... 227
7.3.1. Introduction ..... 227
7.3.2. FEMM Simulations ..... 227
7.3.3. Experimental Setup ..... 228
7.3.4. Results ..... 230
7.3.5. Discussion ..... 239
7.4. Conclusion ..... 240
**Chapter 8 Summary and Future Work** ..... 242
8.1. Summary of Thesis Contributions ..... 242
8.2. Proposals for Future Work ..... 244
8.2.1. Optimised Transmitter Configuration ..... 244
8.2.2. Consolidation of Circuit Subsystems ..... 244
8.2.3. Commercialisation and Medical Device Classification ..... 244
8.2.4. Miniature Transmitter with External Sensor Array ..... 245
8.2.5. Breathing Motion Compensation ..... 245
**Bibliography** ..... 247

# List of Figures

Figure 2.1: Magnetic force on a permanent magnet due to an applied field. ..... 7
Figure 2.2: Magnetic torque on a bar magnetic due to a uniform field..... 7
Figure 2.3: Cross section of the concept magnetic catheter. ..... 9
Figure 2.4: Deflection testing of different magnetic tips and sheath materials..... 10
Figure 2.5: Calculation of tip deflection. ..... 10
Figure 2.6: Electromagnetic coil actuator. ..... 11
Figure 2.7: Simulated magnetic field and gradient of the electromagnet along its central axis with a current of 20 A. ..... 11
Figure 2.8: Simulated normalised field and gradient with axial distance from the electromagnet. ..... 12
Figure 2.9: Simulated contour plot of the magnetic field distribution around the electromagnet. ..... 12
Figure 2.10: Magnetic tips used in the testing. Here each sphere has a 2 mm diameter and each cylinder is 2.5 mm in length and diameter..... 12
Figure 2.11: Comparing deflections with (top row) and without (bottom row) a silicone rubber sheath. ..... 13
Figure 2.12: Comparing the deflections of chains of spherical magnets with and without a Pebax 2533 outer sheath. ..... 14
Figure 2.13: Deflections of 10 spheres in the chain at 40 mm and 80 mm from the electromagnet. A Pebax 2533 sheath was used in this test. ..... 15
Figure 2.14: Comparing deflection of spheres and cylinders with and without a Pebax 2533 sheath with respect to a uniform applied magnetic field strength. ..... 15
Figure 2.15: In this analytical model for two magnetic spheres in contact, the first sphere is rigidly fixed in place and aligned with the x-axis. The centre point of the second sphere is free to move in a circular path to some angle $\phi$ relative to the first sphere and also to rotate around its own axis by some angle $\psi$. A uniform external magnetic field $B$ is also present and points in the $y$ direction. ..... 19
Figure 2.16: Simplified test setup schematic. ..... 23
Figure 2.17: Experimental setup showing the position of the Helmholtz coils and magnetic sphere chain deflection. The contour plot of the magnetic field is also shown with the field normalised to the value at the centre of the coils. From simulation, the field in the test region varies by less than 0.1 %..... 23
Figure 2.18: An example of the deflected chain showing how the angle $\phi$ between each sphere is calculated. The first sphere is rigidly held in place with a small clamp. The clamp

was specially designed to allow free movement of the spheres around the first constrained sphere ..... 24
Figure 2.19: Comparing tip deflection in the case of two magnetic spheres from theoretical modelling and experimental testing. Error bars indicate standard deviation..... 25
Figure 2.20: Comparing tip deflection in the case of three magnetic spheres from theoretical modelling and experimental testing. Error bars indicate standard deviation..... 25
Figure 2.21: Comparing tip deflection in the case of four magnetic spheres from theoretical modelling and experimental testing. Error bars indicate standard deviation..... 26
Figure 2.22: Error in deflection angle between the experimental results and theoretical model for each of the three cases investigated ..... 27
Figure 2.23: The simulated position of the four sphere case with an applied field of 35 mT along *y*. The arrows indicate the direction of magnetisation. The dashed lines show the position of the spheres in the absence of the anisotropic energy term. The magnetisation of the first sphere is assumed to be aligned with the *x*-axis in the absence of the anisotropic energy term. ..... 28
Figure 2.24: (a) Permanent magnet tip and (b) position sensing coil wound on the outside.. 30
Figure 2.25: Test setup showing the catheter model with the magnet tip with the position sensor attached. The sensor data is processed by the PC which then sends the control signals to a high current power supply which, in turn, drives the electromagnet..... 31
Figure 2.26: Test setup with an electromagnet coil placed above the tracking systems transmitter. By controlling the current in the coil, the position of the magnetic catheter tip can be controlled. ..... 31
Figure 2.27: Closed loop control block diagram. ..... 32
Figure 2.28: Open loop step input tests showing the *z* displacement of the sensor and the corresponding input coil current..... 33
Figure 2.29: Open loop ramp input current applied to the electromagnet coil. The attractive force becomes highly nonlinear in close proximity to the electromagnet. Beyond 10 A, very non-linear behaviour results. ..... 33
Figure 2.30: Closed loop response to a step input set point. ..... 34
Figure 2.31: Closed loop performance with a staircase shaped trajectory. ..... 35
Figure 2.32: Closed loop performance with a sinusoid trajectory. Higher frequencies are more difficult to track accurately. ..... 35
Figure 2.33: Unstable behaviour of the system with incorrect controller gain settings. ..... 36
Figure 3.1: Coordinate system for the tracking algorithm. The sensor is positioned at $(x, y, z)$ with an orientation denoted by $\theta$ and $\varphi$. The magnetic field resulting from the $i^{th}$ coil is indicated, and the associated flux is determined using the dot product between the sensor's directional unit vector and the magnetic field at that point. ..... 43
Figure 3.2: Subsystem overview. ..... 45

Figure 3.3: NDI Aurora system with generator and processor unit. ..... 46
Figure 3.4: A selection of Aurora sensors..... 46
Figure 3.5: Ascension trakSTAR. ..... 47
Figure 3.6: (a) Wireless tracker and (b) EM transmitter board for the Calypso 4D system [92]. ..... 47
Figure 3.7: SuperDimension transmitter board [96]. ..... 48
Figure 3.8: (a) EM transmitter and (b) instruments with built in EM sensors for the Veran SPINDrive system [98]. ..... 49
Figure 3.9: Transmitter array development. ..... 51
Figure 3.10: Data acquisition hardware. ..... 51
Figure 3.11: Four arrangements of eight coils tested to find an optimum arrangement. ..... 53
Figure 3.12: Comparing 8, 9 and 16 coil formations. ..... 54
Figure 3.13: Position error in relation to the number of points used in multi-start algorithm. ..... 55
Figure 3.14: Comparing multi-start and single-start point algorithms with increasing noise power. Twenty start points are used in this case. ..... 55
Figure 3.15: (a) Planar PCB coil which consists of 25 turns, side length of the PCB is 72 mm, trace thickness of 0.5 mm and copper thickness of 70 µm. (b) Vector diagram for magnetic field due to a filament current *I* where ***a*** is a vector in the direction of the filament, ***b*** is a vector pointing from an observation point to the end of the filament, and ***c*** is a vector pointing from to the start of the current carrying filament. ..... 56
Figure 3.16: Error between filament model and a direct integration of the current density over a 7 cm length of PCB trace. ..... 57
Figure 3.17: ICNIRP exposure guidelines for low frequency magnetic flux density [109]. . 57
Figure 3.18: Scaled ICNIRP limits showing the maximum allowable induced voltage. ..... 59
Figure 3.19: Drop-off magnetic field with radial distance from a planar coil with increasing angle to the central axis. ..... 59
Figure 3.20: Predicted magnetic flux density at 2 cm from the coil with 500 mA for different side lengths and number of turns. ..... 61
Figure 3.21: Predicted coil inductance for different side lengths and number of turns. ..... 62
Figure 3.22: Predicted coil resistance with for different side lengths and number of turns... 62
Figure 3.23: Simulated contour plot showing the magnetic flux density around a single coil per unit Amp. ..... 62
Figure 3.24: Layout of each filament for a two layer 19 turn coil with side length of 15mm. ..... 63
Figure 3.25: Filament layout on each PCB layer. ..... 63
Figure 3.26: Induction sensor with ferromagnetic core ..... 66
Figure 3.27: Aurora 5-DOF sensor by NDI ..... 67

Figure 3.28: Typical Helmholtz coil formation [121]. ..... 68
Figure 3.29: Predicted axial magnetic field of the calibrator when carrying 1 A. ..... 68
Figure 3.30: Calibrator with sensor inserted. ..... 69
Figure 3.31: Cross section of calibrator design. ..... 69
Figure 3.32: Low frequency response of the Aurora 610057 sensor. ..... 70
Figure 3.33: Wide band frequency response of the Aurora 610057 sensor with equivalent circuit model fit. ..... 70
Figure 3.34: Equivalent circuit model for an induction sensor ..... 71
Figure 3.35: Output of the sensor with increasing amplitude of applied magnetic field at 25 kHz. ..... 72
Figure 3.36: Sensor inductance with applied DC magnetic field. ..... 73
Figure 3.37: Basic circuits for (a) induced voltage measurement and (b) induced current measurement. ..... 74
Figure 3.38: An example waveform containing a signal of interest buried under noise and interfering signals. ..... 76
Figure 3.39: Simulated demodulator output. ..... 76
Figure 3.40: Frequency spectrums of the input signal, and the demodulated output before and after filtering. ..... 77
Figure 3.41: General structure of an FIR filter. ..... 78
Figure 3.42: General structure of IIR filters. ..... 79
Figure 3.43: Input signals and demodulation reference signals for the synchronous and asynchronous case. ..... 83
Figure 3.44: Comparing the output of each demodulation quadrature component for the synchronous and asynchronous case. ..... 83
Figure 3.45: Comparing the output phase of two channels of the demodulator for the synchronous and asynchronous case. ..... 84
Figure 3.46: Input signal to the demodulator. ..... 87
Figure 3.47: Settling time of the demodulator with an FIR low pass filter with 500 taps. ..... 87
Figure 3.48: Comparing FIR and IIR filters with similar stopband and passband characteristics. ..... 88
Figure 3.49: Comparing the settling time of IIR and FIR filters for a given stopband attenuation. ..... 88
Figure 3.50: Demonstrating the performance of an FIR filter in terms of percentage error of a demodulated signal in relation to the SNR of the signal. ..... 89
Figure 3.51: Calculation time for demodulation for different sample lengths and numbers of inputs. ..... 89
Figure 3.52: Filter coefficients for each window function. ..... 90
Figure 3.53: Frequency response of each window function. ..... 91

Figure 3.54: Block diagram of each driver channel. ..... 92
Figure 3.55: Constant current driver board. ..... 92
Figure 3.56: Constant current op-amp configuration. ..... 93
Figure 3.57: Constant current op-amp configuration with inductive load. ..... 93
Figure 3.58: Simulated open loop frequency response of the LM7171. ..... 94
Figure 3.59: Compensated op-amp configuration. ..... 95
Figure 3.60: Open loop frequency response of $V_{fb}(s)/V_{in}(s)$. ..... 95
Figure 3.61: Closed loop frequency response of $V_{fb}(s)/V_{in}(s)$. ..... 96
Figure 3.62: Phase margin of $V_{fb}(s)/V_{in}(s)$ with variation with $C_c$ and $R_c$. ..... 96
Figure 3.63 Typical Class B amplifier. ..... 97
Figure 3.64: Thermal bonding of output transistors and biasing diodes. ..... 98
Figure 3.65: Basic schematic of the constant AC current source. A Class B amplifier is used to boost the output power of a high speed op-amp. The current through the coil is fed back using a sense resistor. To increase the phase margin of the system a series combination of a resistor and capacitor are placed in parallel with the coil for compensation. The sinusoidal reference source is generated using DDS with an AD9833 IC. ..... 98
Figure 3.66: Two closed loop controlled coils with mutual coupling. ..... 99
Figure 3.67: Attenuation of unwanted induced currents for $I_1(s)/V_2(s)$. ..... 100
Figure 3.68: Uncompensated output for 20 kHz input signal. Excessive ringing results due to the small phase margin. ..... 102
Figure 3.69: Compensated output for 20 kHz input signal. No ringing is observed on the output. ..... 102
Figure 3.70: Turn on time for the closed loop system. ..... 103
Figure 3.71: Closed loop response to step changes in amplitude. ..... 103
Figure 3.72: Experimental frequency response of the closed loop system measured using a Powertek GP-12 Gain-Phase Analyser. ..... 103
Figure 3.73: Internal structure of the INA128 instrumentation amplifier [132]. ..... 105
Figure 3.74: Frequency response of the INA128 [132]. ..... 105
Figure 3.75: Basic schematic of the instrumentation amplifier circuit. The gain selector resistor is not shown in this figure. ..... 105
Figure 3.76: Instrumentation amplifier used to detect the voltage induced in the search coil. The circuit is placed in a grounded steel container to shield the circuit from the magnetic field generated by the source coils. A gain of approximately 500 is used. ..... 106
Figure 3.77: Experimental frequency response of instrumentation amplifier and filtering. 106
Figure 3.78: Test setup for measuring emitted magnetic field from a cable. ..... 108
Figure 3.79: Summing amplifier schematic ..... 108
Figure 3.80: Summing amplifier constructed on Veroboard. ..... 109
Figure 3.81: Simulink block diagram per channel. ..... 110

Figure 3.82: PCI 6259 DAQ card. 110
Figure 3.83: Effects of undersampling. Frequencies above $f_s / 2$ are shifted to frequencies in the range of 0 to $f_s / 2$. It is as if the input frequency spectrum is folded back upon itself as shown [138]. 113
Figure 3.84: A 1 kHz sine wave sampled at 20 kHz, 4 kHz and 800 Hz. When undersampled, the apparent frequency reduces to 200 Hz. 114
Figure 3.85: Simulated undersampled frequency spectrum. An 8 kHz sample rate is used to sample a multi-frequency signal with components at 20.25, 21.25 …. 27.25 kHz 114
Figure 3.86: Sample signal multiplied by a carrier at 20.25 kHz, all frequencies are again shifted. 115
Figure 3.87: Arduino Due microcontroller [139]. 115
Figure 3.88: Block diagram of the Arduino Due demodulator software. 117
Figure 3.89: Block diagram for the analog front-end circuit. 118
Figure 4.1: (a) Vertical sensor holder, (b) horizontal sensor holder. 121
Figure 4.2: Duplo block dimensions. 122
Figure 4.3: Test setup for static position accuracy tests. The sensor was placed at the centre of a Lego Duplo block and moved in discrete steps around the base plate which was mounted directly over the coil array. The testing was carried out in a volume approximately 25 cm × 25 cm × 25 cm . 122
Figure 4.4: Coordinate system for the test setup. 122
Figure 4.5: Duplo board mounted over the coil array. 122
Figure 4.6: Test setup for scribble test. The sensor is placed in the Duplo block and "scribbled" around a Perspex plane by hand and its position is calculated and recorded. The *z* error from the plane is then calculated. Four different orientations of the sensor were tested per plane. 123
Figure 4.7: Representation of the scribble tests. The sensor is moved at random over a 2D plane. The error is the difference between the actual *z* position of the plane and the calculated value *z'*. This allows for rapid sampling of thousands of points to arrive at a statistically valid representation of the system performance. 123
Figure 4.8: Magnetic field measurements after calibration perpendicular to the test coil at $x$ = 31.2 mm and $y$ = 31.2 mm. 126
Figure 4.9: Plot of the weighted residuals with a mean error of 5 %. Results are normalised to the first point. 127
Figure 4.10: Comparing weighting functions. 128
Figure 4.11: Diagram showing the position of the test points and the transmitter array. 129
Figure 4.12: Comparing filament model with experimental data along the central axis of a single coil. 134
Figure 4.13: Error plot between model and experimental data along the central axis of a

single coil. ..... 134
Figure 4.14: Coil array layout. All 8 coils are mounted on a Perspex sheet with a sheet side length of 30 cm. Simulation indicated this particular arrangement is optimum in comparison to other arrangements (see Chapter 3). ..... 135
Figure 4.15: Magnetic field along the central axis of the transmitter array ($x = 0$, $y = 0$) comparing the theoretical and experimental result for each of the eight coils. ..... 135
Figure 4.16: 3D scatter plot showing the magnetic field of a single coil in the array. ..... 136
Figure 4.17: Magnetic field noise from each of the 8 coils. ..... 137
Figure 4.18: Magnetic field noise at each of the carrier frequencies with the transmitter disabled. ..... 138
Figure 4.19: Minimum safe distance simulation based on each coil carrying 250 mA in the range 3 kHz to 100 kHz as stipulated by the ICNIRP guidelines. The simulation is centred over the coil array. The contour plot indicates the minimum distance (in mm) from the coils to be within the occupational safety limits. For safe human exposure, a patient must not be exposed to the regions shown. ..... 139
Figure 4.20: Graph showing the RMS accuracy of the system for determining position of the sensor. Three tests were carried out with the sensor rigidly secured in different directions. 216 points were taken in each orientation. ..... 140
Figure 4.21: Graph showing the RMS accuracy of the system for determining the orientation of the sensor. Three tests were carried out with the sensor rigidly secured in different directions. 216 points were taken in each orientation. ..... 140
Figure 4.22: A trajectory showing the performance of the *x*, *y* and *z* coordinate errors for 72 points over two planes. The sensor was orientated along the *z* axis. ..... 141
Figure 4.23: All 8000 scribble test points data plotted for an $-x$ orientated sensor. Each point was arranged in increasing distance from the magnetic source. The mean *z* error is 0.8 mm with a standard deviation of 1.3 mm. If we consider only values within the $95^{th}$ percentile, this error decreases to 0.6 mm with a standard deviation of 0.6 mm. ..... 142
Figure 4.24: Results of scribble test for the $-x$ orientation test on 4 planes. Ideally all points are located on each of the 4 planes. Off plane points indicate errors. ..... 143
Figure 4.25: Test setup for the sensor attached to pendulum. ..... 144
Figure 4.26: Plot of every point gathered during the recorded pendulum motion. ..... 144
Figure 4.27: *x* axis displacement of the pendulum with time. An average sample rate of 22.6 Hz was used. ..... 145
Figure 4.28: Pendulum time displacement with offline measurement with higher sample rate of 64.1 Hz. ..... 145
Figure 4.29: *x* and *y* trajectory of the pendulum when moving in a circular motion. ..... 146
Figure 4.30: Sensor noise displacement for (a) 500 samples, (b) 5000 samples and (c) 5000 samples with an increased sample rate. ..... 147

Figure 4.31: Noise power of the sensor subsystem with a moving average applied to smooth the data. ..... 148
Figure 4.32: Linear *x* scale noise power distribution. ..... 148
Figure 4.33: Comparing the transmitter current noise and the resulting magnetic field noise. ..... 148
Figure 4.34: Swept demodulator output in 1 Hz steps over the operating frequency range. 150
Figure 4.35: Spurious frequency components in the operating frequency range. ..... 150
Figure 4.36: Results of 12 hour currents tests in 3 arbitrary coils. Each current is normalized to its mean value. Coil 2 varied with a standard deviation of 0.0219 %, coil 3 was 0.0113 % and coil 4 was 0.0099 %..... 151
Figure 4.37: Comparing the frequency spectrum of an oversampled and undersampled signal. The first figure uses a sample rate of 160 kHz, while the second is sampled at 8 kHz. Note how the frequency of each signal component have been shifted to a band between 0 and 4 kHz. The new order of the components is now: [24.25, 23.25, 25.25, 22.25, 26.25, 21.25, 27.25, 20.25] kHz which appear from left to right on the undersampled waveform..... 153
Figure 4.38: Time response of the demodulator for a series of input amplitudes. A 20.25 kHz sinusoid signal is measured in the presence of a second signal at 21.25 kHz. A sample rate of 125 μs is used. Five different amplitudes ranging from 100 mV to 1 V are shown. The filter takes approximately 60 ms to settle. ..... 154
Figure 4.39: Linearity of demodulator system. A signal at 20.25 kHz was applied to the ADC and its amplitude varied from 12.5 mV to 500 mV. A 0.31 mV offset is observed when a best fit line is calculated..... 154
Figure 4.40: Effect of frequency mismatch of the demodulator when sampling at 8 kHz. Three signals at 1 kHz, 10 kHz, and 30 kHz were tested. The flat response of the Butterworth filter can clearly be seen here. ..... 155
Figure 4.41: Frequency response of the IIR filter. ..... 155
Figure 4.42: Noise spectrum of the analog front end with different sample rates. At lower sample rates higher frequency noise is folded back onto the lower frequencies, hence increasing the noise density. ..... 156
Figure 4.43: Results of scribble test on 4 planes. Ideally all points are located on each of the 4 planes, off plane points indicate errors. The average error was 1.2 mm away from the plane. ..... 157
Figure 4.44: Scribble test data scatter plot. All 6000 points all plotted against the distance from the centre of the emitter array. ..... 158
Figure 4.45: Results of a 64 point test. The sensor is statically positioned at a number of points in the operating region. The resulting RMS error is 0.99 mm. ..... 159
Figure 4.46: Multi-coil board for gradient tests. ..... 161
Figure 4.47: Magnetic field plots for each coil size showing the experimental data (circles)

and the theoretical modelling (continuous lines) after calibration. ..... 161
Figure 4.48: Experimental gradient of each coil. ..... 162
Figure 4.49: Percentage error between the experimental data and the model data for each coil size. ..... 162
Figure 4.50: Position error in the z direction for each coil size. ..... 163
Figure 4.51: Simulated position accuracy with full coil array with different size coils. ..... 164
Figure 4.52: Simulated coil array error with constant field offset of 100 pT with different size coils. ..... 164
Figure 5.1: Perspex enclosure for the transmitter which measures 2 cm × 30 cm× 30 cm.. 172
Figure 5.2: Electronics enclosure for the system which houses the coil driver circuit, current waveform summing circuit, sensor amplifier and USB DAQ. ..... 173
Figure 5.3: Electronics enclosure with sensor, power, transmitter and USB ports. ..... 173
Figure 5.4: Full system showing the electronics enclosure, transmitter and display (connected to a laptop). ..... 173
Figure 5.5: Lung breathing apparatus. A set of solenoid valves are used to control the pressure in a sealed vessel. A transistor circuit controlled by a microcontroller is used to enable each valve in sequence to replicate the human breathing cycle. ..... 174
Figure 5.6: Plasticised pig lung when fully inflated. ..... 174
Figure 5.7: GE Discovery CT750 CT scanner and the inflated lungs within the vacuum chamber. A scan resolution of 0.65 mm was used for the scan. ..... 175
Figure 5.8: The inflatable lung model setup for the CT scan when (a) inflated and (b) deflated. Below each lung there is a laminated scaled image of the deflated lungs used for lining up the model in a repeatable manner. ..... 176
Figure 5.9: Segmented model of the breathing lung model. ..... 176
Figure 5.10: Example of landmark registration method in 2D. ..... 179
Figure 5.11: Simulated performance of the registration algorithm when applied to a 3D segmented lung model. The algorithm minimises the distance between each test point and the centre line as seen in the figure. (a) shows the point alignment before applying the algorithm and (b) shows the resulting transformed data set. ..... 181
Figure 5.12: View from the bronchoscope inside the phantom with the sensor extended out from the distal end of the instrument port. ..... 181
Figure 5.13: MATLAB display showing the 3d lung model and the calculated position (indicated with a red dot). ..... 182
Figure 5.14: Lung chamber placed above the transmitter array. Additional spacers are added between the transmitter and the chamber to avoid saturation of the sensor. ..... 182
Figure 5.15: Landmark registration of the branch points away from the central airway. Overall registration error of 2.9 mm was recorded. ..... 183
Figure 5.16: Overlay of points gathered during navigation of the main airway after

registration. Erroneous points outside the model are generally due to positioning errors of the inflated lung model relative to the CT scan data. In this test, 94.3% of the 246 test points were found to be inside the airway. ..... 184
Figure 5.17: Results of a navigation of numerous airways. Accuracy decreases away from the main airways due to misalignment of the lung model with the CT scan model. ..... 184
Figure 5.18: Results of the hybrid registration algorithm showing the centreline and the registered dataset. 83.4 % of the points were found to be within the airways. ..... 185
Figure 5.19: Shows the trajectory of a navigation between the trachea and the two target points. The sensor was calculated as being within 2.6 mm from the first target and 3.2 mm from the second target. ..... 186
Figure 5.20: Motion of the sensor towards the targets in *x*, *y* and *z* with respect to time. ..... 186
Figure 5.21: Screenshot of the navigation along this airway during the experiment. ..... 187
Figure 5.22: Displacement of sensor with time due to breathing cycle. The sensor was positioned in three positions, one at the carina, a second at a central location in the lung and finally at a distal branch. The maximum amplitude of displacement was observed in the centre of the lung. ..... 187
Figure 5.23: Individual vector component displacement of senor with time when positioned at a central location in the lung. Maximum displacement is observed in the *z* direction, which in this case is vertical ..... 188
Figure 5.24: Displacement of the sensor with breathing enabled also showing the logic control signal for the breathing valves. A value of 1 indicates inhalation and 0 indicates exhalation. ..... 188
Figure 5.25: Displacement of the sensor in *x*, *y* and *z* along with the breathing logic control signal. ..... 189
Figure 5.26: Displacement of the sensor for a range of positions over a 25 s breathing period. ..... 189
Figure 5.27: Navigation of the main airways with breathing enabled. Breathing motion causes a larger number of the points to be outside the airways during navigation. 52.9% of all test points were found to be within the airway. ..... 190
Figure 6.1: Method of images for shields of finite thickness. The coil placed above the shield at z0 carrying current I is mirrored below the surface by an infinite number of identical coils carrying a current dependent on the permeability of the shield. ..... 194
Figure 6.2: Experimental setup for axial testing of the shielding performance. The distance z, measured from the centre of the sensor, indicates the distance of the sensor from the transmitter and r indicates radial displacement. For the finite element simulations, an identical layout and notation is used. ..... 196
Figure 6.3: Finite element simulations showing the flux patterns of the transmitter coils in the following cases: (a) no shield or distorter, (b) with shield no distorter, (c) no shield with

distorter, (d) shield with distorter. The shield effectively blocks flux lines from reaching the distorter hence minimizing its impact on the flux above the shield. ..... 196
Figure 6.4: Simulations results for the signal gain associated with each shield material. ... 197
Figure 6.5: Simulations results for the field errors due to a large ferromagnetic plate placed below the shield. ..... 197
Figure 6.6: Error contour plot showing the region directly over the shield where fringing effects of the distorter cause larger errors. The errors increase with distance from the centre of the shield and as the shield edge is approached ..... 198
Figure 6.7: Circuit diagram used for the measuring magnetic field output from the sensor. The basic topology is a trans-impedance amplifier which converts the induced current $I_r$ in the receiver coil into a voltage. This reduces the effect of the parasitic capacitance $C_r$ of the receiver and the compensation network of $R$ and $C$ improve the low frequency response.. 199
Figure 6.8: Frequency response of the magnetic amplifier circuit. This response is the gain between the output voltage on the receiver amplifier and the applied transmitter current. A flat response is observed between 100 Hz and 200 kHz, with a deviation of less than 0.5dB in this range. ..... 199
Figure 6.9: (a) Shielded search coil manufactured by NDI for their Aurora tracking system. ( b) Setup for axial single transmitter tests. (c) Single PCB multi-dipole transmitter, which consists of 8 groups of 25 coils. Each group transmits at a different frequency. (d) Ferrite shield comprised of multiple ferrite tiles. (e) Ferromagnetic distorter used for the tests. The steel sheet measures $80\text{ cm} \times 50\text{ cm} \times 1\text{ cm}$ and has a relative permeability of approximately 500. (f) Test setup for 5-DOF system. ..... 200
Figure 6.10: Frequency response of the sensor and amplifier in the presence of the shield materials. ..... 203
Figure 6.11: Gain in the magnetic field due to the shield materials ..... 203
Figure 6.12: Field errors due to the distorter at distances of (a) 24 mm, (b) 120 mm and (c) 216 mm. ..... 204
Figure 6.13: Shielding performance with axial displacement from the transmitter at (a) 500 Hz and (b) 30 kHz. ..... 205
Figure 6.14: Linearity of ferromagnetic shield materials at 500 Hz (a) and 30 kHz (b). Steel is noted for having a higher non-linearity; however due to the small ranges of applied fields this is negligible. ..... 206
Figure 6.15: Position error frequency dependence of shield materials in the presence of the steel distorter. Three sensor positions perpendicular and along the central axis of the transmitter coil are used: (a) 24 mm, (b) 120 mm and (c) 216 mm. ..... 208
Figure 6.16: Position error with axial displacement from the transmitter at (a) 500 Hz and (b) 30 kHz. ..... 209
Figure 6.17: Error results of the full 5-DOF tracking test. Each test consists of 96 points

spread over a 25 cm × 25 cm × 25 cm volume with the following shield and distorter arrangements: (a) No shield or distorter, (b) No shield with distorter, (c) Ferrite shield with distorter and (d) MuMetal shield and distorter. Each graph shows the error as a function of the *z* displacement from the planar transmitter. The mean RMS position error in each case is (a) 1.2 mm, (b) 67.3 mm, (c) 1.8 mm and (d) 2.3 mm. ..... 210
Figure 6.18: Orientation error results of the full 5-DOF tracking test with the following shield and distorter arrangements: (a) No shield or distorter, (b) No shield with distorter, (c) Ferrite shield with distorter and (d) MuMetal shield and distorter. The mean RMS orientation error in each case is (a) 1 °, (b) 115.1 °, (c) 1.9 °, and (d) 2.1 °. ..... 210
Figure 7.1: Coupling schematic between the transmitter, the distorter and the sensor. ..... 215
Figure 7.2: Simulated field measurement frequency response, $D(s)$, due to a distorter. ..... 217
Figure 7.3: Schematic representation of the test setup used for finite element simulation and experimental tests. ..... 217
Figure 7.4: Simulated frequency response error, $D(s)$, from five sensor locations with the conductive disk placed at 39.9 mm from the transmitter coil. ..... 218
Figure 7.5: Simulated frequency response error, $D(s)$, from five sensor locations with the conductive disk placed at 135.9 mm from the transmitter coil. ..... 219
Figure 7.6: Simulated frequency response error, $D(s)$, from five sensor locations with the conductive disk placed at 212.7 mm from the transmitter coil. ..... 219
Figure 7.7: Simulated frequency response error, $D(s)$, surface plot for ten different disc locations with the sensor coil placed at 35.2 mm from the transmitter coil. ..... 220
Figure 7.8: Simulated frequency response error, $D(s)$, surface plot for ten different disc locations with the sensor coil placed at 131.2 mm from the transmitter coil. ..... 220
Figure 7.9: Simulated frequency response error, $D(s)$, surface plot for ten different disc locations with the sensor coil placed at 227.2 mm from the transmitter coil. ..... 221
Figure 7.10: The aluminium disc which was used as the conductive distorter for all tests. The disc is 3 mm thick, with an inner radius of 13.25 mm and an outer radius of 105.25 mm. . 222
Figure 7.11: Experimental setup used for the testing system distortion. The transmitter coil is fixed on the Perpex base, with the sensor positioned using standard Lego Duplo blocks. The height of the disk is changed by adding Duplo blocks, two of which are rigidly secured to the disc itself. ..... 222
Figure 7.12: Experimental frequency response error, $D(s)$, from five different sensor locations with the conductive disk placed at 39.9 mm from the transmitter coil. ..... 223
Figure 7.13: Experimental frequency response error, $D(s)$, from five different sensor locations with the conductive disk placed at 135.9 mm from the transmitter coil. ..... 224
Figure 7.14: Experimental frequency response error, $D(s)$, from five different sensor locations with the conductive disk placed at 212.7 mm from the transmitter coil. ..... 224
Figure 7.15: Experimental frequency response error, $D(s)$, surface plot from ten different

disc locations with the sensor coil placed at 35.2 mm from the transmitter coil. ..... 225
Figure 7.16: Experimental frequency response error, *D*(*s*), surface plot from ten different disc locations with the sensor coil placed at 131.2 mm from the transmitter coil. ..... 225
Figure 7.17: Experimental frequency response error, *D*(*s*), surface plot from ten different disc locations with the sensor coil placed at 227.2 mm from the transmitter coil. ..... 226
Figure 7.18: Simulated attenuation of a cylindrical body model 350 mm in diameter and 200 mm in height with a conductivity of 0.1 S/m. ..... 228
Figure 7.19: Circuit diagram of the transmitter and receiver circuit with trans-impedance amplifier. ..... 229
Figure 7.20: Experimental gain between the sensor amplifier output and transmitter input current at an axial displacement of 280 mm. ..... 230
Figure 7.21: (a) Test rig showing the transmitter and receiver coil along with the Lego Duplo positioning fixture. (b) Photo of a test subject during a test. ..... 230
Figure 7.22: Surface plot of the amplifier gain with a test subject between the transmitter and sensor for varying sensor position. ..... 231
Figure 7.23: Gain error surface plots for three different test subjects. ..... 232
Figure 7.24: Surface plot showing the interpolated -3 dB error point for each test position. ..... 233
Figure 7.25: Surface plot showing the interpolated 5% error frequency position for each test point. ..... 233
Figure 7.26: Surface error plots showing the gain error at 600 kHz, 800 kHz and 1MHz. . 234
Figure 7.27: High frequency equivalent circuit of the transmitter and test subject. ..... 235
Figure 7.28: Comparing the effect of a Perspex spacer between the test subject and the transmitter. ..... 236
Figure 7.29: Comparing the effect of capacitive coupling between the sensor and the body by adding a copper foil shield. ..... 236
Figure 7.30: Schematic of the sensor amplifier including parasitic capacitance due to the human body. ..... 237
Figure 7.31: Simplified schematic used to determine the analytical output of the amplifier. ..... 237
Figure 7.32: Simulated effect of parasitic capacitance on the gain error in the receiver. .... 238
Figure 7.33: Revised schematic showing a capacitively-coupled voltage into the system from the test subject. ..... 239

# List of Tables

Table 2.1: Comparison of the Young's modulus of common catheter materials [32]–[34]. ..... 9
Table 2.2: Deflection angle comparison for different magnet groups with and without an outer sheath. The sheath material was silicone rubber in this test. A magnetic field strength of 1 mT was used. ..... 13
Table 2.3: Deflection angle for an increasing number of spheres in the chain with and without an outer sheath. Pebax 2533 was used with this test. A magnetic field strength of 10.8 mT was used for this test. ..... 14
Table 3.1: EM tracking design iterations. ..... 50
Table 3.2: Comparing the simulated performance of each coil arrangement. ..... 53
Table 3.3: ICNIRP Limits for occupational exposure where *f* is the frequency in Hz. ..... 58
Table 3.4: PCB manufacturing tolerances. ..... 60
Table 3.5: Comparing sensor technologies and sensor arrangements of different EM tracking systems. ..... 65
Table 3.6: Comparison of cable shielding performance ..... 107
Table 3.7: Delays required to generate cosine reference signal. ..... 111
Table 4.1: Comparing weighting function value standard deviation. ..... 127
Table 4.2: Percentage error after calibration. ..... 128
Table 4.3: Comparison between the LM and TR algorithms. ..... 130
Table 4.4: Effect of function tolerance on position error, iteration count and algorithm runtime. ..... 131
Table 4.5: Comparison between bounded and unbounded solution space. ..... 131
Table 4.6: Comparing the effect of using either a numerical or analytical form of the objective functions Jacobian. ..... 132
Table 4.7: Effect of scaling in the LM algorithm ..... 132
Table 4.8: Algorithm convergence rate for worst case scenario of the initial solution estimate ..... 133
Table 4.9: Comparing LM and TR with improved algorithm ..... 133
Table 4.10: Magnetic field noise at each carrier frequency with and without the transmitter. "On" refers to when the transmitter is fully engaged and powered on; "Off" refers to when it is fully powered down. ..... 137
Table 4.11: Position and orientation accuracy of the shielded sensor. ..... 139
Table 4.12: Comparison of probe types. ..... 141
Table 4.13: Approximate noise voltage densities for each stage of the sensor subsystem. ..... 149
Table 4.14: Comparison between induced currents resulting from the closed loop and open

loop configurations. ..... 152
Table 4.15: Attenuation of induced currents in each coil when using closed loop current control. ..... 152
Table 4.16: Demodulator performance. ..... 154
Table 4.17: Background noise voltage density. ..... 156
Table 4.18: Scribble test results. ..... 157
Table 4.19: Electrical characteristics of each coil used to investigate the effect of coil size. ..... 161
Table 4.20: Table showing the percentage error of the magnetic field models and the resulting position error for each coil size. ..... 163
Table 4.21: Comparison of quoted accuracy of research EM systems. ..... 165
Table 4.22: Comparison of update rates of research based EM tracking systems. ..... 167
Table 4.23: System cost breakdown. ..... 168
Table 5.1: Maximum displacement at experienced at each test point. ..... 190
Table 6.1: EM tracking operating frequency comparison. ..... 193
Table 6.2: Shield simulation parameters. ..... 197
Table 6.3: Shield parameters. ..... 201
Table 6.4: Distorter effects with shields. ..... 206
Table 6.5: 5 DOF test results. ..... 211
Table 7.1: Parameters used for the simulation of the effects of parasitic capacitance changes. ..... 238

# List of Abbreviations

| | |
|---|---|
| AC | Alternating Current |
| ADC | Analog to Digital Converter |
| AM | Amplitude Modulation |
| AMR | Anisotropic Magneto Resistance |
| BJT | Bipolar Junction Transistor |
| BNC | Bayonet Neill–Concelman |
| CMR | Colossal Magneto Resistance |
| CMRR | Common Mode Refection Ratio |
| CT | Computed Tomography |
| DAC | Digital to Analog Converter |
| DAQ | Data Acquisition |
| DC | Direct Current |
| DDS | Direct Digital Synthesis |
| DOF | Degree of Freedom |
| EM | Electromagnetic |
| FDA | Food and Drug Administration |
| FEA | Finite Element Analysis |
| FEMM | Finite Element Method Magnetics |
| FFT | Fast Fourier Transform |
| FIR | Finite Impulse Response |
| GMR | Giant Magneto Resistance |
| GP | Gain Phase |
| HP | Hewlett Packard |
| ICNIRP | International Commission on Non-ionizing Radiation Protection |
| IC | Integrated Circuit |
| IIR | Infinite Impulse Response |
| LCR | Inductance Capacitance Resistance |
| LM | Levenberg-Marquardt |
| LUT | Look Up Table |
| NDI | Northern Digital |
| NI | National Instruments |
| MCU | Microcontroller Unit |
| MIS | Minimally Invasive Surgeries |

| | |
|---|---|
| MRI | Magnetic Resonance Imaging |
| OD | Outer diameter |
| OR | Operating Room |
| PC | Personal Computer |
| PCB | Printed Circuit Board |
| PCI | Peripheral Component Interface |
| PI | Proportional-Integral |
| PLL | Phase Locked Loop |
| P&O | Position and Orientation |
| RMS | Root Mean Squared |
| SAR | Successive Approximation |
| SNR | Signal to Noise Ratio |
| SPI | Serial Peripheral Bus Interface |
| SVD | Single Value Decomposition |
| TI | Texas Instruments |
| TMR | Tunnel Magneto Resistance |
| TR | Trust Region |
| USB | Universal Serial Bus |

# Chapter 1
# Introduction

## 1.1. Overview

This chapter provides an overview of the thesis, examining the motivation for the research and the relevant background information. The objectives of the thesis are presented and the structure is outlined.

Electromagnetic (EM) tracking refers to the process of determining both the position and orientation of an object using magnetic fields. EM steering makes use of the attractive and repulsive forces generated by magnets to move objects effectively wirelessly. Both methods have been used successfully in a variety of minimally invasive surgeries and interventions for a wide range of applications.

Magnetism as an actuating force has been used in medicine for many years. As early as 1928, electromagnets were used to remove shrapnel from the human body [1]. Other early examples saw the use of permanent magnets for bronchoscopic navigation in 1948 [2]. EM steering has found application in navigating cardiovascular guide wires [3], gastrointestinal examinations [4], [5] and neurosurgery [6]. A commercial example of magnetic steering system is the Stereotaxis Niobe which uses large permanent magnets to steer magnetic catheters [3].

EM tracking uses the spatial variation of magnetic fields to determine position or orientation information, sometimes both simultaneously. Early examples include the linear differential transformer, which is used as a linear position sensor, developed in 1949 [7]. The first described method for determining both the position and orientation of an object was developed as early as 1961 [8]. In modern medicine EM tracking has found application in a wide range of minimally invasive procedures such as eye tracking [9], bronchoscopy [10], liver biopsy [11] and robotic surgery [12]. EM tracking typically uses low frequency magnetic fields (< 1 MHz) which can pass freely through human tissue without significant attenuation. This is advantageous as direct line of sight is not required for operation.

The primary end application for this research is that of navigation within the lung, in particular enabling access to peripheral regions of the lung where the branching of the

bronchi becomes small. In these regions, standard navigation techniques such as bronchoscopy are ineffective yet these locations are where many early stage cancers develop [13], [14]. Lung cancer is the deadliest form of cancer [15] and the development of effective methods for early diagnosis of cancer has the potential to save many lives as a result of early detection and treatment [16]. A navigation platform for use within the lung will allow for access to suspect lung cancer nodules as indicated by pre-operative CT scans and pave the way for potential future work with semi-automated robotic navigation for safe and reliable diagnosis.

## 1.2. Thesis Objectives

The initial aim of the research was to develop a catheter navigation platform that utilises EM fields to both steer and track the position of a catheter, with the end application of biopsy of suspect cancer nodules within the lung. The first objective represents an investigation into magnetic steering. After an initial investigation into the practicality of magnetic steering, it became apparent that its use in lung navigation was unfeasible. Hence the second objective, catheter tracking, represents the majority of the work presented.

There exists a number of commercial EM tracking systems. However all are expensive (>€ 10,000) and have certain limitations. In particular, almost all commercial systems have high sensitivity to external magnetic fields such as those that could be used as a steering mechanism or imaging, such as in MRI. Most components of EM tracking systems are readily available and relatively low cost. We show how a low cost alternative to commercial systems can still have comparable performance. Novel implementations of each subsystem are presented.

The end goal of this EM tracking system is part of a complete virtual bronchoscopy system for navigation within the lung. Hence, the third objective is to demonstrate and evaluate how the system performs in a pre-clinical setting. For this purpose, a breathing lung model was constructed and navigated using the EM tracking system. This represented a realistic end application for the system.

The next objective involved the design of magnetic shielding for the EM transmitter. In many clinical settings, there are a range of sources of magnetic distortion. In particular operating tables, instruments and other equipment are typically made out of stainless steel or other similar materials. To make the system feasible for use in these settings, distortion effects must be reduced. Many commercial systems have magnetic shielding built in but these are proprietary designs and little information has been documented on shielding of this type.

Finally, the effect of interference resulting from both conductive materials and human patients on magnetic field measurements was investigated. An understanding of the

frequency dependent accuracy of EM tracking is essential in choosing an appropriate operating frequency. Low frequencies suffer from low amplitude measurements which are prone to noise while high frequencies are very susceptible to eddy current effects in conductive materials and capacitive effects from human interaction with the magnetic fields.

## 1.3. Thesis Structure

This thesis is divided into six main work chapters which examine the various aspects of the research conducted.

Chapter 2 covers all aspects of magnetic steering that was investigated. We first examine the potential use of DC electromagnetic coils for deflecting catheters with permanent magnetic attachments. This is followed by a detailed mathematical analysis of the deflection mechanics of chains of permanently magnetised spheres in the presence of external fields from an electromagnet. This chapter concludes with a demonstration of the position control possible with magnetic actuation which demonstrates how magnetic fields can be used to both steer and track an object simultaneously.

Chapter 3 details the design and implementation of the EM tracking system. Each subsystem is described in detail in terms of the design requirements and the relevant theory to support the design. Practical construction of the system is also explored.

Chapter 4 demonstrates the operation and testing of the system in terms of the position and orientation accuracy, system operation, the impact of noise and a number other system parameters.

In Chapter 5, we demonstrate the testing and evaluation of the EM tracking system in a more realistic environment. For this, a plasticised pig lung is used as a phantom. A simple yet effective system is constructed that allows the lungs to be inflated and breathe in a controllable way. The EM tracking is registered to the coordinate frame within a 3D computerised model of the lung and the tracking sensor is successfully navigated through the main airways of the lung.

In Chapter 6, a novel EM shielding is examined and tested showing how large ferromagnetic objects, which generally have a major detrimental effect of system accuracy, are blocked from disrupting the performance of the tracking system.

In Chapter 7, the effect of conductive materials and the human body on magnetic field measurements is examined over a wide frequency range to investigate the impact of the choice of operating frequency on the reliability of EM tracking systems.

Finally, the key findings of the thesis are reviewed in Chapter 8 and recommendations for future work are presented.

# Chapter 2

# Preliminary Investigations of Magnetic Catheter Steering*

## 2.1. Overview

In this chapter, we present an investigation into the potential use of magnetic fields for catheter steering within the lung. A theoretical description of catheter steering is presented and experimental results document the advantages and disadvantages of magnetic actuation. A novel design for a magnetically steered catheter for lung navigation is presented and a number of prototype designs are examined. The large size and power requirements of the external magnets to exert a usable force on the limited magnet volume however rendered this design impractical.

This chapter also includes a detailed analysis of the deflection of spherical permanent magnets in the presence of external magnetic fields. Chains of spherical magnets as catheter steering tips was the end goal of this investigation. The resulting mathematical model accurately predicts the deflection of the sphere chain.

To demonstrate the potential use of magnetic steering in combination with an EM tracking system, a simple closed loop scheme to control the position of a catheter model is presented. Here, a single electromagnet is used to control the height of a catheter with a PI controller adjusting the coil current to reach a specified height.

The main findings presented in this chapter are:

- An evaluation of magnetic steering for navigation within the lung.
- Demonstration of tracking and steering of a permanent magnet catheter tip.
- Detailed analysis of the deflection mechanics of chains of permanently magnetised spheres for catheter actuation.

* This chapter is based on K. O'Donoghue and P. Cantillon-Murphy, "Deflection modeling of permanent magnet spherical chains in the presence of external magnetic fields", *Journal of Magnetism and Magnetic Materials*, 343, 251-256, Oct 2013, and K. O'Donoghue, D. Hogan, M. Healy and P. Cantillon-Murphy, "Magnetic Catheter Guidance in a Human Lung Model: an initial feasibility study." *Joint Workshop on New Technologies for Computer/Robot Assisted Surgery*, Madrid, Spain, July 2012.

## 2.2. Literature Review

We first explore some of the common uses of magnetic steering in medical applications. Magnetics steering has found use in a wide range of applications such as neurosurgery, cardiovascular procedures and gastrointestinal examinations. However, for the application of lung navigation, no prior work has been reported.

### 2.2.1. Stereotaxis Niobe

The only example of a commercially available and FDA-approved magnetic steering system is the Niobe Magnetic Navigation System provided by Stereotaxis. The system comprises of two large permanent magnets, each approximately weighing 350 Kg [17], which are mechanically rotated and translated in order to generate a desired magnetic field in the region of interest. The magnets generate a uniform navigation field of 0.08 T. The position of these magnets relative to a small seed magnet placed at the tip of a catheter determines the force and torque experienced by the tip. Instrument tracking is typically achieved by fluoroscopy. The system is focused on delivery of catheter and guide-wire based therapies in the heart and the surrounding vasculature [18]. The standard system uses fluoroscopic imaging and it has been seen that its use can reduce fluoroscopic exposure times to both the patient and physician [3].

Stereotaxis Niobe has a number of major disadvantages when compared to our potential final design. First, a dedicated OR is required. Second, permanent magnets cannot be switched off which means careful precautions must always be taken when in proximity to the magnets due to potential crush injuries and damage to electronic equipment. As of 2008, the Stereotaxis system had been used in 15,000 procedures with a complication rate of less than 0.1 %. However this comes at the cost of patient fluoroscopic exposure and an initial investment of $ 2,000,000 for the purchase of the system [19].

### 2.2.2. Magnetic Pills and Micro-robots

Another area of magnetic navigation that has become popular in recent years is the use of magnetic fields to guide untethered micro-robots and pills, as well as for targeted drug delivery. Yesin et al [20] demonstrated the guidance of a nickel ellipsoid of dimensions 950 μm × 450 μm through the blood stream, modelling the viscous properties of blood as well as the magnetisation of the ellipsoids. A combination of Helmholtz and Maxwell coils were used to magnetise the ellipsoids and exert force respectively. Ishiyama et al [21], [22] have published a number of studies on spiral shaped magnetic micro-machines. These devices, having a design similar to a screw, are turned about their axis by a rotating magnetic field, which allows them to move through viscous media.

### 2.2.3. Navigation within MRI

While a large number of guidance techniques use custom made magnetic coils, it is worth mentioning that the huge field generated by MRI, typically in the range of 1.5-2 T, have been successfully used to magnetise ferromagnetic objects, which then can be steered with the MRI gradient coils or additional steering coils. Roberts et al have demonstrated methods for steering a catheter tip by using a three axis coil placed at the tip. By controlling the currents in each coil, the magnetic moment of the tip is changed and aligns with the MRI field accordingly [23]. MRI environments have the advantage that they can fully magnetise ferromagnetic objects, which is difficult in normal circumstances. Lalande et al make use of this fact to magnetise a set of ferromagnetic spheres which are placed at the tip of a catheter. Additional gradient coils are then used to exert force on the catheter [24]. Matheiu et al have shown that MRI can also be used to aid in the navigation of micro-particles using both additional Maxwell coils [25], as well as the imaging gradient saddle coils in MRI [26].

## 2.3. Magnetic Actuation Theory

Permanent magnets such as those used by Stereotaxis provide very powerful magnetic fields [3]. However, as a result, they are difficult to control as they require mechanical actuation to control the magnetic fields and the magnets cannot be turned off. To mitigate against this effect, our designs used electromagnets which allow for direct control of the magnetic fields by adjusting the current levels in each magnet. The design of electromagnets for wireless actuation depends on many criteria and limiting factors. Field strength, field gradient, field uniformity, linearity and useful range are the key design specifications while the limiting factors relating to the feasibility of construction include cost, cooling, materials, size and weight.

In order to position a magnetic object, the two main considerations are force and torque. In a uniform magnetic field, the torque experienced by a magnet is such that the north - south pole aligns with the external field. In such a field no force would be experienced by the magnet. For force, a gradient in the field is required to generate a magnetic potential difference. Similar to an object placed in a gravitational potential field relative to a ground state at the surface of the earth, the magnet aims to reside at the lowest energy state.

The basic equation for the force experienced by an ideal magnetic dipole where $\boldsymbol{B}$ is the magnetic flux density in the region and $\boldsymbol{m}$ is the magnetic dipole moment is given by (2.1) [27]. The gradient of the magnetic field is the primary factor that describes the force which a magnet will experience. Equation (2.2) shows a simplified expression which is accurate for the case where a permanent magnet is along the axis of an electromagnetic coil and where the permanent magnet is at an angle $\theta$ to the applied magnetic field. Figure 2.1 shows a basic

representation of the force on a bar magnet near an electromagnet, where the gradient of the magnetic field decreases closer to the magnet. Hence an attractive force is experienced.

$$\boldsymbol{F} = \nabla(\boldsymbol{m} \bullet \boldsymbol{B}) \tag{2.1}$$

$$|\boldsymbol{F}| = |\boldsymbol{m}| \frac{\partial B_z}{\partial z} \cos\theta \tag{2.2}$$

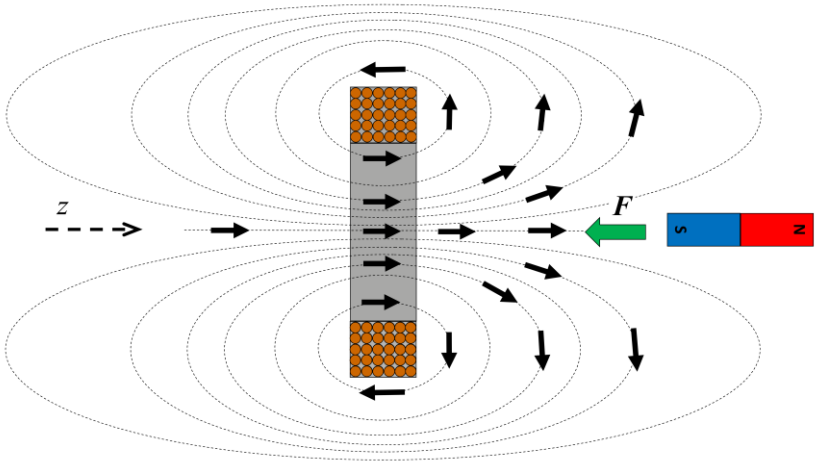



Figure 2.1: Magnetic force on a permanent magnet due to an applied field.

The torque experienced by a magnetic dipole is given by (2.3) [27]. Again, a simplified version of this expression is given by (2.4). Figure 2.2 shows the direction of magnetic torque experienced by a bar magnet in a uniform magnetic field.

$$\boldsymbol{T} = \boldsymbol{m} \times \boldsymbol{B} \tag{2.3}$$

$$|\boldsymbol{T}| = |\boldsymbol{m}||\boldsymbol{B}| \sin\theta \tag{2.4}$$

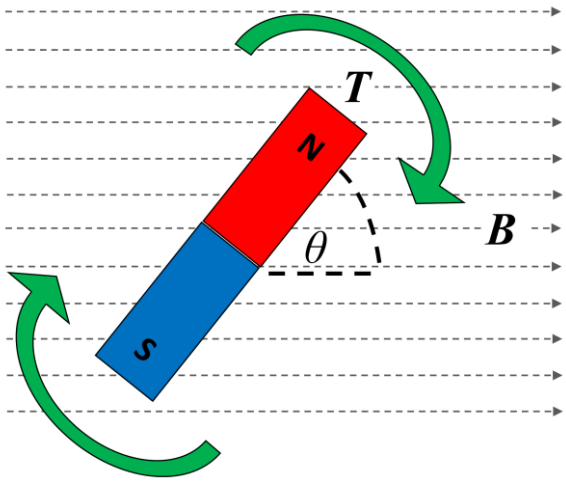



Figure 2.2: Magnetic torque on a bar magnetic due to a uniform field.

For a small, permanently magnetised object, the magnetisation may be approximated as an ideal dipole, as has been verified experimentally [28], [29]. The magnetic dipole moment of a small permanent magnet is given by (2.5) where $V$ is the volume of the magnet, $B_r$ is the remnant flux density of the material and $k_d$ is the demagnetisation factor for the geometric

shape of the magnet. For a sphere, $k_d$ is 1/3 and this value approaches 0 as the aspect ratio of shape increases *i.e.* a long rod shaped magnet has $k_d \approx 0$ [30].

$$|\boldsymbol{m}| = (1 - k_d)\frac{B_r V}{\mu_0} \tag{2.5}$$

In order to design an electromagnet, typically the Biot-Savat law is used which is given by (2.6) where $I$ is the current flowing in a thin conductor, $\mu_0$ is the magnetic permeability of free space and $\boldsymbol{r}$ is a vector describing the distance from the path of the current flow to any point in 3D space.

$$\boldsymbol{B} = \frac{\mu_0}{4\pi}\int \frac{I \times \hat{\boldsymbol{r}}}{|\boldsymbol{r}|^2} dl \tag{2.6}$$

The design of electromagnets is heavily constrained by the power and current handling capabilities of the conductors. Typically, excessive amounts of heat results even when generating modest magnetic field strengths. Zickler quotes a rule of thumb for limiting current densities in air cooled electromagnets which states that for large coils the current density should be limited to 1 A/mm$^2$ and 2 A/mm$^2$ for small thin coils [31]. Liquid cooling offers a huge increase in the power handling capability. Zickler again describes a rule of thumb that dictates that the current densities in a water cooled system can be increased to 10 A/mm$^2$ and even up to 80 A/mm$^2$ in certain designs.

## 2.4. Proposed Magnetic Catheter Design

The initial concept for the magnetic catheter was based on the potential use of magnetic actuation to navigate a flexible instrument to a desired location within the lung. This design was constrained by the diameter of the peripheral airways of the lungs where early stage cancers typically develop. A maximum outer diameter of approximately 2.6 mm was stipulated as this allowed the catheter to be used with the instrument port of standard bronchoscopes.

The design consisted of two main parts; a steerable magnetic catheter with an EM tracker, and a flexible outer sheath. The two parts would be steered together within the airways to a potential cancer nodule, at which point the internal magnetic catheter would be removed, leaving behind the outer sheath which then acts as an instrument port for a biopsy forceps or needle. The magnetic catheter would be steered with a combination of the magnetic tip and a wire driven component, the combination of the two potentially giving larger bending angles. A guidewire would also be used for axial displacement of the catheter tip. An EM tracking sensor would also be built into the catheter, which necessitated a custom system as commercially available alternatives are incompatible with external field strengths greater than a few mT (see Chapter 3). Figure 2.3 shows a cross-section of the proposed catheter design.

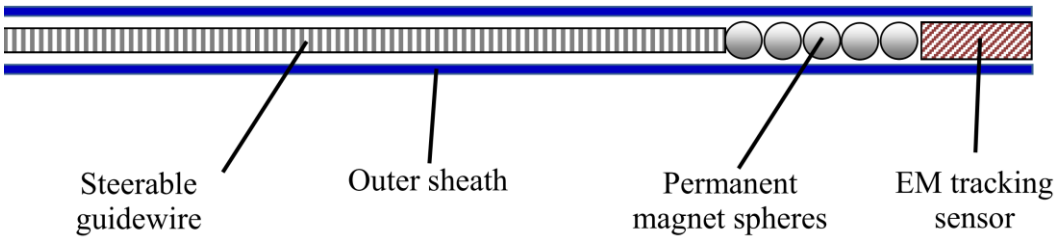



Figure 2.3: Cross section of the concept magnetic catheter.

## 2.5. Deflection Testing For Magnetic Catheters

In this section, the proposed catheter design from the previous section is analysed by testing the deflection of a magnetically tipped catheter with different catheter materials. A number of different magnet configurations are tested as well as different catheter materials.

### 2.5.1. Catheter Materials

For the deflections tests, two different catheter materials were used, silicone rubber and Pebax 2533. The role of the catheter material is to act as an instrument channel after the steerable catheter has been removed, as well as holding the magnets in place to stop them from getting lost within the body. Silicone was used as it is a very flexible material, with a Young's modulus of in range of 1-5 MPa [32]. Pebax 2533 is a type of thermoplastic elastomer that is often used in commercial catheter designs [33]. Pebax is a less flexible material with a Young's Modulus of approximately 14 MPa [34]. Both materials used had a wall thickness of 0.15 mm and an ID of 2 mm. Table 2.1 shows a comparison between the test materials and other common catheter materials in terms of their Young's moduli.

| Material | Young's modulus [MPa] |
|---|---|
| Silicone rubber | 1-5 |
| Pebax 2533 | 12-14 |
| PVC | 2400-4100 |
| Latex | 1-5 |
| PTFE (Teflon) | 500 |
| LDPE | 240 |

Table 2.1: Comparison of the Young's modulus of common catheter materials [32]–[34].

### 2.5.2. Test Setup

For the deflection tests, two electromagnetic coils were powered in series to generate the required magnetic fields for reasonable deflection of the catheters. Each catheter was positioned at incremental distances from the electromagnets. Each catheter was elevated to a

plane that passed through the centre of the coils. An overhead camera recorded the deflection and these images were post-processed to determine the deflection angles. A ruler was used as reference for the image processing and to measure the distance from the coils to the catheters. Figure 2.4 shows an example of this test setup. The tip deflection was calculated using (2.7) where *x* and *y* are shown in Figure 2.5.

$$\alpha = \arctan(\frac{y}{x}) \tag{2.7}$$

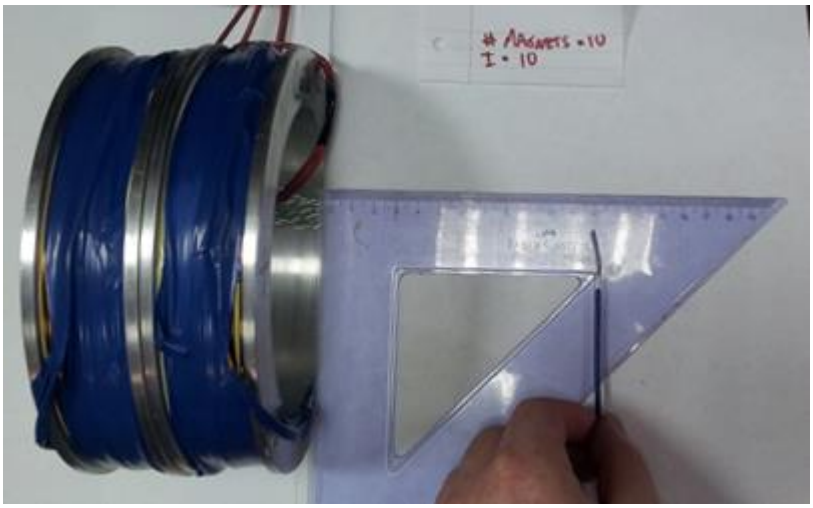



Figure 2.4: Deflection testing of different magnetic tips and sheath materials.

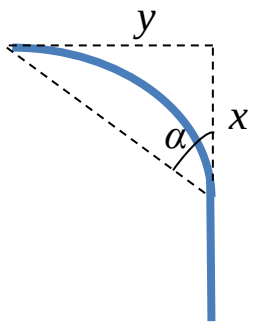



Figure 2.5: Calculation of tip deflection.

### 2.5.3. Electromagnetic Coil Actuator

The two identical electromagnetic coils used to generate the steering magnetic fields for the catheter tests consist of 200 turns of 1.5 mm wire wound on an aluminium former with an inner former diameter of 14 cm and an outer diameter of 18 cm. One electromagnet is shown in Figure 2.6. The max coil current is approximately 20 A. However at this operating current, the temperature of the coil rises very quickly to approximately 80° C. When carrying a current of 20 A, the magnetic field at the centre of the coil is approximately 30 mT and this is predicted using analytical models for the magnetic field. Figure 2.7 shows the simulated magnetic field and field gradient of the electromagnet along its central axis. Figure 2.8 shows a normalised plot of the field and gradient where the quantities are normalised with

respect to their peak values. Clearly the magnetic field and gradient roll off quickly with distance. Since the torque and force experienced by an electromagnet are directly related to the magnetic field and gradient respectively, the useful range of such a coil is limited. Figure 2.9 shows a contour plot of the 2D magnetic field around the coil. A similar roll off in the magnetic field strength is also seen off axis as is apparent from this figure.

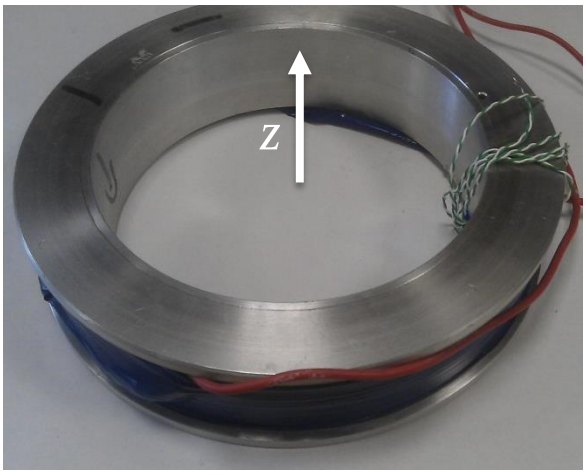



Figure 2.6: Electromagnetic coil actuator.

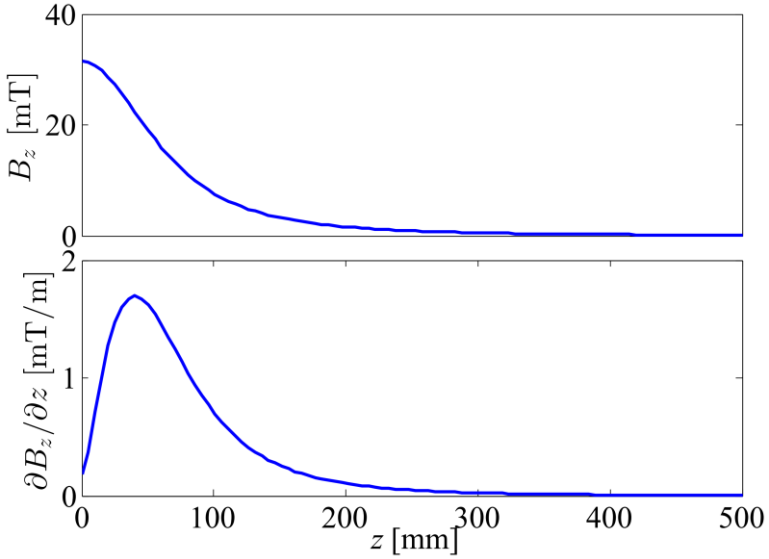



Figure 2.7: Simulated magnetic field and gradient of the electromagnet along its central axis with a current of 20 A.

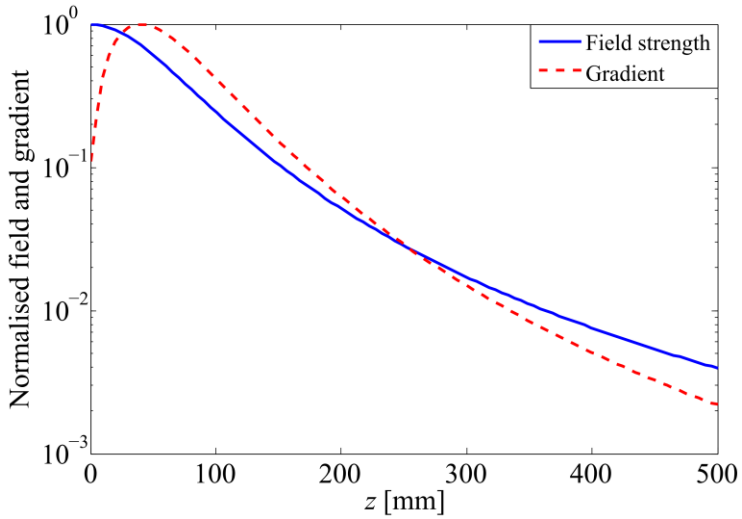



Figure 2.8: Simulated normalised field and gradient with axial distance from the electromagnet.

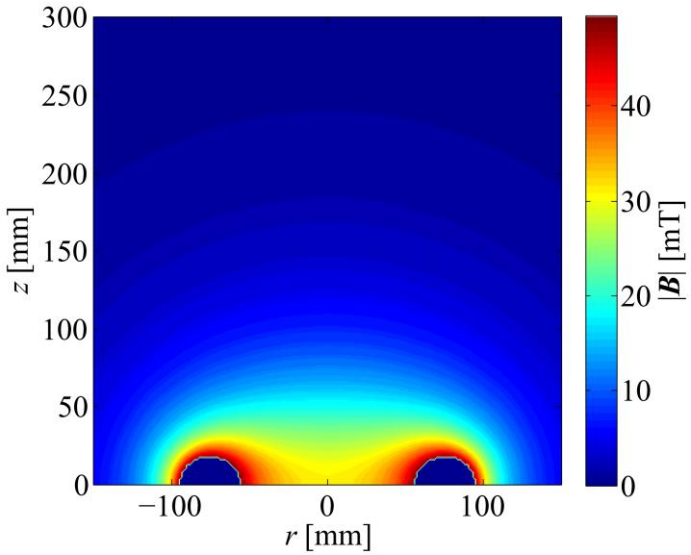



Figure 2.9: Simulated contour plot of the magnetic field distribution around the electromagnet.

### 2.5.4. Magnetic Catheter Tips

A number of different arrangements of catheter magnets were tested. The most useful arrangements were found to consist of chains of spherical magnets, or spheres in combination with cylinders. The advantage of the cylinders is that they have a larger volume than similar sized spheres and the magnetic force and torque is directly proportional to the magnet volume. Figure 2.10 shows an example of tips used for the following tests. All magnets used in the tests were N42 grade Neodymium magnets.



Figure 2.10: Magnetic tips used in the testing. Here each sphere has a 2 mm diameter and each cylinder is 2.5 mm in length and diameter.

### 2.5.5. Results

**Comparing Tip Arrangements**

The first tests examined the deflection of a number of different tip configurations, namely spheres, cylinders and combinations of spheres as seen in Figure 2.10. The spheres and cylinders both were 3.2 mm in length, a total of 15 magnets were used in each test. Table 2.2 shows the results of this test. The applied magnetic field in the test region was approximately 1 mT with a gradient of 0.2 mT/m. Figure 2.11 shows the deflections of the catheter tips with and without the silicone rubber. Clearly we see that in the absence of a constricting sheath material, that the deflections are considerably larger.

| | Deflection Angle [Degrees] | |
|---|---|---|
| Tip arrangement | No sheath | With sheath |
| Spheres | 47.8 | 20.1 |
| Cylinders and spheres | 37.4 | 14.6 |
| Cylinders | 11.1 | 10.8 |

Table 2.2: Deflection angle comparison for different magnet groups with and without an outer sheath. The sheath material was silicone rubber in this test. A magnetic field strength of 1 mT was used.

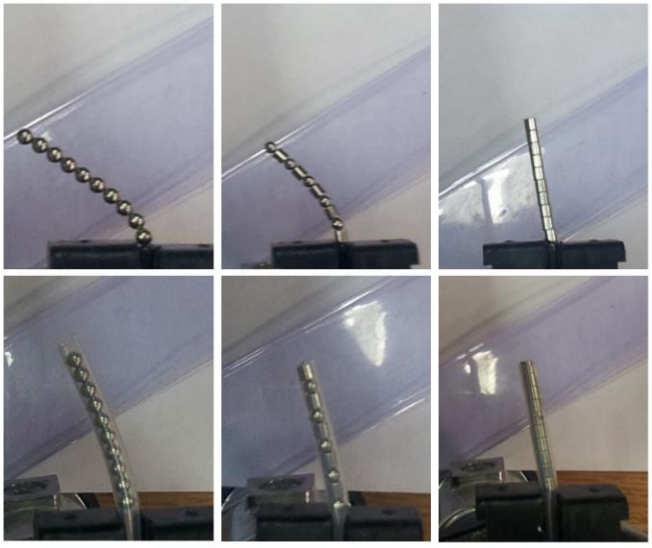


Figure 2.11: Comparing deflections with (top row) and without (bottom row) a silicone rubber sheath.

**Comparing Sphere Chain Length**

Since spheres gave the greatest deflection in the previous test, the number of spheres was varied to see its effect on the resulting deflection. The sheath material was replaced with Pebax 2533 and the applied field in this case was 10.8 mT. Smaller spheres with a diameter of 2 mm were also used. The results of this test are shown in Table 2.3. By increasing the numbers of spheres, greater deflection results. However, increasing the number of spheres also increases the radius of curvature required to achieve a certain deflection which may be limited depending on the geometry of the navigation space.

| | Deflection Angle [Degrees] | |
|---|---|---|
| No. of spheres | No sheath | With sheath |
| 10 | 73.7 | 11.3 |
| 11 | 75.4 | 15 |
| 12 | 77.9 | 20.6 |
| 13 | 79.2 | 21 |
| 14 | 81.2 | 26 |
| 15 | 83.2 | 29 |

Table 2.3: Deflection angle for an increasing number of spheres in the chain with and without an outer sheath. Pebax 2533 was used with this test. A magnetic field strength of 10.8 mT was used for this test.

**Deflection with Distance**

In the next test we examined how the deflection varies with distance from the electromagnet. Ten spheres with 2 mm diameter were used with a Pebax 2533 outer sheath and the catheter was moved in 10 mm steps away from the electromagnet. Figure 2.12 shows the results of this test. Figure 2.13 shows images of the deflections at 40 mm and 80 mm from the coil. As expected, the deflections decrease with distance from the electromagnet. This is due to the fast roll off in the magnetic field strength with distance. Hence, for useable deflection, excessive amounts of power would be required. Much larger electromagnets would result, which in the constrained environment of the endoscopy clinic is undesirable.

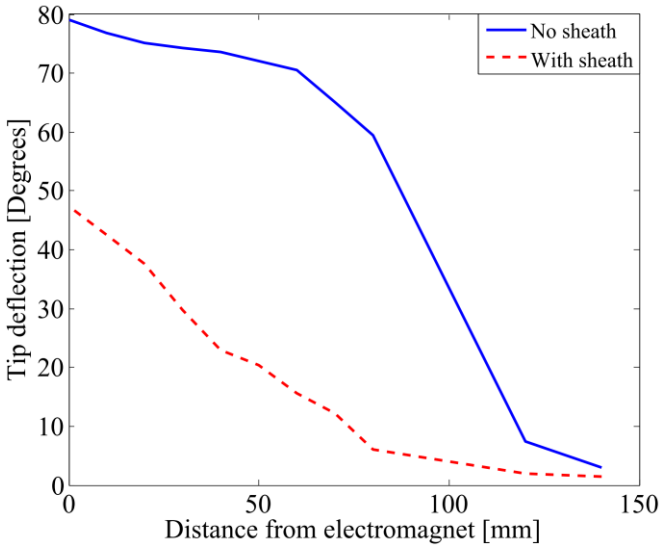



Figure 2.12: Comparing the deflections of chains of spherical magnets with and without a Pebax 2533 outer sheath.

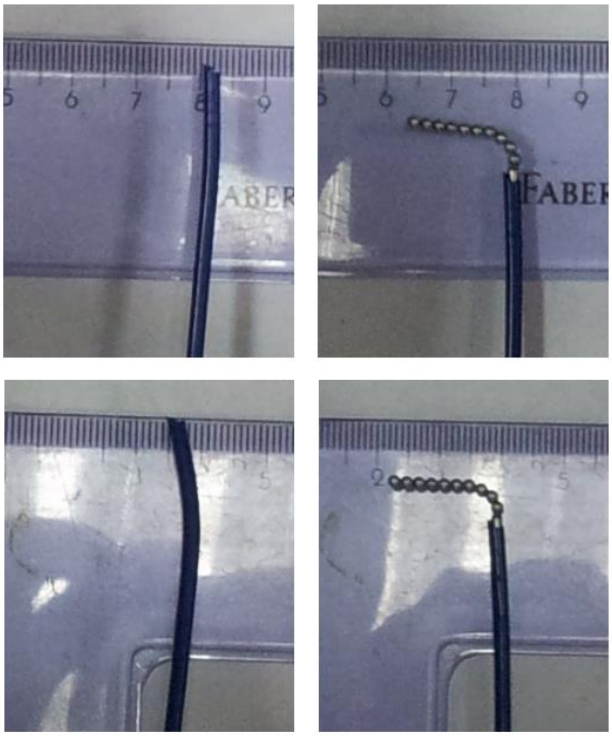


Figure 2.13: Deflections of 10 spheres in the chain at 40 mm and 80 mm from the electromagnet. A Pebax 2533 sheath was used in this test.

### Deflections with Increasing Magnetic Field Strength

The final test used two coils in a Helmholtz configuration (see Section 2.6.7.2) to generate a uniform magnetic field. The strength of this field was varied and the resulting deflections were analysed. Combinations of 15 spheres and cylinders were used here. Figure 2.14 shows the results of this test. As with the previous test, large deflections were observed with spheres alone. However with the addition of a sheath material (Pebax 2533) deflections reduced dramatically. With this particular catheter, fields of approximately 15 mT would be required which are extremely difficult to produce at distance from a magnet.

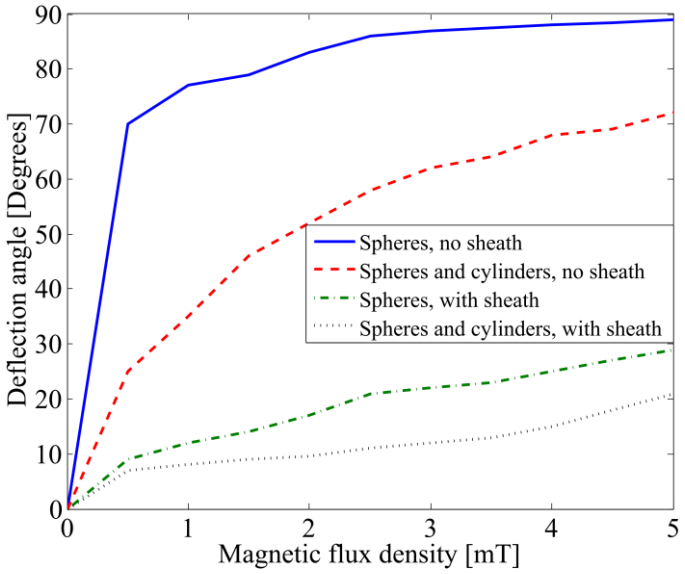



Figure 2.14: Comparing deflection of spheres and cylinders with and without a Pebax 2533 sheath with respect to a uniform applied magnetic field strength.

### 2.5.6. Discussion

From the results presented in this section, it is clear for useful catheter deflection with an outer sheath material, excessive magnetic fields are required. The thickness of both sheath materials was low (<0.2 mm) and both had low elastic moduli, *i.e.* both are quite flexible and elastic. Even with such materials, considerable resistance to movement was observed, which emphasises the limited magnetic force which may be exerted without using very high power and large magnets. For a minimally invasive procedure, such as navigation within the lung, the volume of magnetic material is severely constrained and therefore strong external magnetic fields must be used. For comparison, the Stereotaxis system uses an operating strength of approximately 80 mT [18] and large permanent magnets to attain these fields. Massive electromagnets would be required to generate useable forces for catheter navigation. In conclusion, while for certain applications magnetic steering has its advantages, the low forces which can be attained with reasonably sized electromagnets is too limited to be advantageous over standard wire driven catheters, which can easily achieve 90° and 180° deflections with small diameters.

## 2.6. Deflection Modelling of Spherical Chains of Permanent Magnets

Following the catheter tests described earlier, a theoretical investigation of the deflection of the spherical magnet chains was carried out [35]. This was in a bid to expand the understandings of the underlying mechanics behind magnetic deflection.

### 2.6.1. Introduction

In this section, a model for the interaction of a chain of permanently magnetised spheres in the presence external magnetic potential fields is presented. The use of millimetre-sized spheres as a magnetic navigation device in minimally procedures surgeries is explored. It has been found that chains of spherical magnets used as distal attachments can provide greater deflections for catheter devices than mechanical catheters in specific settings [36]. By using chains of spheres, greater deflections are achieved which allows the use of much lower strength steering magnets than those used in current magnetic navigation systems such as the commercially available Stereotaxis Niobe [36] and in research systems such as those presented by Martel et al. [37], [38]. With a lower magnet strength requirement, a magnetic steering platform might potentially be made small enough to be a semi-portable system such that it can be easily set up in an operating room for a clinical procedure without modification to the room or impeding access to the patient with bulky equipment.

A classical physics formulation based on minimisation of the system potential energy is employed. This is achieved analytically for simple cases ($N$=2) and numerically for larger

numbers of spheres. In the static case, a system will approach a stable equilibrium position which minimises the potential energy of the system, or in other words, when all the forces and moments sum to zero [39]. A similar approach has been used by Stambaugh et al. to examine pattern formation in layers of permanent magnets [40] where numerous bar magnets were encapsulated in spheres and placed in layers. These layers were then shaken for a period until the layers reached an equilibrium position.

The majority of magnetic chain modelling to date has been on the micro- and nano- scales. For example, chain formation of ferromagnetic gold nanoparticles has been demonstrated experimentally [41]. Magnetic nanoparticles on GaAs substrates have been shown to form chains at moderate applied fields of 0.7 T and form discrete clusters when exposed to large 17 T fields [42]. Dynamic modelling of the time response of magnetic particles has also been analysed when in nanowire [43] and particulate dispersion formations [44]. Similar methods have been used to analyse the electrostatic chain formation of lipid headgroups using Monte Carlo simulations [45].

The analysis of solid permanent magnets differs significantly from magnetic particles. For example, deformation of spherical droplets of magnetic particles into prolate ellipsoids significantly complicates the required calculations [46]. These effects can be neglected in solid permanent magnets. Also, saturation and temperature effects are easily neglected for modern permanent magnet materials (e.g. NdFeB) under typical conditions [47]. Chains of permanently magnetised spheres have been used in the analysis of sound propagation due to the strong attraction force between the spheres [48] but there has been little or no research examining how a chain would interact with external fields. Beleggia et al have presented an extensive investigations of the force between permanent magnets in arbitrary shapes using potential energy formulations [49]–[51], but this was limited to force calculations and not shape formation.

Magnetic catheter deflection has been demonstrated by Martel et al. where a catheter tip comprising of ferromagnetic spheres, which are free to rotate in compartments, has been steered using a modified MRI [24], [37] . The Stereotaxis Niobe system makes use of cylindrical permanent magnets as a catheter tip and uses large steering permanent magnets to control the catheters position [3], [36].

This section is structured as follows. First, a theoretical model of the interaction between the spheres and external potential fields when constrained to a 2D plane is presented. Analytical expressions are derived for the two sphere case, while numerical simulations are described for chains of $N$ spheres. These models are then tested experimentally with chains exposed to uniform magnetic fields up to 35 mT. Finally the results are discussed in the context of the clinical application to catheter steering.

### 2.6.2. Spherical Permanent Magnets

Consider the magnetic field of a uniformly magnetised sphere of radius *a*. The magnetic field is given by (2.8) [52] , where $M_s$ is the volume magnetisation in A/m, *r* is the distance from the centre of the sphere in m, $\theta$ is the angle measured from the direction of magnetisation, $\hat{\boldsymbol{r}}$ is a unit vector pointing in the radial direction, $\boldsymbol{\theta}$ is a unit vector in a clockwise sense about the *x* axis starting from $z = 0$, and $\mu_0$ is the magnetic permeability of free space:

$$\boldsymbol{B}(\boldsymbol{r}) = \begin{cases} \dfrac{2\mu_0 M_s}{3} & r < 0 \\ \dfrac{\mu_0 M_s}{3}\dfrac{a^3}{r^3}(2\cos\theta\hat{\boldsymbol{r}} + \sin\theta\boldsymbol{\theta}) & r \geq 0 \end{cases} \tag{2.8}$$

The magnetic field outside the radius of the sphere is identical to the magnetic field resulting from an ideal magnetic dipole whose dipole moment is given by $m = 4/3\pi a^3 M_s$. The dipole is aligned with the direction of the sphere's magnetisation. Hence, in all calculations, the fields generated by each sphere are assumed to be an ideal dipole, which drastically simplifies the interaction equations.

### 2.6.3. Magnetic Energy

If each magnet can be considered as a dipole, the standard Zeeman energy formula, $U = -\boldsymbol{m}\cdot\boldsymbol{B}$, can be used to calculate the potential energy due to an external magnetic field. For the dipole-dipole interaction between each sphere, (2.9) may be used to determine the potential energy resulting from the interaction where $\boldsymbol{m}_i$ and $\boldsymbol{m}_j$ represent the magnetisation vector of each magnet and $\boldsymbol{r}_{ij}$ is the position vector between each magnet [27] .

$$U_{dd}^{ij} = \frac{\mu_0}{4\pi\left|\boldsymbol{r}_{ij}\right|^3}[\boldsymbol{m}_i\cdot\boldsymbol{m}_j - 3(\boldsymbol{m}_i\cdot\hat{\boldsymbol{r}}_{ij})(\boldsymbol{m}_j\cdot\hat{\boldsymbol{r}}_{ij})] \tag{2.9}$$

In addition to the dipole interactions, the magnetocrystalline anisotropy of the material must also be considered. This anisotropy tends to move the magnetisation of a permanent magnet away from its easy axis to minimise its internal potential energy. The magnetocrystalline anisotropic energy of a magnet of volume *V* with a anisotropy constant *K* may be approximated by [52] :

$$U_{ma} = VK\sin^2\gamma \tag{2.10}$$

where $\gamma$ is the angle between the direction of magnetisation and the easy axis of the magnet. By summing the energy resulting from the external field, the dipole-dipole interaction and the magnetocrystalline anisotropy, the total energy of the system may be formulated, which in turn can be minimised to determine the final formation of a group of spheres. In this work, the anisotropy term will only be considered for the first sphere in the chain, which is assumed to be locked in place. Hence the only way for the sphere to minimise its potential

energy is by shifting its magnetisation away from the easy axis. For all other spheres in the chain, it is assumed that their mechanical alignment minimises the potential energy and the anisotropy term given by (2.10) can be neglected.

### 2.6.4. Two Sphere Case

Consider a simple system with two spherical magnets in a 2D plane. The anisotropic energy term is initially neglected to facilitate an analytical solution for this simplified case. Figure 2.15 shows two identical spheres of diameter *D*. The first sphere is rigidly fixed in place at the origin and aligned with the *x*-axis, while the second is free to rotate around the first magnet a diameter distance away. Its orientation is also free to rotate around its own principal axis. A uniform magnetic field is applied perpendicular to the alignment of the first sphere.

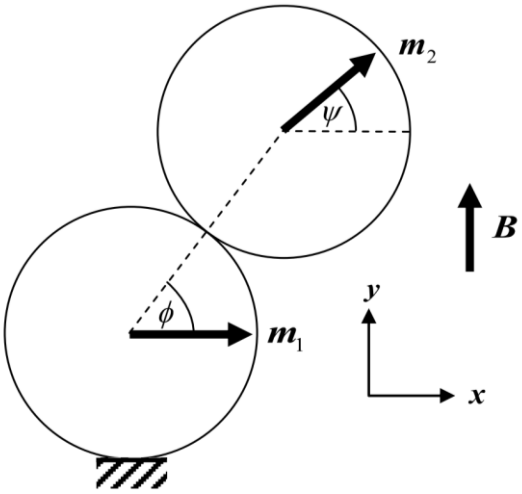



Figure 2.15: In this analytical model for two magnetic spheres in contact, the first sphere is rigidly fixed in place and aligned with the x-axis. The centre point of the second sphere is free to move in a circular path to some angle $\phi$ relative to the first sphere and also to rotate around its own axis by some angle $\psi$ . A uniform external magnetic field *B* is also present and points in the *y* direction.

The position of the centre point of the second sphere is given by (2.11) and the magnetisation of each sphere is given by (2.12) and (2.13)

$$\boldsymbol{r} = D(\cos\phi\,\boldsymbol{x} + \sin\phi\,\boldsymbol{y}) \tag{2.11}$$

$$\boldsymbol{m}_1 = m_1\boldsymbol{x} \tag{2.12}$$

$$\boldsymbol{m}_2 = m_2(\cos\psi\,\boldsymbol{x} + \sin\psi\,\boldsymbol{y}) \tag{2.13}$$

Combining (2.9), (2.11)-(2.13) the energy of the second sphere, $m_2$, due to dipole-dipole interaction with the first sphere, $m_1$, can be simplified to (2.14).

$$U_{\text{int}} = U_{dd}^{12} = \frac{\mu_0 m_1 m_2}{4\pi D^3}[\cos\psi - 3\cos\phi\cos(\phi - \psi)] \tag{2.14}$$

If the two spheres are exposed to a uniform magnetic field at right angles to the *x*-axis and

the first sphere, $m_1$, remains fixed in space, the second sphere's potential energy is adjusted by the Zeeman contribution given in (2.15).

$$U_{ext} = -m_2 B \sin\psi \tag{2.15}$$

The Zeeman energy contribution of $m_1$ is neglected as it is fixed in position and its own potential energy does not affect the final position of the system. In order to determine the minimum energy position of the system, the partial derivative with respect to the two independent variables must be calculated, which results in (2.16) and (2.17) when the magnetic strength of each sphere is equal ($m_1 = m_2$).

$$\frac{\partial U}{\partial \phi} = \frac{3\mu_0 m^2}{4\pi D^3} \sin(2\phi - \psi) \tag{2.16}$$

$$\frac{\partial U}{\partial \psi} = \frac{\mu_0 m^2}{8\pi D^3} \sin\psi - \frac{3\mu_0 m^2}{8\pi D^3} \sin(2\phi - \psi) - mB\cos\psi \tag{2.17}$$

Setting (2.16) and (2.17) equal to zero and solving yields a unique relationship between $\phi$ and $\psi$ as given by (2.18) and (2.19).

$$\psi = 2\phi \tag{2.18}$$

$$\psi = \arctan\left(\frac{8\pi D^3}{\mu_0 m} B\right) \tag{2.19}$$

To account for the anisotropic energy contribution, (2.10) is added to the total system energy. With the addition of the $\gamma$ variable, no analytical solution is possible. However the resulting partial derivatives can be simplified to a single non-linear function of one variable which may be solved using numerical methods such as Newton's method or other root finding techniques.

### 2.6.5. N Spheres

In order to extend this model to a chain of *N* identical spheres in a 2D plane, we first consider the dipole-dipole interaction energy between the $i^{th}$ and $j^{th}$ sphere by using (2.9) with (2.20), (2.21) and (2.22) for the position vector for the $i^{th}$ magnet and the magnetisation of each sphere respectively. For the first magnet, $r_1 = 0$, hence $\phi_1 = 0$ and its magnetisation is given by (2.21), which includes the anisotropic offset angle. As mentioned in Section 2.6.3, the anisotropy of this first magnet is also considered as its orientation is fixed in place.

$$\boldsymbol{r}_i = D\sum_{\alpha=2}^{i} (\cos\phi_i \boldsymbol{x} + \sin\phi_i \boldsymbol{y}) \text{ for } i > 1 \tag{2.20}$$

$$m_1 = m(\cos\gamma \boldsymbol{x} + \sin\gamma \boldsymbol{y}) \tag{2.21}$$

$$m_i = m(\cos\psi_i \boldsymbol{x} + \sin\psi_i \boldsymbol{y}) \tag{2.22}$$

The system potential energy due to the dipole-dipole interactions is given by (2.23).

$$U_{dd} = \sum_i \sum_{j>i} U_{dd}^{ij} \tag{2.23}$$

The system potential energy due the position of the spheres relative to an external uniform field is then given by (2.24).

$$U_{ext} = -mB(\sin\gamma + \sum_{i=2}^{N} \sin\psi_i) \tag{2.24}$$

The magnetocrystalline anisotropy is incorporated, as before, by adding (2.10) to the total system energy summation. As noted in Section 2.6.3, the anisotropy term is only considered for the first sphere in the chain since all subsequent spheres will act to mechanically align their easy axis of magnetisation with the applied field.

The effects of gravity can also be easily incorporated into this model. However the gravitational effects were found to be negligible in the experimental setup when the number of spheres are small (*i.e.* less than 5). This is verified by considering that the force between two of the 4.5 mm diameter spheres used in the experiment when in contact can be shown to be approximately 1000 times greater than the gravitational force.

As with the two sphere case, the minimum energy position vector can be calculated by differentiating the total energy function with respect to the independent variables, of which there are $2N+1$. This results in a system of $2N+1$ non-linear equations. The solution cannot be determined analytically, and hence a numerical approach is required.

### 2.6.6. Numerical Simulation

As mentioned, for the *N* sphere case, a system of non-linear equations results. To solve this type of problem, there are a range of algorithms and methods available, the choice of which depends on the size of the problem and the complexity of the equations. Some examples of algorithms include the trust-region method, Levenberg-Marquardt [53] and Monte Carlo simulations [54] . In this work the trust-region method was used.

The trust region method is an iterative algorithm that fits a quadratic model around an initial estimate of the solution. This model is only "trusted" in a region that surrounds this initial point. The size of this trust region varies depending on whether the model is found to be in agreement with the objective function. By solving this approximate model, a better estimate of the solution results. This intermediate solution is used as the next starting point for the algorithm. By iterating this approach, a solution can be found which satisfies a given set of criteria of the function tolerances and step size limits [55], [56].

MATLAB (Mathworks Corp., Natick, Massachusetts) was used to solve the system of equations, by first analytically calculating the derivatives of the energy function using the MATLAB Symbolic Toolbox, and then using these derivatives to form the system of equations that was solved using the MATLAB Optimization Toolbox. Typical computation times for $N = 4$ spheres was 400 ms on a desktop computer operating at 2.5 GHz.

### 2.6.7. Experimental Setup

#### 2.6.7.1. Magnets

The spherical magnets used were N42 grade, nickel plated neodymium-iron-boron rare earth magnets (KJ Magnetics, Jamison, Pennsylvania). The remnant magnetic flux density of each magnet as given by the manufacturer's datasheet is 1.32 T, which corresponds to an internal magnetisation of $1.05\times10^{6}$ A/m. Each sphere used in the experiment was 4.5 mm in diameter. The magnetocrystalline anisotropy constant of the magnets was estimated using (2.25) [52]. Where $H_{ci}$ is the intrinsic coercivity of the magnet given as 1040 kA/m by the manufacturer. This resulted in an anisotropy constant, $K = 686$ kJ/m$^3$.

$$K = \frac{H_{ci} M_s \mu_0}{2} \tag{2.25}$$

#### 2.6.7.2. Helmholtz Coil

In order to generate a uniform magnetic field for the experiments, a pair of custom Helmholtz coils was constructed. A Helmholtz coil is a set of two circular coils which carry equal current and are placed a radius distance apart along their central axis [57]. This arrangement results in an approximately uniform magnetic field in the region between the coils. Each coil consists of 200 turns of enamelled copper wire, with an inner diameter of 14 cm and an outer diameter of 18 cm. The magnetic field between the coils was measured using a Hirst GM08 gaussmeter (Hirst Magnetic Instruments, Falmouth, England). The resulting field between the coils was found to be 2.51 mT ± 0.25 mT per amp flowing through the coils. From simulation, the field from an ideal set of Helmholtz coils of these dimensions was observed to be homogeneous in the region at the centre of the coils approximately $8\,\text{cm}\times8\,\text{cm}$, with a field variation of < 0.1 %.

#### 2.6.7.3. Test Apparatus

A test rig was constructed to securely hold the first magnet in place between the Helmholtz coils. The rig consisted of a simple clamp placed at the centre of the coils, with the sphere chain free to move in space. The clamp was positioned such that the applied field would be at right angles to the orientation of the first sphere, which was rigidly held by the clamp. Due to the strong attraction between each sphere and the fact that the chains tested were only up to four spheres in length, the effect of gravity was observed to be negligible, and no additional fixture was used to keep the spheres rotating on a level plane. A camera was held in place above the magnets to capture images of their positions. Figure 2.16 and Figure 2.17

show the experimental setup used.

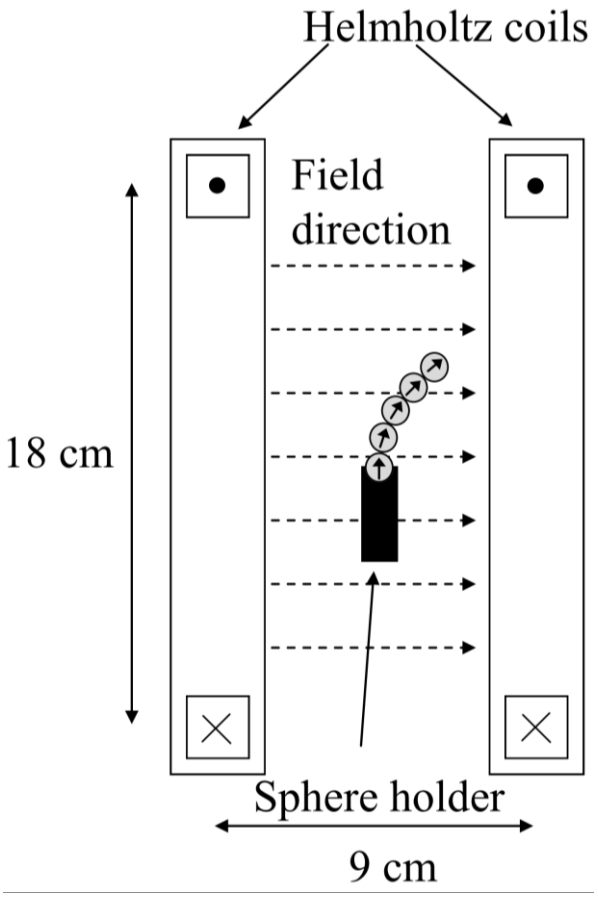



Figure 2.16: Simplified test setup schematic.

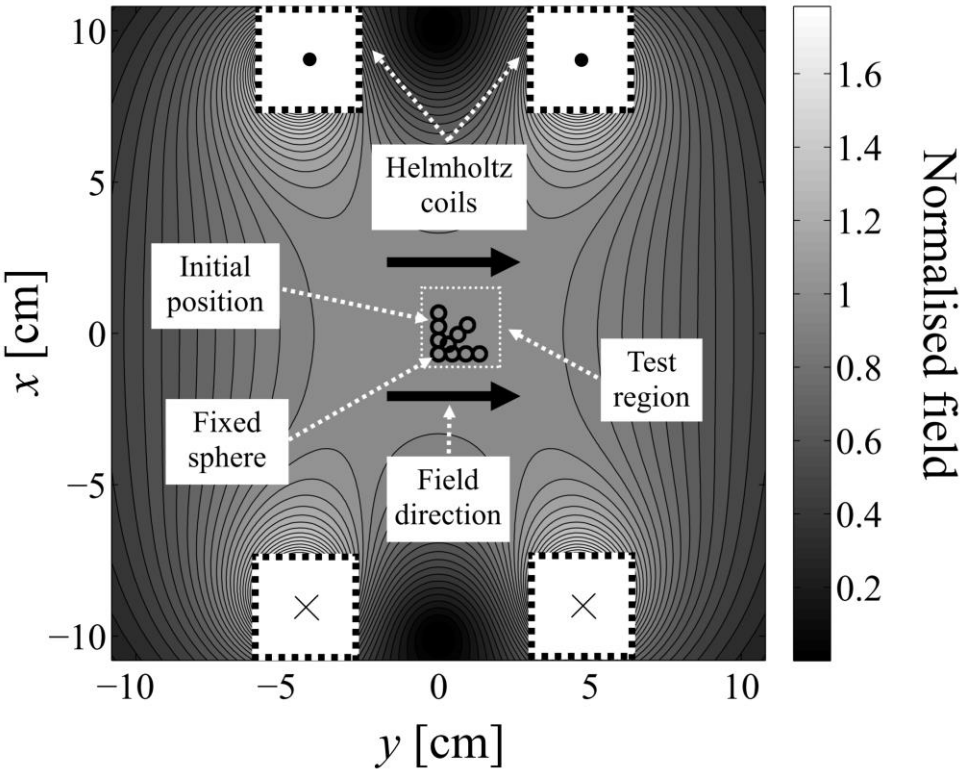



Figure 2.17: Experimental setup showing the position of the Helmholtz coils and magnetic sphere chain deflection. The contour plot of the magnetic field is also shown with the field normalised to the value at the centre of the coils. From simulation, the field in the test region varies by less than 0.1 %




Figure 2.18: An example of the deflected chain showing how the angle $\phi$ between each sphere is calculated. The first sphere is rigidly held in place with a small clamp. The clamp was specially designed to allow free movement of the spheres around the first constrained sphere

To calculate the positions of each sphere in space relative to the first fixed position sphere, the camera images were processed using the MATLAB Image Processing Toolbox. A simple program was developed to determine the centre of each sphere and calculate the angles between each sphere relative to the *x*-axis. The orientation of each sphere was not examined. Figure 2.18 shows the camera view and the angle definitions.

### 2.6.8. Results

Three tests were carried out using 4.5 mm spheres with chains of two, three and four magnets in length. Each test was repeated three times and averaged, with different spheres used in each iteration to reduce errors due to irregularities in sphere construction and magnetisation. Each chain was exposed to uniform magnetic fields up to 35 mT from the Helmholtz coils. Figure 2.19, Figure 2.20 and Figure 2.21 show the results of each of these tests.

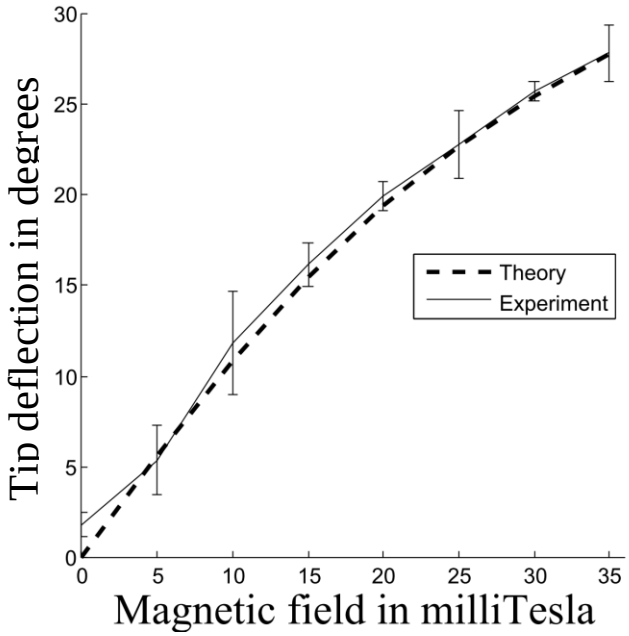



Figure 2.19: Comparing tip deflection in the case of two magnetic spheres from theoretical modelling and experimental testing. Error bars indicate standard deviation.

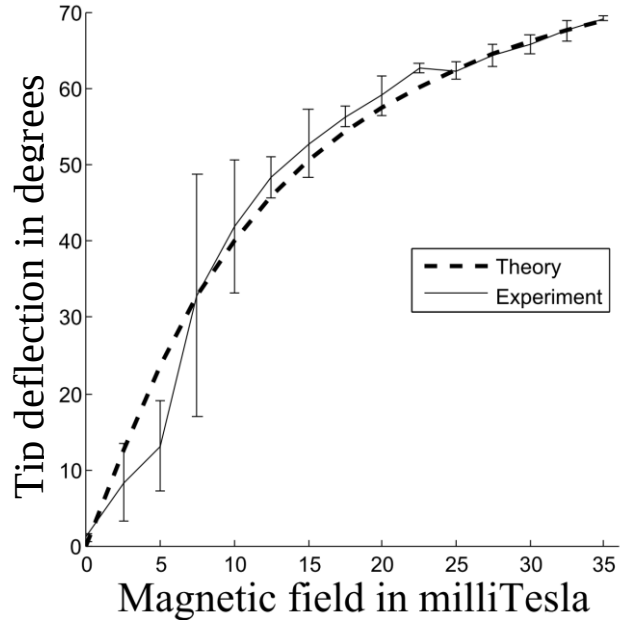



Figure 2.20: Comparing tip deflection in the case of three magnetic spheres from theoretical modelling and experimental testing. Error bars indicate standard deviation.

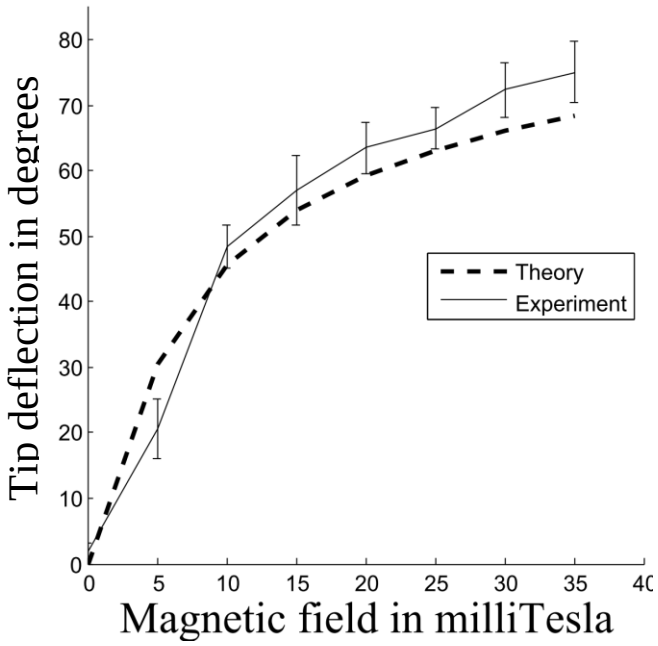



Figure 2.21: Comparing tip deflection in the case of four magnetic spheres from theoretical modelling and experimental testing. Error bars indicate standard deviation.

In Figure 2.19, we see that the experimental graph closely matches the theoretical model. However in Figure 2.20 and Figure 2.21 it can be seen that the error has increased, and in Figure 2.21 it is clear that the model underestimates the actual deflection. This error occurs when the magnets overcome the stiction holding them in place, which results in an erratic motion whereby the magnet overshoots its equilibrium position and comes to rest at a random position beyond it, depending on the surface friction. The error increases as the number of unmodeled variables increases such as the friction between the spheres. The number of local minima in the energy function also increases, which leads to more possible resting points for the spheres.

The primary source of error in this model is the effect of contact friction between each sphere. If we consider the small contact area of each sphere, and the relatively large force generated by the dipole-dipole interaction, it is clear that friction is a major factor. The force between each magnet can easily be calculated. This force can then be considered as the normal force which is proportional to the static friction force holding each magnet in place, which in turn is a function of the orientation of each sphere.

It can be seen that the friction force reduces when the spheres move out of alignment due to the presence of the external field, which can be seen from the experimental error in Figure 2.22. In this figure, we see that the error between the model (which neglects friction) and the experiment reduces with increasing field strength, *i.e.* when each sphere is less aligned with its neighbours than in the zero field case. The actual friction is difficult to model, as it varies considerably from sphere to sphere, as well as on the surface of each. Near the poles, the magnets generally become damaged very quickly due to the contact force. This damage increases the friction.

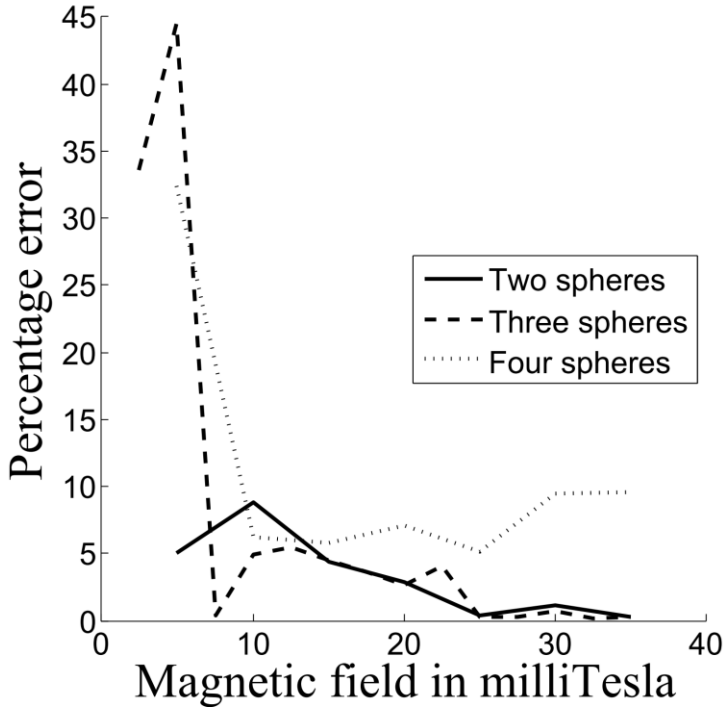



Figure 2.22: Error in deflection angle between the experimental results and theoretical model for each of the three cases investigated

These effects make accurately predicting the deflection difficult, but the model is nonetheless very useful in approximately determining the final position of the sphere chain, particularly in the case of stronger (*e.g.* > 10 mT) external fields where percentage error in tip deflection is less than 10 %.

To investigate the effects of the magnetic anisotropy given by (2.25) of the first sphere, a comparison with and without this term is shown in Figure 2.23 which shows the results of a simulation of four spheres with an applied field of 35 mT. The results of the model with and without the anisotropy energy term are shown. With the added anisotropy, slightly larger deflections are observed overall. However only the position of the second sphere changes significantly and the position of each additional sphere relative to the second sphere remains largely unchanged. The direction of each sphere is also minimally affected. Neglecting the anisotropic energy term from the simulation for the test shown in Figure 2.19 was seen to nearly double the percentage error, but had a negligible effect on the results in Figure 2.20 and Figure 2.21 for the three and four sphere cases respectively.

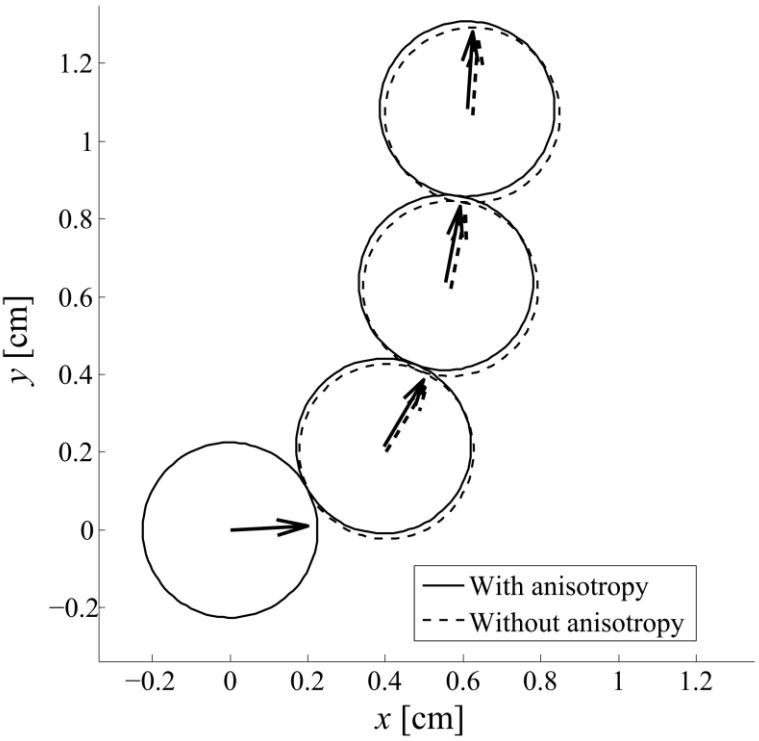



Figure 2.23: The simulated position of the four sphere case with an applied field of 35 mT along *y*. The arrows indicate the direction of magnetisation. The dashed lines show the position of the spheres in the absence of the anisotropic energy term. The magnetisation of the first sphere is assumed to be aligned with the *x*-axis in the absence of the anisotropic energy term.

### 2.6.9. Conclusion

A theoretical model for the interaction of chains of permanently magnetised spheres at the millimetre scale has been presented. This model is formulated by summing the potential energy of each element of the system and minimising this function to determine its final equilibrium position. Analytical expressions for the two sphere case in the absence of magnetic anisotropy have been derived, and numerical methods for the more complex $N$ sphere case have been demonstrated. The models presented are 2D. However this can easily be expanded to 3D although this doubles the complexity of computation as each sphere now has four position and alignment variables. Experimental results have shown reasonable agreement between the model and the tests with improved agreement at larger externally applied fields (*e.g.* >10 mT). The primary source of error is the friction between each sphere, which is difficult to model due to the random nature of friction on each sphere from manufacturing and other effects. The model error was seen to decrease as the spheres move out of alignment due to reduction in the friction force. The resulting model, while only accurate to within 10-15 %, is very useful in the design of magnetic attachments for catheter deflection. Magnetic anisotropy needs to be considered, particularly in the two sphere case. In practical applications, deflection feedback control would be used to bring the system to the desired position, with the theoretical model serving as an initial estimate.

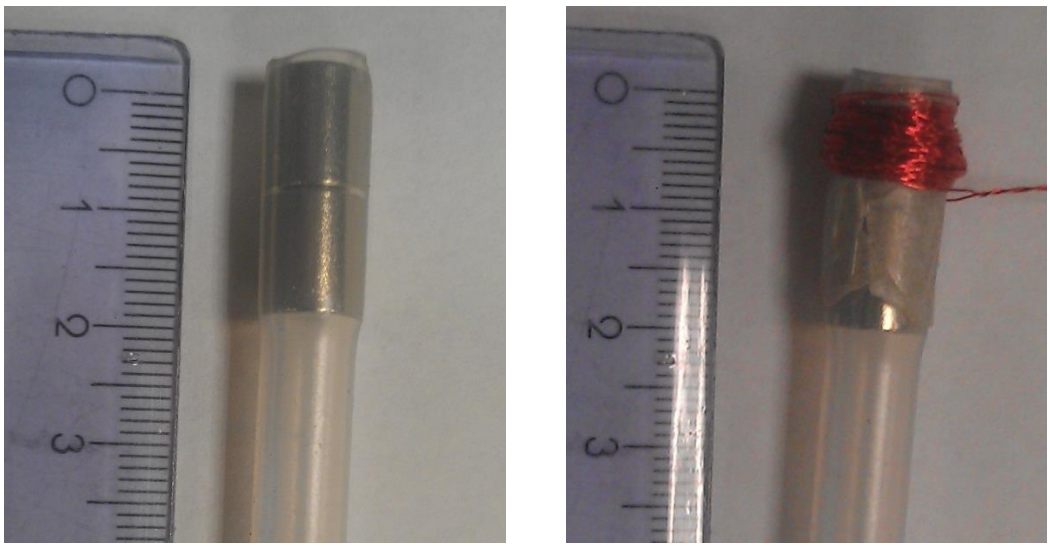
## 2.7. EM Tracking and Steering

### 2.7.1. Overview

In this section we demonstrate both magnetic steering and tracking of a magnetically tipped catheter model. This stands as a proof of concept showing how magnetic fields can be used to both track and move an object simultaneously, without interference from the different magnetic fields. This experiment uses our custom EM tracking system which will be described in Chapter 3. The operating frequency ranges of each system are sufficiently separated that interference is not observed. The actuator operates from 0-200 Hz while the tracking system operates between 20 and 30 kHz. A simple silicone catheter made with an N42 grade neodymium permanent magnet and a sensor coil at its tip was controlled with a simple closed loop control system that allows accurate positioning of the catheter tip. Good performance is observed over a small operating region. However the nonlinear attractive force of the electromagnet can easily cause instability. For simplicity, only the vertical displacement of the sensor is considered.

### 2.7.2. Magnetic Catheter and Tracking Sensor

A simple catheter comprising a silicone rubber tube and two cylindrical magnets was assembled. Two N42 neodymium magnets that measured 10 mm in length and 6 mm in diameter were used for the magnetic tip. The catheter dimensions are much larger than useful in most practical applications in order to increase the volume of permanent magnet material and maximise the attractive force on the catheter. The commercial sensors used with our EM tracking system (see Chapter 3) are sensitive to DC magnetic fields. Hence a custom sensor coil was wound around the permanent magnet tip. One hundred turns of 0.15 mm copper wire were used for the sensor winding. The irregular winding pattern seen here has an insignificant effect on the systems accuracy. The silicone tube had an OD of 6.7 mm with a wall thickness of 1.3 mm. The silicone used had a durometer grade of 50 A. Figure 2.24 shows the catheter model before and after the sensor winding.



(a) (b)

Figure 2.24: (a) Permanent magnet tip and (b) position sensing coil wound on the outside.

### 2.7.3. Test Setup

Figure 2.25 shows a representation of the test setup used for the control of the catheter position. The catheter was rigidly clamped in place 9 cm away from the magnet tip. The catheter was then allowed to freely deflect under its own weight. The electromagnet was placed 9 cm above the equilibrium position of the catheter tip and the magnetic force was used to counteract the gravitational force pulling the tip downwards. The EM tracking system's transmitter was located below the setup. For the tracking experiment, only the vertical height, *z*, of the sensor was considered. The *z* axis of the transmitter is perpendicular to the transmitter and along the central axis of the electromagnet. By measuring the signal from the sensor, the position of the catheter tip was determined. A simple control system was implemented in MATLAB which in turn controls the coil current by using the analog output of a NI PCI 6259 DAQ card which interfaces with a high current power supply. A Delta Elektronika SM 52-30 power supply was used for this purpose. The supply can deliver up to 30 A at 52 V and can be directly controlled using an analog voltage in the range of 0-5 V. Figure 2.26 shows a picture of the test setup.

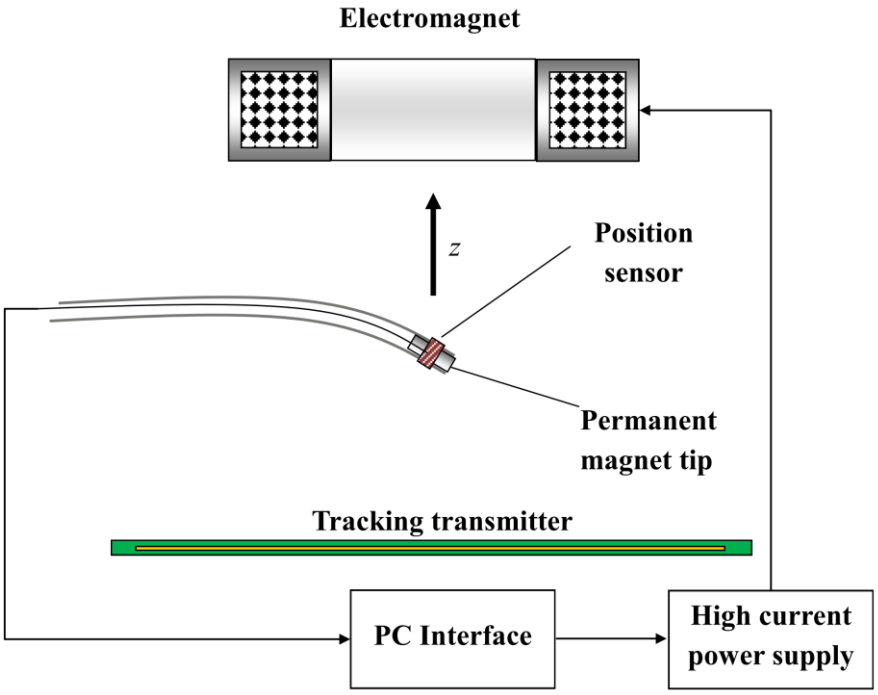



Figure 2.25: Test setup showing the catheter model with the magnet tip with the position sensor attached. The sensor data is processed by the PC which then sends the control signals to a high current power supply which, in turn, drives the electromagnet.

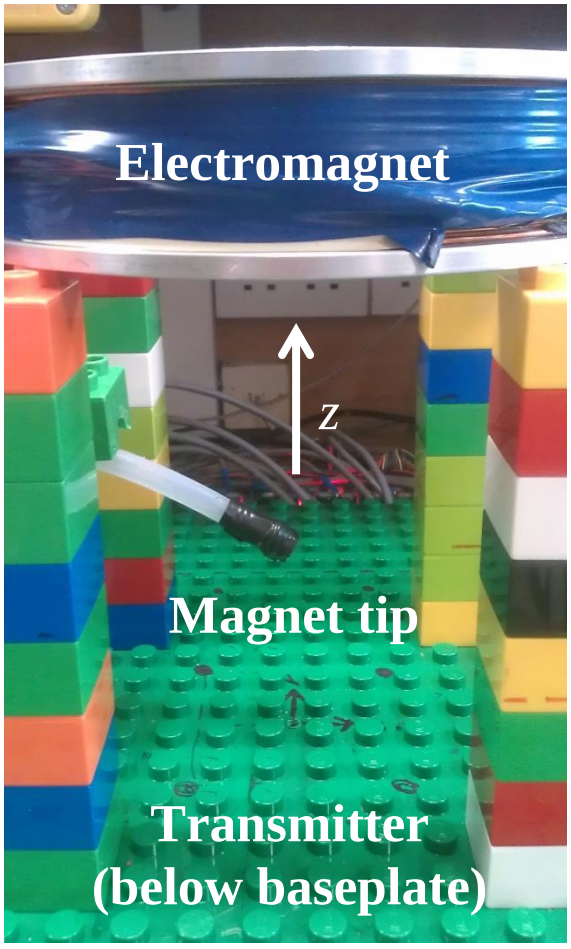



Figure 2.26: Test setup with an electromagnet coil placed above the tracking systems transmitter. By controlling the current in the coil, the position of the magnetic catheter tip can be controlled.

### 2.7.4. Controller Design

For the control system, a simple proportional plus integral (PI) controller was used. This method was used as it is simple to implement and can minimise steady state errors. Since the system is nonlinear, a simple proportional controller would give very poor performance. The input to the control system is the difference between the desired position setpoint, *r(t)*, and the estimated sensor position denoted by *z'(t)* as given in (2.26). Equation (2.27) shows the standard equation for a PI controller in the time domain. The parameters $K_p$ and $K_i$ can be adjusted to change the dynamics of the controller. If these values are too high the system quickly becomes unstable. These parameters were manually adjusted until the system gave satisfactory performance which was specified as low steady state error and stable settling. The final values used were $K_p = 0.02$ and $K_i = 0.1$. The actual system operates in discrete time with an average sample rate of approximately 20 Hz which varies depending on the convergence of the EM tracking algorithm although it rarely varies by more than 1 Hz. Hence, a discrete time version of the controller is given by (2.28) where $T_s$ corresponds to the sampling period and $n$ to the incremental sampling index. A non-recursive digital integrator was used here due to the short duration of the test.

$$e(t) = r(t) - z'(t) \tag{2.26}$$

$$u(t) = K_p e(t) + K_i \int_0^t e(\tau) d\tau \tag{2.27}$$

$$u[n] = K_p e[n] + K_i T_s \sum_{j=0}^{n} e[j] \tag{2.28}$$

Figure 2.27 shows a block diagram of the control scheme used in this test.

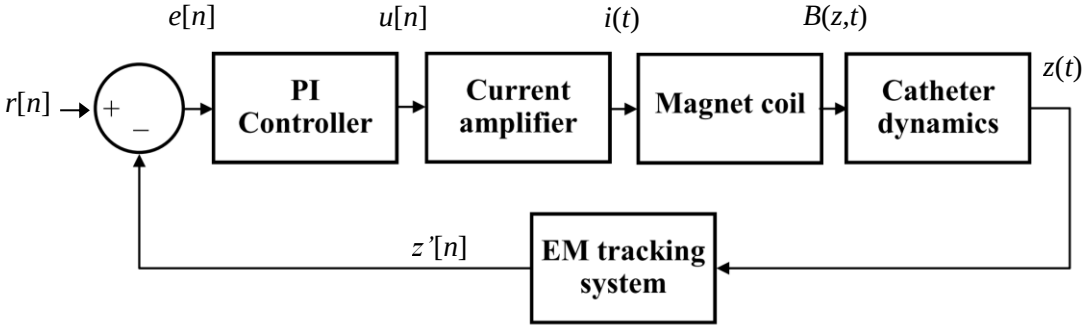



Figure 2.27: Closed loop control block diagram.

### 2.7.5. Open Loop Tests

The first tests investigated the open loop performance of the system, and no controller was used. Figure 2.28 shows the response of the catheter position to step inputs in current. With larger displacement steps, the catheter experiences larger overshoots of its equilibrium position although in general the dynamics appear to stay consistent over this small

displacement range. Figure 2.29 shows a similar test but with a slowly increasing ramp current waveform. We see that a mostly linear relationship is seen between the current and position and a linear model could be used to for the controller design in this operating region. However beyond a coil current of approximately 10 A, the tip is rapidly pulled up towards the electromagnet. This behaviour is typical in electromagnetic actuation systems and a controller is almost always required for stable positioning.

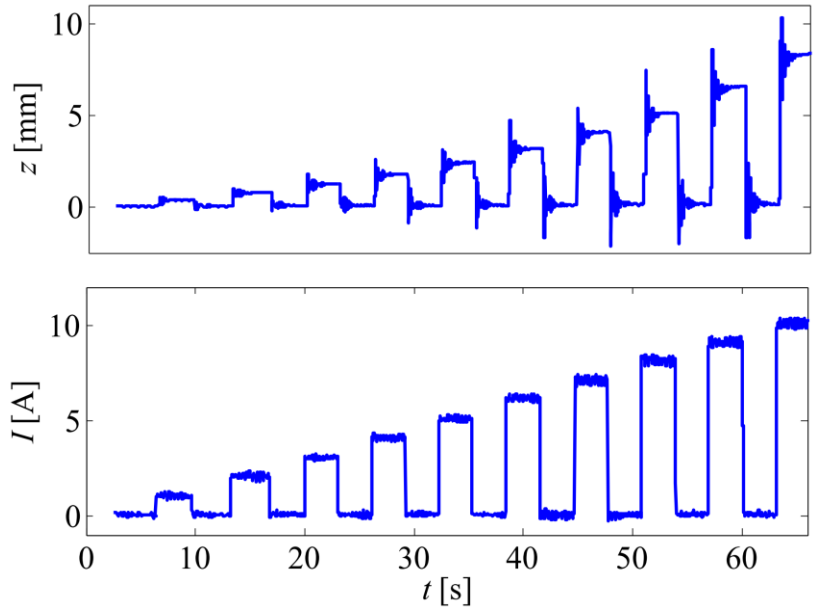



Figure 2.28: Open loop step input tests showing the $z$ displacement of the sensor and the corresponding input coil current.

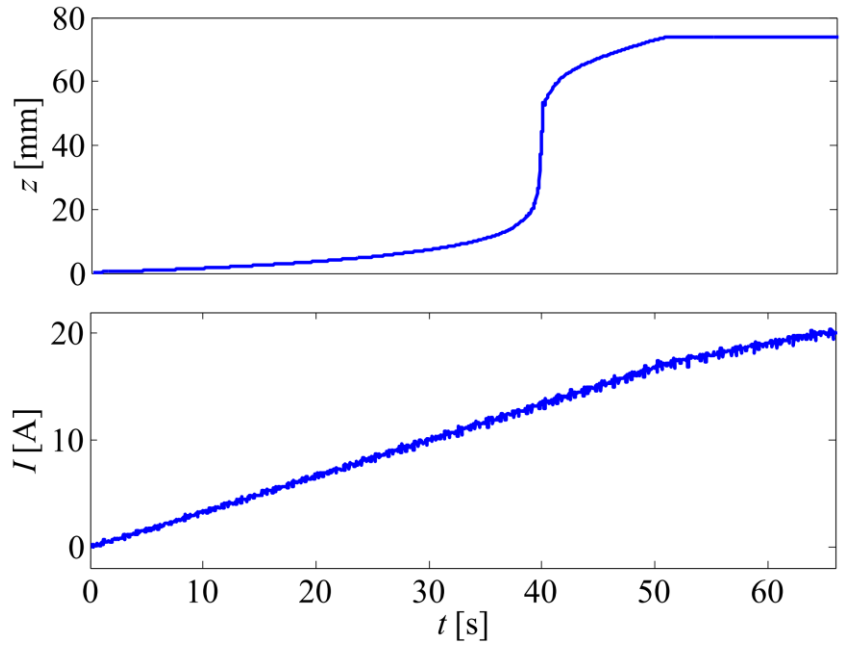



Figure 2.29: Open loop ramp input current applied to the electromagnet coil. The attractive force becomes highly nonlinear in close proximity to the electromagnet. Beyond 10 A, very non-linear behaviour results.

### 2.7.6. Closed Loop Results

After manually tuning the controller parameters, the performance of the system was evaluated for a number of reference signal inputs. First a simple step response is seen in Figure 2.30. There is a small overshoot of the setpoint although the system eventually settles after approximately 5 s. It was observed that if the controller gains were set too high then the overshoot was large enough to cause instability. Values of $K_p > 0.025$ and $K_i > 0.2$ generally caused instability.

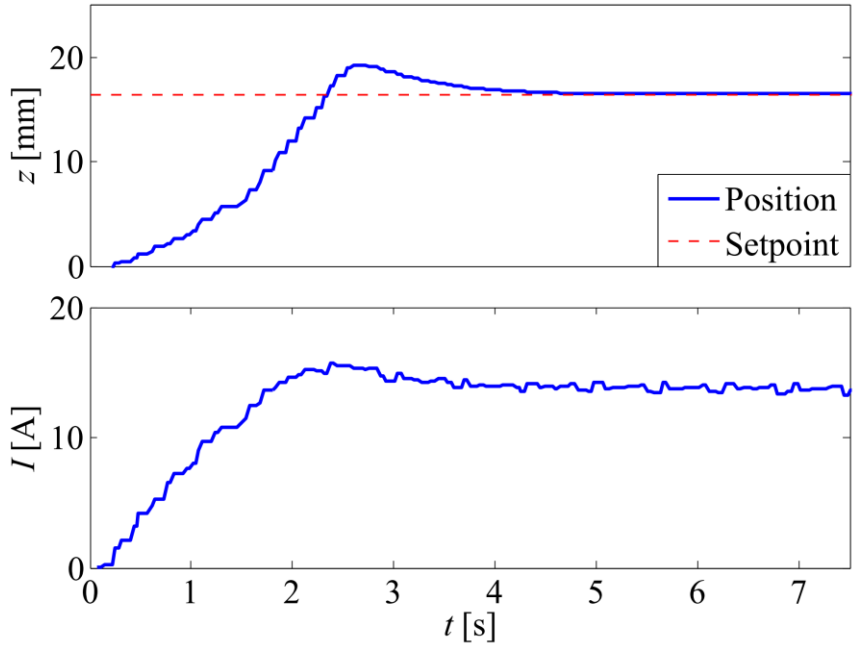



Figure 2.30: Closed loop response to a step input set point.

Figure 2.31 shows the response to a staircase like waveform. We see that the system becomes more oscillatory as the tip moves closer to the electromagnet. Ideally an adaptive control scheme might be used here to change the controller gains depending on the proximity to the electromagnet. Figure 2.32 shows the response to a sinusoidal reference signal. We see that there is a small lag between the reference signal and the tip position, due to the slow response time of the controller. Faster response generally led to instability.

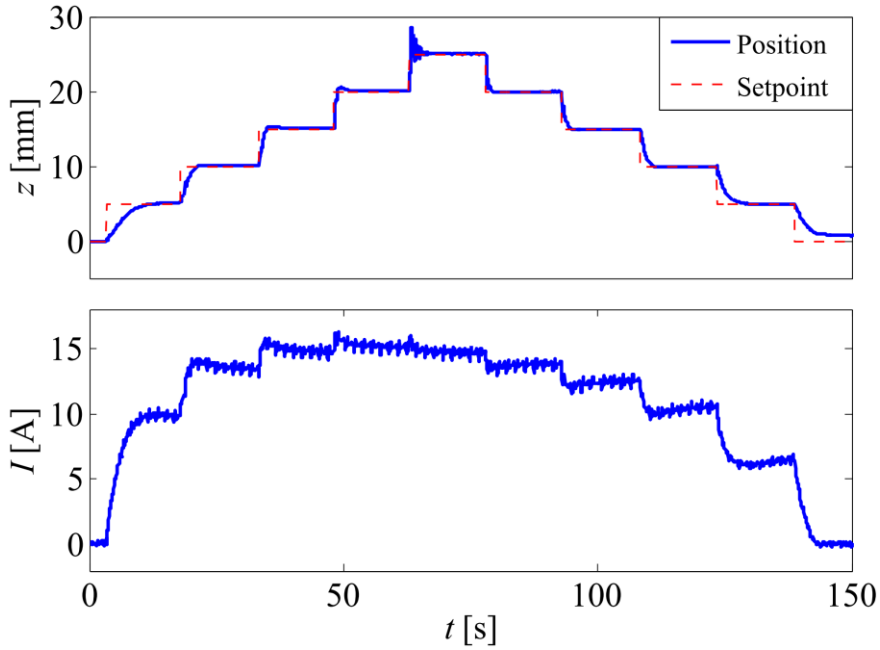



Figure 2.31: Closed loop performance with a staircase shaped trajectory.

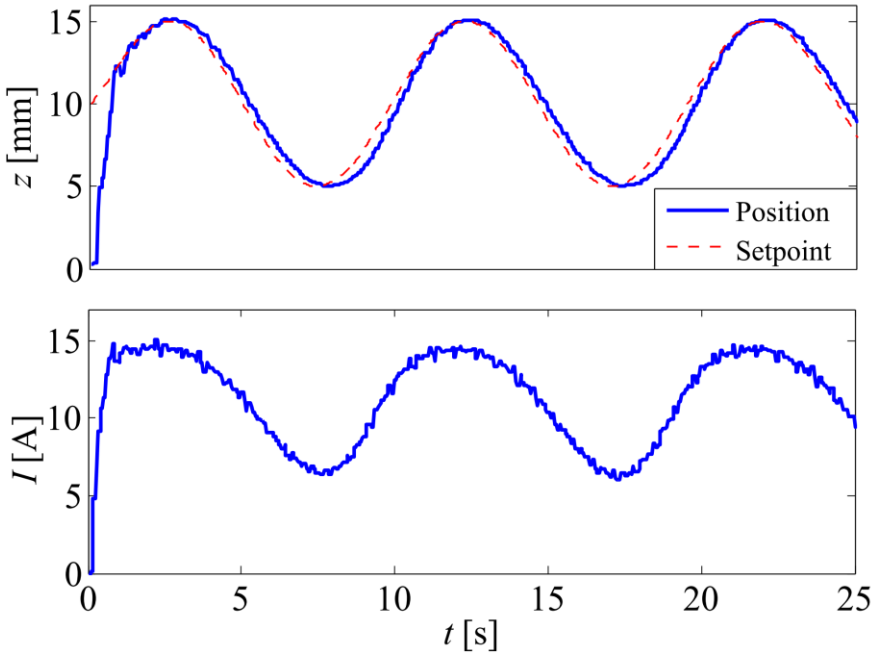



Figure 2.32: Closed loop performance with a sinusoid trajectory.

Finally, Figure 2.33 shows the response of the system when the controller becomes unstable. Large position swings are observed and the coil current oscillates aggressively. This is partly due to the saturation of the amplifier and the massive increase in magnetic force as the tip approaches the magnet.

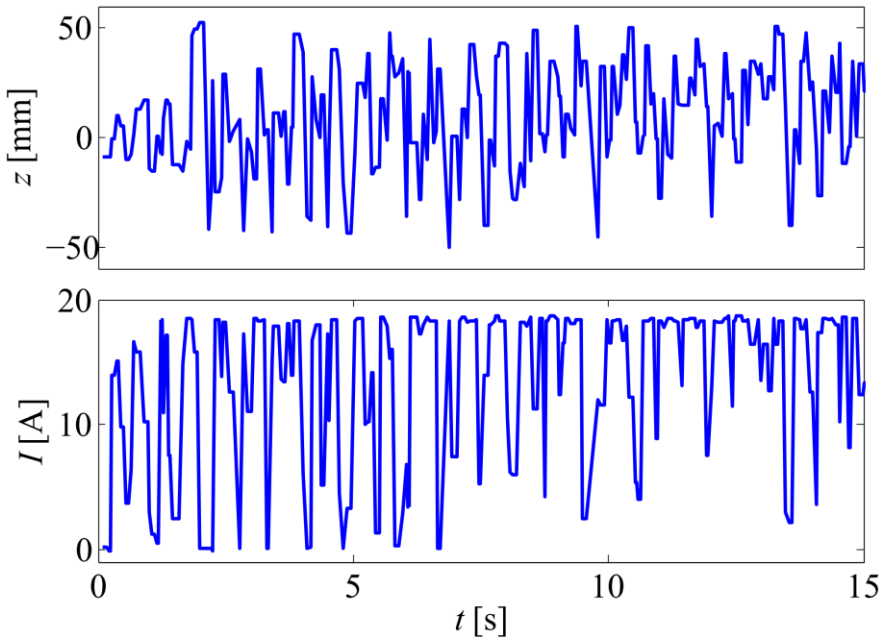



Figure 2.33: Unstable behaviour of the system with incorrect controller gain settings.

### 2.7.7. Discussion

It has been demonstrated in this section how two separate electromagnetic systems, one for steering and one for tracking, can work together in a single system to accurately deflect a catheter model. Currently available EM tracking systems cannot operate in such an environment, mostly as a result of the types of sensors used which typically saturate in the presence of relatively low magnetic fields. While we have shown that for the application to lung navigation, due to the dimensional constraints within the operating space, magnetic navigation is unsuitable. Notwithstanding this observation, we have shown that even with a very rudimentary control algorithm, accurate control is achievable. Future applications for this type of system, which allows accurate tracking in the presence of secondary magnetic fields, include certain MRI procedures as well as catheter navigation using the Stereotaxis system without the need for fluoroscopy for catheter tracking.

## 2.8. Summary

In this chapter we examined in detail the potential use of electromagnets for catheter steering with particular application to lung navigation. The primary results are as follows:

- The magnetic force and torque that can be exerted on catheter of dimensions suitable for lung navigation required excessively large and powerful external electromagnets to be of advantage over standard wire-steered catheters.
- A detailed mathematical model for the deflections of chains of spheres for magnetic catheter tips has been developed and tested experimentally. Experimental results show the accuracy of the model, although friction of the spheres adds an appreciable

error to the model results.

- A novel implementation of a magnetically steered and tracked catheter model has been presented. With a simple control algorithm, 1D control was achieved for controlling the vertical height of the catheter. This experiment verifies the parallel operation of EM steering and tracking without interference from one the other.

# Chapter 3

# EM Tracking: Design and Implementation[†]

## 3.1. Overview

This chapter details the design and development of an electromagnetic system for determining position and orientation of a small magnetic sensor with application in a virtual bronchoscopy system. The background theory and relevant literature of EM tracking is briefly discussed while the details of each subsystem of the EM tracking system are explored in detail. In particular, novel methods for controlling the transmitter field strength and demodulating the resulting magnetic field components are presented.

Key contributions presented in this chapter include:

- A novel closed loop constant current driver circuit that provides stable AC current waveforms to an array of magnetic coils. The arrangement also decouples each coil from one another, effectively cancelling out their mutual inductances.
- An asynchronous demodulator that uses simulated reference signals and composite analog input signals to determine multiple frequency components with a reduced number of input signals to be sampled.
- A new under-sampling methodology for EM tracking which allows the use of sub-Nyquist sampling rates to sample and demodulate the magnetic signals of interest.
- An efficient matrix-based demodulation method which allows for rapid calculation of each frequency component in a composite magnetic signal.

## 3.2. Introduction

The system uses planar magnetic coils transmitting low frequency magnetic fields (< 30 kHz) and implemented on printed circuit board (PCBs), as well as a miniature pick-up

[†] This chapter is based on K. O'Donoghue, D. Eustace, J. Griffiths, M. O'Shea, T. Power and P. Cantillon-Murphy, "Catheter position tracking system using planar magnetics and closed loop current control,", *IEEE Transactions on Magnetics*, 50(7), 1-9, July 2014 and K. O'Donoghue and P. Cantillon-Murphy, "Low cost super-Nyquist asynchronous demodulation for use in EM tracking systems", *IEEE Transactions on Instrumentation and Measurement*, *in press*, Aug 2014.

coil placed at the distal end of a catheter. By measuring induced voltage in the pick-up coil caused by an array of magnetic sources at various frequencies, position and orientation can be determined by solving a non-linear system of equations. The hardware system consists of an 8 coil array of transmitting coils, an 8mm receiver coil and associated amplifiers. The software filters and demodulates the input signals and calculates the position and orientation using MATLAB.

There are numerous different electromagnetic tracking methods described previously. Using planar coils for position detection has been demonstrated by Plotkin et al [9]. There are also a number of commercially available electromagnetic (EM) tracking systems such as Northern Digital's Aurora and Ascension's trakSTAR [58], [59], which are used in a range of medical procedures. However these are typically prohibitively expensive and are also susceptible to magnetic interference [60].

Many magnetic tracking methods make use of the dipole approximation to simplify the required calculations [61], [62], [8] and other research has investigated methods to improve this approximation [63]. However, significant errors can occur when using this approximation. We mitigate these errors and increase accuracy by directly calculating the exact magnetic fields with a filamentary conductor based method as described by Sonntag et al [64].

Planar arrangements of source coils is well documented in research [9], [65], [66], [67] and in commercially available systems [68]. The use of PCB coils for position tracking has not been documented in any other published work. Planar PCB technology has many other applications such as in wireless energy transfer [64], [69], antenna design [70] and low cost inductors [71]. Its use in position tracking has the advantage that the coils can be easily mass produced almost identically, much more than a similar set of coils wound in traditional methods. The exact position of each track can easily be determined, allowing for very accurate prediction of the generated magnetic fields with analytical methods.

In this chapter we present a novel closed loop current feedback amplifier for controlling the magnetic field used for position sensing. This ensures long term stability of the field while also reducing crosstalk interference. We present a detailed description of the drive circuitry required to control the AC magnetic fields for position sensing. The vast majority of prior work either neglects the details of associated drive circuits or use methods that could potentially lead to long term drift in the magnetic fields. Common approaches include the use of a resonant LC tank circuit driven by square wave excitations [9], [65]. Other methods include the use of audio-amplifiers to drive source coils as seen in [72], [73]. However these methods rely on the parameters of the amplifiers and the load and there is no reference to feedback for stable current control. Since the magnetic fields generated are directly proportional to coil current, having a constant current operation ensures variations due to temperature and other conditions do not adversely affect the current level. The operation of

the system is then dependent on the accuracy and stability of the current measurement, which with careful consideration can easily be made to be reliable.

Magnetic field strength typically used for EM tracking applications is usually low (<100 μT) as it is limited by exposure restrictions [74]. The resulting measurements are then low in amplitude normally ranging from microvolts to millivolts. Precision detection methods are critical to reliably gather data, particularly as errors in magnetic field measurements directly affect position and orientation accuracy. Measurement errors of greater than 5 % have been observed to cause unacceptable accuracy errors in position. Numerous methods exist for measuring low amplitude AC signals such as these, one of the most popular being synchronous detection [75], [76] as it gives narrow bandwidth and excellent noise rejection. Many tracking systems make use of synchronous detection [9], [73] as typically multiple frequencies with narrow bandwidths form the signal of interest. Fourier transform methods [77] have also been used for this purpose but requires large numbers of samples to give good resolution. Our first iteration of the EM tracking system utilised synchronous demodulation. The reference signal in a synchronous demodulator is typically directly related to the signal to be detected, *i.e.* locked together in frequency as they originate from the same source [78]. In our application, the coil current serves as a reference signal [9], but for a system with 8 coils and 1 sensor, this requires 9 signals to be sampled. This requires a multichannel ADC which operates at a much higher aggregate sampling frequency than would be required if less signals were to be measured. To simplify these requirements, the second iteration used simulated reference signals, which results in asynchronous demodulation [79]. If the frequency mismatch is small in comparison to the bandwidth of demodulator there is minimal loss in accuracy with this method in comparison to synchronous demodulation.

To reduce the cost of the demodulation hardware component of the system we use undersampling, also known as super-Nyquist sampling, in order to reduce the sample rate of our system. This methodology is frequently used in high frequency receivers [80] as well as low frequency synchronous demodulation [81]. Undersampling has been used in position sensing for single axis inductive position sensors [82], but has not been applied to a full 5 degree of freedom (DOF) position and orientation system. The lower sample rate allows the use of cheaper ADCs and also gives more computation time between samples which is useful for implementing complex demodulation methods on microcontrollers. Many precision ADCs operate at lower sample rates to ensure accuracy and reduce noise, in particular dual slope integrating types [81]. Hence undersampling can provide high accuracy without the increased cost for high speed, high precision ADCs.

## 3.3. Theory of EM Tracking

### 3.3.1. Overview

Here we examine the basic topologies of EM tracking systems and the different building blocks that make up a typical system. The governing equations for our implementation are presented and commonly used commercial systems are examined.

### 3.3.2. EM Tracking Topologies

EM tracking in its simplest form uses the spatial variation of magnetic fields to determine the position of a sensor. Simple systems such as linear variable differential transformers (LVDTs) use changing magnetic coupling between coils to determine linear displacements in servo mechanisms. As the position of a magnetic core between the two coils is changed, the magnetic coupling also changes, and these changes can be converted into accurate position information [83]. Magnetic rotary encoders also use changing magnetic field measurements to determine position. All these examples are single degree of freedom and operate on relatively simple mathematical relationships. To determine the full 3D position of an object and also its associated orientation dramatically increases the complexity.

An early example of the use of EM tracking for 3D position and orientation was demonstrated in 1962 by Kalmus et al [84]. Here, a low frequency magnetic field was used for tracking the relative position of one vehicle to another with separation on the order of 200 ft. Raab et al proposed a similar concept in 1979 for head tracking in fighter aircraft [85]. Raab also worked with Polhemus, a company which was among the first to sell commercial EM tracking systems for both military and medical applications.

EM tracking systems for medical applications can be broadly segmented into two types:

- Small insertable magnetic source with external magnetic sensors.
- Small insertable magnetic sensor with external magnetic field sources.

Small in this sense is on the millimetre scale such that they can be introduced within the human body and, as expected, the required size is dependent on the location within the body where sensing is required. For both types, the small sensor or source can be both wireless and wired. For example a permanent magnet acting as a source can be wirelessly located within the human intestinal system [4] or wired sensors can be used for catheter localisation [58].

Many research papers have documented the use of small permanent magnets as the magnetic source for EM tracking [86]. Permanent magnets have the advantage that they are passive devices which can simplify systems by removing drive requirements for the source. They also have the advantage in this application as they can be used as an actuation element as

well as a position sensing component [29]. The main disadvantage is that the magnetic fields are typically very small and the Earth's magnetic field must be considered as the fields are DC.

The majority of commercially available medical systems use small sensors, with external magnetic field generation [58], [87], [88]. This is due to the fact that typically the sensors can be made very small and the magnetic field source can be something other than DC, hence the effect of the Earth's magnetic field can be easily mitigated. With AC magnetic field systems, higher frequencies can be used to give larger signal levels increasing their accuracy and useful range.

### 3.3.3. Formulation of Governing Equations

As can be seen elsewhere [9], [65], [66], [89], AC EM tracking systems are typically based on Faraday's law to induce a voltage in a search coil. Our system consists of a sensor coil in the presence of an AC magnetic field, which is connected to an amplifier. The AC magnetic field is a superposition of 8 separate magnetic field sources. By measuring and demodulating the induced voltage, the associated flux through the coil due to each source is determined and from this the position and orientation may be determined. Consider the orientation, $\boldsymbol{n}$, of the sensor to be defined in Cartesian coordinates by (3.1).

$$\boldsymbol{n} = \sin\theta\cos\varphi\hat{\boldsymbol{x}} + \sin\theta\sin\varphi\hat{\boldsymbol{y}} + \cos\theta\hat{\boldsymbol{z}} \tag{3.1}$$

where $\theta$ and $\varphi$ are rotation angles in spherical coordinates.

The magnetic field from the $i^{th}$ coil at the point $(x, y, z)$ is a non-linear vector function of three components of flux density given by (3.2).

$$\boldsymbol{B}_i(x, y, z) = \begin{bmatrix} B_{xi} & B_{yi} & B_{zi} \end{bmatrix} \tag{3.2}$$

A matrix containing each magnetic field magnetic field component is defined by (3.3).

$$\mathbf{B} = \begin{bmatrix} B_{x1} & B_{y1} & B_{z1} \\ B_{x2} & B_{y2} & B_{z2} \\ \vdots & \vdots & \vdots \\ B_{x8} & B_{y8} & B_{z8} \end{bmatrix} \tag{3.3}$$

The associated flux due to each coil is then given by (3.4)

$$\Phi_i = A\left[ B_{xi}\sin\theta\cos\varphi + B_{yi}\sin\theta\sin\varphi + B_{zi}\cos\theta \right] \tag{3.4}$$

where $A$ is the area of the sensor. For mathematical convenience, the flux is assumed to be measured from an infinitely small volume. Figure 3.1 shows the development of this expression and the coordinate system used. The induced voltage is dependent on the frequency of excitation. If we consider that a single scaling factor, $k_i$, can be used for each excitation frequency which accounts for area, number of turns and detector amplifier gain, a vector of sensor sensitivities including the carrier signal could be expressed with (3.5).

$$\boldsymbol{k} = [k_1\sin\omega_1 t \quad k_2\sin\omega_2 t \quad \ldots \quad k_8\sin\omega_8 t] \tag{3.5}$$

Hence the induced voltage on the output of the detector amplifier will be a single composite AC signal given by (3.6).

$$v = k\mathbf{B}\boldsymbol{n}^T = k\boldsymbol{\Phi}_{meas} \tag{3.6}$$

This voltage is demodulated and scaled to arrive at the flux due to each coil. Once the flux has been calculated, the position and orientation can be determined by using an iterative nonlinear least squares algorithm such as the Levenberg-Marquardt (LM) or Trust Region (TR) method [90]. The objective function to be solved for a set of 8 emitting coils is given by (3.7).

$$F(x, y, z, \theta, \phi) = \sum_{i=1}^{8} (\Phi_{meas}^{i} - \Phi_{calc}^{i})^2 \tag{3.7}$$

which is the sum of squares of the difference between the measured flux $\Phi_{meas}$ and the flux calculated using models of the magnetic field. The minimum number of measurements required is 5, however 8 is used here to give better convergence of the algorithm. Larger numbers of measurements improve the accuracy and convergence of the algorithm. The position finding algorithm was implemented using MATLAB [91] (Mathworks Corp, Natick, MA) although many other software languages such as Python or Octave could be used for this purpose.

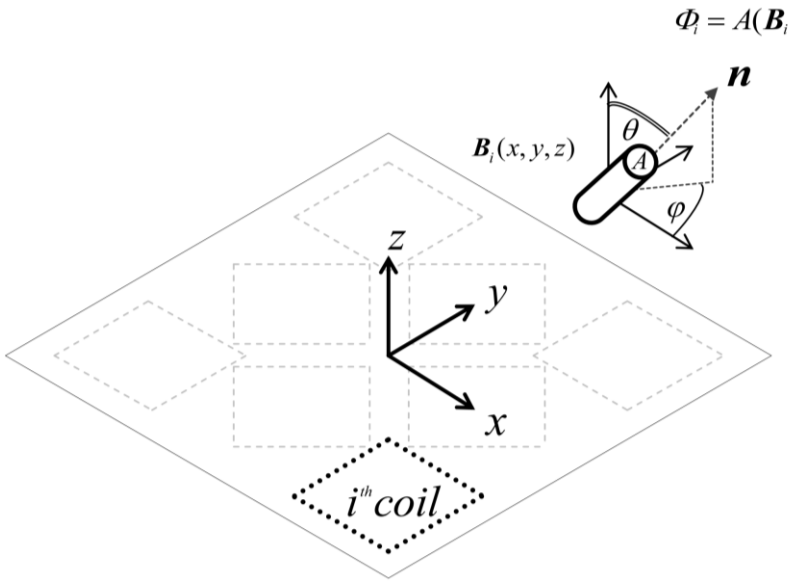



Figure 3.1: Coordinate system for the tracking algorithm. The sensor is positioned at $(x, y, z)$ with an orientation denoted by $\theta$ and $\varphi$. The magnetic field resulting from the $i^{th}$ coil is indicated, and the associated flux is determined using the dot product between the sensor's directional unit vector and the magnetic field at that point.

### 3.3.4. EM Tracking Subsystems

A typical EM tracking system has many sub-systems, both in hardware and software, here we briefly describe each sub-section of our system. Figure 3.2 shows an overview of each subsystem.

**Signal Generator:** A reference signal to control the current amplifier for driving the

transmitter is required. Ideally this reference gives multiple stable reference signals for each channel of the transmitter.

**AC Current Source:** An amplifier or driver is required to deliver the current required to generate the desired magnetic field from a transmitter. This source should be stable and not drift over time as deviations can directly affect system accuracy.

**Transmitter:** A source of magnetic fields that are spatially varying functions in the region of operation. The AC current source directly controls the strength of the magnetic field emanating from the transmitter. Generally the frequencies are sufficiently low and the relative distances are small so that we can assume near field conditions and that the fields vary in a fixed fashion. Similarly at low frequencies it can be assumed the waves do not propagate through space or form reflections at boundaries.

**Region of Operation:** A region of space in which the system has been designed to operate. Ideally this volume should be free from magnetic or conductive materials or other sources of magnetic fields. Since the frequency of operation is relatively low, human tissue and plastic materials can be ignored as they have a negligible effect on the system.

**Sensor:** A small magnetic field sensor that is moved within the region of operation and records the magnetic fields at a particular point in space. The sensor should be sufficiently small and biocompatible such that it can be safely placed within a patient.

**Sensor Amplifier:** Typically the sensor voltage is very small in amplitude; hence a high sensitivity precision amplifier is required. To reduce interference, this amplifier should be placed in a shielded enclosure.

**Data Acquisition:** An ADC system is required to sample the waveforms from the sensor amplifier. This ADC should have sufficiently high sample rate, linearity and resolution to accurately capture the magnetic field components. The sampled data must then be sent to a computer or additional processor unit for demodulation.

**Demodulation:** The demodulator is responsible for extracting the amplitude and phase of each magnetic field component. This can be implemented in either software or hardware, although software allows for flexibility in its implementation and zero drift with temperature and other effects. The demodulator should be fast enough not to contribute any unacceptable lag before sending the magnetic field measurement to the computer.

**Magnetic Field Model:** An accurate model of the magnetic field from the transmitter is required to calculate the position. The calculation must also be efficiently implemented to minimise calculation time as this model will be used many times before a final solution is reached due to the iterative nature of the algorithms used.

**Position and Orientation Algorithm:** An algorithm to compare the output of the demodulator and the magnetic field model is required to determine the position and orientation of the sensor. This algorithm must find the set of positions and orientations such that it minimises the difference between the measured magnetic fields and the model.

**Display:** A user display then plots the sensor's position in real time. Generally for medical navigation, a 3D model of the anatomy surrounding the sensors position is overlaid with the sensor's position.

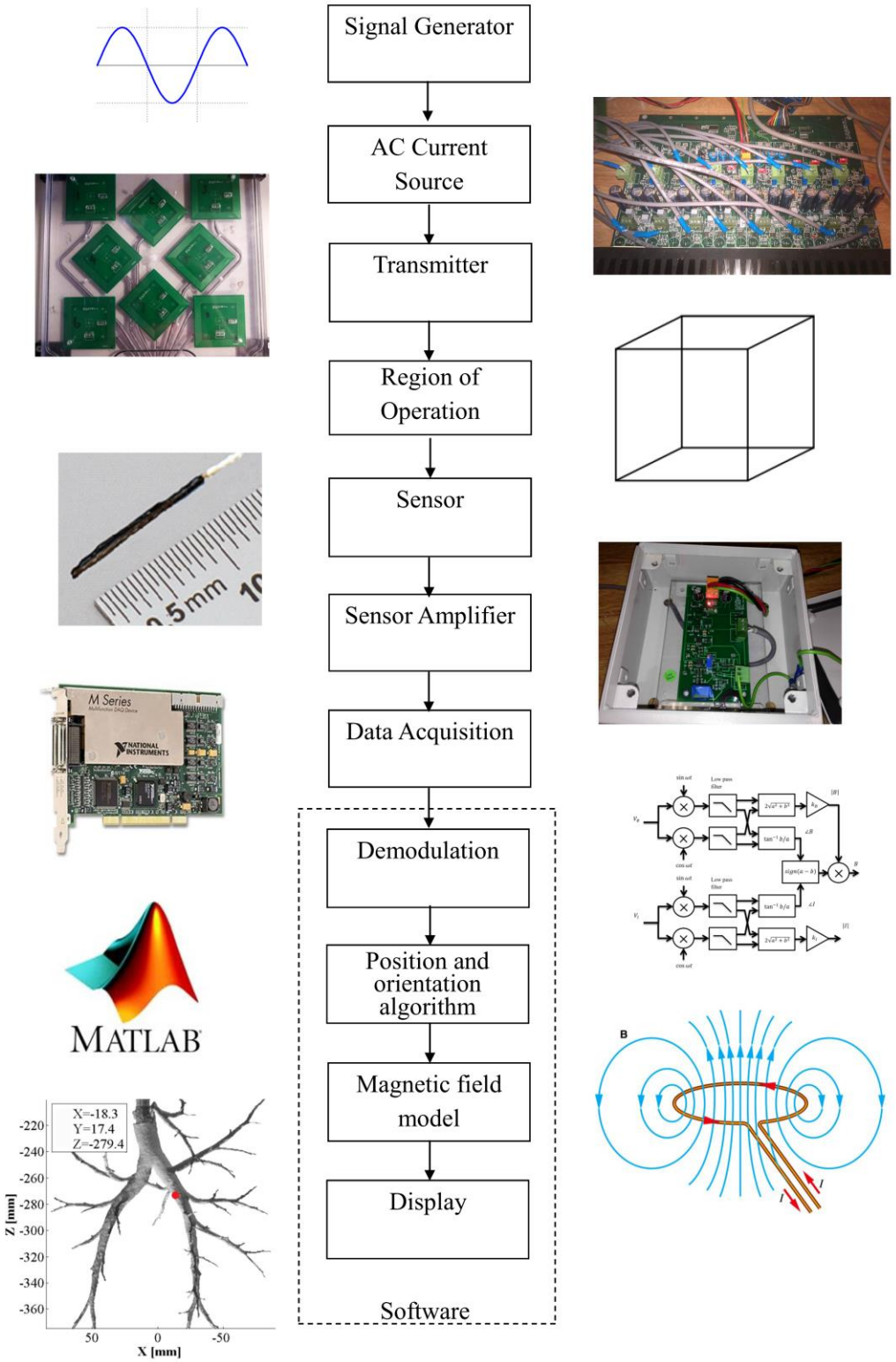



Figure 3.2: Subsystem overview.

## 3.4. Commercial EM Tracking Systems

There are a number of EM tracking systems currently on the market catering to clinical requirements for various procedures. Here we briefly present the most commonly used systems.

### 3.4.1. NDI Aurora

Aurora is a tracking system developed by NDI that tracks instruments by using low frequency alternating magnetic fields, which are in turn is detected by a small coil with a ferromagnetic core. The field generator takes the form of either a table top version which consists of a wide plate which is placed below the patient or by a planar field generator which is positioned using a positioning arm. Figure 3.3 shows the Aurora system. Basic sensors give 5 degrees of freedom (DOF). For 6 DOF, two 5 DOF sensors are mounted perpendicularly at the sensor tip. Sensors come in a range of sizes [58] of which a few examples are shown in Figure 3.4. Aurora is among the most popular EM tracking systems and is used in range of clinical procedures [58], [68]. Aurora 5 DOF sensors have a quoted RMS position error of 1.2 mm and an orientation error of 0.5° with an update rate of 40 Hz [88].




Figure 3.3: NDI Aurora system with generator and processor unit.




| 0.5mm × 8mm | 0.8mm × 11mm | 0.8mm × 9mm |
|---|---|---|
| 5 DOF | 5 DOF | 6 DOF |

Figure 3.4: A selection of Aurora sensors.

### 3.4.2. Ascension trakSTAR

Ascension Technology Corporation provides the trakSTAR electromagnetic tracking system. This system uses pulsed DC magnetic fields to determine position. The field generator can be of two possible arrangements; a dipole transmitter which consists of three orthogonal concentric circular coils or non-dipole transmitters which contain numerous flat transmitters arranged on a flat board [56]. The probe sensor is a three-axis ring core fluxgate magnetometer and 5 or 6 DOF variations are available [49]. Previous versions of this technology include the microBird and Flock of Birds. Ascension has been recently purchased by NDI. Figure 3.5 shows the trakSTAR processor unit and transmitter.




Figure 3.5: Ascension trakSTAR.

### 3.4.3. Calypso 4D

Varian Medical Systems provides among the few wireless EM tracking systems with their Calypso 4D system [92]. This system allows the tracking of a small transponder which retransmits the EM energy absorbed from the transmitter board. This system was originally developed for tracking movement of prostate tumours [93] however different variants of the system can be used for general tracking of instruments and patient movements. Figure 3.6 (a) shows an example of a wireless transponder which measures 8 mm in length and 1.5 mm in diameter. The transmitter board can be seen in Figure 3.6 (b).

(a) (b)



Figure 3.6: (a) Wireless tracker and (b) EM transmitter board for the Calypso 4D system [92].

### 3.4.4. Superdimension iLogic System

The iLogic system has been developed by superDimension Ltd (Hertzilya, Israel) and is an example of an FDA approved electromagnetic tracking system for use in lung bronchoscopy. The system is proprietary, but its basic operation relies on a flat field generator board (47 cm × 56 cm × 1 cm) placed below patient. This board emits a low frequency magnetic field which is detected at the tip of the instrument by a small 6-DOF pickup coil which is 1 mm in diameter and 8 mm long [94]. Figure 3.7 shows this transmitter board placed below an operating table.

When the probe position is determined, its position is incorporated into a preoperative CT scan of the region of interest. A virtual representation of the lung is used to aid in the positioning of the device. The system is relatively safe with rates of pneumothorax being reported to be as low as 3.5-7.5 % [51]. An average target registration error of $6.12 \pm 1.7$ mm has been reported [95]. The probe tip is maneuvered using standard wire driven methods in the form of a 8-way steering mechanism [10].

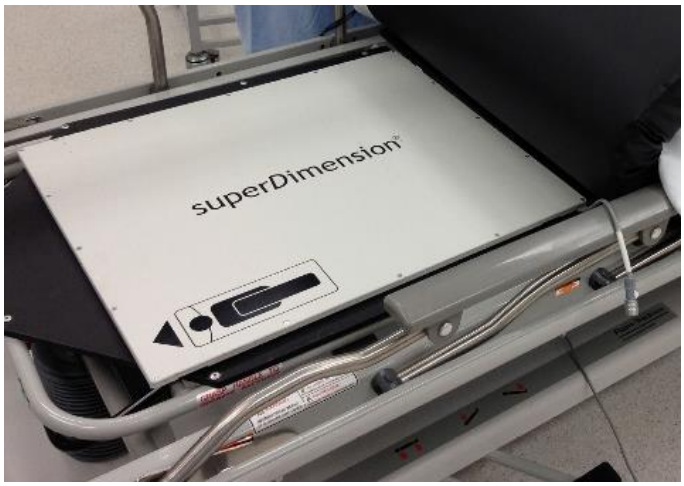



Figure 3.7: SuperDimension transmitter board [96].

### 3.4.5. Veran SPINDrive

The SPINDrive system by Veran Medical is another example of an FDA approved electromagnetic tracking system for use in lung navigation [97]. The system uses a transmitter that is held above the patient generating magnetic fields as shown in Figure 3.8 (a). Veran provides a range of instruments such as catheters and biopsy needles that contain built in EM sensors that detect the transmitted magnetic fields. Figure 3.8 (b) shows a range of different instruments used by the system. The smallest sensor for the system measures 0.43 mm in diameter with a length of 8 mm. The system also uses secondary sensors which are placed on the patient for registration and to record motion due to breathing [98].

(a) (b)

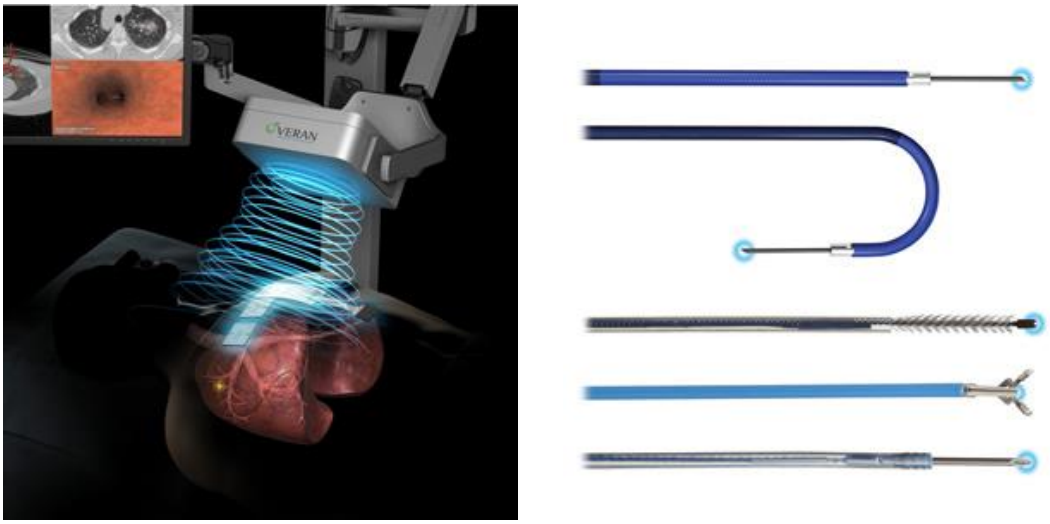



Figure 3.8: (a) EM transmitter and (b) instruments with built in EM sensors for the Veran SPINDrive system [98].

## 3.5. Overview of System Iterations

The EM tracking system over went four distinct system iterations over the course of the design process, which involved modifications to the demodulation system, data acquisition and transmitter arrangement. In terms of subsystems, each iteration shared the following sections:

- transmitter current driver
- magnetic field sensor
- sensor amplifier
- position and orientation (P&O) algorithm

Each phase of the development is detailed below and is also summarised in Table 3.1. Figure 3.9 shows the development of the transmitter array and Figure 3.10 shows the different data-acquisition hardware used in each phase.

**Phase 1**

The primary difference between the 1st iteration or the system and the other versions is the demodulator system. Here, a full synchronous demodulation scheme was implemented using Simulink. The sensor voltage as well as the current in each transmitter coil was recorded using an NI PCI DAQ card. The system was synchronous as the current waveform was used directly as a reference. The update rate was relatively low as the Simulink system was slow due to the large amount data to be processed (see Section 3.11). The transmitter array in this phase was arranged on a Perspex board with multiple mounting holes to allow the position of each coil to be changed as required (Transmitter A in Figure 3.9).

**Phase 2**

For the second iteration, the aim was to reduce the system cost and simplify the hardware

requirements. This was achieved by removing the NI DAQ system and replacing it with a low cost ADC and microcontroller setup. The signals were acquired and demodulated on the microcontroller. After demodulation, the magnetic field measurements were sent to MATLAB to determine the sensor's position. A novel undersampling method was used to reduce the overall sample rate required by the system to allow more demodulation calculation time (see Sections 3.11 and 3.13).

**Phase 3**

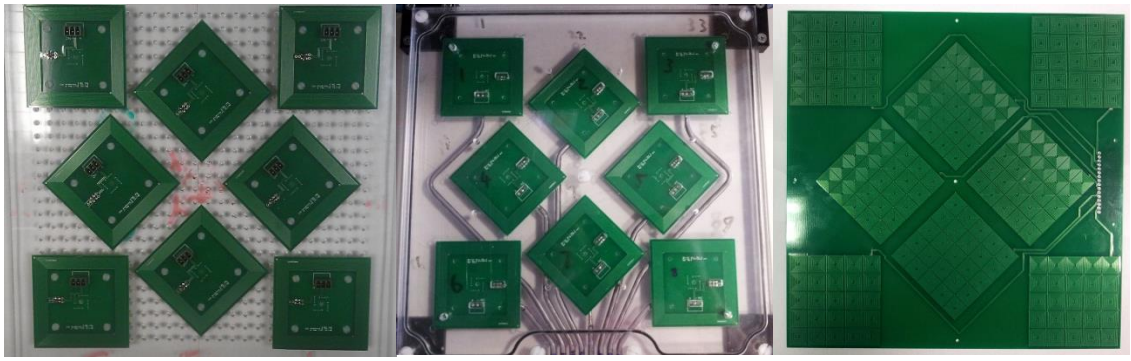
The third iteration was used for pre-clinical testing with a breathing lung model to verify the systems operation in a realistic clinical setting. For this application the transmitter array used the same structure but the transmitter coils were placed in a Perspex enclosure which was 2 cm thick (Transmitter B in Figure 3.9). This encapsulated form allowed the transmitter to be conveniently placed below a region of interest in a medical setting. At this point, for ease of implementation, an NI data acquisition card was again used (instead of the microcontroller and external ADC). However a more portable USB DAQ was used. This allowed the EM tracking system to be implemented using a basic laptop computer. The demodulation scheme was also vastly improved upon using efficient matrix calculations to quickly demodulate the magnetic signals. This allowed for faster update rates than was previously possible along with real time display of the sensor position on a CT lung model.

**Phase 4**

For the final phase, the transmitter was completely redesigned to be formed on a single PCB. Each coil was also replaced with multiple smaller coils which can be considered dipoles due to their size. This dipole was chosen to enhance the calculation time and accuracy of the magnetic field models and also to simplify calculations when dealing with the added complexity of shielding materials (see Chapter 6).

| Phase | Transmitter arrangement | Data acquisition | Demodulation method | Demodulator software | ADC channels | Update rate |
|---|---|---|---|---|---|---|
| 1 | A | NI PCI DAQ card | Synchronous | MATLAB with Simulink | 9 | 10Hz |
| 2 | A | TI external ADC | Asynchronous (undersampled) | Microcontroller implementation | 2 | 10Hz |
| 3 | B | NI USB DAQ card | Asynchronous | MATLAB | 2 | 20-30Hz |
| 4 | C | NI USB DAQ card | Asynchronous | MATLAB | 2 | 20-30Hz |

Table 3.1: EM tracking design iterations.



Transmitter A Transmitter B Transmitter C

Figure 3.9: Transmitter array development.

NI PCI-6259 TI ADS8838 NI USB-6216

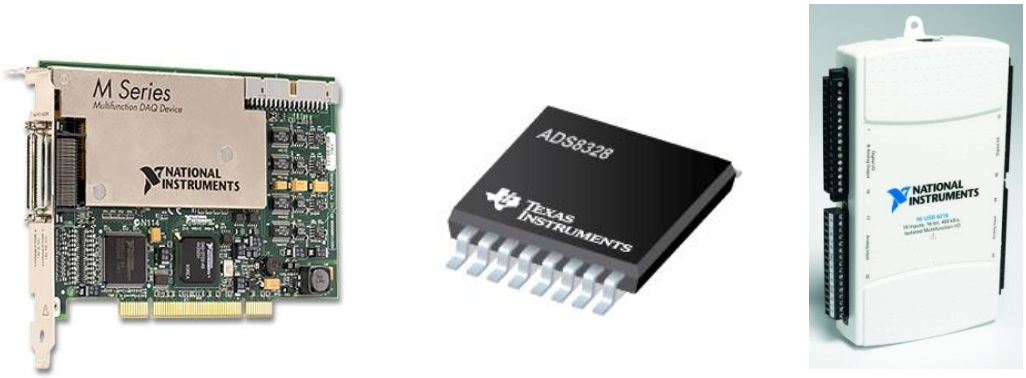



Figure 3.10: Data acquisition hardware.

## 3.6. EM Tracking Simulations

### 3.6.1. Overview

In this section we describe simulations used to choose the formations of the transmitter coil array. Magnetic field models (see Section 3.7) for a set of simulated coils are used to test the position finding algorithm. The position of each magnetic source in the array has a large impact on the convergence of the algorithm and the useful operating volume above the transmitter. For the simulations in this section, the formulations described in Section 3.3.3 are utilised and the MATLAB Optimisation Toolbox is used to implement the nonlinear least squares algorithm.

### 3.6.2. Transmitter Array Optimisation

Many EM tracking systems use 3D arrangements of sensors or transmitters to determine the position and orientation information [99], [100]. However many of these systems rely on 3-axis sensors or small permanent magnets to be placed on the instrument to be tracked, both of which can be relatively large and difficult to miniaturise without loss of performance

[101]–[103]. Typically the smallest implantable sensors are single axis induction coils with AC excitation fields are typically used. In comparison to three axis sensors, single axis sensors can only measure flux in a particular direction and not the full vector quantity of the magnetic field. As a result, the required calculations are more time consuming as iterative non-linear solvers must be used [65], [66]. With three axis sensors, non-iterative algebraic methods may be used to rapidly determine position from the resulting measurements, as well as the fact that fewer measurements are often required [104]–[106].

In order to determine the position and orientation of an object in free space using a single axis magnetic field sensor, there exist a number of different methods. One approach is to use complex 3D structures comprising of multiple magnetic fields sources [102], [107] which may be used to determine position. Of these different methods, a planar magnetic field source approach has been demonstrated to give a high degree of accuracy with the added benefit of compact form factor [9], [65], [66], [88]. The design challenge with this approach is to optimise the position of a set of planar coils such that enough spatial information can be derived from single axis flux measurements, with added redundancy to ensure convergence. These systems can be very sensitive to the position of the magnetic sources. Hence careful design is essential. In order to determine 5 degrees of freedom of a single axis sensor, at least 5 measurements must be taken to ensure the system of equations can accurately determine the position and orientation of the sensor.

### 3.6.3. Testing Methodology

For the tests, the magnetic fields from each transmitter formation to be tested was simulated and used in a set of calculations to determine the position and orientation of simulated sensor. For each transmitter formation, the following steps were taken in each test:

- A random sensor position is chosen in the range 20 cm × 20 cm × 20 cm, with two rotations in the standard spherical coordinate system.
- The flux as seen by this sensor is calculated at this random point.
- A random amount of noise, proportional to the flux value, is added to the calculated flux to simulate noise errors.
- The algorithm is then solved using the centre of the operating region as the starting point.
- The above steps are repeated 1000 times, the mean position error is then calculated.

### 3.6.4. Coil Formations

Planar coil arrays have been demonstrated to be an effective means of creating magnetic fields for EM tracking. Their use have been documented by Paperno et al [9], [65] as well as commercially in the NDI Aurora system [58] and the SuperDimension iLogic [108]. For

medical environments they are ideal as they can be placed beneath the patient or built into the operating table causing minimal obstruction to the clinicians.

Four coil arrangements were tested; the shape of each set is shown in Figure 3.11. Each grid is 250 mm × 250 mm, while the operating region of the sensor is chosen to be a cube of side length 200 mm, positioned 50 mm away from the planar grid. Table 3.2 shows the results of three tests with all 4 patterns with varying levels of noise as described in Section 3.6.3. We can clearly see that Pattern A in Figure 3.11 gave the best results as it yields the lowest position error overall. This pattern was a scaled version of the coil array used by Plotkin et al [9], [65] and was used in the first three iterations of our EM tracking system. Additional variations on this pattern were tested however there was little improvement observed over this particular arrangement.

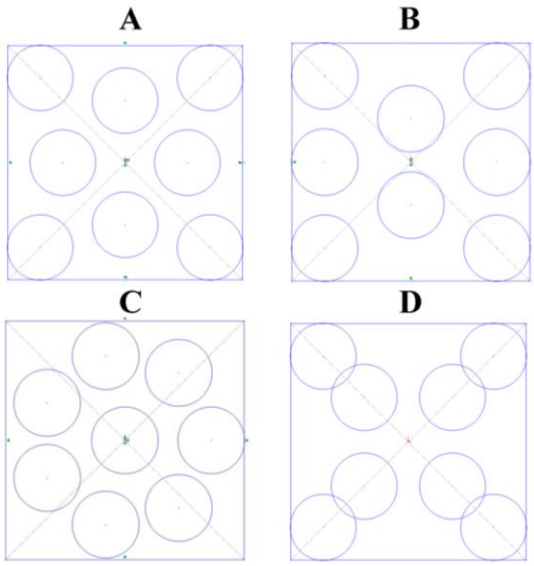



Figure 3.11: Four arrangements of eight coils tested to find an optimum arrangement.

| | Pattern A | Pattern B | Pattern C | Pattern D |
|---|---|---|---|---|
| **Normalised noise power [dB]** | | -71 | | |
| **Mean error [mm]** | 2.6639 | 11.7 | 3.9166 | 6.266 |
| **Normalised noise power [dB]** | | -37 | | |
| **Mean error [mm]** | 6.912 | 16.0808 | 7.4687 | 15.1878 |
| **Normalised noise power [dB]** | | -31 | | |
| **Mean error [mm]** | 9.8909 | 20.0432 | 9.4713 | 17.6687 |

Table 3.2: Comparing the simulated performance of each coil arrangement.

### 3.6.5. Formations with 9 and 16 Coils

As a comparison with the chosen 8 coil arrangement, evenly distributed sets of 9 and 16 planar coils were also tested. Figure 3.12 shows accuracy of each arrangement with

increasing noise power. As can be seen, larger numbers of coils increase the accuracy, but this comes at the cost of higher complexity in the driving the coil array.

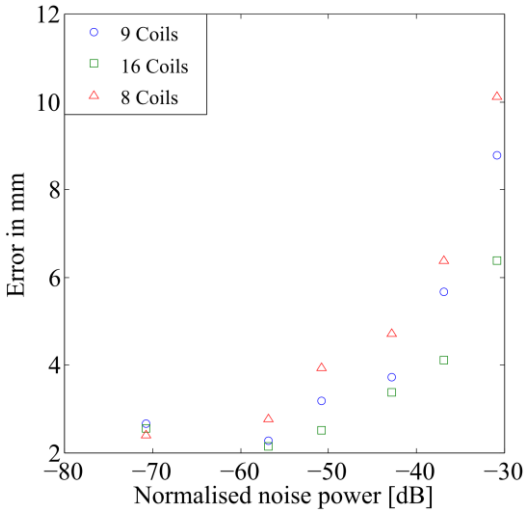



Figure 3.12: Comparing 8, 9 and 16 coil formations.

From the above result, it is apparent that even at low levels of noise, errors are still larger than 2 mm. This problem is due to the fact that the algorithm often finds local minima in the least squares function which is not the true solution, (*i.e.* the global minimum). This occurs since the algorithm starts at a single point, which in this case was chosen to be at the centre of the operating area, while the actual solution may vary significantly from this initial point. As a result, the algorithm fails to find the actual solution. To overcome this problem, the algorithm can be repeated using multiple starting points before choosing which solution gives the best result. Figure 3.13 shows how mean error dramatically decreases as the number of starting point iterations are used. The performance in the presence of noise is shown in Figure 3.14. This increased error comes at the cost of considerable increase in computation time. In an actual implementation of the system, previous position estimation can be used as a starting point for the next calculation as it can be assumed that the displacement will be relatively small between each calculation. If an incorrect local minima if reached by the algorithm, generally the least squares residual will be significantly larger than the correct solution and can be used as an indicator if the algorithm has failed.

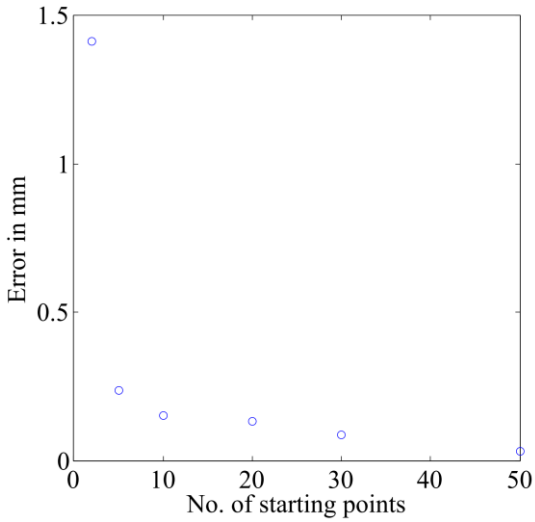



Figure 3.13: Position error in relation to the number of points used in multi-start algorithm.

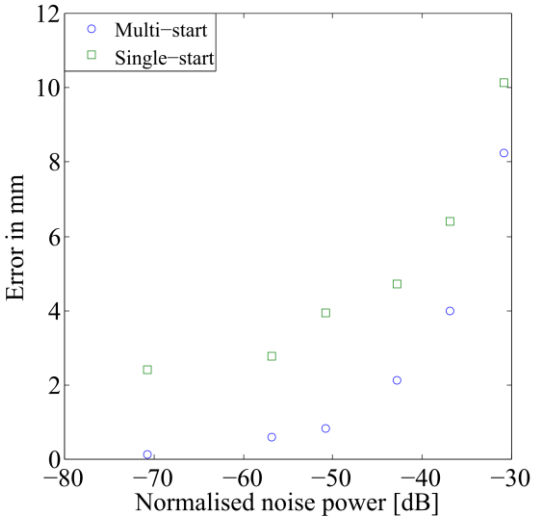



Figure 3.14: Comparing multi-start and single-start point algorithms with increasing noise power. Twenty start points are used in this case.

## 3.7. Magnetic Field Transmitter Design

### 3.7.1. Magnetic Field Modelling

In order to predict the magnetic field of a current carrying conductor, typically the Biot-Savart law is utilised, which is given by (3.8) where $\boldsymbol{J}$ is the current density, $\mu_0$ is the permeability of free space and $\boldsymbol{r}$ is a vector pointing from a point within the current distribution to an observation point [27].

$$\boldsymbol{B}(\boldsymbol{r}) = \frac{\mu_0}{4\pi} \iiint_V \frac{(\boldsymbol{J}dV) \times \boldsymbol{r}}{r^3} \tag{3.8}$$

Hence if the spatial distribution of current in a coil formation is known, the resulting magnetic field can easily be determined. While the Biot-Savart law is typically only specified for magnetostatic cases, it is still valid up to moderately high frequencies (< 100 kHz).

### 3.7.2. Filament models

For our system, the coils used for the source of the AC magnetic fields are formed as planar windings on a printed circuit board. This facilitates ease of manufacture and reproducibility, *i.e.*, each coil can be made almost identical. Square coils were chosen as they result in simpler PCB layout. If we consider that the coil is formed from a number of straight filaments, by calculating the magnetic field due to each filament the magnetic field can be accurately calculated. The following summation formula, (which is derived from the Biot-Savart law) was used to calculate the total magnetic field due to each coil [64]:

$$\boldsymbol{B}(\mathbf{r}) = \frac{\mu_0 I}{4\pi} \sum_{i=1}^{n} \left( \frac{\boldsymbol{c}_i \times \boldsymbol{a}_i}{\left|\boldsymbol{c}_i \times \boldsymbol{a}_i\right|^2} \right) \left( \frac{\boldsymbol{a}_i \cdot \boldsymbol{c}_i}{\left|\boldsymbol{c}_i\right|} - \frac{\boldsymbol{a}_i \cdot \boldsymbol{b}_i}{\left|\boldsymbol{b}_i\right|} \right) \tag{3.9}$$

where $\boldsymbol{a}_i$ is a vector in the direction of the filament, $\boldsymbol{b}_i$ is a vector pointing from an observation point $\boldsymbol{p} = (x, y, z)$ to the end of the filament, and $\boldsymbol{c}_i$ is a vector pointing from $\boldsymbol{p}$ to the start of the current carrying filament as seen in Figure 3.15. Equation (3.9) can also be calculated very efficiently, and the magnetic fields of each coil can be determined in a single calculation. By comparing the performance of the filament approach to the Biot-Savart method, considering the filamentary and volume integration methods, the calculated magnetic fields were almost identical. This is shown in Figure 3.16.

(a) (b)

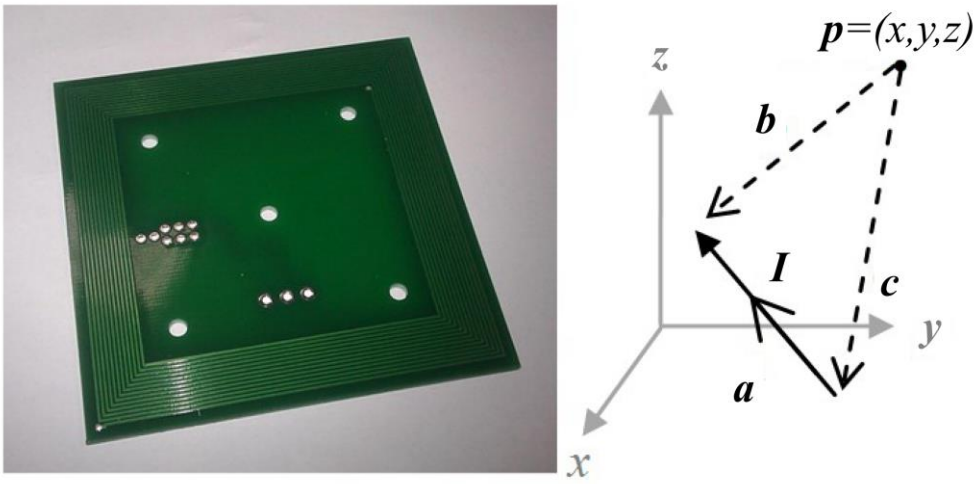



Figure 3.15: (a) Planar PCB coil which consists of 25 turns, side length of the PCB is 72 mm, trace thickness of 0.5 mm and copper thickness of 70 µm. (b) Vector diagram for magnetic field due to a filament current *I* where ***a*** is a vector in the direction of the filament, ***b*** is a vector pointing from an observation point to the end of the filament, and ***c*** is a vector pointing from to the start of the current carrying filament.

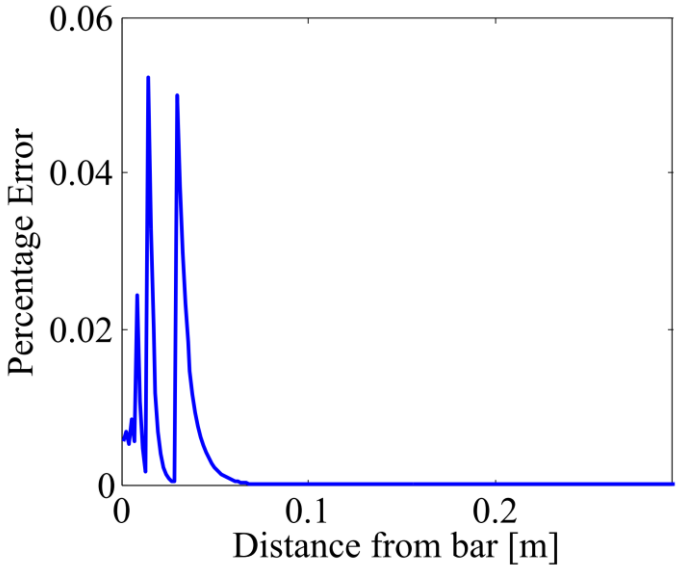



Figure 3.16: Error between filament model and a direct integration of the current density over a 7 cm length of PCB trace.

### 3.7.3. ICNIRP Exposure Limits

Human exposure to alternating magnetic fields must be considered when designing a system of this type which, when in operation, will be constantly exposing its users. The ICNIRP has strict guidelines in this regard [109]. In the range 3 kHz to 100 kHz, the max occupational exposure is set to 100 μT RMS [109]. For multiple frequency exposure, the magnitudes of the each magnetic field source must be summed together. Figure 3.17 and Table 3.3 show the ICNIRP limits.

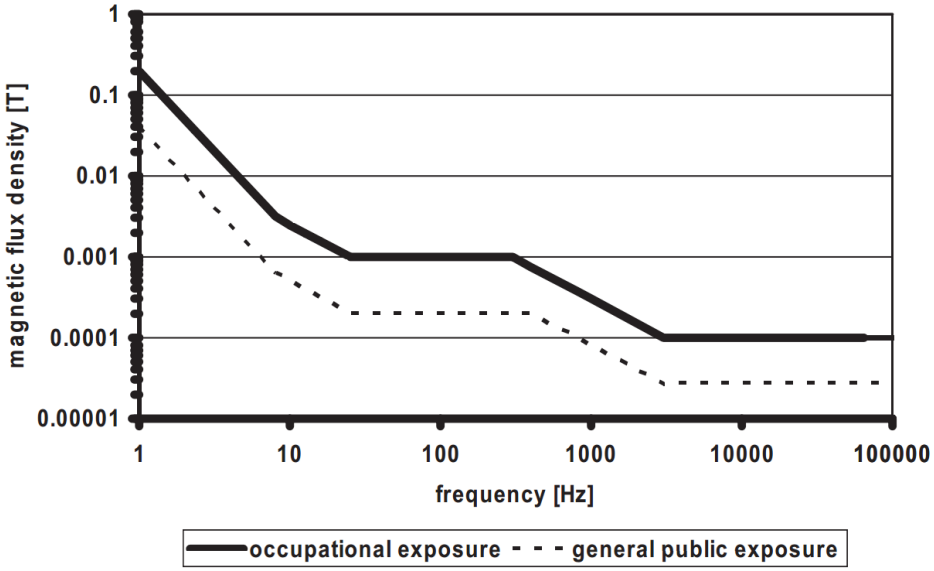



Figure 3.17: ICNIRP exposure guidelines for low frequency magnetic flux density [109].

| | Occupational exposure | |
|---|---|---|
| **Frequency range** | **E-field strength E ($kVm^{-1}$)** | **Magnetic flux density B (T)** |
| 1 Hz-8 Hz | 20 | $0.2/f^2$ |
| 8 Hz-25 Hz | 20 | $2.5 \times 10^{-2}/f$ |
| 25 Hz-300 Hz | $5 \times 10^2/f$ | $1 \times 10^{-3}$ |
| 300 Hz-3 kHz | $5 \times 10^2/f$ | $0.3/f$ |
| 3 kHz-10 MHz | $1.7 \times 10^{-1}$ | $1 \times 10^{-4}$ |

Table 3.3: ICNIRP Limits for occupational exposure where $f$ is the frequency in Hz.

### 3.7.4. Determination of Required Field Strength and Frequency

For AC EM tracking systems that are based on Faraday's law to induce a voltage in a sensor, the primary factors influencing the amplitude of this induced voltage (excluding the sensor parameters) are the strength of the magnetic field and the frequency of the excitation. Ideally the sensor sensitivity is linearly proportional to the excitation frequency. If we take the sensitivity of the sensor to be 0.1146 (see Section 3.8) and scale the ICNIRP limits, we arrive at Figure 3.18 which shows the maximum allowable induced voltage in the sensor. In general, the higher the frequency the better the SNR whilst also being within the allowable magnetic flux density range. Since there are 8 coils transmitting simultaneously, the actual field strength per coil must be approximately divided 8 to ensure that the total contribution of each coil does not exceed the limits.

The maximum field strength will be experienced in close proximity to the coil in order to get the largest permissible field at larger distances from the coil. The reduction in the magnetic field strength is generally inversely proportional to the cubed distance for the force, which is quite a dramatic reduction even over a short distance. Figure 3.19 shows the normalised field reduction of a planar coil with distance. Three radial lines at increasing angles to the central axis are shown in this figure, with similar distance dependence. At displacements of 30 cm, we see that the field has dropped by a factor of approximately 1000. The EM tracking specifications required for the system required tracking in volume approximately 25 cm × 25 cm × 25 cm. At these distances to give acceptable SNR, a minimum induced sensor voltage after amplification of at least 10 mV was deemed necessary. Assuming a value for the amplification of 500, the required flux density per coil and frequency can be determined by iteratively varying the number of turns, coil dimensions and coil current, and examining the predicted induced voltage at distances of 30 cm from the coils. The final coil design has 25 turns, a side-length of 70 mm and carries 200 mA. This was predicted to give an output of 290 mV at 30 cm from a single coil, when operating at 25 kHz.

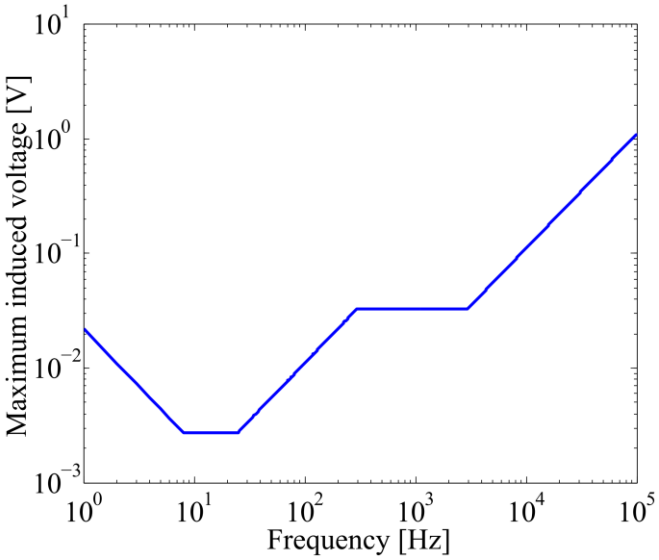



Figure 3.18: Scaled ICNIRP limits showing the maximum allowable induced voltage.

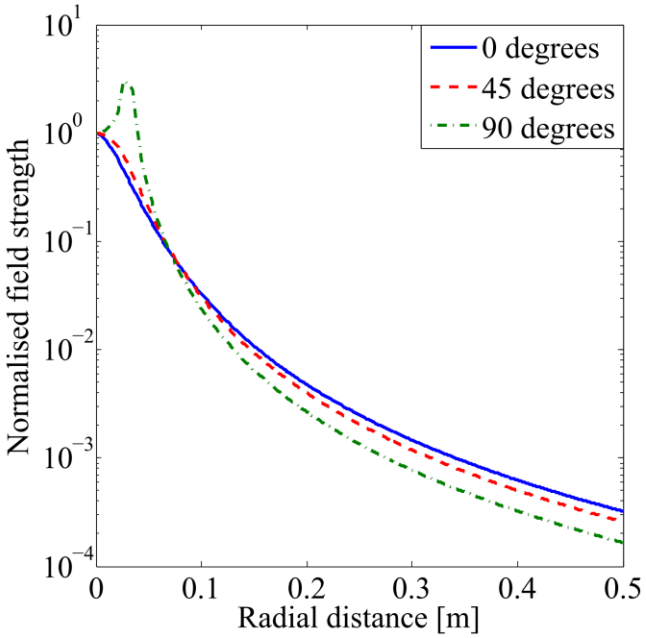



Figure 3.19: Drop-off magnetic field with radial distance from a planar coil with increasing angle to the central axis.

### 3.7.5. PCB Design

In MATLAB, a program was written that determines the position of each filament for a square coil with a given side-length and a specified number of turns. The spacing, width and thickness of each trace is also specified. A two layer PCB was chosen so to increase the number of turns in a given area. Square coils were used as they are easier to design and layout for PCB manufacture. Multi-layer boards can also be used but they have a much increased cost as well as the fact that heating of internal traces is more problematic. The physical layout of each coil is constrained by the manufacturing tolerances specified by the PCB fabricator as well as the thermal constraints set by the sizing of the conductors. The main manufacturing tolerance specifications of interest are the minimum trace width,

minimum trace separation and via-to-trace separation. The boards were manufactured by Quick-Tech (Hertfordshire, UK) and they specify the following tolerances:

| | |
|---|---|
| Minimum trace separation | >0.15 mm |
| Minimum trace width | >0.15 mm |

Table 3.4: PCB manufacturing tolerances.

For the thermal constraints, typically the maximum current is specified for a PCB trace and is dependent on the trace width, thickness and desired temperature rise over ambient as well as if it is an internal or external trace. This maximum current for an external trace is given by the empirical equation (3.10) where $\Delta T$ is the desired temperature rise above ambient, *w* is the width of the trace and *t* is the thickness of the trace [110].

$$I_{\max} = 5.2 \times 10^{-9} \Delta T^{0.44} (wt)^{0.725} \tag{3.10}$$

For a 10° temperature rise, carrying a current of 1 A and the 70 µm thickness, the required width is 0.15 mm. To give plenty of headroom accounting for density of the windings, a width of 0.5 mm was chosen for the trace. The max current for each coil was set conservatively to 500 mA to minimise the overall current draw and power consumption of active devices. The spacing between each turn was set to 0.25 mm to give slightly more clearance than the manufacturer's tolerances. A 70 µm thick copper PCB was used to decrease the resistance in contrast to the standard 35 µm used in the majority of PCBs.

The driver board for the system was designed to use a standard bench power supply with an input voltage of ±15 V, with the previously specified 500 mA max current per coil, the next limiting factor is the impedance of the coil. The maximum impedance is calculated based on the peak voltage being 15 V with a peak current of 500 mA, which results in a value of 30 Ω as indicated by (3.11).

$$\left|Z_{\max}\right| = \frac{V_{peak}}{I_{peak}} \tag{3.11}$$

Assuming the transmitter coil comprises of inductive and resistive component, the total impedance is given by (3.12), where *R* is the total resistance of the coil and the sense resistor and *L* is the inductance of the coil.

$$\left|Z_{\max}\right| = \sqrt{R^2 + \left(2\pi fL\right)^2} \tag{3.12}$$

Setting $R = 10\ \Omega$ and solving results in a maximum inductance of approximately 150 µH, assuming a maximum operating frequency of 30 kHz.

Along with calculating the magnetic field distribution for each coil size, the inductance and resistance is also calculated to ensure that it is below the specified limits. The resistance is simply calculated by determining the total length of the coil and using (3.13) where $\rho$ is the resistivity of copper ($1.68 \times 10^{-8}\ \Omega$m).

$$R = \rho \frac{l_{coil}}{wt} \tag{3.13}$$

The inductance is calculated using the modified Wheeler formula which is given by (3.14) where $K_1$ and $K_2$ are shape dependant parameters which for a square coil have values of 2.34 and 2.75 respectively [111]. The two parameters $l_{avg}$ and $\gamma$ are dependent on the distribution of the coil and are given by (3.15) and (3.16) where $l_{out}$ is the outer side-length of the coil and $l_{in}$ is the inner side-length of the coil.

$$L = K_1 \mu_0 \frac{N^2 l_{avg}}{1 + K_2 \gamma} \tag{3.14}$$

$$l_{avg} = \frac{l_{out} + l_{in}}{2} \tag{3.15}$$

$$\gamma = \frac{l_{out} - l_{in}}{l_{out} + l_{in}} \tag{3.16}$$

The design parameters of the coils were iterated to find a suitable outer side-length and turns ratio whilst still being below the specified limits. In addition to the inductance and resistance limits, the coils were designed to have an RMS magnetic flux density of less than 100 µT at a distance of 2 cm from the coil to be within the ICNIRP limits.

Figure 3.20, Figure 3.21 and Figure 3.22 shows the variations of the magnetic flux density at 2 cm, the inductance and resistance respectively for a selection of coil side-lengths and number of turns. The final design was chosen to have a side length of 70 mm, which yields an inductance of 79 µH and a resistance of 2.9 Ω. Figure 3.23 shows the resulting magnetic field distribution around the coil when carrying 1 A which was calculated using (3.9).

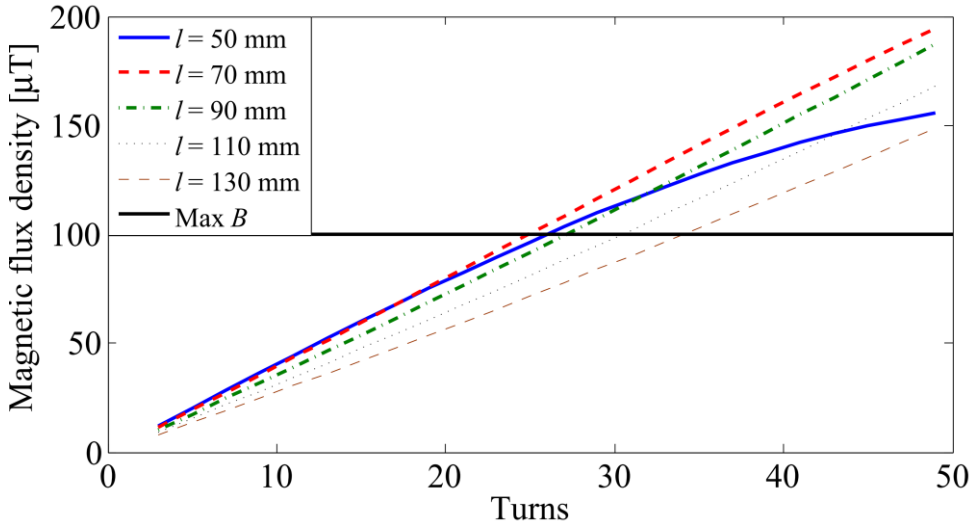



Figure 3.20: Predicted magnetic flux density at 2 cm from the coil with 500 mA for different side lengths and number of turns.

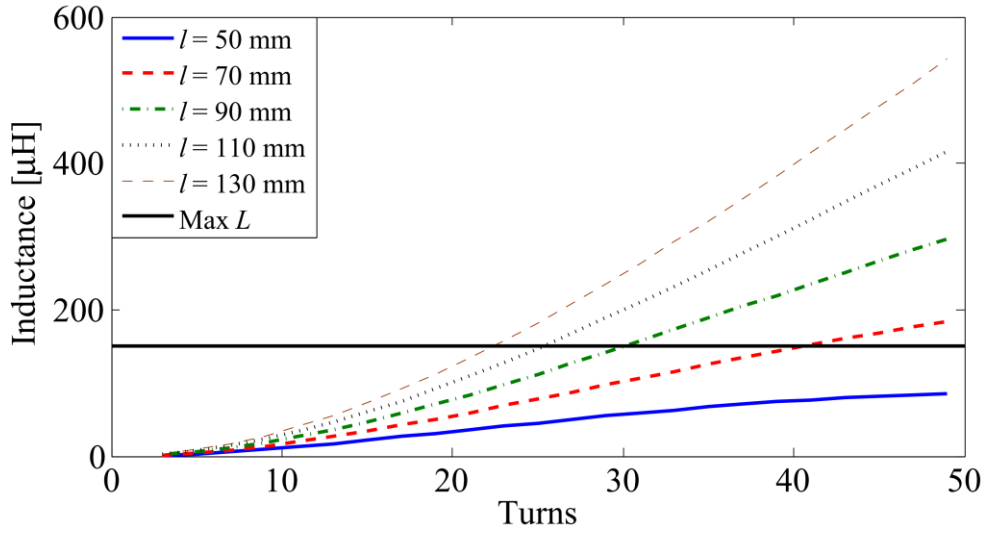



Figure 3.21: Predicted coil inductance for different side lengths and number of turns.

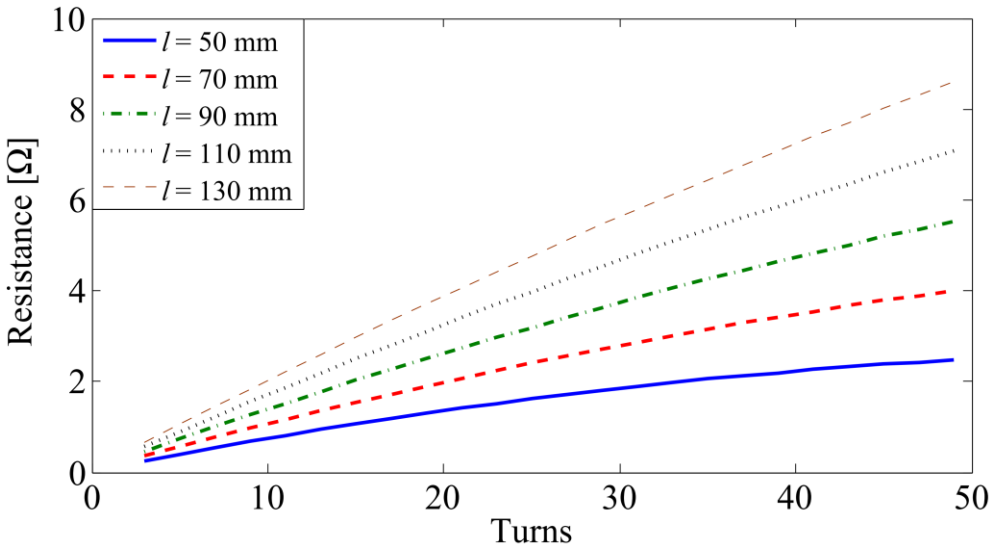



Figure 3.22: Predicted coil resistance with for different side lengths and number of turns.

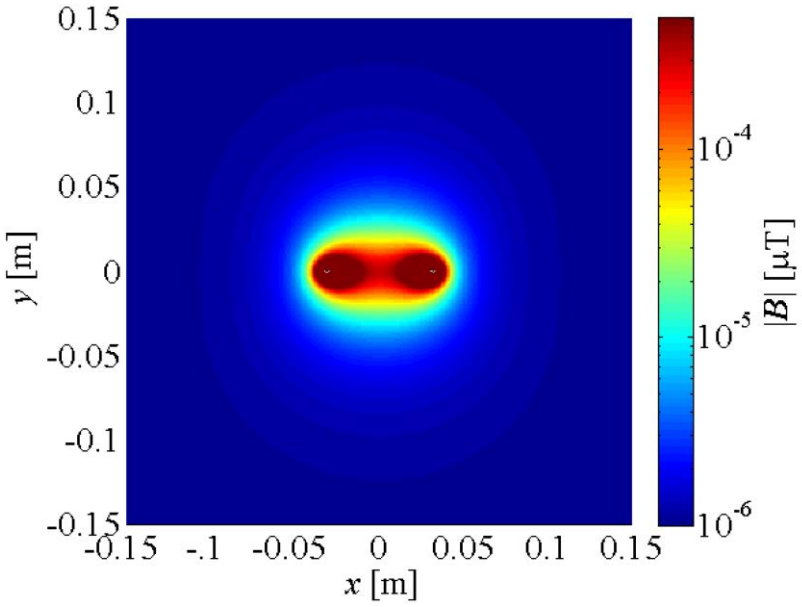



Figure 3.23: Simulated contour plot showing the magnetic flux density around a single coil per unit Amp.

Figure 3.24 shows the output of the MATLAB program for a 19 turn coil with a 15mm side length. Figure 3.25 shows the traces on each layer individually. The two entry terminals here are shown on the bottom right corner however they can be placed anywhere along the trace. Using the geometry resulting from the final design parameters, the coil was drawn using Designspark PCB from Radionics.

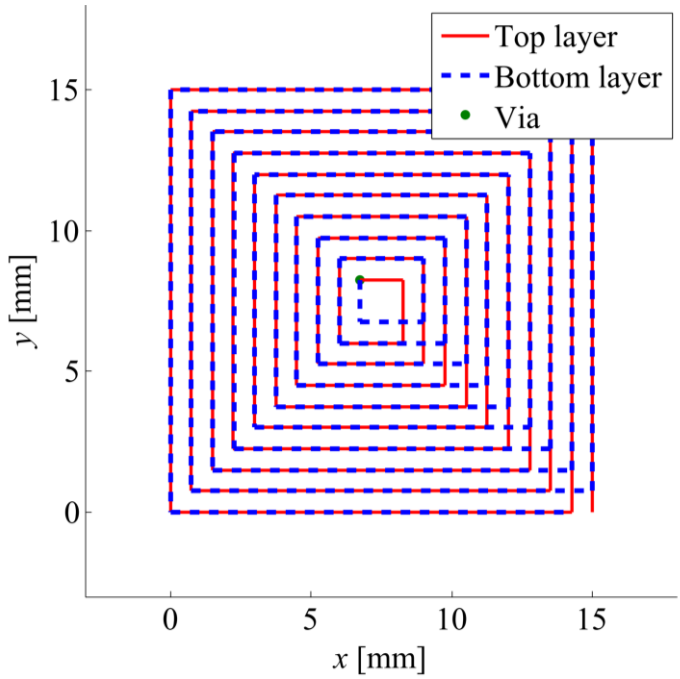



Figure 3.24: Layout of each filament for a two layer 19 turn coil with side length of 15mm.

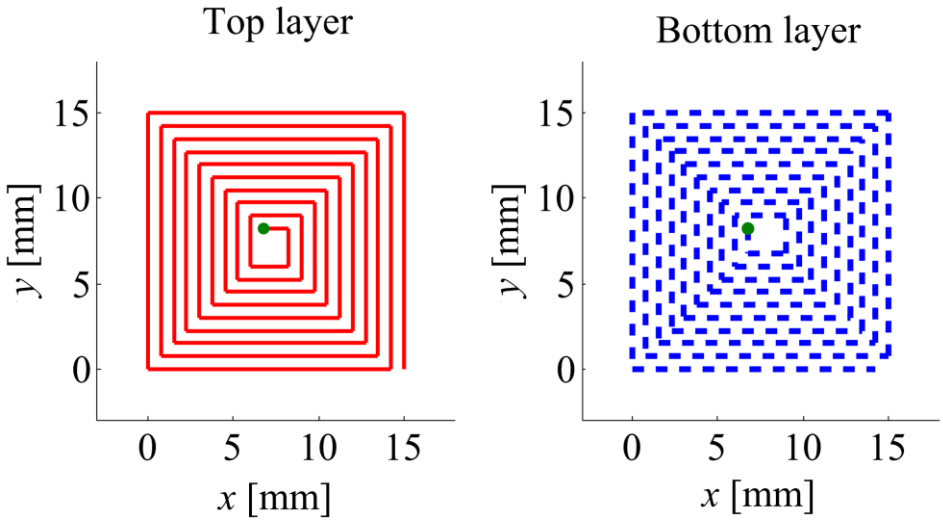



Figure 3.25: Filament layout on each PCB layer.

## 3.8. Magnetic Field Sensors

### 3.8.1. Sensor Types

There are a wide variety of different magnetic sensing technologies; the following list briefly outlines the basic types which are often used in EM tracking applications. Table 3.5 shows

the range of sensor types and sensor arrangements used in a variety of research systems.

**Magnetoresistance**

Magneto-resistance refers to the change of the electrical resistance of a material in the presence of a magnetic field. The effect is due to an increase in electron collisions when a magnetic field is applied perpendicular to a current flow. This phenomenon is generally referred to as anisotropic magneto-resistance (AMR) as the sensors typically are arranged in strips and the effect is observed when magnetic fields are applied at any angle other than the primary axis. Other variations on this effect include gigantic magneto-resistance (GMR), colossal magneto-resistance (CMR), and tunnel magneto-resistance (TMR) although standard AMR is the most commonly used [112].

**Hall Effect**

Hall effect sensors are among the most popular magnetic field sensors available and are used in a large range of applications ranging from the automotive industry to mobile phones. Their low cost, small size and ease of use are the main factors contributing to their popularity. The basic principle of operation is that when a magnetic field is applied perpendicular to a current flow, a voltage proportional to the applied field is developed across the conductor. While Hall effect sensors are not as sensitive as other sensing methods, their low cost, small size and linearity make them a popular choice [113]. A major disadvantage for precision measurements is the presence of Earth's magnetic field which is always detected using the Hall Effect.

**Fluxgate**

A fluxgate magnetometer comprises of a piece of ferromagnetic material wrapped in a coil and an excitation current is applied. In the presence of no external magnetic field, the current generated in a secondary winding wrapped on the same core with the same number of windings will be the same. However if an external magnetic field is applied, the operating point on the BH hysteresis loop is offset, and the resulting current on the secondary winding will change due to this offset [114]. This change in flux generates a voltage which is proportional to the applied field. Fluxgate sensors can detect both AC and DC magnetic fields.

**Pick-Up/Induction Coil**

Possibly the simplest of all magnetic field sensors is the inductive pickup coil, which consists of a coil with an air or ferromagnetic core. The underlying fundamentals involve Faraday's law which states that an alternating flux will generate a voltage on a coil placed perpendicular to the applied field. These sensors are easy to manufacture and can be designed to operate over a wide range of frequencies. One disadvantage is that only alternating magnetic fields can be detected, but this limitation can be overcome by adding a vibrational oscillator to the system which sets the coil moving through space at a particular oscillatory frequency to generate alternating an flux from a DC field [115], [116].

| Magnetic source | Sensor technology | Axis number of sensor | Sensor arrangement | Ref |
|---|---|---|---|---|
| Permanent magnet | AMR | 3-axis | Planar array | [117] |
| Permanent magnet | Hall effect | 3-axis | Planar array | [104] |
| Permanent magnet | AMR | 3-axis | Cubic array | [99] |
| Magnetised rod | Fluxgate | 3-axis | Planar array | [118] |
| Planar array of transmitter coils | Pickup coil | 1-axis | Single sensor | [66] |
| Permanent magnet | Hall effect | 1-axis | Planar array | [119] |
| 3-axis coil transmitter | Pickup coil | 2-axis | Single sensor | [106] |
| 2-axis coil transmitter | Pickup coil | 3-axis | Single sensor | [106] |
| 2-axis transmitter | Pickup coil | 3-axis | Single sensor | [120] |
| Planar array of transmitter coils | Pickup coil | 1-axis | Single sensor | [9] |
| Permanent magnet | Fluxgate | 3-axis | Multiple sensors | [103] |

Table 3.5: Comparing sensor technologies and sensor arrangements of different EM tracking systems.

### 3.8.2. Induction Coil Theory

Faraday's law states that the induced voltage in any closed circuit is equal to the negative of the time derivative of the magnetic flux through the circuit. The general form of Faraday's law is given by (3.17) which is based on the time derivative of the surface integral for the total magnetic flux perpendicular to an area element $d\boldsymbol{A}$ resulting from a magnetic flux density vector, $\boldsymbol{B}$ [27].

$$v = -\frac{d}{dt}\oiint_A \boldsymbol{B} \cdot d\boldsymbol{A} \tag{3.17}$$

If the area $\boldsymbol{A}$ is relatively small compared to the gradient of the magnetic field, this expression can be simplified to (3.18).

$$v = -\frac{d}{dt}(\boldsymbol{B} \cdot \boldsymbol{A}) \tag{3.18}$$

The magnetic flux density $\boldsymbol{B}$ is related to the magnetic field strength $\boldsymbol{H}$ in the free space by (3.19).

$$\boldsymbol{B} = \mu_0 \boldsymbol{H} \tag{3.19}$$

Taking this into account, as well as the fact that the number of turns, $N$, in the closed circuit is directly proportional to the output voltage we arrive at (3.20).

$$v = -\mu_0 N \frac{d}{dt}(\boldsymbol{H} \cdot \boldsymbol{A}) \tag{3.20}$$

If the closed circuit has a ferromagnetic core, the size of the induced voltage will be increased in proportion to its apparent magnetic permeability $\mu_a$. This is due to the increased flux moving through the circuit as the ferromagnetic core tends to concentrate the flux lines. The apparent permeability of a core is related to the materials relative permeability, $\mu_r$, by (3.21) where the demagnetisation factor is given by $k_d$ [116].

$$\mu_a = \frac{\mu_r}{1 + k_d(\mu_r - 1)} \tag{3.21}$$

The demagnetisation of the core, $k_d$, is a geometry dependant parameter and can be difficult to accurately calculate. However by approximating the core to be elliptical in shape, the demagnetisation factor may be estimated using (3.22) where $d_c$ is the diameter of the core and $l_c$ is the length of the core [116]. Figure 3.26 shows an example induction sensor with a ferromagnetic core.

$$k_d \cong \frac{d_c^2}{l_c^2}\left(\ln\frac{2l_c}{d_c} - 1\right) \tag{3.22}$$

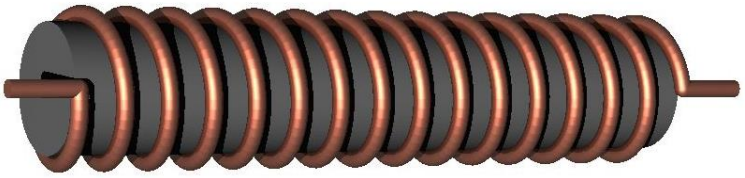


Figure 3.26: Induction sensor with ferromagnetic core

The longer the core is in relation to its diameter, the lower the demagnetisation factor. Closed magnetic structures such as toroidal cores have a demagnetisation factor of 0. The magnetic flux density is now given by (3.23) which includes the effect of the demagnetisation factor.

$$\boldsymbol{B} = \mu_a \mu_0 \boldsymbol{H} \tag{3.23}$$

The ferromagnetic core can dramatically increase the sensitivity of sensor. However, this comes at the cost of linearity. All ferromagnetic materials are inherently non-linear in nature, hence the output of the sensor will now have some non-linear behaviour which can depend on many factors such as frequency, temperature, field strength etc. [115]. Increased noise is also observed from ferromagnetic materials due to Barkhausen noise [116]. If the applied magnetic field to the sensor is sinusoidal in nature as in (3.24) where $H_0$ is the amplitude of the excitation and $\omega$ is the angular frequency, the resulting induced voltage in the sensor is given by (3.25). In this equation $\boldsymbol{n}_H$ and $\boldsymbol{n}_A$ are unit vectors showing the direction of the applied magnetic field and the sensors axial direction respectively.

$$\boldsymbol{H} = H_0 \sin(\omega t)\boldsymbol{n}_H \tag{3.24}$$

$$v = -\mu_0 \mu_a N H_0 A \omega \cos(\omega t)(\boldsymbol{n}_H \cdot \boldsymbol{n}_A) \tag{3.25}$$

From (3.25) it is clear that the output voltage is directly proportional to the applied frequency as well as the amplitude of the magnetic field. For a given sensor, by changing the operating

frequency we directly affect its sensitivity.

### 3.8.3. NDI Sensor analysis

Commercially available sensors by NDI were used with our system. They were chosen as they have a high sensitivity and are available in small sizes allowing for easy integration in custom medical devices. To fully understand the operation of the NDI sensors, an extensive range of tests were carried out to evaluate their sensitivity, frequency response and linearity. These tests were carried out with an unshielded 5-DOF sensor. Although other variants of the Aurora sensors have different sizes, all have similar sensitivity. Figure 3.27 shows an example of the sensor used.

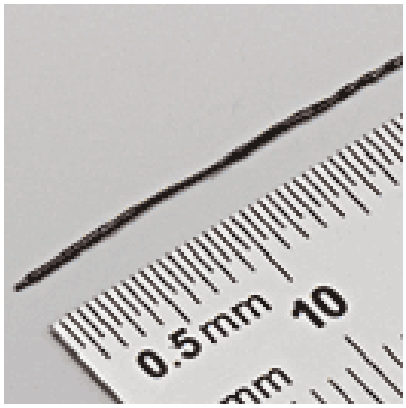



Figure 3.27: Aurora 5-DOF sensor by NDI

### 3.8.4. Sensor Calibrator

In order to calibrate and test the sensor, a known magnetic field must be generated as a reference. However a further requirement is that the sensor coil is perfectly aligned with the magnetic field. In order to generate a uniform and known magnetic field, a Helmholtz coil was constructed. A Helmholtz coil in its most basic form is two coils of wire placed a radius distance apart that carries the same current [57]. Figure 3.28 shows a representation of a typical Helmholtz coil. For the calibrator design, 10 turns of wire are used, with each conductor accurately spaced to ensure accurate prediction of the magnetic field. For increased alignment and positioning of the two coils, the former was constructed out of a solid cylindrical piece. To ensure alignment of the sensor coil with the calibrator, a grove was made in the solid former such that the sensor would fit securely in the axial direction of the coils. To accurately measure the current, a high precision 100 Ohm resistor was used as a sense resistor in series with the two coils.

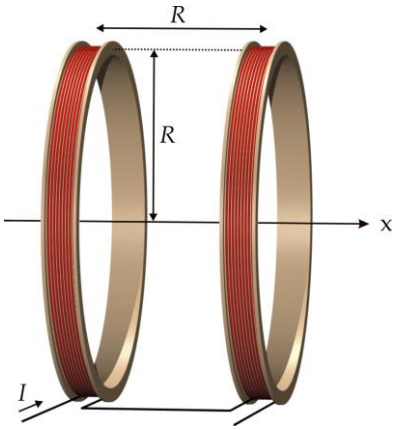



Figure 3.28: Typical Helmholtz coil formation [121].

The magnetic field inside the calibrator was determined analytically to be 321 μT/A using the following procedure. Equation (3.26) predicts the on-axis magnetic field of a single circular current loop where $R$ is the radius of the loop, $x$ is the axial displacement from the centre of the loop [27].

$$B(x) = \frac{\mu_0 I R^2}{2(R^2 + x^2)^{3/2}} \tag{3.26}$$

By considering each turn forming the coil individually and summing them together the overall magnetic field can be calculated as in (3.27) where $x_i$ is the offset for each coil position. The position of the first winding is assumed to be at $x = 0$.

$$B(x) = \frac{\mu_0 I R^2}{2} \sum_{i=1}^{N} \left[ \frac{1}{(R^2 + (x - x_i)^2)^{3/2}} + \frac{1}{(R^2 + (x - x_i - R)^2)^{3/2}} \right] \tag{3.27}$$

In a 1 cm region around the centre of the coils, the mean magnetic field is 320.7 μT with a standard deviation of 0.331 μT which is approximately a 0.1 % variation. Figure 3.29 shows a prediction of the field within the calibrator. Figure 3.30 shows the actual calibrator with the sensor inserted and Figure 3.31 shows a cross section view.

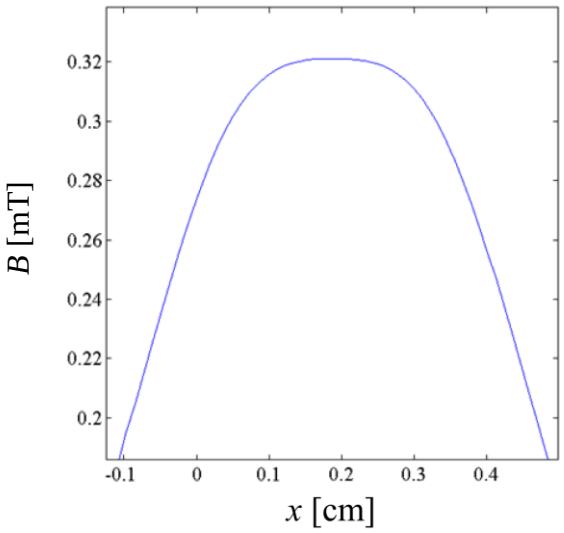



Figure 3.29: Predicted axial magnetic field of the calibrator when carrying 1 A.

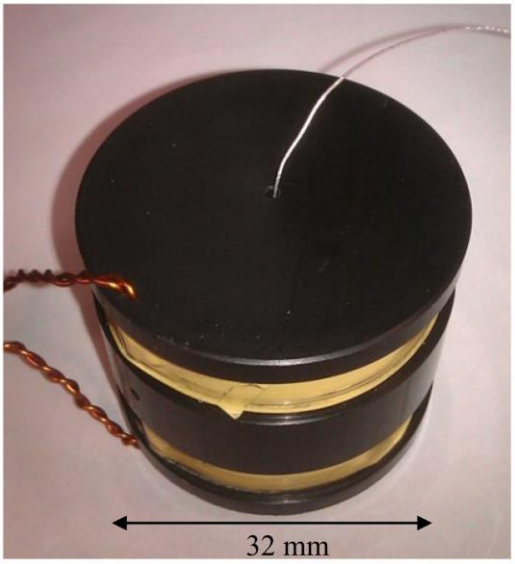



Figure 3.30: Calibrator with sensor inserted.

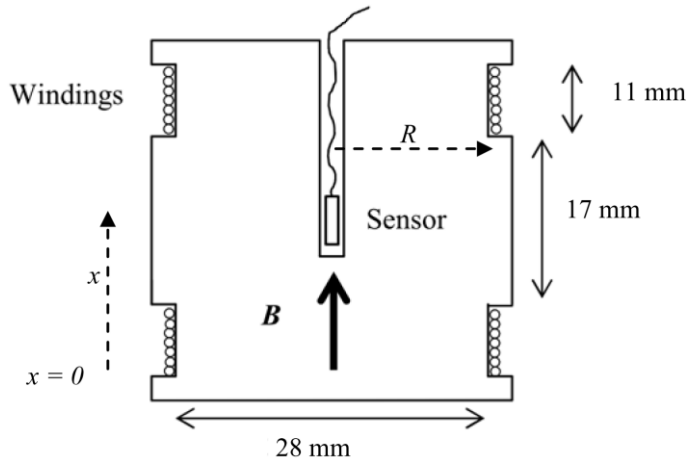



Figure 3.31: Cross section of calibrator design.

### 3.8.5. Test Setup

For all the sensor performance tests, the Helmholtz calibrator coil was used. An AC signal was applied to the calibrator terminals and the resulting input current measured using a sense resistor. This current is used to determine the magnetic field within the calibrator. The sensor under test was then placed at the centre of the calibrator coil and the output voltage recorded.

### 3.8.6. Sensor Frequency Response

The low frequency sensor response (1-30 kHz) was evaluated and this is shown in Figure 3.32. An approximately linear relationship is observed between the input frequency and the resulting sensitivity. A best fit line through the origin is used to find a linear model of the sensor. By calculating the slope of this line, the sensitivity of the sensor in this region was found to be 0.1142 Volts per Tesla per Hertz. Figure 3.33 shows the frequency response over a much wider frequency range from 1 kHz – 1 MHz. A resonant peak at approximately

115 kHz is observed, this is due to resonance between the inductance of the sensor and the parasitic capacitance of the windings.

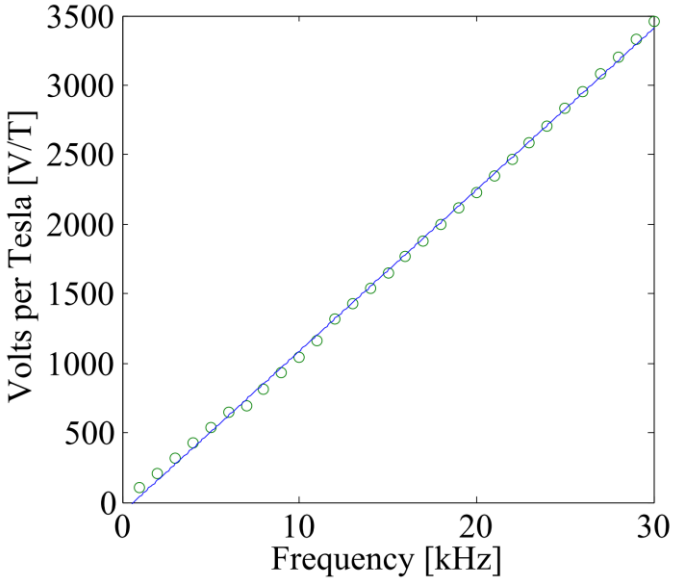



Figure 3.32: Low frequency response of the Aurora 610057 sensor.

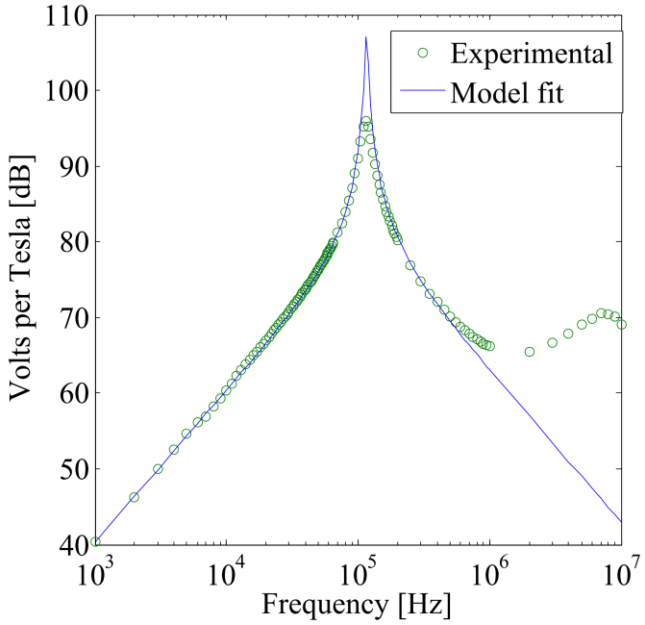



Figure 3.33: Wide band frequency response of the Aurora 610057 sensor with equivalent circuit model fit.

### 3.8.7. Sensor Equivalent Circuit Model

Almost all induction sensors have a similar equivalent circuit model which directly dictates their frequency response. Figure 3.34 shows a typical schematic of this equivalent circuit where $R_s$ is the resistance of the wire, $L_s$ is the inductance of the windings, $C_s$ is the parasitic capacitance of the windings, $V_{in}$ is the induced voltage and $V_{out}$ is the voltage seen at the output terminals of the sensor.

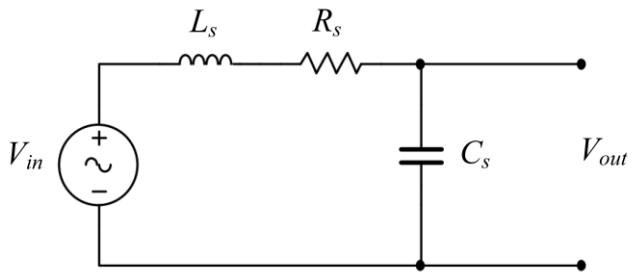



Figure 3.34: Equivalent circuit model for an induction sensor

The following transfer function describes the relationship between the input and output voltages in this network, where $s = jw$ under steady state conditions.

$$V_{out} = V_{in}\left(\frac{\frac{1}{L_s C_s}}{s^2 + \frac{R_s s}{L_s} + \frac{1}{L_s C_s}}\right) \tag{3.28}$$

The input voltage is related to the applied magnetic flux density along the sensor's central axis by the following relationship where $k_c$ is the sensitivity in Volts per Tesla per Hertz and $B_z$ is the amplitude of the magnetic flux density along the axial direction of the Helmholtz coil.

$$V_{in} = -B_z k_c s \tag{3.29}$$

The overall transfer function between the input magnetic field and the output voltage on the sensor terminals is then given by:

$$\frac{V_{out}}{B_z} = \frac{\frac{-k_c s}{L_s C_s}}{s^2 + \frac{R_s s}{L_s} + \frac{1}{L_s C_s}} \tag{3.30}$$

The sensitivity $k_c$ was found experimentally to be 0.0166 V/THz. Using an LCR meter, the low frequency inductance was found to be 2.076 mH and the DC resistance was found to be 71.8 Ω. By adjusting the value of the capacitance $C_s$ until the resonant point matched that as recorded experimentally, its value was found to be $C_s$ = 900 pF. At higher frequencies, large deviations are observed by the model partly due to input impedance of the measurement apparatus as well as high frequency effects such as reflections and the frequency response of the current sense resistor. The resistance of the wire is also non-linear with frequency due to the skin-effect and proximity effect. However it is seen that up to approximately 500 kHz this model matches well with the experiment.

### 3.8.8. Linearity with Magnetic Field Amplitude

The NDI sensors have a small ferromagnetic core which tends to focus the flux through the sensor, hence increasing its sensitivity. However, all ferromagnetic materials exhibit non-

linear behaviour as the magnetic field strength increases. To investigate the level of this non-linearity, the amplitude of the applied magnetic field was increased and the output voltage recorded. Figure 3.35 shows the response of the sensor at 25 kHz to an applied magnetic field strength of increasing amplitude. The resulting response is observed to be linear in this range. Typically in the tracking volume, the magnetic fields are in the range of 10 nT-10 µT. Hence the sensor in this range can be assumed to be linear.

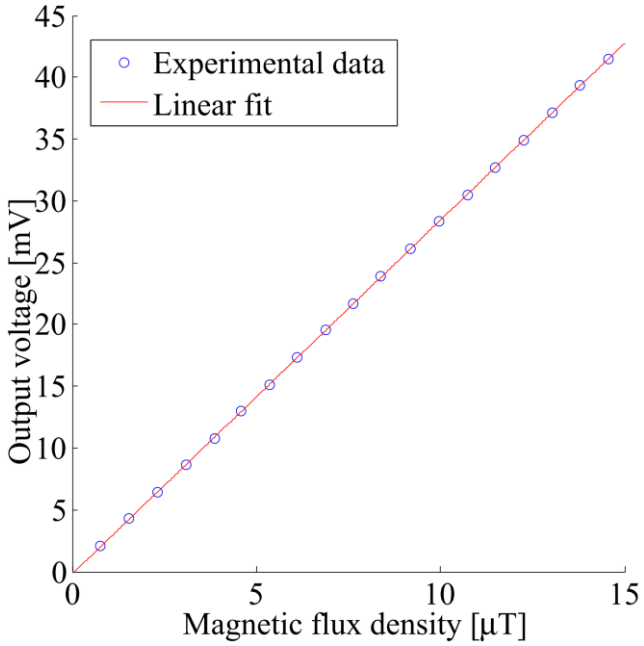



Figure 3.35: Output of the sensor with increasing amplitude of applied magnetic field at 25 kHz.

To investigate the sensor nonlinearity for larger values of applied magnetic field, the calibrator was instead powered from a high-current DC power source. This was required as the levels of current required to drive the sensor into its non-linear region was excessive. The inductance of the sensor was recorded as the calibrator current was increased and subsequently decreased. The inductance is directly related to the operating point of the ferromagnetic structure of the sensor; hence changes in inductance directly indicate saturation in the core. These inductance measurements were taken at 1 kHz. Ferromagnetic materials typically also exhibit hysteresis, *i.e.* their magnetic properties change depending on the previous state of its magnetisation. To determine if the sensor exhibits hysteresis, the current was decreased immediately after it had been reached its maximum level. If the inductance was different as the field was decreased this would indicated hysteretic behaviour. Figure 3.36 shows the results of these tests. Clearly, beyond approximately 300 µT the inductance of the sensor begins to reduce considerably indicating that it has become highly nonlinear.

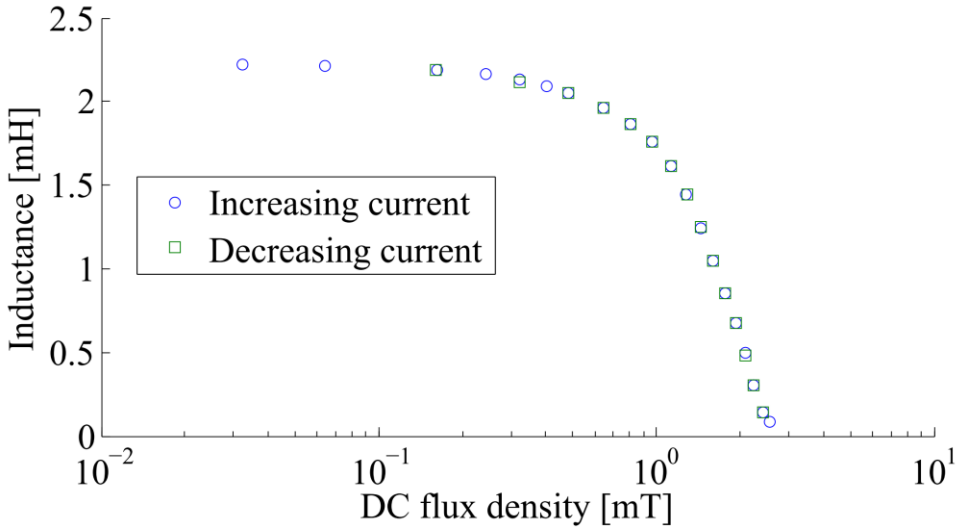



Figure 3.36: Sensor inductance with applied DC magnetic field.

### 3.8.9. Induced Voltage versus Induced Current Measurements

When using induction coil sensors, there are two basic types of measurements typically used; voltage or current. For voltage measurements, generally the sensor is connected into a high impedance amplifier which results in effectively no current flow. The alternative is to short the sensor terminals and measure the resulting current flow. The resulting output voltage from the measurement amplifier has a very different frequency response, and depending on the required information, one or other may be more suitable. However both approaches perform similarly in terms of measurement noise. Figure 3.37 shows basic representations of the two configurations.

Equation (3.28) represents the induced voltage in the coil including the parasitic capacitance, which results in a bandpass characteristic. With a current-to-voltage operational amplifier circuit, the effect of parallel capacitance is removed as the inverting input acts as virtual ground. The resulting waveform has a highpass characteristic, and the cut-off frequency directly depends on the *L/R* time constant of the sensor. Additional compensation networks can extend this cut-off frequency to much lower frequencies. The resulting frequency response is flat over a wide range of frequencies. Hence if a flat frequency response is required, a current measurement is preferred. However in our case, where simply the field amplitude is of interest, voltage measurements are more suitable. The balanced effect of a differential measurement has the added effect of improved common mode rejection. A differential current to voltage topology is possible but is much more complex than a simple instrumentation amplifier for the voltage measurement case.

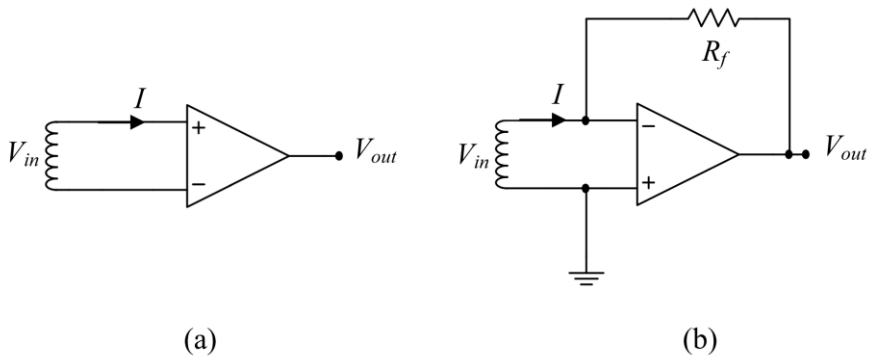



Figure 3.37: Basic circuits for (a) induced voltage measurement and (b) induced current measurement.

## 3.9. Demodulation Methods

### 3.9.1. Introduction

In order to calculate the amplitude of the AC magnetic field experienced by the sensor many techniques are available. Generally, the signals of interest are small in amplitude with relatively large noise levels as well as interference from the other transmitting channels. The most common method to extract the signals of this type is synchronous demodulation, also known as synchronous detection or lock-in amplification [122]. Other methods include Fourier analysis [77], cross-correlation [123], Prony's method [124], Goertzel's algorithm [125] or simply band-pass filtering and measuring the amplitude directly [126]. Each method has its merits and disadvantages in terms of complexity and precision. However synchronous demodulation was found to give excellent performance in this application and was used for our system.

### 3.9.2. Synchronous Demodulation

Synchronous demodulation is a method for extracting information from an AC carrier signal. The basic concept is that the amplitude and phase of an AC signal can be calculated through multiplication by a reference signal that is locked in frequency with the original signal. The multiplication by the reference signal, shifts the signal down to a lower frequency, typically DC, which is then easier to accurately measure. The "locking" of frequencies can be implemented in many ways although the simplest is to use the source of the signal as a reference. In the case of EM tracking systems, generally the current in the transmitter is used as a reference signal since the detected voltage of the sensor is directly related to this source current [9]. Synchronous detection is often used in AM radio receivers although phase locked loops (PLLs) are used to extract the carrier frequency as the source is distant from the receiver [127].

Consider an input signal given by:

$$v(t) = V\sin(\omega t + \varphi) \tag{3.31}$$

The amplitude and phase can be determined by multiplying by two reference signals at the same frequency:

$$Y(t) = \sin(\omega t) \tag{3.32}$$

$$X(t) = \cos(\omega t) \tag{3.33}$$

After some manipulation the following two signals result:

$$v_Y(t) = v(t)Y(t) = \frac{V}{2}\left[\cos\varphi - \cos(2\omega t + \varphi)\right] \tag{3.34}$$

$$v_X(t) = v(t)X(t) = \frac{V}{2}\left[\sin\varphi - \sin(2\omega t + \varphi)\right] \tag{3.35}$$

If the DC component of the signal is extracted by using an appropriate low pass filter, the following amplitudes are found.

$$v'_Y(t) = \frac{V}{2}\cos\varphi \tag{3.36}$$

$$v'_X(t) = \frac{V}{2}\sin\varphi \tag{3.37}$$

The amplitude and phase can then be calculated using the following simple relations:

$$V = 2\sqrt{\left(v'_X(t)\right)^2 + \left(v'_Y(t)\right)^2} \tag{3.38}$$

$$\varphi = \tan^{-1}\left(\frac{v'_X(t)}{v'_Y(t)}\right) \tag{3.39}$$

To demonstrate this type of demodulation, consider the case of a simulated 20 kHz sine wave with an amplitude of 10 mV shown in Figure 3.38. The signal is distorted by adding a combination of white noise, and other sine wave components at 50 Hz and 21 kHz. The signal is multiplied by a reference signal also at 20 kHz (and in phase with the input) before undergoing low pass filtering to remove the higher frequency components. The output of this demodulator is shown in Figure 3.39 where we can see the DC output of the filter is near 10 mV (*i.e.* the input amplitude). Figure 3.40 shows this example in the frequency domain, where after multiplication we see the sum and difference terms at DC, 1 kHz, 19.95 kHz, 20.05 kHz, 40 kHz and 41 kHz.

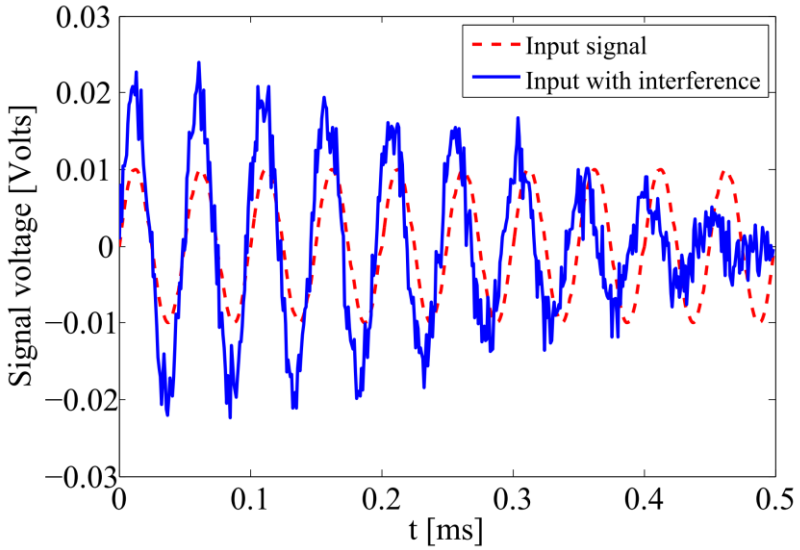



Figure 3.38: An example waveform containing a signal of interest buried under noise and interfering signals.

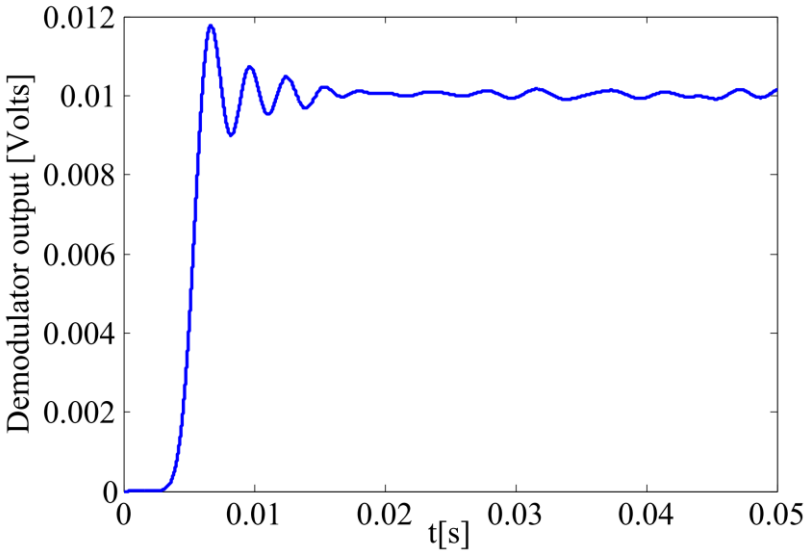



Figure 3.39: Simulated demodulator output.

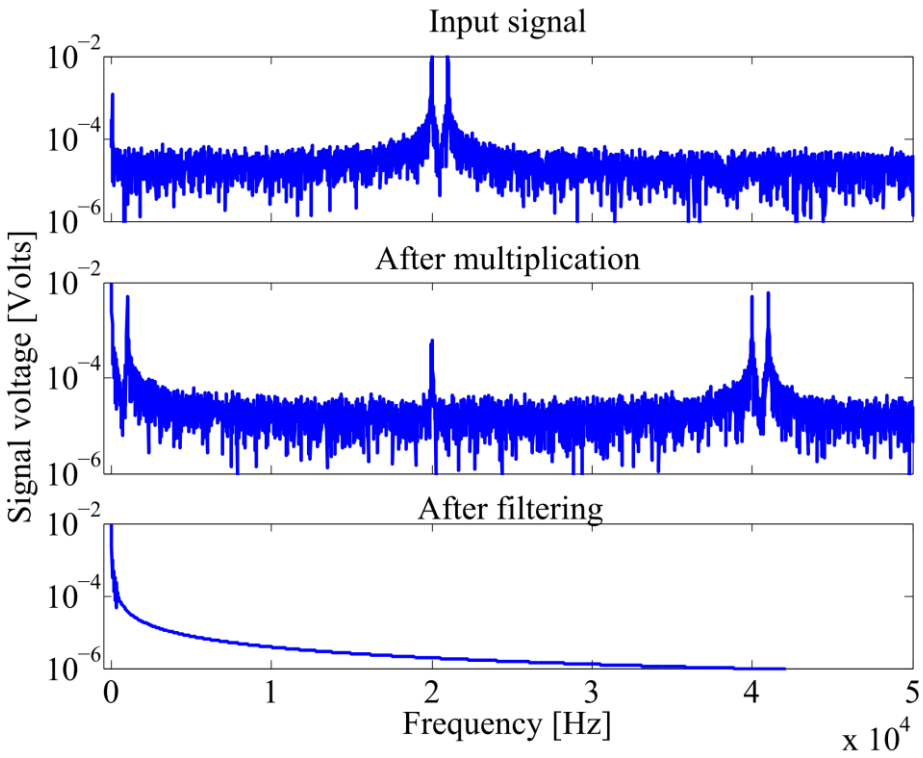



Figure 3.40: Frequency spectrums of the input signal, and the demodulated output before and after filtering.

### 3.9.3. Digital Filtering

An important component of the demodulator subsystem is the digital filter. After multiplication by the reference signal, the voltage component of interest is now at or close to DC in frequency. All other spurious frequency components can then be regarded as noise and must be minimised. Since the desired signal is close to DC, a low pass filter is required. In the various iterations of the system, both IIR and FIR digital filters were used.

The first requirement of the filter is to remove the other adjacent frequency components from the transmitter waveform. These are located at frequencies that result from the sum and difference of the signals in the frequency domain. For example, two signals at 10 kHz and 11 kHz, demodulated by a 10 kHz signal will result in a signal at both 0 Hz and 1 kHz, as well at 20 kHz and 21 kHz. The second requirement is that the passband of the filter be narrow enough to remove wideband white noise that was centred around the signal component of interest. The passband must be made narrow enough to give an adequate SNR as the narrower the passband, the lower the average noise power.

**FIR Filters**

Finite impulse response (FIR) filters are so called because their impulse response has a finite duration (*i.e.* the response settle after a given number of samples). The general structure of an FIR filter is a weighted sum of input samples as seen in Figure 3.41. By choosing different weighting factors, the frequency response of the filter can altered as required. After each delay, the scaled value is known as a “tap” and the number of taps determines the

settling time for the filter. If the filter has *N* taps, then it will require *N* samples to fully settle down. FIR filters have no feedback and as a result are inherently stable. (3.40) represents the implementation of the FIR filter in the time domain, while (3.41) represents its frequency response in the *z*-domain [128].

$$y[n] = \sum_{j=0}^{N} b_j x[n-j] \tag{3.40}$$

$$H(z) = \frac{Y(z)}{X(z)} = \sum_{j=0}^{N} b_j z^{-j} \tag{3.41}$$

FIR filters have the following useful properties:

- requires no feedback, which makes them less susceptible to rounding errors
- always stable
- linear phase
- simple to design.

The primary disadvantage of FIR filters is that they typically require large amounts of taps for sharp filtering characteristics which can make them computationally expensive.

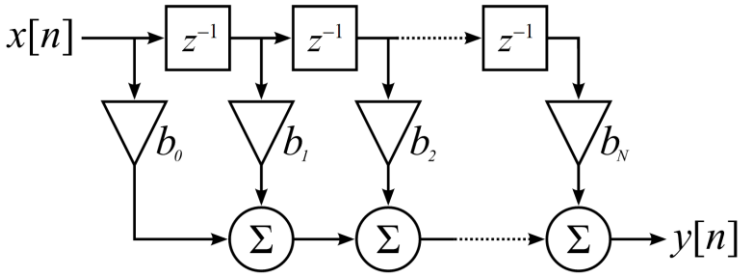



Figure 3.41: General structure of an FIR filter.

**IIR Filters**

Infinite impulse response (IIR) filters are similar FIR filters. However they have additional feedback terms. The feedback term makes IIR filters similar to continuous time filters in that they have an infinite impulse response and can potentially be unstable. Figure 3.42 shows the general structure of an IIR filter, while (3.42) shows the time domain implementation of an IIR filter and (3.43) describes its frequency response. The addition of the feedback terms adds poles to the transfer function and the position of these poles affects the stability of the filter [128].

$$y[n] = \sum_{i=0}^{M} a_i y[n-i] + \sum_{j=0}^{N} b_j x[n-j] \tag{3.42}$$

$$H(z) = \frac{Y(z)}{X(z)} = \frac{\sum_{j=0}^{N} b_j z^{-j}}{1 + \sum_{i=1}^{M} a_i z^{-i}} \tag{3.43}$$

Generally IIR filters can be shorter in length than an IIR filter for a given frequency response, and as a result they are more computationally efficient. However, when narrow

band filters are used, the resulting settling time can be much greater than that of an FIR filter. The stability is also a key factor, and rounding errors can often seriously degrade the filter performance from its original design.

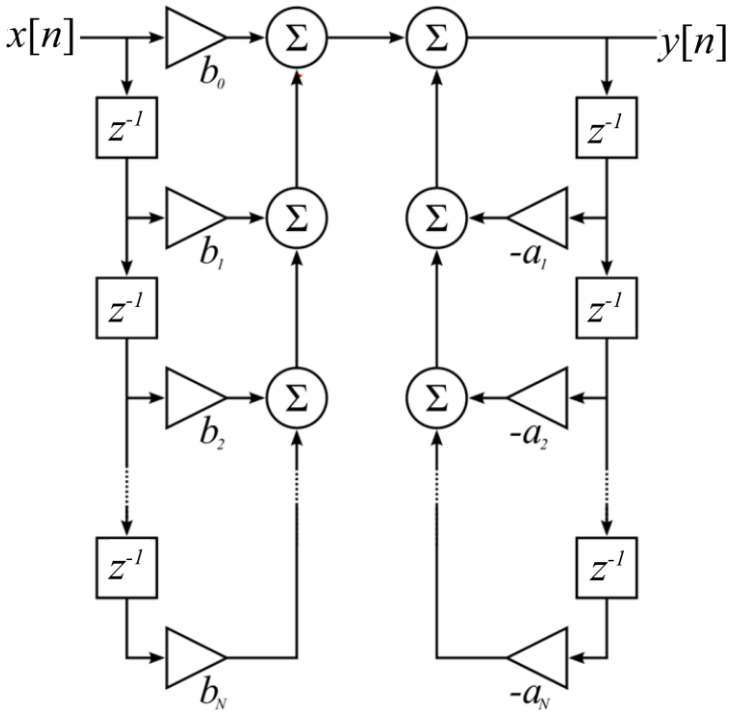



Figure 3.42: General structure of IIR filters.

### 3.9.4. Asynchronous Demodulation

The reference signal in a synchronous demodulator is typically directly related to the signal to be detected; *i.e.* locked together in frequency since they originate from the same source [78], [122]. This has the advantage of reducing errors due to frequency drift and simplifying the number of signals required to demodulate if the phase between both signals is known and constant as both quadrature components are not required. Only a single reference signal is required and not both the sine and cosine signal pair[‡].

In an EM tracking system such as that presented here with digital demodulation multiple signals need to be sampled and processed. The coil current serves as a reference signal [9], but for a system with 8 coils and 1 sensor, this requires 9 signals to be sampled. This requires a multichannel ADC which operates at a much higher aggregate sampling frequency than would be required if less signals were to be measured. To simplify these requirements, simulated reference signals can be used, which results in asynchronous demodulation [79]. If the frequency mismatch is small in comparison with the bandwidth of demodulator filter, there is minimal loss in accuracy with this method in comparison to synchronous demodulation as will be shown in Section 3.9.7. With this approach however, we lose phase

[‡] In our system the phase is constant; however both quadrature components were used to reduce errors in case the phase drifted over time.

information as the phase between the sensor voltage and the simulated waveforms is not referenced to its source, the current waveform. To recover phase information and still keep the number of waveforms to be sampled to a minimum, each of the current waveforms can be summed together to form a single composite waveform (since they are each at different frequencies). Hence with two signals we can now derive sufficient information to calculate the amplitude and phase of the 8 magnetic field contributions. Demodulation of both the magnetic field components and the current waveforms is required to determine the necessary information and hence we denote this method as "Double Demodulation" as is described in the following section.

### 3.9.5. Double Demodulation

Consider a tracking system consisting of *N* emitting coils, each coil carrying a current component of the following form:

$$i_i(t) = I_i \sin\left(\omega_i t + \varphi_{I_i}\right) \tag{3.44}$$

Where $I_i$ is the amplitude of the $i^{th}$ emitting coil waveform, $\omega_i$ is the excitation frequency and $\varphi_{I_i}$ is the current phase relative to an arbitrary reference. Summing all *N* current waveforms results in:

$$i(t) = \sum_{i=1}^{N} I_i \sin\left(\omega_i t + \varphi_{I_i}\right) \tag{3.45}$$

The induced voltage on the sensor has the following general form:

$$v(t) = \sum_{i=1}^{N} V_i \sin\left(\omega_i t + \varphi_{V_i}\right) \tag{3.46}$$

where $V_i$ is the amplitude of each induced voltage component and $\varphi_{V_i}$ is the associated phase. Motion of the sensor is ignored in the above equations as typically in medical applications, the movement is relatively slow and gradual. It is also generally ignored in most research systems [9], [129]. Each frequency component is extracted using the following two simulated reference signals:

$$Y_i = \sin \omega_i t \tag{3.47}$$

$$X_i = \cos \omega_i t \tag{3.48}$$

This demodulation results in the amplitudes and phases of all the frequency components relative to the simulated reference signal as follows:

$$\boldsymbol{V} = \left[V_1 V_2 \ldots V_n\right] \tag{3.49}$$

$$\boldsymbol{I} = \left[I_1 I_2 \ldots I_n\right] \tag{3.50}$$

$$\boldsymbol{\varphi_V} = \left[\varphi_{V_1} \varphi_{V_2} \ldots \varphi_{V_n}\right] \tag{3.51}$$

$$\boldsymbol{\varphi_I} = \left[\varphi_{I_1} \varphi_{I_2} \ldots \varphi_{I_n}\right] \tag{3.52}$$

However this phase information is of little use, as the important information is the phase

between the voltage and current which found by subtracting the individual phases as follows:

$$\Delta\varphi = \varphi_V - \varphi_I \tag{3.53}$$

With this phase difference information we can now determine the sign of the each magnetic field components, which is crucial to indicate whether the sensor is directed towards or away from the magnetic source.

### 3.9.6. Effect of Frequency Mismatch

With a simulated reference signal, it can be difficult to exactly lock the frequency to the signal source without the use of phase locking techniques. In our system this often results in a small mismatch in frequency between the simulated references and the measured signals. However this problem is addressed by using some simple mathematical relations as will be shown here.

Consider a single frequency where the current and voltage waveforms are given by (3.54) and (3.55) respectively.

$$i(t) = I\sin\left(\omega t + \varphi_I\right) \tag{3.54}$$

$$v(t) = V\sin\left(\omega t + \varphi_V\right) \tag{3.55}$$

If the reference signal is not locked precisely in frequency with these signals the resulting demodulated components will not be DC values after filtering, but rather slowly varying AC signals. Typically, frequency mismatch is less than 1 Hz, hence this is the frequency of the filtered signal. If we consider the current waveform (3.54) to be demodulated using two quadrature signals at a slightly different frequency $\omega'$ as follows:

$$Y(t) = \sin(\omega' t) \tag{3.56}$$

$$X(t) = \cos(\omega' t) \tag{3.57}$$

Multiplying these reference signals with the current waveform results in:

$$i(t)Y(t) = \frac{I}{2}\left[\cos((\omega - \omega')t + \varphi_I) - \cos((\omega + \omega')t + \varphi_I)\right] \tag{3.58}$$

$$i(t)X(t) = \frac{I}{2}\left[\sin((\omega - \omega')t + \varphi_I) - \sin((\omega + \omega')t + \varphi_I)\right] \tag{3.59}$$

Extracting the low frequency components leaves the following two quadrature signals:

$$i_X = \frac{I\sin\left(\Delta\omega t + \varphi_I\right)}{2} \tag{3.60}$$

$$i_y = \frac{I\cos\left(\Delta\omega t + \varphi_I\right)}{2} \tag{3.61}$$

where the difference in frequency is given by:

$$\Delta\omega = \omega - \omega' \tag{3.62}$$

The amplitude can then be readily determined using the following square law:

$$I = 2\sqrt{i_X{}^2 + i_Y{}^2} \tag{3.63}$$

The phase has the following form:

$$\gamma_I = \tan^{-1}\frac{I_X}{I_Y} = \Delta\omega t + \varphi_I \tag{3.64}$$

The resulting phase $\gamma_I$ is a saw-tooth waveform. The waveform is a saw-tooth as opposed to the ramp function found mathematically as the inverse tan function is bounded at $\pm\pi$, hence the signal wraps around this interval forming a saw-tooth. Repeating this process with the voltage waveform and subtracting the phases, this saw-tooth component cancels to reveal the actual phase:

$$\gamma_V - \gamma_I = \varphi_V - \varphi_I \tag{3.65}$$

Hence, with this double demodulation scheme, an asynchronous signal of mismatched frequency can still be used to calculate the phase difference and amplitude of interest. The range of acceptable mismatch is limited by the bandwidth of the demodulation filter.

### 3.9.7. Comparing Synchronous and Asynchronous Demodulation

To illustrate the double demodulation methodology and demonstrate the effect of frequency mismatch, consider an example with the following two input waveforms:

$$v_1(t) = 2\sin(2\pi ft + \pi/3)$$
$$v_2(t) = 2\sin(2\pi ft)$$

where the input frequency $f$ is 1 kHz. If the reference signals are synchronous, then their frequency is exactly 1 kHz. However consider an asynchronous scenario where the reference signals are at 1.1 kHz. Hence the frequency mismatch is 100 Hz. Figure 3.43 shows the input waveform $v_1(t)$ as well as the two reference signals (with amplitude = 1). Figure 3.44 shows the output of each quadrature component after filtering. In the synchronous case, a DC amplitude results after settling. Calculating the magnitude of the two quadrature vectors results in the actual amplitude of the input signal. Now consider the asynchronous case also shown in Figure 3.44. Instead of two DC amplitudes, a sinusoidal signal at 100 Hz is observed. However, after combining the two signals, we again arrive at the DC signal containing the input amplitude. Hence the output is the same, even with a significant frequency mismatch of 100 Hz.

To demonstrate the double demodulation method of calculating the phase difference between the two input signals, the phase of the two signals is calculated individually as shown in Figure 3.45. To arrive at the correct phase difference of $\pi/3$ radians, we must subtract the phase from $v_1$ and $v_2$. This is also the case in the asynchronous case, even though the two resulting waveforms is that of a saw-tooth with frequency 100 Hz. Hence with a either a synchronous or asynchronous reference signal both the phase difference and amplitude of

each component of interest can be readily determined with no loss in accuracy.

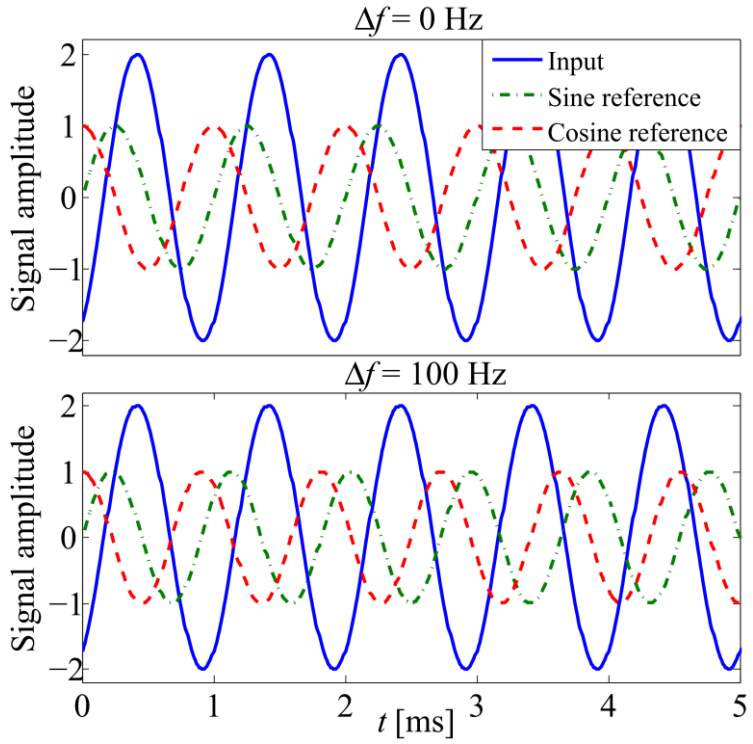



Figure 3.43: Input signals and demodulation reference signals for the synchronous and asynchronous case.

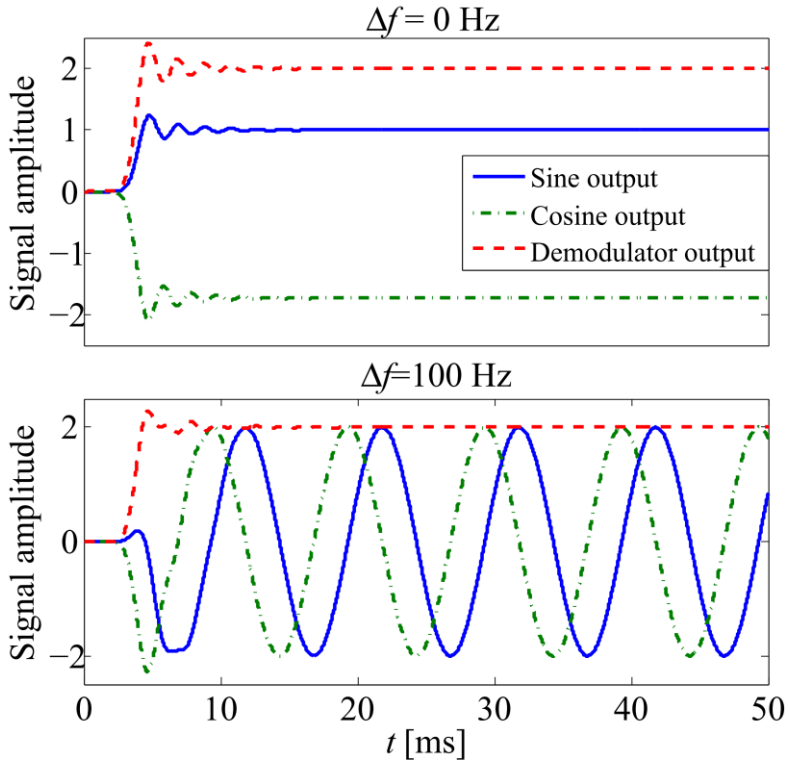



Figure 3.44: Comparing the output of each demodulation quadrature component for the synchronous and asynchronous case.

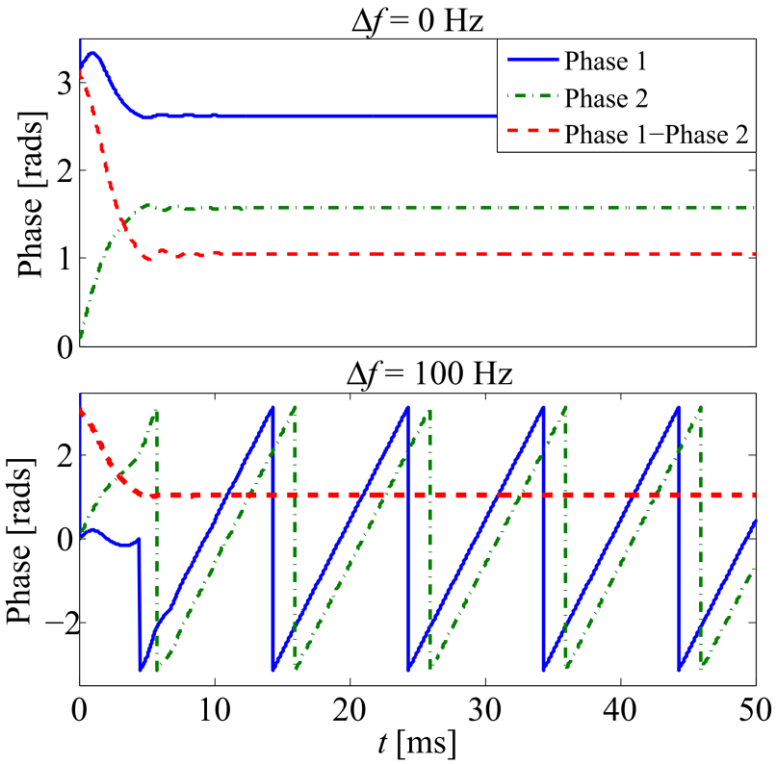



Figure 3.45: Comparing the output phase of two channels of the demodulator for the synchronous and asynchronous case.

### 3.9.8. Efficient Matrix Demodulation Implementation

To increase the speed of the demodulation process, a novel method based on efficient matrix multiplication was developed and implemented. This method involves recording a number of samples at a time, then directly processing and filtering each frequency component in a single calculation, as opposed to processing in real time each sample in turn as is typical. This has the advantage of faster calculation time for the complex filtering processes required. It can also be expanded to include multiple signals. The novelty of this method is that using a very simple and efficient mathematical formulation, all necessary information can be derived from the measured signals and this approach has not been applied to EM tracking systems in the past.

We consider the input signal to have the form of (3.66) which is the summation of $N$ voltage signals at different frequencies $f_i$ sampled at $f_s$, each with amplitude $V_i$ and an associated phase $\varphi_i$. $n$ here represents the sampled number of the discrete input signal. If we collect $p$ samples, the sampled waveform can be denoted by the matrix $\mathbf{X}$ as shown in (3.67).

$$x[n] = \sum_{i=1}^{N} V_i \sin\left(\frac{2\pi f_i n}{f_s} + \varphi_i\right) \tag{3.66}$$

$$\mathbf{X} = \left[x[0]\ \ x[1]\ \cdots\ x[p-1]\right] \tag{3.67}$$

The demodulation waveform can be represented as a complex exponential which concisely contains both quadrature components required to determine both the phase and magnitude of

a particular frequency component. Equation (3.68) shows this exponential function where *j* represents a complex number. For each of the *N* frequency components, this exponential form can be represented by a single matrix **E** shown in (3.69).

$$\varepsilon_i[n] = e^{\frac{2\pi f_i n j}{f_s}} \tag{3.68}$$

$$\mathbf{E} = \begin{bmatrix} \varepsilon_1[0] & \cdots & \varepsilon_N[0] \\ \vdots & \ddots & \vdots \\ \varepsilon_1[p-1] & \cdots & \varepsilon_N[p-1] \end{bmatrix} \tag{3.69}$$

The simplest form of synchronous demodulation involves integrating the product of the input waveform and the demodulating exponential. In the discrete domain, this is achieved by a simple summation given by (3.70), note that the output of this is a complex quantity. This summation can be carried out efficiently as a matrix multiplication as given in (3.71).

$$V_i = \frac{2}{p}\sum_{n=0}^{p-1}\left(x[n]\varepsilon_i[n]\right) \tag{3.70}$$

$$\mathbf{Y} = [V_1 \;\; V_2 \cdots V_N] = 2\mathbf{XE} \tag{3.71}$$

This method however can be improved upon by introducing an FIR filter structure. The summation method in (3.71) is in actual fact a very simple type of low pass FIR filter where each tap coefficient is 1. The filtering characteristics are important as different FIR filters can more effectively filter out unwanted frequency components. Consider an FIR filter denoted by $f_i$ with *p* coefficients (*i.e.* equal to the number of input samples), the output of such a filter can be represented as in (3.72).

$$y[n] = \sum_{i=0}^{p-1} f_i x[n-i] \tag{3.72}$$

The final output of the FIR filter (i.e. when $n = p-1$) is the required term, as every point in between is simply a transient state of the filter as it settles. Due to the inherent stability of FIR filters, after an input signal has reached the final tap in the filter, the output is fully settled. In other words, at this point the amplitudes of each demodulated frequency component can be extracted. Each filter coefficient can be represented by a single matrix **F** as seen in (3.73). The 1/*p* term from (3.70) is incorporated into each coefficient of **F**.

$$\mathbf{F} = [f_0 \;\; f_1 \cdots f_{p-1}] \tag{3.73}$$

This FIR filter can be applied to the demodulator by scaling each input sample of **X** with the corresponding FIR coefficient given by **F**. This is achieved using an element by element multiplication as seen in (3.74). Here the symbol ∘ implies element by element matrix multiplication (also known as the Hadamard product) in order to differentiate it from standard matrix multiplication.

$$\mathbf{Y} = 2(\mathbf{X} \circ \mathbf{F})\mathbf{E} \tag{3.74}$$

The amplitude of each frequency component can be determined by calculating the absolute

value of **Y,** which is a complex quantity, using (3.75), while the phase is then calculated using the complex argument of **Y** as in (3.76).

$$\left[V_1 V_2 \cdots V_N\right] = \left|\mathbf{Y}\right| \tag{3.75}$$

$$\left[\varphi_1 \varphi_2 \cdots \varphi_N\right] = \arg(\mathbf{Y}) \tag{3.76}$$

This method may be expanded to accommodate multiple input signals, denoted by $x_i[n]$, by expanding (3.67) to include *q* input signals to get (3.77). (3.73) must also be extended so that it has the same number of rows as there are input signals (*i.e. q* rows), which results in (3.78) . The filter coefficients in each row of **F** may be identical or they can be chosen to give each input signal different frequency responses to each input signal. However, for our system each row was identical.

$$\mathbf{X} = \begin{bmatrix} x_0[0] & x_0[1] & \cdots & x_0[p-1] \\ & & \vdots & \\ x_q[0] & x_q[1] & \cdots & x_q[p-1] \end{bmatrix} \tag{3.77}$$

$$\mathbf{F} = \begin{bmatrix} f_0 & f_1 \cdots f_{p-1} \\ & \vdots & \\ f_0 & f_1 \cdots f_{p-1} \end{bmatrix} \tag{3.78}$$

To demonstrate the method, consider the input waveform shown in Figure 3.46. This signal is multiplied by a reference signal and then filtered with an FIR low pass filter which is shown in Figure 3.47. This filter contains 500 taps and we see that from Figure 3.47 after 400 taps the filter output has levelled off. Hence, the relevant information is available after almost all of the signal has propagated through the filter delay line structure. By ignoring the intermediate stages of the filter and calculating the output only at the last tap, we reduce the number of calculations required to determine the filter output. This type of method cannot be implemented with an IIR filter due to its recursive nature. In an IIR filter, the current output depends on a number of previous outputs and inputs. Hence every intermediate calculation is required. In an FIR implementation this implies that a PC has more free computation time to implement other applications.

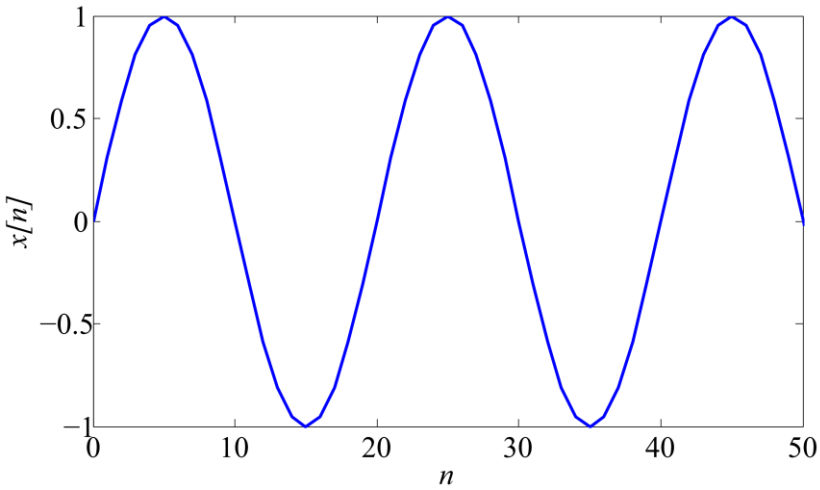



Figure 3.46: Input signal to the demodulator.

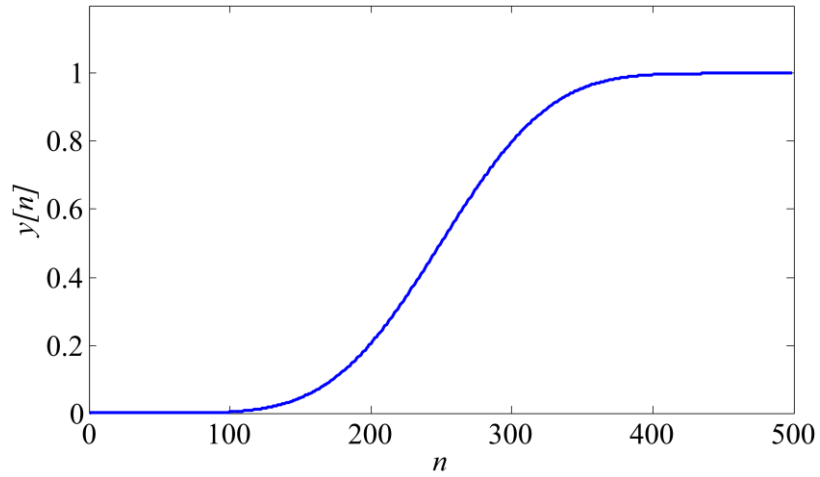



Figure 3.47: Settling time of the demodulator with an FIR low pass filter with 500 taps.

FIR filters generally give better performance in terms of settling time for a given passband and stopband requirement. For example consider two filters, one IIR and one FIR, which have been designed to give a normalised passband cut-off frequency of 0.0025 ( $f / f_s$ ) and a 100 dB stopband of 0.02. The transient performance of each of these filters is shown in Figure 3.48 where we see that the IIR filter takes considerably longer time to settle. Figure 3.49 compares the settling time between IIR and FIR filters for a range of stopband cut-off frequencies and it can be clearly seen that generally there is orders of magnitude between the settling times for similar filtering performance.

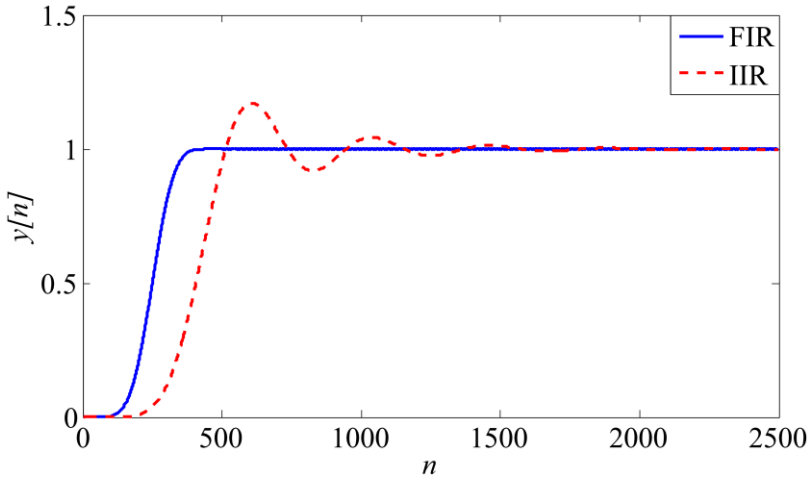



Figure 3.48: Comparing FIR and IIR filters with similar stopband and passband characteristics.

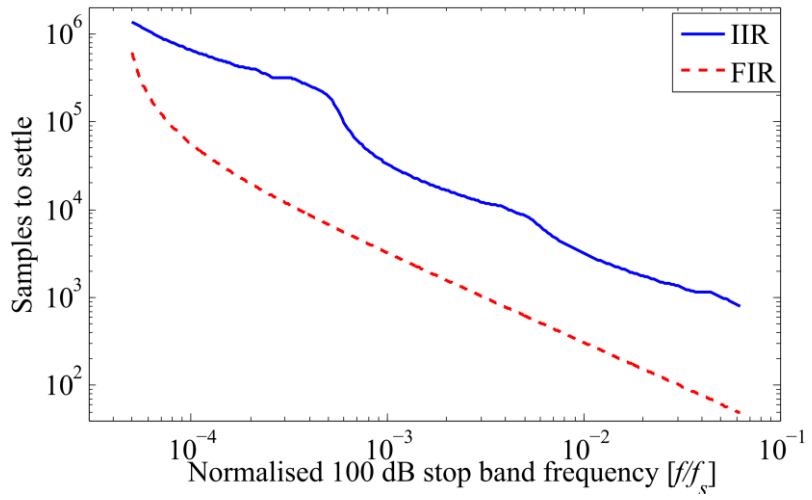



Figure 3.49: Comparing the settling time of IIR and FIR filters for a given stopband attenuation.

If the signal of interest is corrupted with excessive amounts of noise, reducing the size of the filter passband decreases associated errors. This can be achieved by increasing the number of taps in the FIR filter. Figure 3.50 shows how the SNR affects the resulting error in the amplitude of the demodulated signal. We see here that even with very low SNR, the signal can still be demodulated if we increase the number of filter taps and collect the associated number of samples. This can be dynamically changed depending on the noise level to maintain accurate demodulation. However, as well as increased time required to sample the waveforms, calculation time also increases, as shown in Figure 3.51.

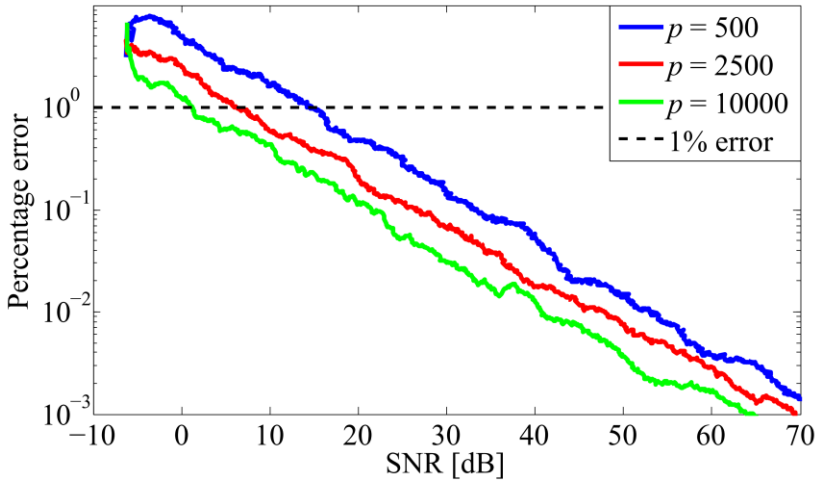



Figure 3.50: Demonstrating the performance of an FIR filter in terms of percentage error of a demodulated signal in relation to the SNR of the signal.

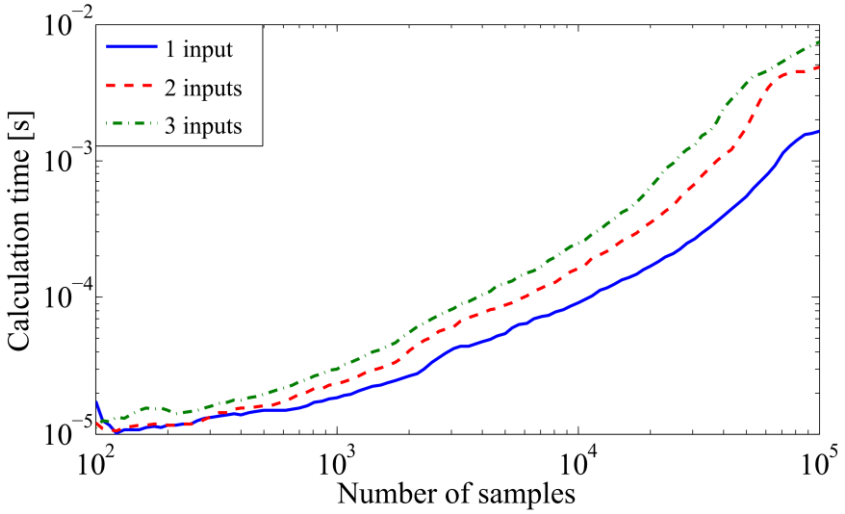



Figure 3.51: Calculation time for demodulation for different sample lengths and numbers of inputs.

### 3.9.9. Choice of Window Functions

As mentioned previously, the choice of window function has a dramatic effect on the shape of the frequency response of an FIR filter. Here we examine a number of common FIR window functions and an appropriate form is chosen. First consider the rectangular window function given by (3.79) where each tap carries an equal weighting factor.

$$w(n) = 1 \tag{3.79}$$

Other common windows examined include the triangular window given by (3.80), the Hamming window in (3.81), and the Flat-Top window in (3.82) [130].

$$w(n) = 1 - \left| \frac{n - \frac{N-1}{2}}{\frac{N+1}{2}} \right| \tag{3.80}$$

$$w(n) = 0.54 + 0.46\cos\left(\frac{2\pi n}{N-1}\right) \tag{3.81}$$

$$w(n) = a_0 - a_1 \cos\left(\frac{2\pi n}{N-1}\right) + a_2 \cos\left(\frac{4\pi n}{N-1}\right) - a_3 \cos\left(\frac{6\pi n}{N-1}\right) + a_4 \cos\left(\frac{8\pi n}{N-1}\right) \quad (3.82)$$

For (3.82), the following coefficients were used: ,

$$a_0 = 0.2155 \; a_1 = 0.4166 \; a_2 = 0.2772 \; a_3 = 0.0835 \; a_4 = 0.0069$$

The Dolph-Chebyshev window function was also examined although its coefficients cannot be represented in a concise form and are not presented here [130]. For each window function, a 25 tap filter was used. The filter coefficients are plotted in Figure 3.52. Each filter is scaled to give a passband gain of 0 dB. The Chebyshev window was calculated with a specified side-lobe attenuation of -100 dB, while all other windows were simply functions of the number of taps. Figure 3.53 shows the normalised frequency response for each of these filters. We see that the Chebyshev window gives the best stop band attenuation, although its transition bandwidth is larger than some of the other windows such as the triangular window for example. Stopband attenuation is critical in our application as the neighbouring frequency components after filtering must be removed. Hence the Chebyshev filter was chosen for our system.

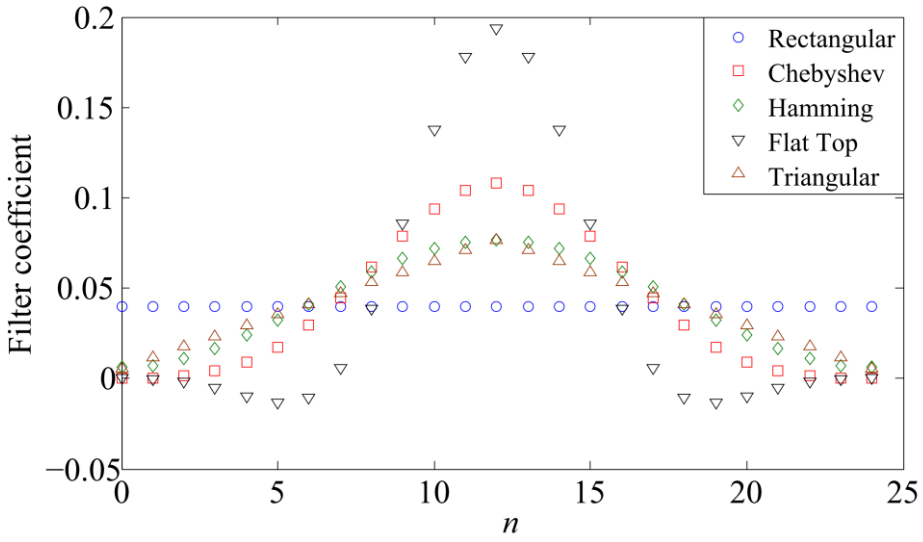



Figure 3.52: Filter coefficients for each window function.

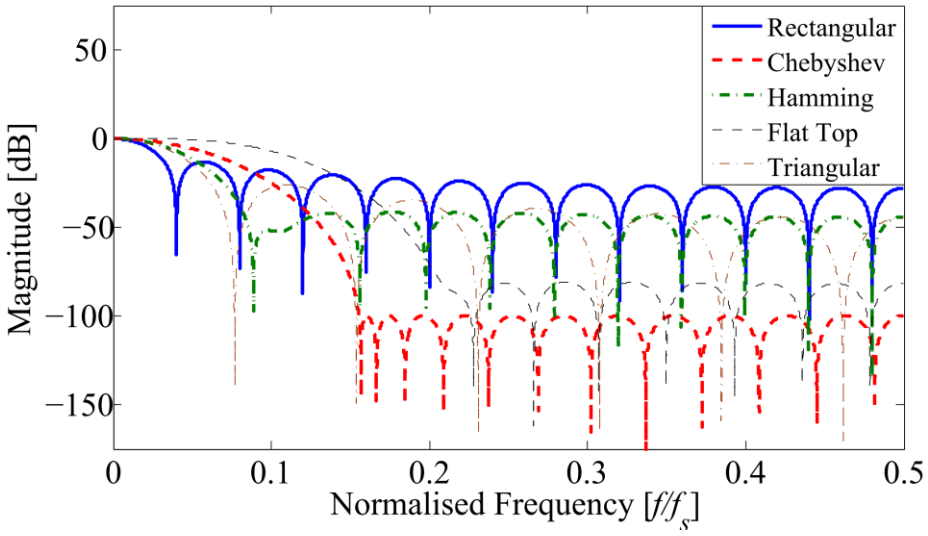



Figure 3.53: Frequency response of each window function.

## 3.10. Circuit Design and Construction

### 3.10.1. Constant AC Current Driver

To accurately control the AC current in each coil, a custom driver circuit was designed and implemented. The purpose of this circuit was to deliver a constant AC current to each coil. The circuit has 8 channels for simultaneously driving 8 separate coils at different frequencies and current amplitudes, with a frequency range of 0-50 kHz and a current range of up to 500 mA.

Key design requirements were as follows:

- Low harmonic distortion
- Stable output current
- Adjustable current and frequency selection

A feedback configuration dramatically reduces harmonic distortion in the current waveform as well providing a high stability current source. Many EM tracking systems use open-loop circuits to control the excitation current. However, this approach is prone to temperature drift and changes in the inductance of the coil due to proximity of metallic distorters. Long term stability of the coil current allows for the current levels assumed to be effectively constant which simplifies the measurement of the magnetic field from the sensors. This novel closed loop method also effectively cancels the mutual coupling between each coil in the transmitter array and has not been presented elsewhere in literature for application in EM tracking system.

Figure 3.54 shows a block diagram of the coil driver board. A signal voltage source, derived from a direct digital synthesis (DDS) sine wave generator, is filtered and applied to a high speed amplifier circuit. The closed loop topology uses the coil current as a feedback signal to

accurately control its amplitude. Figure 3.55 shows the final PCB showing all eight channels of the driver.

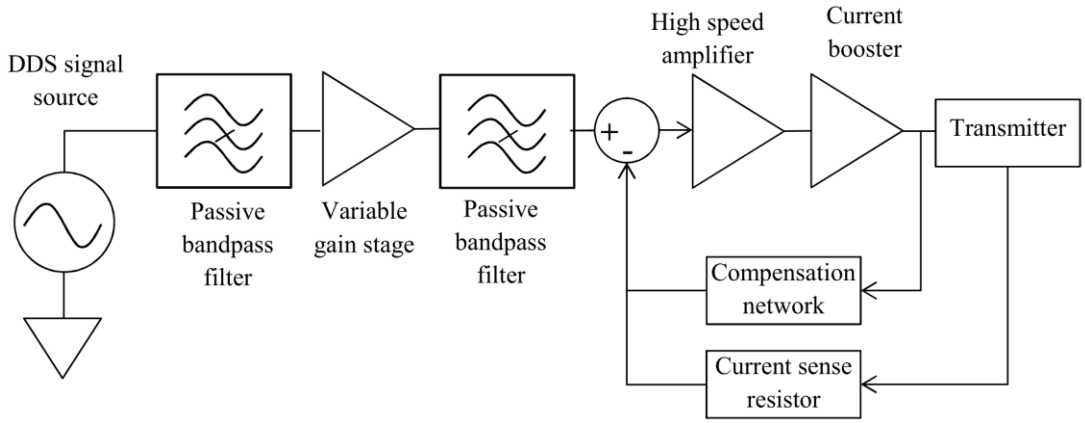



Figure 3.54: Block diagram of each driver channel.

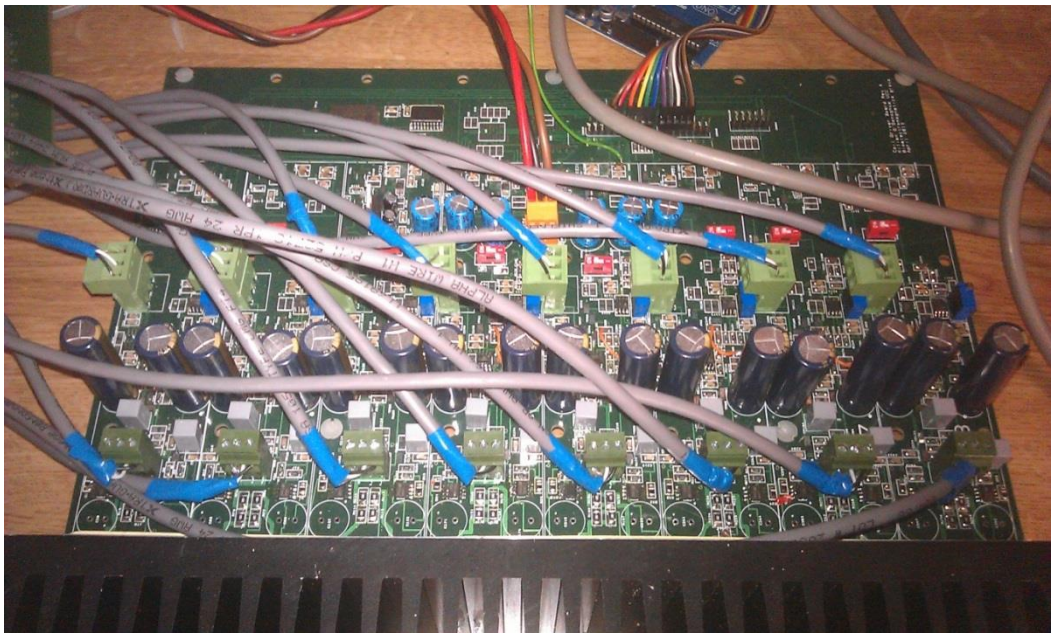


Figure 3.55: Constant current driver board.

### 3.10.2. Driver Circuit Design and Stability Analysis

The basic concept for the drive circuit design is based around a simple voltage-to-current operational amplifier circuit shown in Figure 3.56. The op-amp works to drive the voltage across $R_s$ to match the input; the output current in this case is given by (3.83).

$$I_{out} = \frac{V_{in}}{R_s} \tag{3.83}$$

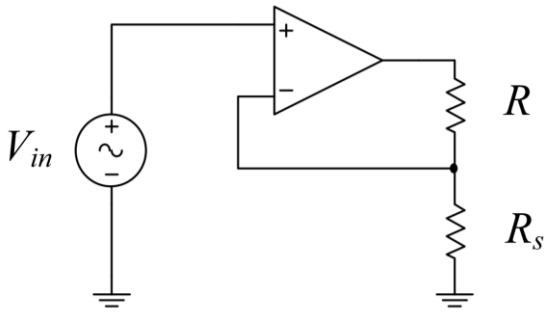



Figure 3.56: Constant current op-amp configuration.

When the load, indicated by $R$ in Figure 3.56, is inductive, care must be taken as the phase margin of the system can become very low, potentially causing instability and ringing. Consider the circuit in Figure 3.57, where the transmitter is represented by an inductance $L_t$ and a resistance $R_t$. The transfer function between the output voltage of the op-amp and the resulting current is given by (3.84).

$$\frac{I_{out}(s)}{V_o(s)} = \frac{1}{R_s + R_t + sL_t} \tag{3.84}$$

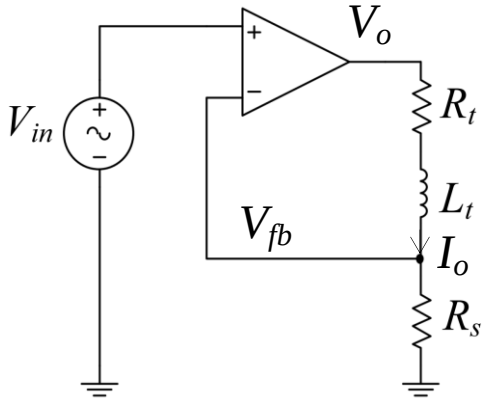



Figure 3.57: Constant current op-amp configuration with inductive load.

At higher frequencies, the inductance term dominates and the phase approaches -90°. Hence if the load current is fed back to the input, the phase margin of the amplifier is reduced. A typical open loop transfer function for an op-amp can be approximated as a first order system such as (3.85) where $A_{OL}$ is the open loop gain and τ is the time constant of the dominant pole.

$$A(s) = \frac{A_{OL}}{1 + s\tau} \tag{3.85}$$

Typically $A_{OL}$ is very large, and the pole frequency is normally in the range of 10 - 100 Hz, as determined by the internal compensation capacitor. At higher frequencies, the op-amp ideally has a phase of -90°. This op-amp phase lag coupled with the 90 degree lag of the current waveform greatly can easily result in a very low phase margin. Equation (3.86) represents the open loop transfer function between the input voltage and the feedback voltage on the inverting input terminal.

$$\frac{V_{fb}(s)}{V_{in}(s)} = \left(\frac{R_s}{R_t + R_s + sL_t}\right)\left(\frac{A_{OL}}{1+s\tau}\right) \tag{3.86}$$

An LM7171 op-amp was used to control the current in each coil as it has a high bandwidth which allows it to quickly account for variations in the coil current and reject disturbances as well as account for non-linear behaviour in the power boost stage. (3.87) represents a second order open-loop model for the op-amp that was derived from its datasheet. Figure 3.58 shows a bode-plot of this transfer function.

$$A(s) = \left(\frac{3\times10^6}{1+.0016s}\right)\left(\frac{1}{1+1.6\times10^{-8}s}\right) \tag{3.87}$$

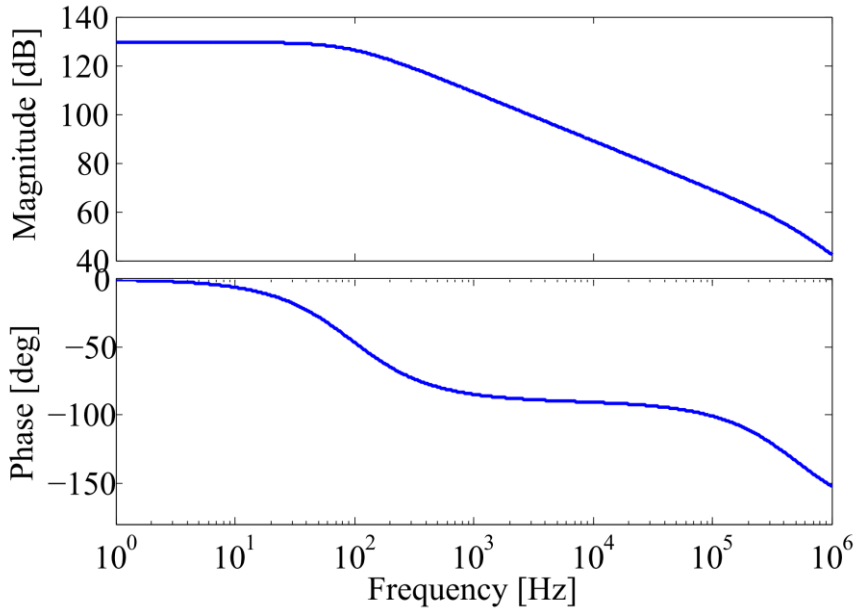



Figure 3.58: Simulated open loop frequency response of the LM7171.

For simulation, the coil was estimated to have an inductance of 75 µH and a resistance of 3 Ω. The sense resistor was set to 1 Ω. These parameters, in conjunction with (3.86) and (3.87) results in a phase margin of just 6.65°, which is stable but with very low damping meaning that it is susceptible to ringing. Hence, some compensation is required to improve performance. There are a variety of methods possible for this stabilisation such as a dedicated compensator controller feeding the input to the op-amp. However a simpler method is to adapt the feedback with a passive compensation network as shown in Figure 3.59.

By appropriately choosing $C_c$ and $R_c$, the phase margin can be dramatically improved. The addition of the capacitor reduces the phase lag introduced by the inductor over a certain frequency range, which depends on the value of the resistor and the capacitor. By decreasing the phase at higher frequencies, specifically around the unity gain point, the phase margin can be substantially increased.

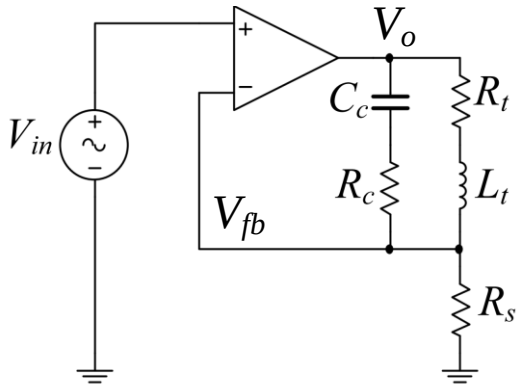



Figure 3.59: Compensated op-amp configuration.

The size of the compensation components are determined by simulating the open-loop response of the amplifier and examining the resulting phase response. $R_c$ should be chosen to be large in comparison to $R_t$ such that at the desired operating frequency the impedance of the coil is low enough to shunt almost all of the output current. This ensures that the current measured though the sense resistor is a good representation of the coil current. After iterative testing, $R_c$ was chosen to be 5 kΩ and $C_c$ was set to 70 nF. Figure 3.60 shows a comparison between the open-loop responses of the system with and without the compensation network. We see that the size of the phase lag at higher frequencies is greatly reduced with the compensated system. The resulting phase margin is now 84.4°.

Figure 3.62 shows how the values of $R_c$ and $C_c$ of this compensation network affects the phase margin. Here it is seen that generally higher values of for both components give better large phase margins. The larger the phase margin, the better the stability and performance of the system.

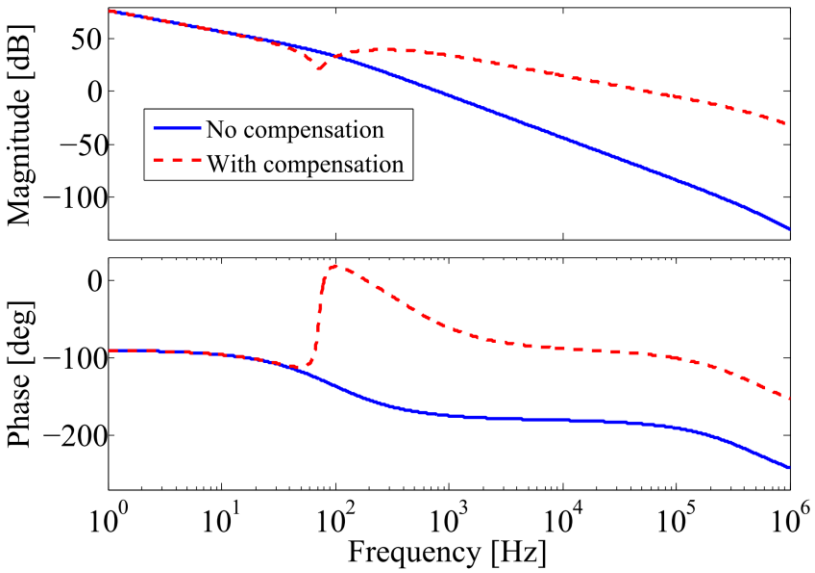



Figure 3.60: Open loop frequency response of $V_{fb}(s)/V_{in}(s)$.

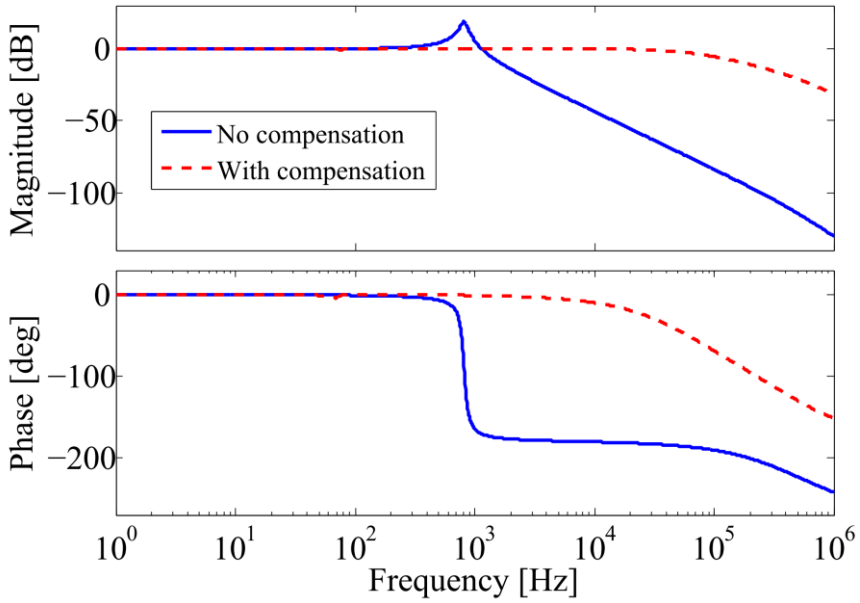



Figure 3.61: Closed loop frequency response of $V_{fb}(s)/V_{in}(s)$.

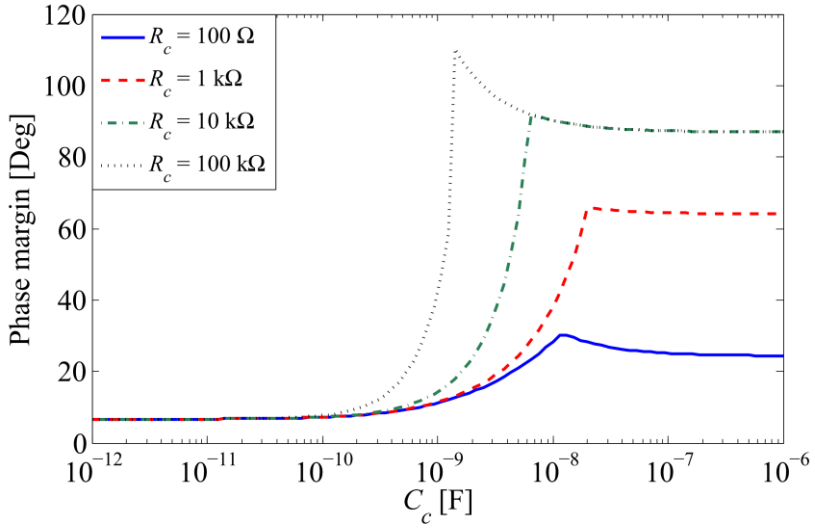



Figure 3.62: Phase margin of $V_{fb}(s)/V_{in}(s)$ with variation with $C_c$ and $R_c$.

### 3.10.3. Power Amplifier Stage

The limitation of many operational amplifiers is the maximum output current that can be delivered, typically no more than tens of milliamps. Depending on the application output, voltage swing might also be an issue. To boost the output power, an additional Class B amplifier stage with discrete power transistors was used. This increases the maximum output power to approximately 25 W per channel.

Figure 3.63 shows a typical arrangement of this type of amplifier where $Q_1$ carries the main load current during positive cycles of the input waveform, while $Q_2$ sinks current during the negative cycles. The diode and resistor arrangement is to bias the two transistors and to reduce crossover distortion as the conducting transistor switches from $Q_1$ to $Q_2$. If $R_1$ and $R_2$ are identical, the voltage drop through each will be equal causing the centre of the two

diodes to be at the centre of the rail to rail voltage. Each diode then offsets the input voltage by its forward voltage drop, which is approximately 0.7 V. Ideally, this voltage offset matches the base emitter voltage drop of the BJTs which results in a smoother transition from its non-conducting state.

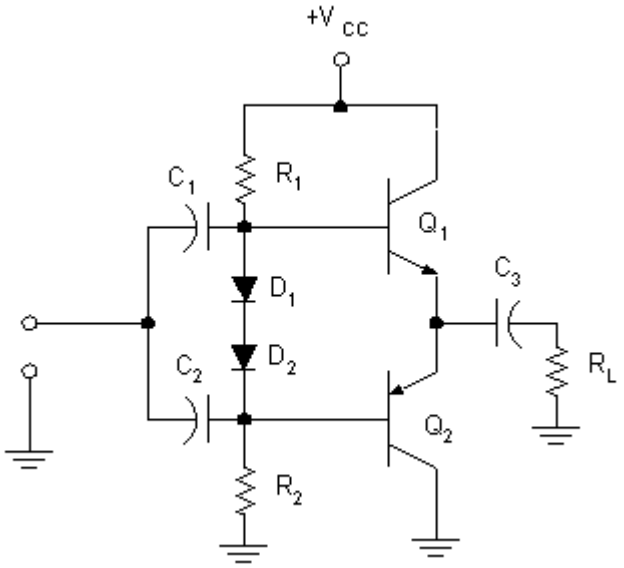



Figure 3.63 Typical Class B amplifier.

A disadvantage of this circuit topology is its thermal instability. Typically, the transistors dissipate far more power than the diodes, and as a result, they operate at a higher temperature. The characteristics of the transistor vary exponentially with temperature, hence a well-matched diode/transistor pair will quickly become unmatched unless they are thermally bonded together, and so that both components' characteristics vary in a similar manner with increasing temperature. To further increase the stability, small value resistors of a few ohms may be connected to the emitters of the two transistors. The purpose of these resistors is to reduce the sensitivity of the transistor performance to temperature by having a linearising effect as well as adding negative feedback.

A further improvement to increase the stability is to replace the resistors in the biasing section with constant current sources. The resistors in Figure 3.63 effectively set the quiescent current for the amplifier. The disadvantage of this arrangement is thermal drift as this unstable current source varies with temperature and changes in the voltage drop of the diodes. Stable current sources are available in 3-terminal IC packages that provide a much more stable current source due to a feedback mechanism that is utilised. Figure 3.65 shows an overall schematic for each channel of the driver.

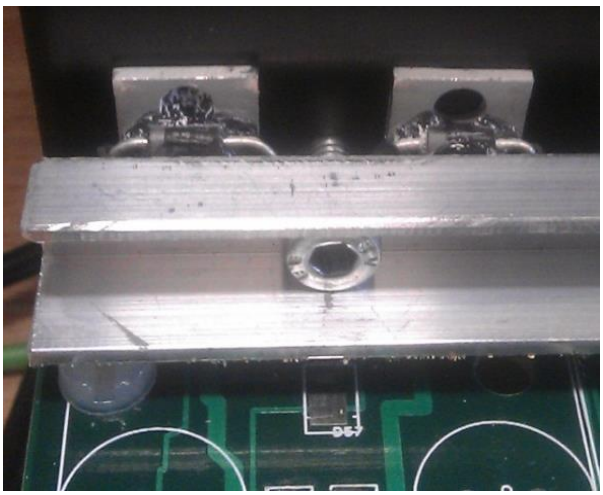


Figure 3.64: Thermal bonding of output transistors and biasing diodes.

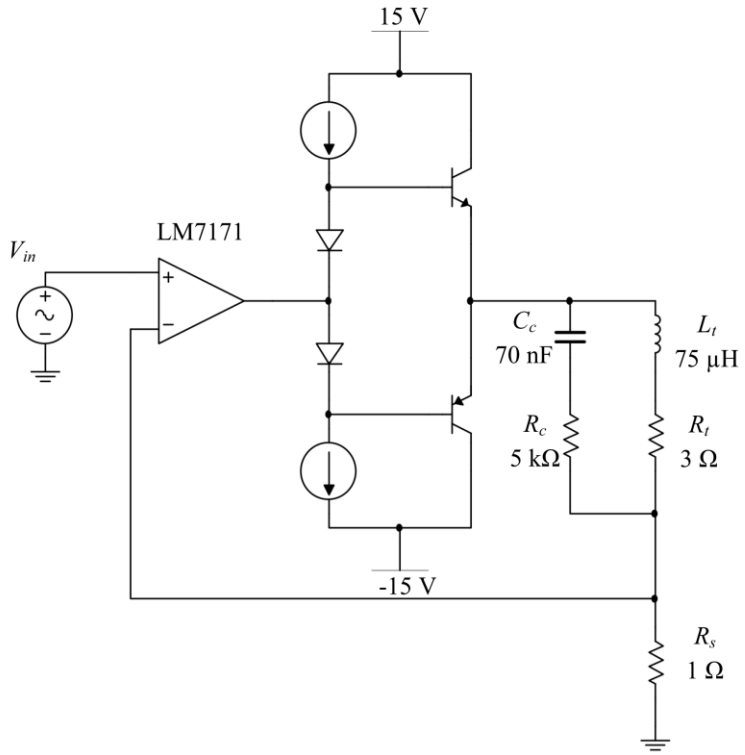



Figure 3.65: Basic schematic of the constant AC current source. A Class B amplifier is used to boost the output power of a high speed op-amp. The current through the coil is fed back using a sense resistor. To increase the phase margin of the system a series combination of a resistor and capacitor are placed in parallel with the coil for compensation. The sinusoidal reference source is generated using DDS with an AD9833 IC.

### 3.10.4. Coupled Transmitter Analysis

In the previous sections, it was assumed that only a single coil was in operation. However for many AC tracking systems, arrays of coils are used simultaneously to generate the required magnetic field. Due to the close proximity of each coil in the array, mutual inductance can be problematic as secondary currents can be induced in neighbouring coils. The larger the mutual inductance between two coils, the larger this induced current. This further complicates the resulting magnetic field. However the closed loop system designed here

effectively decouples each coil making them independent. Here we present a mathematical analysis of this behaviour. A simplified schematic is used, although this analysis can easily be expanded to include the full schematic.

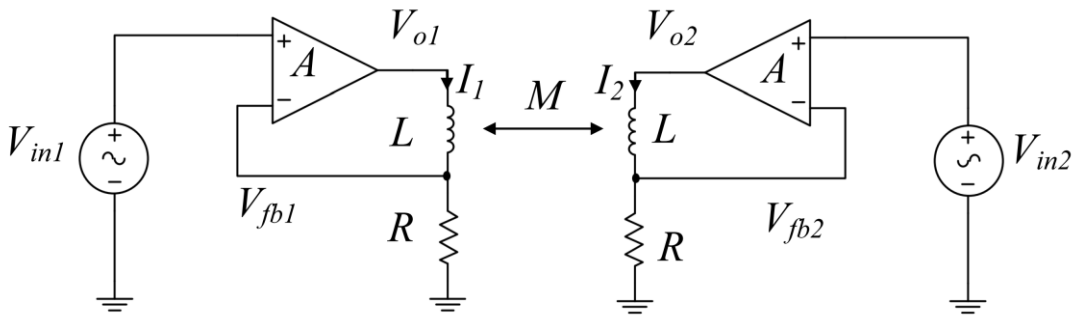



Figure 3.66: Two closed loop controlled coils with mutual coupling.

Figure 3.66 shows a simplified schematic of two controlled coils with similar inductance and negligible resistance. Each coil has a mutual inductance denoted by *M*. The two operational amplifiers are assumed to be ideal with a gain of *A*. The output voltage of the first amplifier is given by Kirchoff's voltage law including the effect of the induced voltage from the second coil is given by (3.88). Considering the governing equation for an ideal op-amp to be given by (3.89), the output voltage of the amplifier can also be written as (3.90).

$$v_{o1}(t) = L\frac{di_1}{dt} + M\frac{di_2}{dt} + Ri_1(t) \tag{3.88}$$

$$V_o = A(V_+ - V_-) \tag{3.89}$$

$$v_{o1}(t) = A(v_{in1}(t) - Ri_1(t)) \tag{3.90}$$

Applying the Laplace transform to (3.88) and (3.90) (ignoring initial conditions as only the steady state performance is required) we arrive at (3.91) and (3.92). If combine both (3.91) and (3.92) and make the assumption that $A \gg 1$, two coupled equations for the current in each coil given by (3.93) and (3.94) result.

$$V_{o1}(s) = LsI_1(s) + MsI_2(s) + RI_1(s) \tag{3.91}$$

$$V_{o1}(s) = A(V_{in1}(s) - RI_1(s)) \tag{3.92}$$

$$I_1(s) = \frac{AV_{in1}(s)}{Ls + AR} - \frac{MsI_2(s)}{Ls + AR} \tag{3.93}$$

$$I_2(s) = \frac{AV_{in2}(s)}{Ls + AR} - \frac{MsI_1(s)}{Ls + AR} \tag{3.94}$$

To simplify these expressions and to solve for the individual currents, we use the substitution given by (3.95), which leaves us with (3.96) and (3.97).

$$G(s) = \frac{1}{Ls + AR} \tag{3.95}$$

$$I_1(s) = AG(s)V_{in1}(s) - MsG(s)I_2(s) \tag{3.96}$$

$$I_2(s) = AG(s)V_{in2}(s) - MsG(s)I_1(s) \tag{3.97}$$

Solving these two equations with algebraic manipulation, the equation in each coil can be represented as (3.98) and (3.99) respectively.

$$I_1(s) = \frac{AG(s)}{1 + M^2 s^2 G^2(s)} V_{in1}(s) - \frac{sAMG^2(s)}{1 + M^2 s^2 G^2(s)} V_{in2}(s) \tag{3.98}$$

$$I_2(s) = \frac{AG(s)}{1 + M^2 s^2 G^2(s)} V_{in2}(s) - \frac{sAMG^2(s)}{1 + M^2 s^2 G^2(s)} V_{in1}(s) \tag{3.99}$$

Figure 3.67 shows a comparison of the performance of this arrangement between open-loop and closed-loop configurations with the following circuit parameters: $L$ = 75 µH, $M$ = 7.5 µH, $R$ = 1 Ω. The amplifier model given by (3.87) is used for $A$ *(i.e.* the amplifier gain constant $A$ is replaced with a frequency dependent function $A(s)$*)*. In this figure we see that up to approximately 100 kHz, the unwanted induced current is effectively diminished.

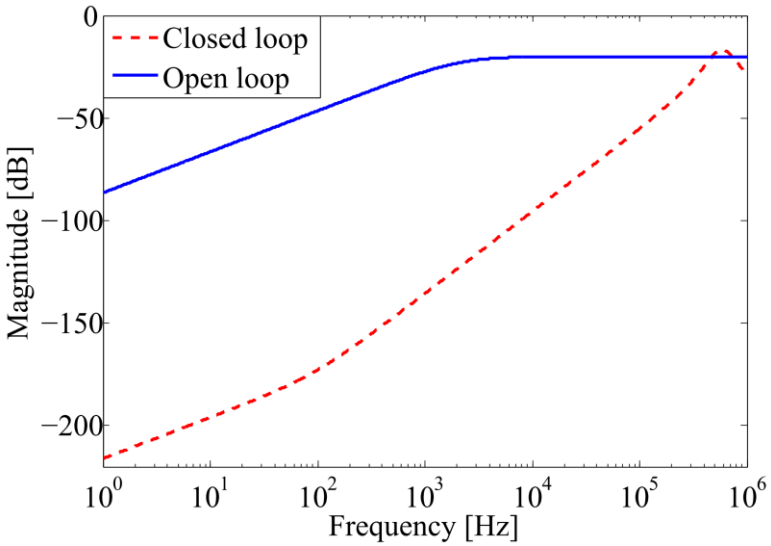



Figure 3.67: Attenuation of unwanted induced currents for $I_1(s)/V_2(s)$.

This analysis can also be expanded to a system with $N$ coils if we take (3.96) and (3.97) and add additional mutually coupled coils each with an individual control loop, which can be concisely represented in matrix form as seen in (3.100).

$$\begin{bmatrix} I_1(s) \\ \vdots \\ I_N(s) \end{bmatrix} = \begin{bmatrix} AG_1(s) & \cdots & 0 \\ \vdots & \ddots & \vdots \\ 0 & \cdots & AG_N(s) \end{bmatrix} \begin{bmatrix} V_{in1}(s) \\ \vdots \\ V_{inN}(s) \end{bmatrix} - s \begin{bmatrix} 0 & \cdots & M_{1N}G_1(s) \\ \vdots & \ddots & \vdots \\ M_{N1}G_N(s) & \cdots & 0 \end{bmatrix} \begin{bmatrix} I_1(s) \\ \vdots \\ I_N(s) \end{bmatrix} \tag{3.100}$$

This notation can be expressed in a more concise form given by (3.101) where $C(s)$ is the coupling matrix. With some matrix algebra, the overall current in each coil can be determined using (3.102) where **1** represents the identity matrix.

$$\mathbf{I}(s) = G(s)\mathbf{V}_{in}(s) - sC(s)\mathbf{I}(s) \tag{3.101}$$

$$\mathbf{I}(s) = (\mathbf{1} + sC(s))^{-1} G(s)\mathbf{V}_{in}(s) \tag{3.102}$$

Equations (3.101) and (3.102) can easily be solved numerically to give a frequency response of each resulting coil current and, hence, analyse the attenuation of the unwanted induced currents. Converting back to the time domain also allows for transient behaviour to be

predicted.

In order to examine the open loop behaviour, consider the output of an open loop voltage source on a coil mutually coupled to *N-1* other coils to be given by (3.103). This can be repeated for every other voltage source in a group resulting in (3.104), which can be simplified to a matrix arrangement given by (3.105). Solving this gives the resulting currents in each coil as (3.106).

$$V_1(s) = I_1(s)R_1 + L_1 sI_1(s) + M_{12} sI_2(s) \cdots M_{1N} sI_N(s) \tag{3.103}$$

$$\begin{bmatrix} V_1(s) \\ \vdots \\ V_N(s) \end{bmatrix} = \begin{bmatrix} sL_1 + R_1 & \cdots & sM_{1N} \\ \vdots & \ddots & \vdots \\ sM_{N1} & \cdots & sL_N + R_N \end{bmatrix} \begin{bmatrix} I_1(s) \\ \vdots \\ I_N(s) \end{bmatrix} \tag{3.104}$$

$$\mathbf{V}(s) = Z(s)\mathbf{I}(s) \tag{3.105}$$

$$\mathbf{I}(s) = Z^{-1}(s)\mathbf{V}(s) \tag{3.106}$$

Equivalently, each coil will carry a current given by (3.107) where $M_{ii} = 0$.

$$I_i(s) = \frac{V_i(s)}{L_i s + R_i} + \frac{s}{L_i s + R_i} \sum_{j=1}^{N} M_{ij} I_j(s) \tag{3.107}$$

### 3.10.5. Signal Generation

In order to generate the required sinusoid reference signal, a programmable function generator was required. For this, a digital synthesis method was used. Direct Digital Synthesis (DDS) is a digital method for generating arbitrary waveforms with high accuracy and stability [131]. For our system, the Analog Devices part AD9833 synthesiser IC was used. This IC generates sine, triangle and square waves up to 12.5 MHz and can easily be programmed using a microcontroller using a serial transmission protocol (SPI). $2^{28}$ different frequencies in this range are selectable; the phase can also be accurately controlled. The size of the frequency step depends on the reference clock where the lower the input clock frequency, the smaller the step between each possible frequency. The AD9833 is limited by the fact that its output amplitude is fixed and it only varies between 0 V and 0.6 V. Hence to obtain a useful signal, the output must be AC coupled to remove the DC offset, filtered to remove higher order harmonics and quantisation artefacts, and amplified or attenuated depending on the required amplitude of the signal. An Arduino Uno microcontroller is used to program each DDS IC to generate the desired set of sinusoids.

### 3.10.6. Current Driver Testing

To demonstrate the performance improvement from the addition of the passive compensation network, the output was measured for a 20 kHz sinusoidal input. Firstly the performance without the network was tested and is shown in Figure 3.68. We can clearly see excessive

ringing in the form of a high frequency oscillation superimposed on the desired output signal. Figure 3.69 shows the output with the addition of the compensation network. No ringing artefacts are visible on the output wave form. The input does not exactly match the output as there is a small DC offset present as is typical in op-amp amplifiers.

Figure 3.70 shows the turn-on time for the transmitter where the output tracks the input almost immediately after the input signal is applied. The response to step changes in amplitude is shown in Figure 3.71, response time is on the order of microseconds. The small signal frequency response was experimentally recorded and this is shown in Figure 3.72. A flat response is observed from approximately 50 Hz up to 100 kHz. Below 50 Hz we see noisy measurements as the system is AC coupled, hence at low frequencies only a very small signal feeds through the system. The output current capability at higher frequencies becomes limited as the input voltage is only limited to $\pm 15$ V and the impedance of the coil increases with frequency.

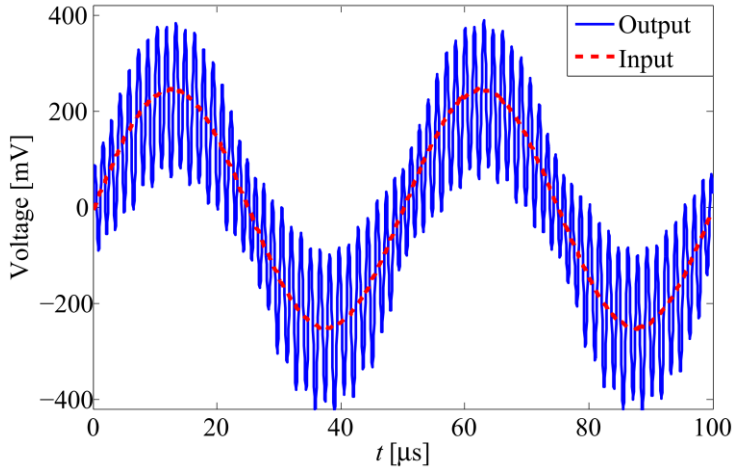



Figure 3.68: Uncompensated output for 20 kHz input signal. Excessive ringing results due to the small phase margin.

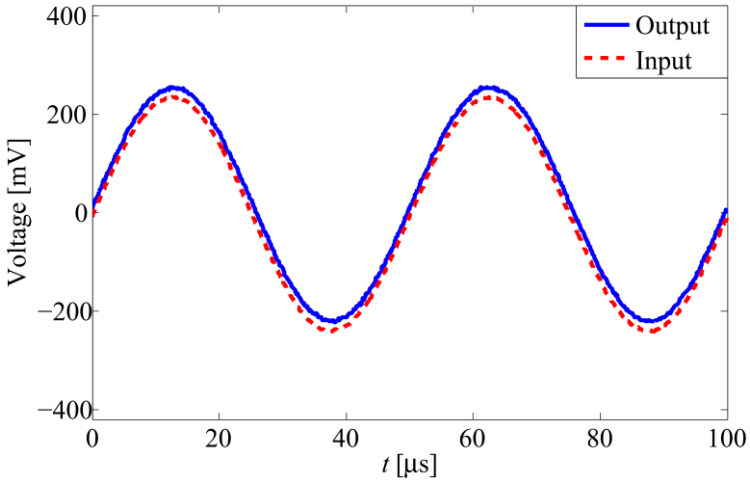



Figure 3.69: Compensated output for 20 kHz input signal. No ringing is observed on the output.

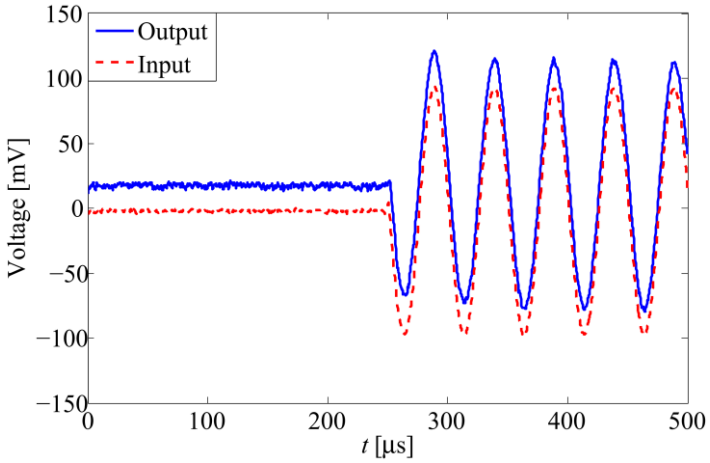



Figure 3.70: Turn on time for the closed loop system.

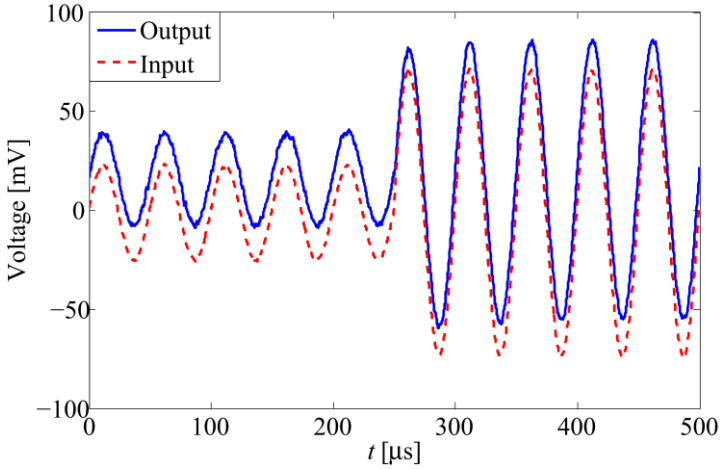



Figure 3.71: Closed loop response to step changes in amplitude.

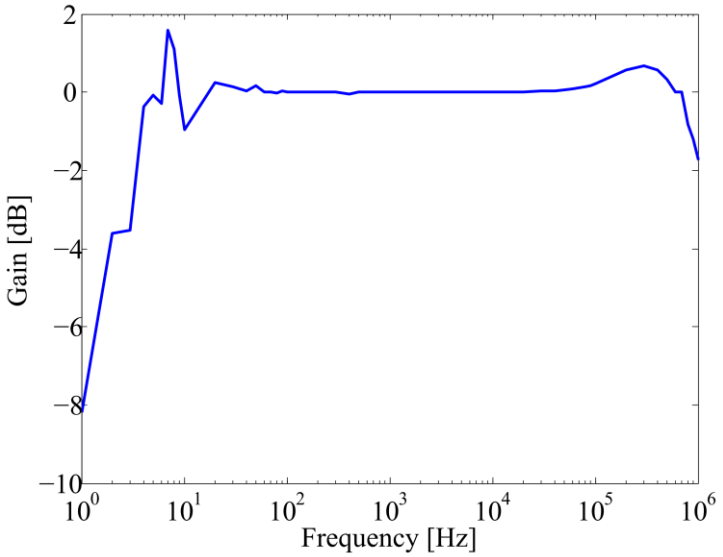



Figure 3.72: Experimental frequency response of the closed loop system measured using a Powertek GP-12 Gain-Phase Analyser.

### 3.10.7. Sensor Amplifier

Standard operational amplifiers are not suited to amplifying small sensor signals due to low

CMRR typically associated with normal inverting and non-inverting gain configuration amplifiers. Single op-amps in a differential amplifier configuration gives better results, but mismatch in the external resistors, even of the order of 0.1 % can result in relatively low CMRR. To overcome these limitations, dedicated small signal amplifiers called instrumentation amplifiers are often used.

An instrumentation amplifier (in-amp) is a closed-loop gain block that has a differential input and a single-ended output with respect to its reference terminal. Typically they have high input impedances (>1 GΩ) which are balanced to a high degree of precision. Low bias currents on the order of 1-50 nA are also normal. Unlike standard op amps, where the gain is set by external resistors between its output and inverting input, in-amps use internal resistor networks to set the gain, often with options to set the gain externally using a resistor, or programmed digitally with certain pin configurations.

Instrumentation amplifiers come in a variety of configurations, but the most common is a buffered difference amplifier circuit comprising 3 op-amps in a single chip although 2 op-amp configurations also exist. The differential input allows common mode noise to be rejected, hence allowing low level signals to be amplified reliably.

An INA128 Texas Instruments instrumentation amplifier with a gain of 500 was used to amplify the induced voltage on the sensor. An external 500 Ω resistor is used to set the overall gain of the amplifier. A schematic of the internal structure of the IC is shown in Figure 3.73. The frequency response of the amplifier is dependent on the selected gain, and the variation of frequency response due to different gain settings is shown in Figure 3.74. This amplifier was constructed on a separate PCB from the drive board to reduce interference. Figure 3.75 shows a basic schematic for the PCB. After the first stage instrumentation amplifier, an active high pass filer with a cut-off frequency of approximately 1 kHz is used to reduce low frequency noise from the 50 Hz mains. Figure 3.77 shows an experimental frequency response for the circuit including the filter where a flat response is seen from 1 kHz to 30 kHz. To further reduce noise pickup from the surroundings and the source coils, the amplifier circuit was placed in sealed steel box which was also grounded. This provided magnetic, as well as electrostatic, shielding to the amplifier. Figure 3.76 shows this circuit and its enclosure.

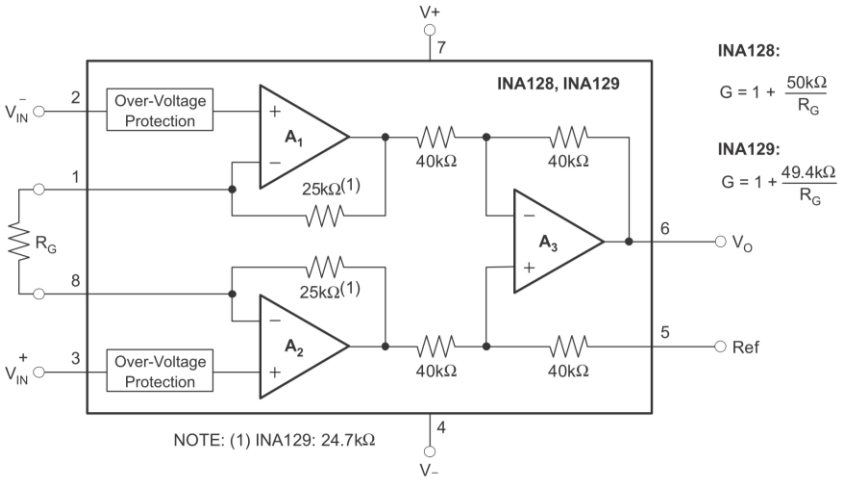



Figure 3.73: Internal structure of the INA128 instrumentation amplifier [132].

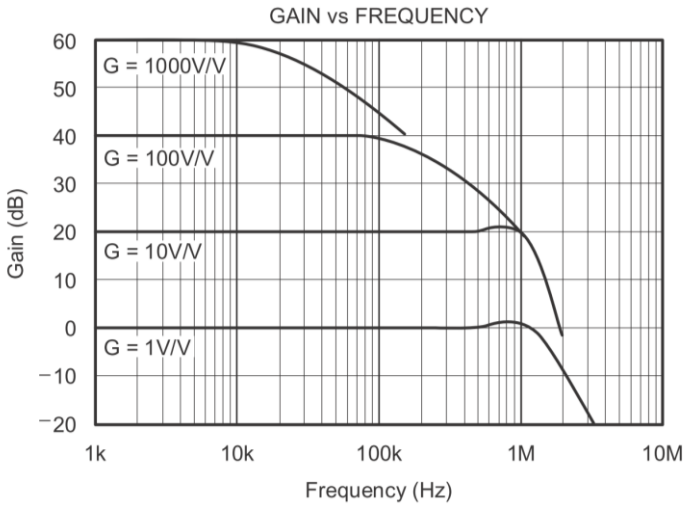



Figure 3.74: Frequency response of the INA128 [132].

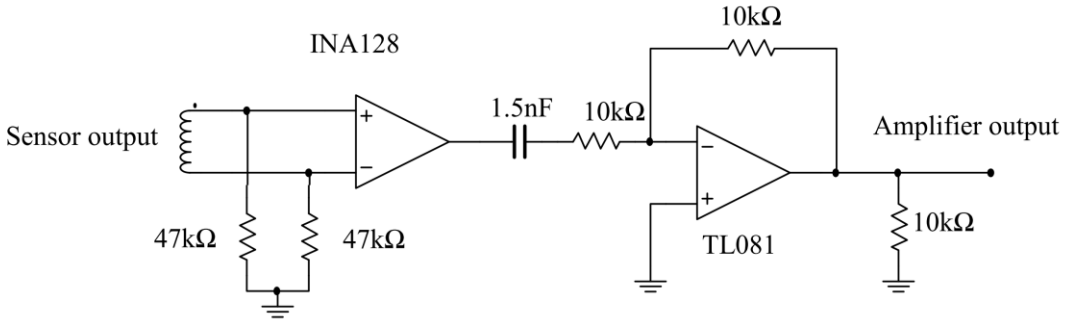



Figure 3.75: Basic schematic of the instrumentation amplifier circuit. The gain selector resistor is not shown in this figure.



Figure 3.76: Instrumentation amplifier used to detect the voltage induced in the search coil. The circuit is placed in a grounded steel container to shield the circuit from the magnetic field generated by the source coils. A gain of approximately 500 is used.

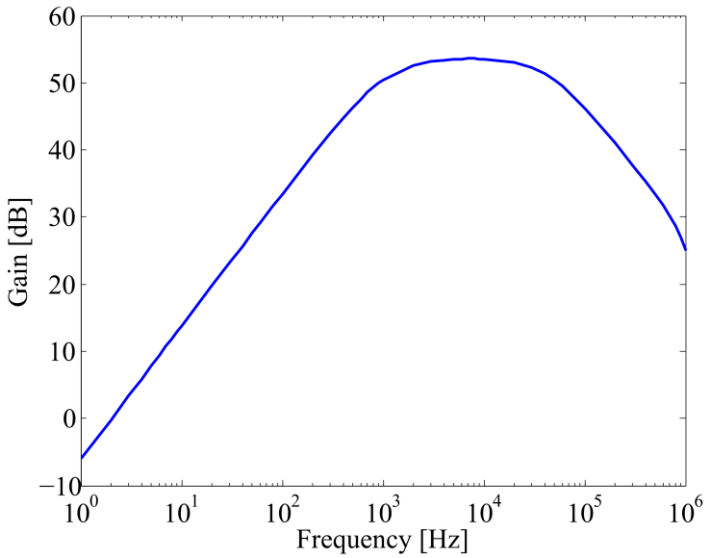



Figure 3.77: Experimental frequency response of instrumentation amplifier and filtering.

### 3.10.8. Cable Considerations

Appropriate cable shielding and associated grounding is an important consideration in the design of precision amplifier systems. In the absence of an external ground shield, noise can easily be capacitively coupled into a cable connecting the transducer or sensor to the amplifier. Having an external grounded conductor, allows these capacitive effects to be reduced by essentially creating a Faraday cage around the cable. However the benefit of this shield is only realised when the shield is grounded at one end of the cable. This is not a problem in this application as the sensor itself is not grounded. Inductive coupling is also a concern as the cables connecting the sensor to the amplifier system act as a magnetic field sensor.

Connections to the amplifier board are via a three input terminal block, since two floating inputs with an additional ground shield can easily be connected. Coaxial BNC connectors would be of little benefit, as typically, BNC connections are referenced to ground, and as a result only have two connectors. In order to use a BNC connector, triaxial cable would be required which is non-standard for this application, as for the majority of instrumentation connections, such as thermocouples, are made using twisted pairs or shielded twisted pairs. At relatively low frequencies (< 100 kHz) there is little benefit to using coaxial cables or similar, as twisted pairs have been proven to give similar performance [133].

Likewise, to reduce transmitted magnetic fields, shielded twisted pairs are used to connect the output of the transmitter driver board to the transmitter array. It was observed that unshielded cables transmitted a considerably larger magnetic field. Hence, to reduce systematic errors, every source of magnetic field distortion at the operating frequencies must be carefully considered.

To test the performance of different types of cable, a simple test measured the emitted magnetic field from different cables. A 1 m length of each cable was formed into a coil with 5 turns (with the same diameter). At the centre of this coil, a second detector coil with 200 turns was placed as seen in Figure 3.78. The cable under test was driven with 50 mA at 200 kHz. The resulting induced voltages are shown in Table 3.6.

| **Cable type** | **Induced voltage [V]** |
|---|---|
| Untwisted wire pair | 4.186 |
| Twisted pair | 2.861 |
| Shielded twisted pair (grounded shield) | 0.142 |
| Shielded twisted pair (ungrounded shield) | 3.443 |
| Coaxial cable (grounded) | 0.086 |
| Coaxial cable (ungrounded) | 3.264 |

Table 3.6: Comparison of cable shielding performance

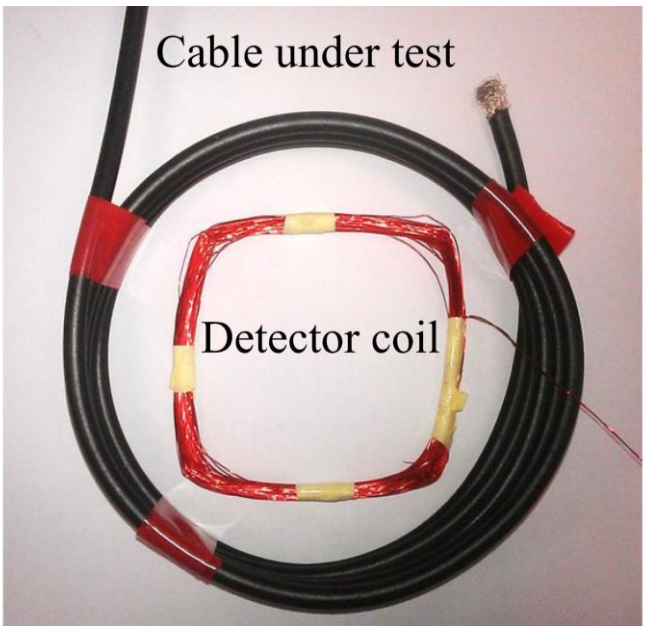



Figure 3.78: Test setup for measuring emitted magnetic field from a cable.

### 3.10.9. Current Waveform Summing Amplifier

In order to form a composite waveform of the current measurements from each sense resistor, an analog summing amplifier was constructed. A basic schematic of this circuit is given in Figure 3.79. The capacitors $C_{DC}$ block any DC component in the signal and the feedback capacitor $C_f$ forms a low pass filter to remove higher frequency noise. Figure 3.80 shows the constructed circuit. The advantage of this approach is that a single waveform may be sampled which contains all the information required to measure the currents and determine the phase information of the magnetic field signal.

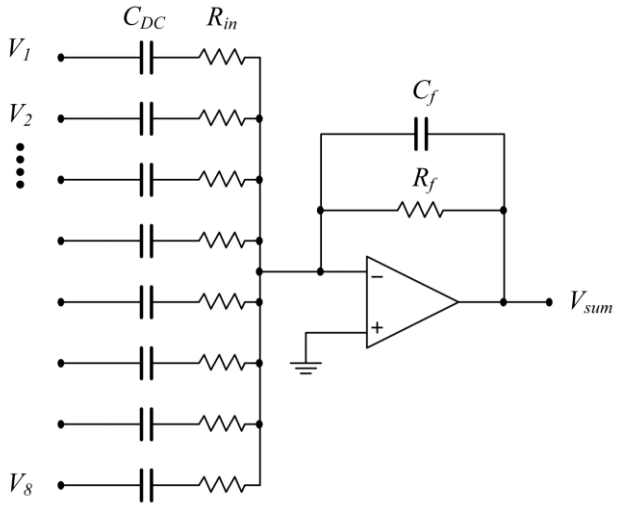



Figure 3.79: Summing amplifier schematic

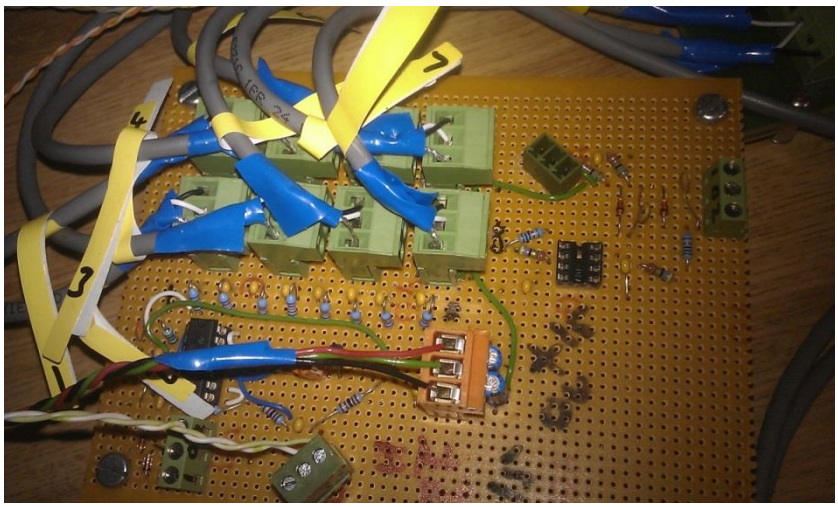


Figure 3.80: Summing amplifier constructed on Veroboard.

## 3.11. Simulink Demodulator Implementation

### 3.11.1. Overview

In order to develop the demodulation and filtering required to accurately extract the signal of interest from the sensor and its amplifier, Simulink (Mathworks Corp. Natick MA) was used. Simulink interfaces with a data acquisition (DAQ) PCI card which samples the output voltage of the sensor along with the current sense voltage for each coil. A synchronous demodulator is implemented in Simulink which extracts the amplitudes of the induced voltages and calculates their associated magnetic fields. The current in each coil is normalised and used as a reference for the demodulation. A delayed version of the waveform is also used as, for the full demodulation, both sine and cosine terms are required. The detected voltage is then scaled by an appropriate set of scaling factors that are determined by calibration of the sensor. To determine the appropriate polarity of the magnetic field, the sign of the calculated phase difference is used. The resulting magnetic field measurement is that detected by the sensor along its long axis. The Simulink output is the magnetic field measurements from each of the eight coils in the source array. Figure 3.1 shows a basic block diagram of the overall operation of the demodulator per channel.

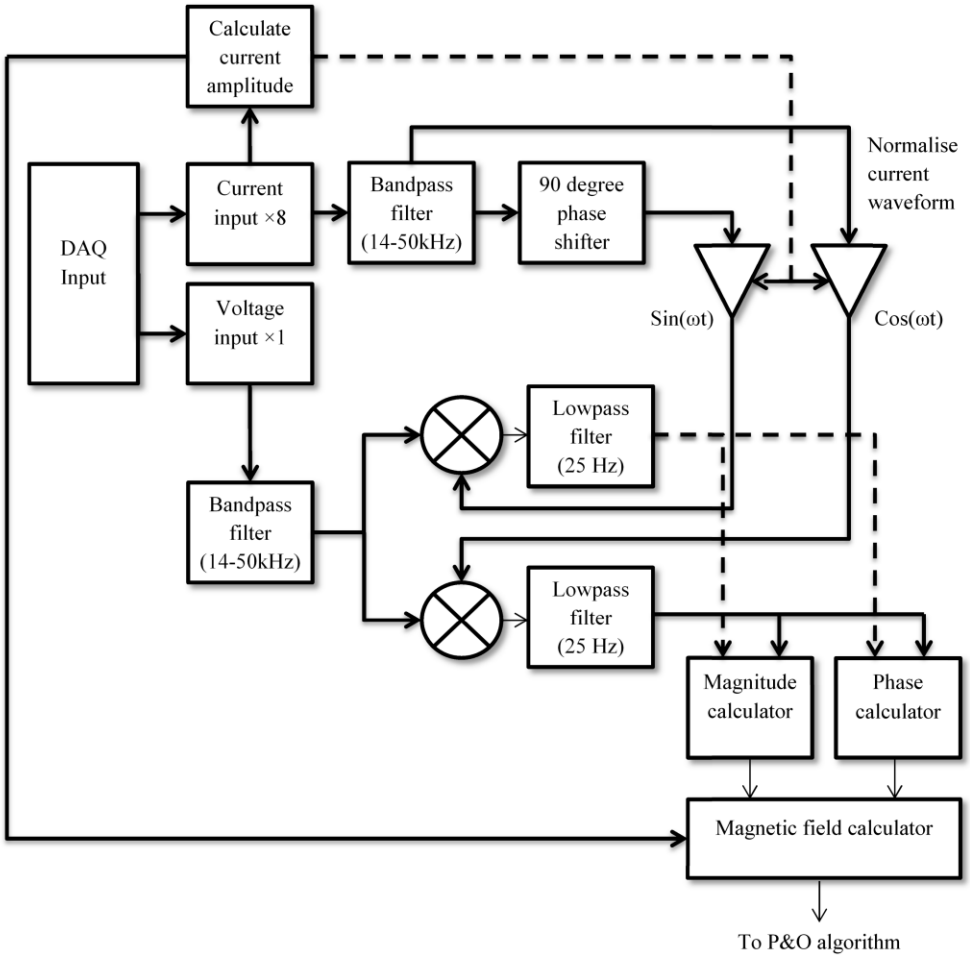



Figure 3.81: Simulink block diagram per channel.

### 3.11.2. Data Acquisition

For the development of the demodulation system and signal processing system, a National Instruments Data Acquisition (DAQ) PCI card was used. The NI PCI 6259 card used has 32 analog inputs with a maximum single channel sampling rate of 1.25 MS/s. However, when using more than one channel, this rate is reduced to a 1 MS/s, which is then divided by the number of channels in use to give the maximum permitted sampling rate. For this system, 9 inputs are required where each channel is then set to sample at 100 kHz. The resulting overall sample rate is 900 kHz. The analog bandwidth of the DAQ is approximately 1 MHz.

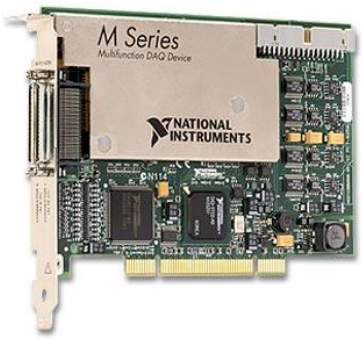



Figure 3.82: PCI 6259 DAQ card.

### 3.11.3. Phase Shifter

A simple method to generate quadrature demodulation references is to use a set of digital delays to shift the reference signal by the required phase lag thus generating it a cosine from the input sinusoid. Both fractional and integer delays can be used, but integer delays are typically more accurate. By choosing a suitable reference signal frequency, a small number of integer delays can be sufficient to generate the cosine term. (3.108) can be used to determine the *Z* delays required for a given input frequency and sampling rate.

$$\min_{N} \rightarrow Z = \frac{f_s}{f}\frac{(1+4N)}{4} \quad Z \in \mathbb{Z} \tag{3.108}$$

By finding the smallest integer *N* for which this expression results in an integer, the integer *Z* gives the minimum number of delays required that will generate the cosine. *N* represents the number of periods by which the waveform must elapse before waveforms arrive at the appropriate phase of 90 degrees. Table 3.7 shows the required number of integer delays required for the signal frequencies. The transmit frequencies were chosen to minimize the number of delays required. The value for *Z* varies depending on the choice of input frequency. The frequency value was chosen so that *Z* resulted as a relatively short number of delay samples. For a given sample rate there exists only a small subset of input frequencies that can be delayed by 90 degrees with integer delay times.

| *f* (Hz) | *N* Periods | *Z* Sample delays |
|---|---|---|
| 20500 | 10 | 50 |
| 21500 | 32 | 150 |
| 22500 | 2 | 10 |
| 23500 | 35 | 150 |
| 24500 | 12 | 50 |
| 25500 | 38 | 150 |
| 26500 | 13 | 50 |
| 27500 | 8 | 30 |

Table 3.7: Delays required to generate cosine reference signal.

### 3.11.4. S Functions

Complex systems in Simulink can often run quite slowly due to the large memory requirements and processing load. However, the run time can be dramatically reduced by making use of S-functions. An S function is a low level C code that can either be written manually or can be automatically compiled. User-made blocks in Simulink can easily be converted into S-functions. Improvements in run time can be more than a factor of a 100, depending on the complexity of the function. The use of S-functions, significantly increased the operation speed of our system due to the complexity of the demodulation process.

### 3.11.5. Filtering

Filtering is used in two stages of the demodulator and performs the following:

- Input DC offset and mains noise filtering
- Demodulator filtering after multiplication

All filters are digital 6$^{th}$ order IIR Butterworth filters. IIR filters were used as they are less computationally demanding than FIR filters, but extra care must be taken of stability due to the presence of poles in the transfer functions. Higher order filters are far more prone to instability

## 3.12. Undersampling for EM Tracking

In order to digitally recover a detected signal of interest, typically an ADC is used to sample the waveform at a rate higher than twice the highest frequency component, as determined by the Shannon-Nyquist sampling theorem [134]. However this theorem is often misunderstood, as it states that the sample rate should be higher than twice the bandwidth of the system, not twice the highest frequency component [135].

For our application, where the signals of interest are low frequency sinusoids with amplitude modulation, undersampling shifts the frequencies without changing the amplitude information. With appropriate choice of sample rate and carrier frequencies, a very low sample rate can be used. This gives more time for calculations on every iteration of the sampler, which allows for demodulation schemes to run on the fly without need for recording long data sets for post processing. This allows the use of low cost ADCs and microcontrollers to demodulate the signals of interest. This undersampling method is often called super-Nyquist sampling [136]. The method was used in Phase 2 of our system (see Section 3.5).

Consider a sinusoidal signal with a frequency of $f$, which is sampled at $f_s$. The apparent frequency of the signal is given by $f_a$. When the sample rate is more than twice the input frequency, the apparent frequency is simply $f_a = f$ as expected. However if the input frequency is greater than $f_s / 2$ but less than $f_s$, the resulting frequency is $f_a = f - f_s$ . In other words, the apparent frequency starts to reduce as the input frequency increases.

To fully understand this process, we must consider the general case where the input frequency, $f$, is greater than $m$ times the sample rate, where $m \in \mathbb{N}$. In general the apparent frequency is given by [137]:

$$f_a = \pm \left| f - m f_s \right| \qquad -f_s / 2 \le f_a \le f_s / 2 \tag{3.109}$$

Higher frequencies are effectively folded back into the spectrum between $\pm f_s / 2$, but the amplitudes remain unaffected. .This effect is demonstrated in Figure 3.83. Undersampling also introduces a change in the sign of the waveform phase:

$$\varphi_a = \varphi \text{sgn}(f - mf_s) \tag{3.110}$$

where $\varphi_a$ is the apparent phase of the waveform [137], sgn is the sign function and $\varphi$ is the phase of the input waveform. The upper frequency range of undersampling is limited by the analog bandwidth of the ADC used.

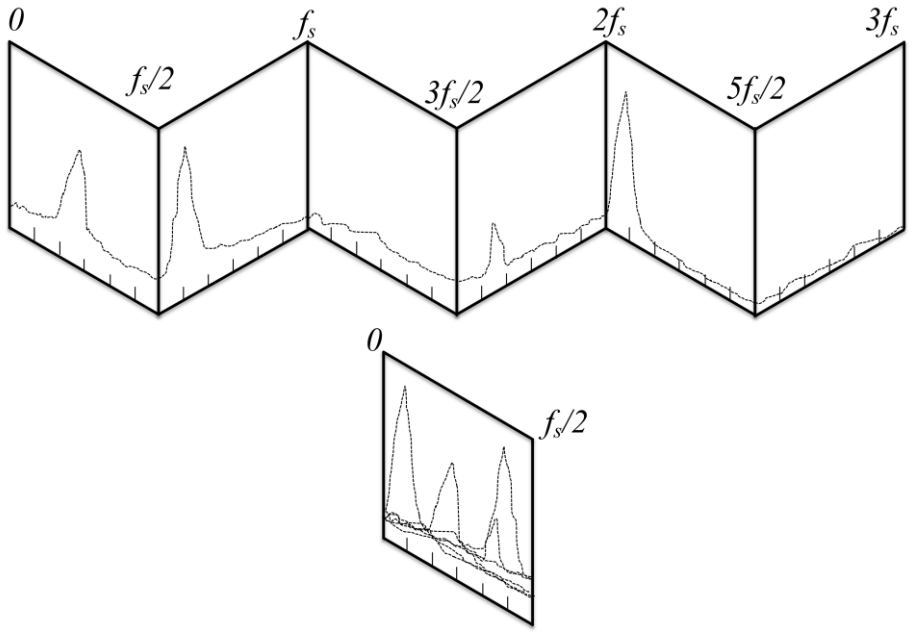



Figure 3.83: Effects of undersampling. Frequencies above $f_s/2$ are shifted to frequencies in the range of 0 to $f_s/2$. It is as if the input frequency spectrum is folded back upon itself as shown [138].

Figure 3.84 shows the effect of different sampling rates on a 1 kHz sine wave. When the signal is undersampled, we see that its apparent frequency is reduced to 200 Hz but its amplitude remains the same. Figure 3.85 shows a simulated spectrum of 8 different frequencies ranging from 20.25 kHz to 27.25 kHz in steps of 1 kHz. We see here that all these frequencies have been mapped to between 0 and 4 kHz when sampled at 8 kHz. The order of the components has also been changed. Figure 3.86 shows the spectrum after multiplication by a reference signal at 20.25 kHz. From these results it is clear that undersampling changes the apparent frequency of a signal, but its amplitude remains unchanged. Care must be taken however to ensure that unwanted aliasing of frequency components of significant amplitude which can be accomplished with appropriate filtering. Hence, sampling at beyond the Nyquist frequency is not required to accurately measure the amplitude of a sinusoid signal.

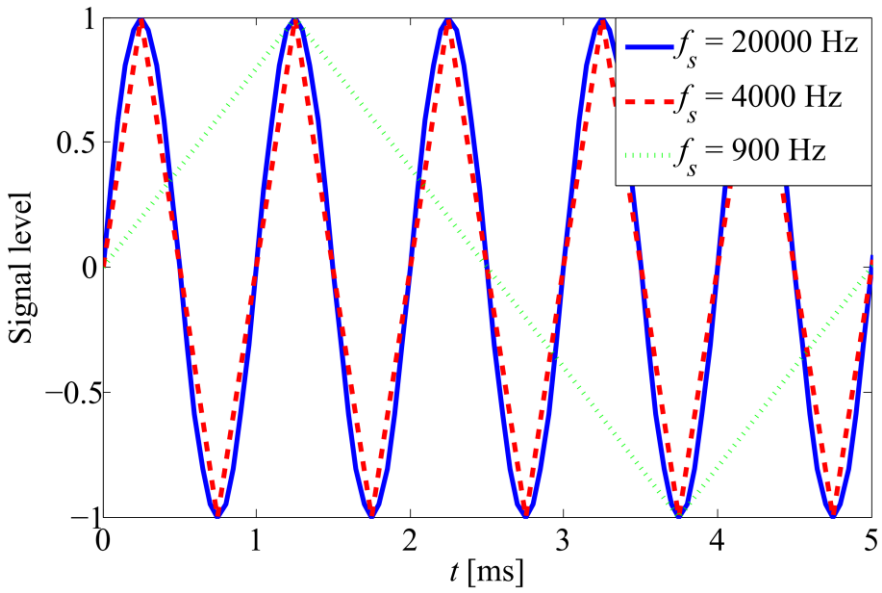



Figure 3.84: A 1 kHz sine wave sampled at 20 kHz, 4 kHz and 800 Hz. When undersampled, the apparent frequency reduces to 200 Hz.

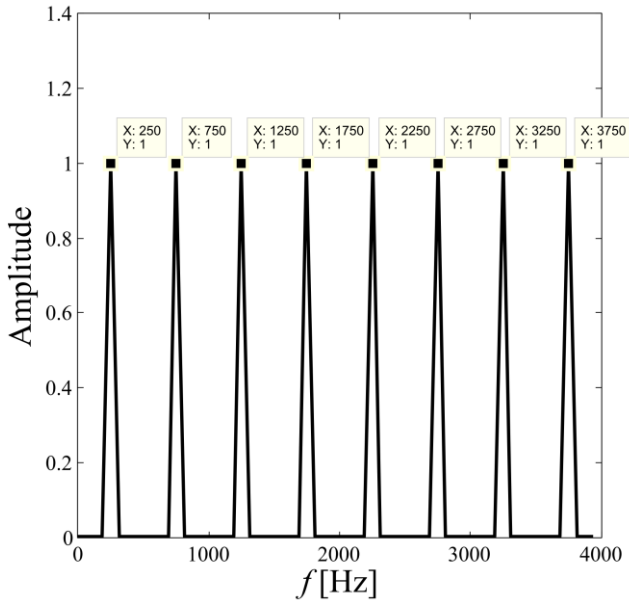



Figure 3.85: Simulated undersampled frequency spectrum. An 8 kHz sample rate is used to sample a multi-frequency signal with components at 20.25, 21.25 …. 27.25 kHz

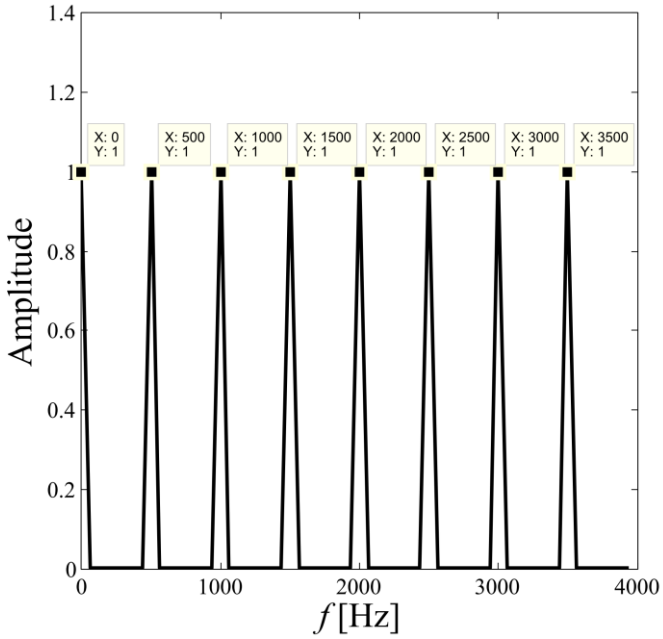



Figure 3.86: Sample signal multiplied by a carrier at 20.25 kHz, all frequencies are again shifted.

## 3.13. Microcontroller Implementation of the Demodulator

### 3.13.1. Arduino Due

A low cost microcontroller was chosen to sample and demodulate the signals. An Arduino Due (Arduino, Ivrea, Italy) development board was used to implement the software for the demodulation scheme. This board uses a 32-bit ARM Cortex M3 processor running at 84 MHz, with 96 kB of SRAM. The processor does not support floating point numbers; hence all calculations were carried out with fixed-point numbers to optimise speed. The Arduino Due board costs $ 54, but the ARM Cortex M3 processor on the board costs less than $ 13. Figure 3.87

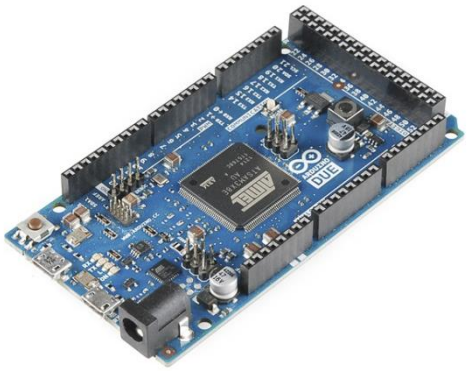


Figure 3.87: Arduino Due microcontroller [139].

### 3.13.2. Demodulator Implementation

Figure 3.88 shows a block diagram of the demodulator operation. The input waveforms are sampled by an external ADC where $V_B$ and $V_I$ denote the sensor voltage and current measurement voltage respectively. These samples are, in turn, multiplied by the reference

signal which is stored in two look up tables (LUTs) for the sine and cosine terms. These multiplied signals are then filtered to yield the quadrature components. When the overall period, *N*, of the reference signals is reached, the LUT resets to its initial position. From the filtered output, the magnitude and the phase of the magnetic field components are calculated. The demodulator requires approximately 40 μs to complete each loop of the code. LUTs were used to minimise computation during the loop. It was found experimentally that LUTs gave faster computation time than direct calculation of each sine and cosine component.

To reduce the length of the LUTs, the carrier frequencies of the emitters are chosen so that when sampled, the overall period of the entire waveform was less than 100 samples. The 8 carrier frequencies used were: 20.25 kHz, 21.25 kHz, 22.25 kHz, 23.25 kHz, 24.25 kHz, 25.25 kHz, 26.25 kHz and 27.25 kHz. When sampled at 8 kHz, the composite waveform has a period of 32 samples. Hence, after 32 samples all the frequencies reset to their starting positions, which results in 16 LUTs (8 for cosine and 8 for sine terms) with 32 points in each.

The choice of carrier frequency was also influenced by the undersampling requirement. The carrier frequencies, sample rate and the size of the frequency step were chosen to ensure that aliased signals do not overlap, and to maximize the separation of the frequencies after aliasing. The higher the separation of the frequencies, the lower the filtering requirements.

In terms of memory usage on the microcontroller, the code itself amounted to 42 kB, while the SRAM usage was estimated at between 3 and 4 kB. Overall a very small amount of the on-board memory was in use. The use of simulated reference signal approximately doubled the SRAM usage and increased the computation cost compared to sampling each signal individually. However, the overall microcontroller usage is still relatively low, which mitigates against an expensive microcontroller although higher processor speeds may be advantageous.

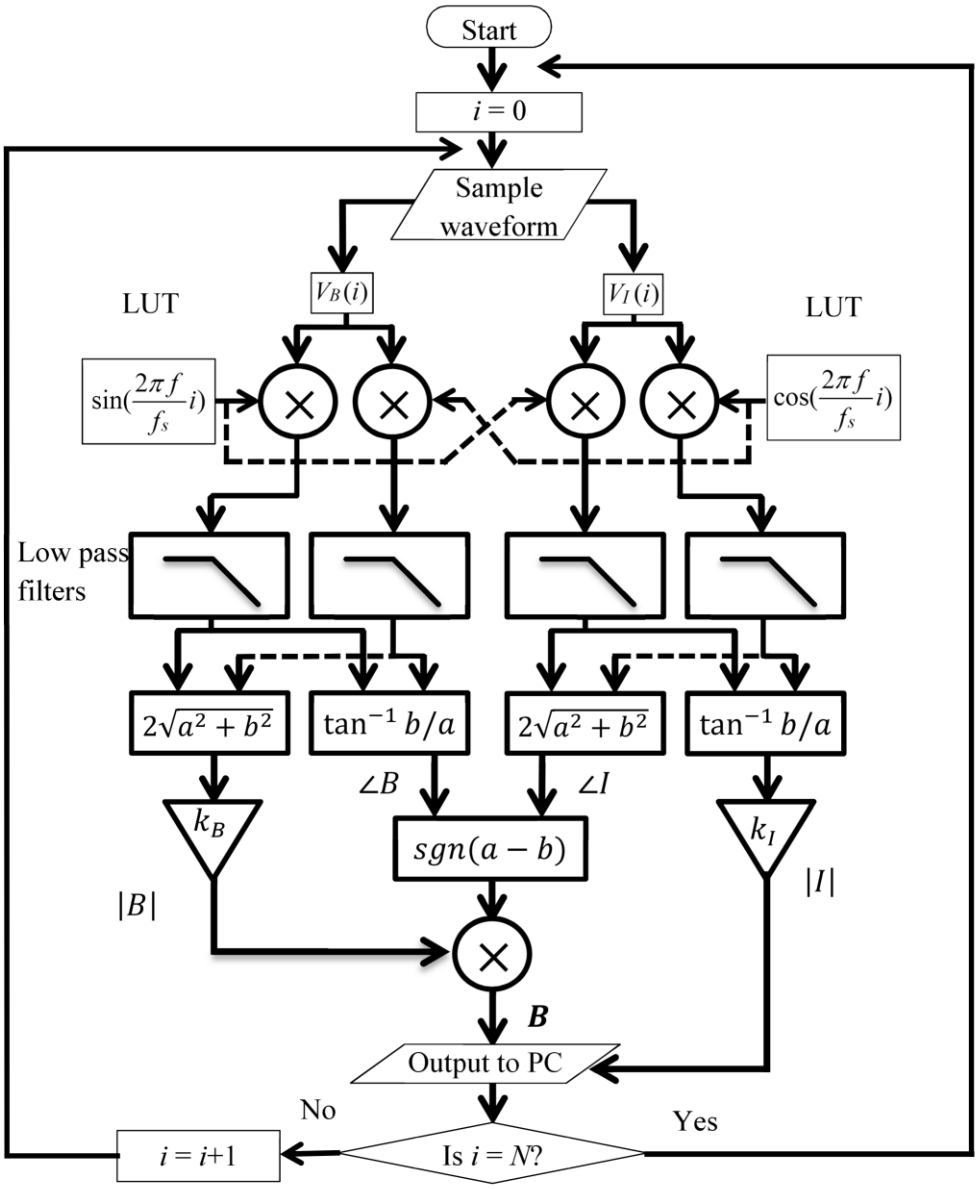



Figure 3.88: Block diagram of the Arduino Due demodulator software.

### 3.13.3. ADC and Analog Front-end

To ensure accuracy at lower signal levels a high resolution ADC was required. For this purpose a TI ADS8328 (Texas Instruments, Dallas, Texas) two channel 16-bit ADC was used. This ADC was chosen as it provided a sufficiently high sample rate, resolution and precision at a reasonable cost (€ 5) as well having an SPI interface allowing for simple data transfer. The SAR topology of this ADC is known to give high accuracy with moderate sample rates as well as good linearity. The analog bandwidth is 500 kHz with a sampling time of 2 µs. The TI ADS8328 is unipolar, and only accepts voltages in the range of 0 V to 4.096 V. Hence the max amplitude of an AC signal is then 2.048 V. An analog front-end circuit was implemented which amplified and added a DC bias to the sensor output signal for the ADC. A further aspect of the front-end is that a programmable attenuator, an LMP7312 by Texas Instruments, is used which scales the input depending on the size of the signal. If the signal strength is larger than the ADC can accommodate, the signal amplitude is reduced.

The signal amplitude of each frequency component is typically between 100 μV and 10 V. The individual current waveforms are also summed together using a standard inverting op-amp summing circuit. Figure 3.89 shows a representation of this entire front-end system.

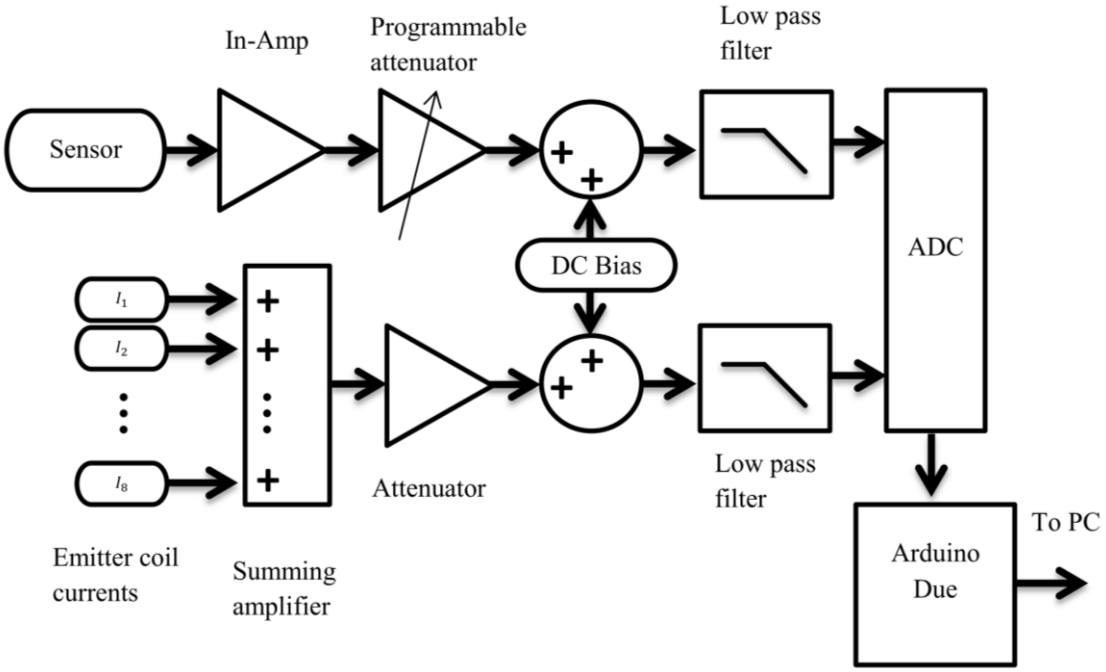
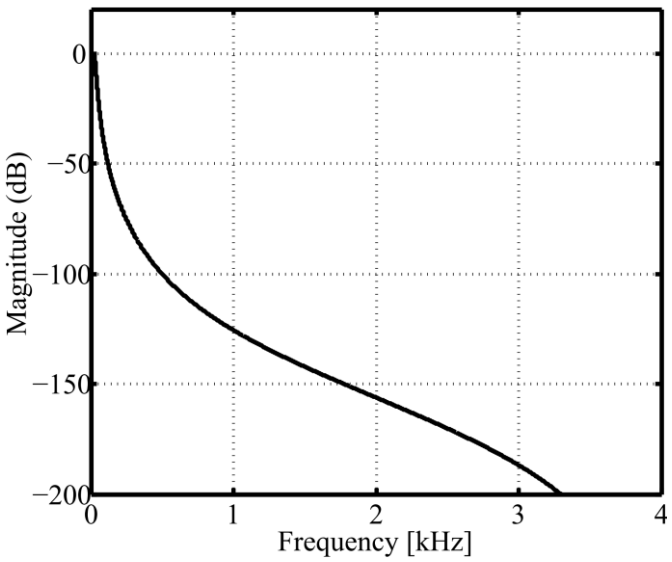



Figure 3.89: Block diagram for the analog front-end circuit.

### 3.13.4. Filtering

A 4th order digital IIR filter is used on each channel to extract the amplitudes of the quadrature components. IIR filters are more appropriate here than FIR filters as they are less computationally intensive. A total of 32 independent filters are used, 2 filters per channel with 8 channels for the sensor voltage and 8 channels for each current component. The 100 dB stop-band of the filter is set to 500 Hz, or $0.0625 f_S$, with a pass band of 20 Hz or $0.0025 f_S$. This stopband was chosen such that after undersampling, each frequency component in the spectrum is spaced by 500 Hz, and hence this filter effectively removes all other frequencies from each demodulator channel. The narrower the passband, the better the noise rejection at the cost of a longer settling time. The filter settling time is approximately 500 samples, or 62 ms.




### 3.13.5. PC Interface

The output of the demodulator is communicated from the Arduino to a desktop PC using a USB interface. The MATLAB Optimisation Toolbox is used to calculate the position and orientation of the sensor. The overall update rate of the position and orientation is around 10 Hz as the tracking algorithm adds between 20 and 30 ms depending on the proximity to the emitter. Faster convergence is observed closer to the emitter.

# Chapter 4
# EM Tracking: Testing and Results[§]

## 4.1. Overview

In this chapter we explore the extensive testing that was carried out on the EM tracking system to verify its performance and accuracy. The testing methodology used is described in detail and the results are discussed. Two methods are used to verify the system's accuracy, (i) by statically positioning the sensor in rigid positions and (ii) a "scribble" based approach where hundreds of test points are gathered in a short period of time on a 2D plane. The testing described here encompasses both Phase 1 and Phase 2 of the system, the primary difference between both setups being the ADC and demodulation subsystems.

A novel calibration algorithm is also presented which is used to minimise errors in the magnetic field models of the transmitter. Magnetic field measurements are presented which verify the accuracy of the field models used after calibration. Additionally, a detailed analysis of the effect of the P&O algorithm parameters is presented, including the function and step size tolerances and the initial estimate of the sensors position. Finally, the level and impact of noise on the system accuracy, as well the dynamic performance and update rate are also presented.

The key results are summarised below:

- A tracking accuracy in the range of 1-1.5 mm.
- An efficient calibration algorithm that rapidly calculates scaling parameters to minimise magnetic field errors.
- Undersampling system error of less than 2 mm with a reduced cost implementation.
- Excellent stability and cross-coupling performance of the AC current driver.
- Verification of the accuracy of the magnetic field models.
- Detailed analysis of the P&O algorithm parameters.

[§] This chapter is based on K. O'Donoghue, D. Eustace, J. Griffiths, M. O'Shea, T. Power and P. Cantillon-Murphy, "Catheter position tracking system using planar magnetics and closed loop current control,", *IEEE Transactions on Magnetics*, 50(7), 1-9, July 2014 and K. O'Donoghue and P. Cantillon-Murphy, "Low cost super-Nyquist asynchronous demodulation for use in EM tracking systems", *IEEE Transactions on Instrumentation and Measurement*, doi: 10.1109/TIM.2014.2343431, Aug 2014.

## 4.2. Tracking Accuracy Experimental Setup

Here we describe the setups used to verify the system accuracy and to generally gather test points used in the analysis and procedures in the following sections.

### 4.2.1. Static Test Setup

To test the operation and accuracy of the system, the sensor was moved around a fixed grid comprising of Lego Duplo blocks. The rigidness and high tolerance manufacture of the Duplo blocks made them ideal for accurately positioning the sensor. The sensors themselves were mounted in the centre of a block in two separate orientations, horizontal or vertical. The vertical orientation tested the accuracy in the *z* direction, while the horizontal was used to test the *x* and *y* accuracy, as the sensor could easily be rotated by 90 degrees by turning the block. These holders are shown in Figure 4.1. Each block was determined to be 31.75 ± 0.02 mm square and 19.2 ± 0.01 mm in height; Figure 4.2 shows the dimensions of one such block. A Duplo baseplate was fixed over a board on which the transmitter coils were mounted. A large array of test points can be gathered by systematically moving the sensor block around a fixed grid of test points. The actual position of the sensor can then be determined by counting the number of blocks moved each time. Figure 4.3 shows the Duplo blocks and the base plate used in the tests. Figure 4.5 shows a side-view of this setup showing how the Duplo board was mounted directly over the coil array. A standard Duplo baseplate was used which measures 38.1 cm × 38.1 cm. This was mounted onto the frame that holds each of the coils in position. Figure 4.4 shows the coordinate system used for all testing.



(a) (b)

Figure 4.1: (a) Vertical sensor holder, (b) horizontal sensor holder.

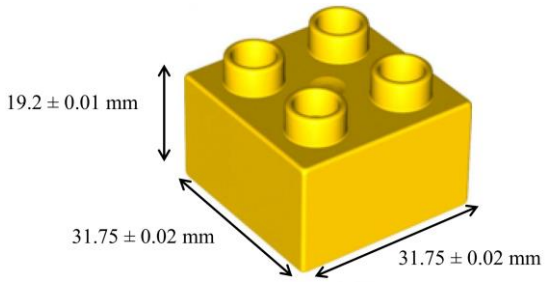



Figure 4.2: Duplo block dimensions.

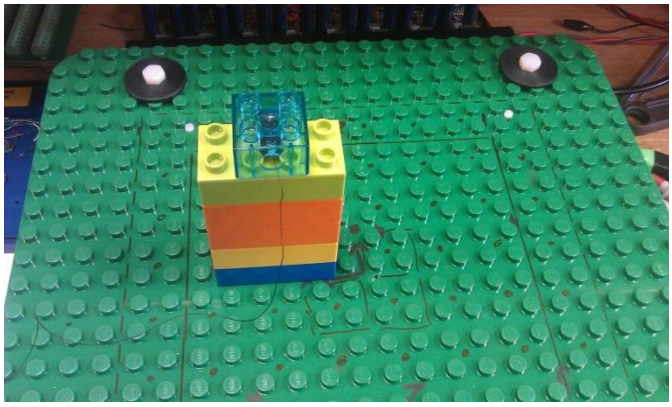


Figure 4.3: Test setup for static position accuracy tests. The sensor was placed at the centre of a Lego Duplo block and moved in discrete steps around the base plate which was mounted directly over the coil array. The testing was carried out in a volume approximately 25 cm × 25 cm × 25 cm .

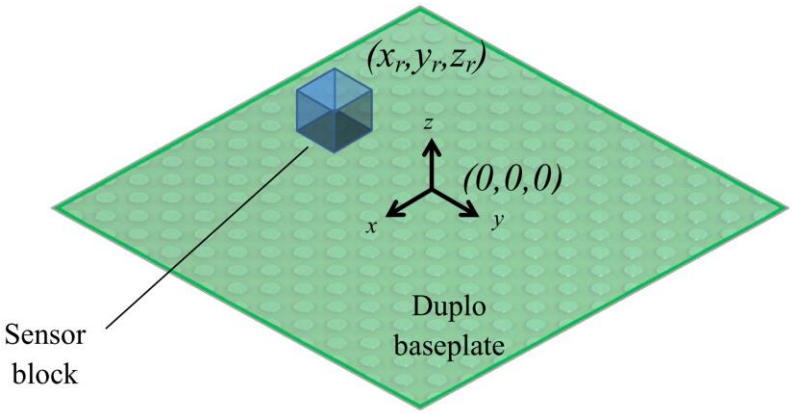



Figure 4.4: Coordinate system for the test setup.

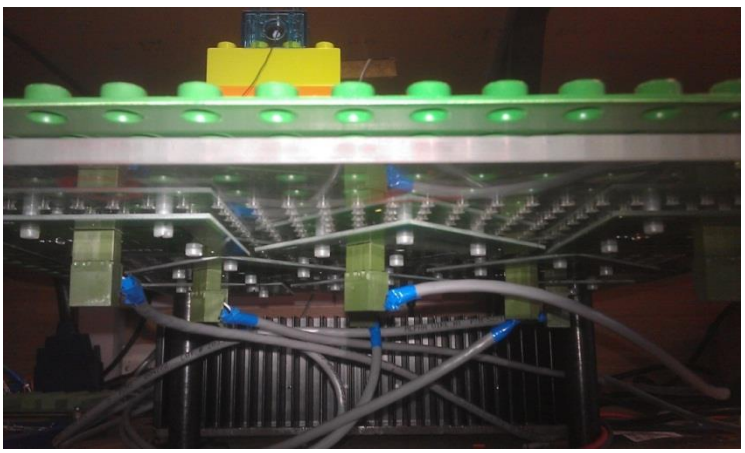


Figure 4.5: Duplo board mounted over the coil array.

### 4.2.2. Scribble Test Setup

A second method to verify the accuracy of the system was based on work at GE Healthcare [13]. In that paper, a methodology is described to verify the accuracy of position tracking systems based only on errors in a single direction away from a horizontal plane. The method involves moving a sensor around on a fixed 2D plane in a "scribble" motion and collecting numerous data points. The distance error between the predicted plane and calculated plane is then calculated. The advantage of this test is that numerous test points can be gathered quickly and examined to give a statistically valid representation of the system's accuracy.

In our system, an *xy* plane was used and hence the *z* error of each point was calculated. A smooth Perspex sheet was used as the plane, and 6 Duplo blocks were mounted on the plane so that it could be elevated above the coil array accurately. On each plane, 6 different approximate sensor orientations was tested, $+x$, $-x$, $+y$, $-y$, $+z$ and $-z$. An *xy* area of approximately 20 cm × 20 cm was used on each *z* plane. 500 points were recorded in each test and each test point was recorded in 1 second intervals. Figure 4.6 shows a picture of the scribble test in action and Figure 4.7 shows a schematic representation of the test.

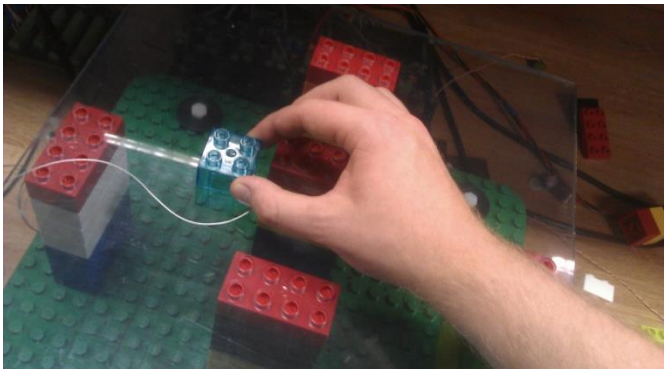


Figure 4.6: Test setup for scribble test. The sensor is placed in the Duplo block and "scribbled" around a Perspex plane by hand and its position is calculated and recorded. The *z* error from the plane is then calculated. Four different orientations of the sensor were tested per plane.

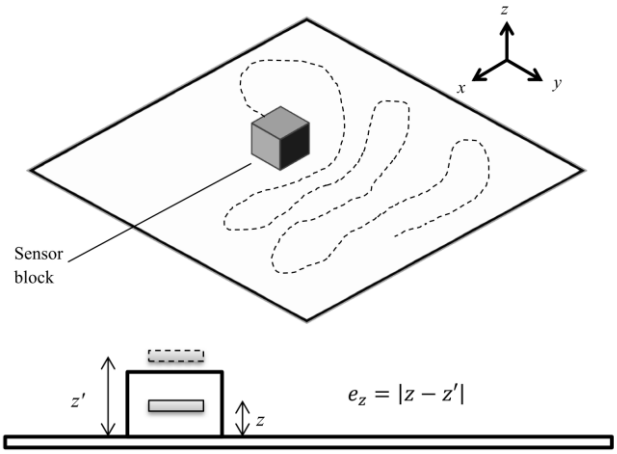



Figure 4.7: Representation of the scribble tests. The sensor is moved at random over a 2D plane. The error is the difference between the actual *z* position of the plane and the calculated value *z'*. This allows for rapid sampling of thousands of points to arrive at a statistically valid representation of the system performance.

### 4.2.3. Error Calculation

The position error between the real sensor location $(x_r, y_r, z_r)$, as measured from the Lego Duplo blocks, and the calculated position $(x_c, y_c, z_c)$ was determined at each test point using (4.1). The orientation error between the actual orientation $(\theta_r, \varphi_r)$ and the calculated orientation $(\theta_c, \varphi_c)$ was similarly calculated using (4.2) [73].

$$e_p = \sqrt{(x_c - x_r)^2 + (y_c - y_r)^2 + (z_c - z_r)^2} \tag{4.1}$$

$$e_o = |\theta_c - \theta_r| + |\varphi_c - \varphi_r| \tag{4.2}$$

The distance from the centre of the coil array is calculated with (4.3).

$$r = \sqrt{x_r^{\,2} + y_r^{\,2} + z_r^{\,2}} \tag{4.3}$$

For the scribble tests, the error away from the plane was calculated with (4.4).

$$e_z = |z_r - z_c| \tag{4.4}$$

All the position and orientation results that are calculated are rounded to the nearest 100 µm and 0.1° respectively as accuracy beyond these significant figures cannot be substantiated.

## 4.3. Calibration Methods

### 4.3.1. Overview

In this section we detail a novel calibration algorithm that uses a nonlinear least squares approach to minimise the error between magnetic field measurements and the numerical model. This calibration is required when a new sensor is being used, as the sensitivity parameters vary slightly from one sensor to another. Other sources of error that can be mitigated using this method are small parameter drifts associated with temperature changes and aging of components that, in particular, affect the sensor amplifier gain, passive and active filtering performance, the amplifier reference signal and its associated control loop.
Initially, the expected sensitivity of the system between the input current and the resulting voltage measurement is first estimated mathematically. Secondly, the gain of the amplifier is measured using the Helmholtz calibrator (see Chapter 3). This results in an overall sensitivity error on the order of 5 %. Our calibration algorithm is then used to further minimise this error.

### 4.3.2. Calibration Algorithm

The first step of the algorithm is to gather a number of test points in the region around each coil. By comparing these test points with the corresponding simulated magnetic fields, an

error function results. By scaling the simulated magnetic fields by a constant, the error between the measurement and the model can be minimised. Each coil in the array is calibrated individually.

If we consider the flux measurements at *m* test points from the $i^{th}$ coil to be represented by $\Phi^i_{meas}$, and the associated predicted flux at this point to be given by $\Phi^i_{calc}$, an objective function given by (4.5) results. In this equation, $\kappa_i$ represents a variable scaling factor that is varied to minimise the error function, $F_i$. As with the P&O algorithm, this can be easily solved using non-linear least squares methods. An initial estimate of $\kappa_i = 1$ is used.

$$F_i(\kappa_i) = \sum_{j=1}^{m} \left( \Phi^i_{meas}(x_j, y_j, z_j, \phi_j, \theta_j) - \kappa_i \Phi^i_{calc}(x_j, y_j, z_j, \phi_j, \theta_j) \right)^2 \tag{4.5}$$

To account for systematic offsets of the sensor's position, a position offset vector given by $\boldsymbol{r}_i^{offset}$ is introduced into the minimisation algorithm. The main need for this vector is that often the exact sensor location inside the holding fixture is difficult to accurately predict, and generally an axial offset of 1-2 mm is present. For the calibration tests, the sensor is positioned along the *x*, *y*, or *z* axis (in the coordinate frame of the transmitter array). As result, depending on the orientation of the sensor, only a single offset term is required, *i.e.* $x_i^{offset}$, $y_i^{offset}$, or $z_i^{offset}$. It was found that with the scaling parameters and 3 position offsets that the algorithm had too many degrees of freedom and would often result in an invalid scaling factor. However with two variables, the algorithm works well and minimises quickly. Equation (4.6) gives the updated objective function with the offset term where (4.7) concisely represents the displacement vector.

$$F_i(\kappa_i, \boldsymbol{r}_i^{offset}) = \sum_{j=1}^{m} \left( \Phi^i_{meas}(\boldsymbol{r}_j - \boldsymbol{r}_i^{offset}, \phi_j, \theta_j) - \kappa_i \Phi^i_{calc}(\boldsymbol{r}_j, \phi_j, \theta_j) \right)^2 \tag{4.6}$$

$$\boldsymbol{r}_j = (x_j, y_j, z_j) \tag{4.7}$$

The algorithm generally works well, although the objective function is biased towards test points closer to the source. This is because the flux measurements are generally larger close to the source, hence the associated errors are also larger. In a summation of the error residuals, points closer to the source have a much greater effect on the overall objective function. To mitigate this effect, each error contribution can be weighted to even out the size of each contribution. This weighted objective function is given by (4.8) where $w_j$ is the weighting factor. The choice of weighting function is described in the following section.

$$F_i(\kappa_i, \boldsymbol{r}_i^{offset}) = \sum_{j=1}^{m} w_j \left( \Phi^i_{meas}(\boldsymbol{r}_j - \boldsymbol{r}_i^{offset}, \phi_j, \theta_j) - \kappa_i \Phi^i_{calc}(\boldsymbol{r}_j, \phi_j, \theta_j) \right)^2 \tag{4.8}$$

### 4.3.3. Weighting Functions

Weighting factors can be added to the objective function to counteract the nonlinear nature of magnetic fields. A very basic approach is to weight each test point with increasing

distance from the source, as is given by (4.9). Generally magnetic field distributions are inversely proportional to the either the square or cube of the distance, depending on the proximity to the source (at larger distances, the dipole approximation dominates which is a cubic function of distance). Hence by weighting with the square or cube of the distance, one can approximately counteract the field distribution, and this is calculated using either (4.10) or (4.11).

$$w_j = \left|\boldsymbol{r}_j\right| \tag{4.9}$$

$$w_j = \left|\boldsymbol{r}_j\right|^2 \tag{4.10}$$

$$w_j = \left|\boldsymbol{r}_j\right|^3 \tag{4.11}$$

A more complex method is to directly cancel the magnetic field distribution at each test point. Using this method, two approaches were used; either by weighting using an inverse flux function or an inverse magnetic field strength formulation given by (4.12) and (4.13) respectively.

$$w_j = \frac{1}{\Phi^i_{calc}(\boldsymbol{r}_j, \phi_j, \theta_j)} \tag{4.12}$$

$$w_j = \frac{1}{\left|\boldsymbol{B}^i_{calc}(\boldsymbol{r}_j)\right|} \tag{4.13}$$

### 4.3.4. Calibration Example

To test the calibration algorithm and its performance, the field resulting from a single coil was examined. Ten test points are taken from an off-axis line perpendicular to the coil. The results were first calibrated without using a weighting function. The results of this are shown in Figure 4.8. The mean error is calculated here as 0.78 %. While this is a close match with the experiment, higher accuracy can be achieved using the weighting functions as will be seen.

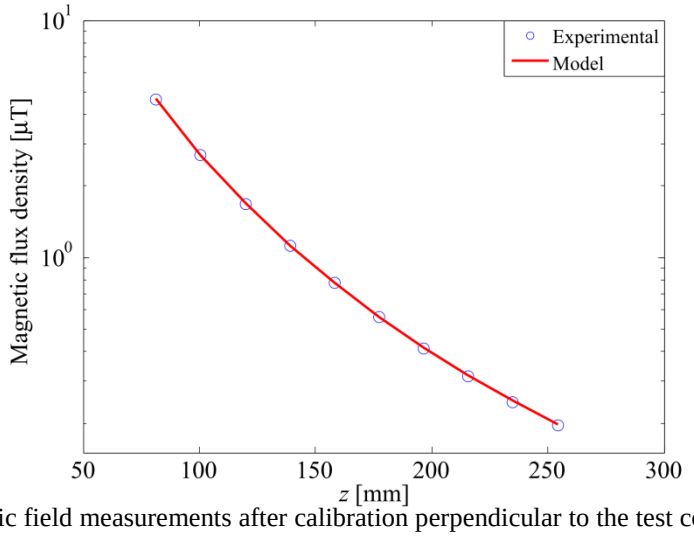



Figure 4.8: Magnetic field measurements after calibration perpendicular to the test coil at $x$ = 31.2 mm and $y$ = 31.2 mm.

To show the effect the weighing factors have, consider the case when the scaling factors are set such that the overall error is approximately 5 %. Figure 4.9 shows a plot of each error point for the objective function summation (*i.e.* each point in the graph is squared and summed to form the objective function) with each different weighting function. The graph is normalised for clarity. We see that the error function is largest near the coil when no weighting is applied and then sharply declines. Depending on the choice of weighting function, the overall errors can be balanced over each test point, giving a more uniform contribution from each point. The standard deviation of each of these residual points is shown in Table 4.1. Here we see that the unweighted case has the largest distribution in values as should be expected. When normalised to the value of the predicted flux or by the cubed distance, the residual error had a smaller distribution, *i.e.* a smaller change in residual error value implying a more even contribution from each test point.

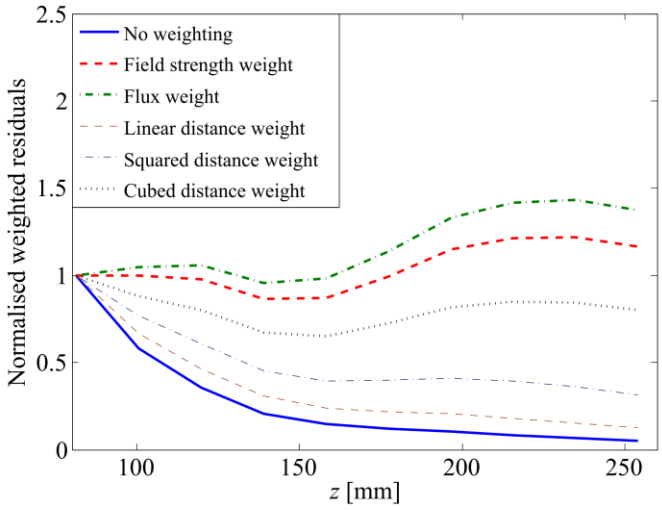



Figure 4.9: Plot of the weighted residuals with a mean error of 5 %. Results are normalised to the first point.

| Weighting function | Standard deviation |
|---|---|
| None | 0.304 |
| Flux weighting | 0.132 |
| Field strength weighting | 0.192 |
| Linear distance weighting | 0.281 |
| Squared distance weighting | 0.219 |
| Cubed distance weighting | 0.104 |

Table 4.1: Comparing weighting function value standard deviation.

After the calibration algorithm has been carried out, the percentage error at each test point was calculated and this is plotted in Figure 4.10. We see here that, as expected, when no weighting is applied, the errors close to the coil are smaller than those farther away. The cubed distance weighting gave the smallest errors far from the transmitter. The overall error for each weighting function is given in Table 4.2. The flux weighting approach was seen to give the overall minimum percentage error.

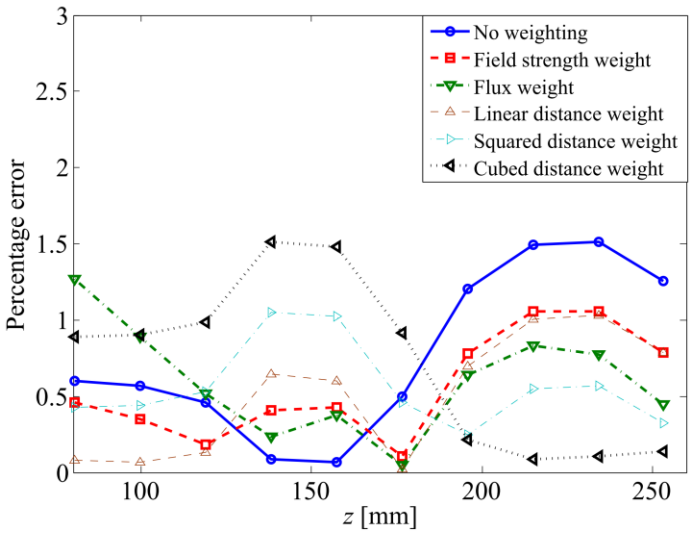



Figure 4.10: Comparing weighting functions.

| Weighting function | Percentage error |
|---|---|
| None | 0.78 |
| Flux weighting | 0.41 |
| Field strength weighting | 0.56 |
| Linear distance weighting | 0.51 |
| Squared distance weighting | 0.56 |
| Cubed distance weighting | 0.72 |

Table 4.2: Percentage error after calibration.

The situation becomes more complex when dealing with test points in different orientations, and hence, depending on the test points gathered, different weighting functions can often yield better results. For example, certain flux measurements can be close to zero when the sensor is approximately orthogonal to the magnetic field at a particular point. These points can easily have larger associated errors, and, in particular when using a flux weighting approach, can result in very large residual contributions. To mitigate these problems, careful choice of test points which avoids potential zero crossings, should be used. A simple choice of test point in this case is along the axis above the source under test, with the sensor also positioned axially.

## 4.4. Testing P&O Algorithm Parameters

### 4.4.1. Overview

The least-squares algorithms used to determine the location of the sensor has a large number of parameters which may alter the performance of the algorithm. In order to optimise these parameters, a series of tests were performed to determine the effect of each parameter on the overall performance on the real system. In order to test the performance of the position and

orientation algorithm (P&O), a set of 54 data points was gathered from 18 different locations above the transmitter. At each location, the sensor was orientated in three different orthogonal directions *i.e.* along the *x*, *y* and *z* axis respectively. Figure 4.11 shows the position of each test point location in relation to the transmitter array. After the magnetic field measurements were taken at each point, they were applied to the P&O algorithm and the sensors location was determined. For each test point, the initial estimate, $\boldsymbol{x}_0$, of the solution vector is chosen to be at the centre of the region of interest, *i.e.* $\boldsymbol{x}_0 = \begin{bmatrix} 0 & 0 & 0.15 & \pi/2 & \pi \end{bmatrix}$. The following outputs were recorded during the tests:

- RMS position error
- Orientation error
- Algorithm iterations
- Algorithm run time
- Objective function residual

At each location, the following algorithm parameters were varied and the test repeated and above outputs recorded:

- Solver: Levenberg-Marquardt or Trust Region
- Function tolerance
- Step size tolerance
- Initial solution estimate $\boldsymbol{x}_0$
- Analytical or numerical Jacobian
- Bounded or unbounded input variables (Trust Region only)
- Scaling type (Levenberg-Marquardt only)
- λ parameter (Levenberg-Marquardt only)

Each of these parameters is discussed in the following sections.

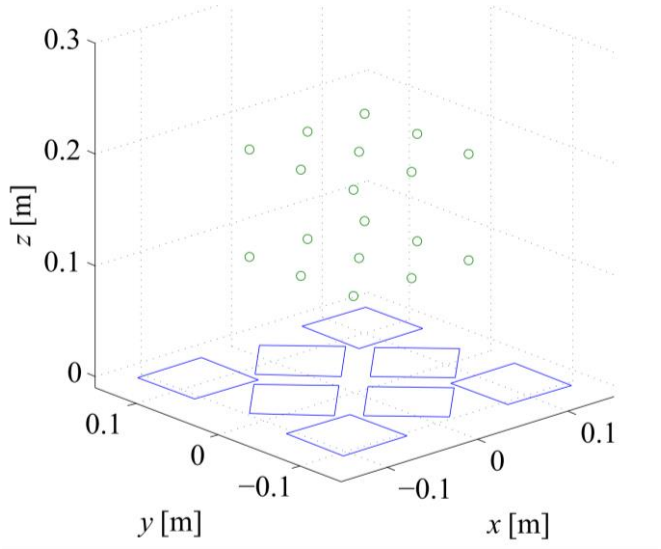



Figure 4.11: Diagram showing the position of the test points and the transmitter array.

### 4.4.2. Choice of Least Squares Solver

In almost all EM tracking systems that determine position using non-linear least squares, the preferred method is the Levenberg-Marquardt (LM) algorithm [65], [107], [119]. A more recent implementation of this algorithm is known as the Trust Region algorithm [140]. Both of these algorithms were tested on real magnetic field datasets to determine which gave the best performance. The MATLAB Optimisation Toolbox uses both algorithms, the default being the Trust Region (TR)[**]. Generally it is noted that the TR algorithm often has a faster convergence than the LM method [140], although this is dependent on the type of problem being solved. When using the LM method, an additional parameter $\lambda$ must be chosen. This parameter affects how fast the algorithm converges to a solution and incorrect choice of this parameter can cause very slow convergence. Table 4.3 shows a comparison between the two solvers with different $\lambda$ values. We see that overall the performance is very similar, although TR uses less iterations.

| $\lambda$ | RMS error [mm] | Iterations | Run time [ms] |
|---|---|---|---|
| 0.01 | 2.61 | 12.7 | 34.1 |
| 0.1 | 2.58 | 12.2 | 30.8 |
| 1 | 2.57 | 11.4 | 28.5 |
| TR comparison | 2.56 | 7.7 | 29.4 |

Table 4.3: Comparison between the LM and TR algorithms.

### 4.4.3. Effect of Function and Step Size Tolerances

Two of the key algorithm parameters are the function tolerance and step size tolerance. Function tolerance relates to how close the residual of the least squares algorithm is to zero before the algorithm stops, while the step size is linked to the size of step the algorithm can take between input arguments. If these parameters are chosen incorrectly, the algorithm becomes more inaccurate or can take an excessive amount of time to converge to a solution. The step-size tolerance is easily selected as it is simply required to be smaller than the expected resolution of the result. For example resolution beyond 100 μm is unrealistic, hence the step size should be $1\times10^{-4}$ or smaller to ensure accuracy.

Table 4.4 shows the effect of changing the function tolerance for the Trust Region method. As the function tolerance increases we see that the position error decreases, however increasing beyond $1\times10^{-16}$ gives no added benefit. We also see that the run time increases considerably if the function tolerance is set too low. A good initial estimate for the function tolerance is to consider each magnetic field measurement in the range of 10 nT to 10 μT, such that the associated error for the least squares objective function will typically be on the order of nano-Teslas. Hence, the squared error function will be approximately in the range of

[**] MATLAB uses two TR methods, Reflective and Dogleg. Dogleg is used for square systems, *i.e.* systems of equations that have the same number of equations as variables. Reflective does not have this requirement.

$10^{-18}$, and a function tolerance in this region should give acceptable results.

| Function tolerance | RMS error [mm] | Iterations | Run time [ms] |
|---|---|---|---|
| $1\times10^{-12}$ | 62.18 | 2.4 | 15.35 |
| $1\times10^{-13}$ | 34.32 | 3.9 | 19.9 |
| $1\times10^{-14}$ | 13.29 | 5.7 | 30.1 |
| $1\times10^{-15}$ | 4.13 | 6.5 | 39.9 |
| $1\times10^{-16}$ | 2.56 | 7.7 | 29.4 |
| $1\times10^{-17}$ | 2.57 | 8.4 | 31.6 |
| $1\times10^{-18}$ | 2.58 | 8.9 | 32.9 |
| $1\times10^{-19}$ | 2.57 | 9.5 | 44.2 |
| $1\times10^{-20}$ | 2.56 | 10.7 | 45.6 |
| $1\times10^{-21}$ | 2.55 | 20.5 | 85.8 |

Table 4.4: Effect of function tolerance on position error, iteration count and algorithm runtime.

### 4.4.4. Bounded or Unbounded Input Variables

When using the Trust Region method, the input variables can be left bounded or unbounded. This bounding implies that the input variables can only lie in a certain range. For example if the expected *x* position of the sensor is in the range of [-150 mm, 150 mm], this variable can be bounded to only exist in this region. This ensures that algorithm failures do not result in a position that is outside the region of interest. Table 4.5 shows a comparison between use of bounded and unbounded input variables. We see that, when bounded, a lower mean error generally results as well as a lower run time.

| | Bounded | | | Unbounded | | |
|---|---|---|---|---|---|---|
| Function tolerance | RMS error [mm] | Iterations | Run time [ms] | RMS error [mm] | Iterations | Run time [ms] |
| $1\times10^{-15}$ | 4.14 | 6.5 | 39.9 | 2.86 | 8.2 | 36.4 |
| $1\times10^{-16}$ | 2.56 | 7.7 | 29.4 | 2.72 | 8.7 | 32.4 |
| $1\times10^{-17}$ | 2.57 | 8.4 | 31.6 | 2.68 | 9.4 | 37.1 |
| $1\times10^{-18}$ | 2.57 | 8.9 | 32.9 | 2.68 | 9.8 | 36.6 |

Table 4.5: Comparison between bounded and unbounded solution space.

### 4.4.5. Analytical or Numerical Jacobian

Most nonlinear least squares solver use the gradient of the objective function to linearise the function around the current iteration point. When the objective function is vector function, the resulting gradient is a matrix known as the Jacobian. At each iteration of the algorithm, the Jacobian must be calculated. If the objective function is analytic (as is the case in our system), the Jacobian matrix may be determined analytically by calculating the derivative of each function with respect to the independent variables. The alternative is calculate the Jacobian numerically using a finite difference approximation. The trade-off is that generally an analytical Jacobian will be more accurate and may have improved convergence; however it often takes longer to calculate due to the size of the resulting equations. Numerically

calculating the Jacobian is generally faster but there is a loss in accuracy. We can see this in Table 4.6 where the analytical Jacobian gives a lower position error at the cost of an increased run time for the algorithm.

| | Numerical Jacobian | | | Analytical Jacobian | | |
|---|---|---|---|---|---|---|
| Function tolerance | RMS error [mm] | Iterations | Run time [ms] | RMS error [mm] | Iterations | Run time [ms] |
| $1\times10^{-15}$ | 4.14 | 6.5 | 39.9 | 4.14 | 7.9 | 45.1 |
| $1\times10^{-16}$ | 2.56 | 7.7 | 29.4 | 2.31 | 9.7 | 44.4 |
| $1\times10^{-17}$ | 2.57 | 8.4 | 31.6 | 2.31 | 10.2 | 46.7 |
| $1\times10^{-18}$ | 2.57 | 8.9 | 32.9 | 2.32 | 10.1 | 49.4 |

Table 4.6: Comparing the effect of using either a numerical or analytical form of the objective functions Jacobian.

### 4.4.6. Levenberg-Marquardt Scaling

When using the LM algorithm, if the problem is badly scaled (*i.e.* that different input variables effect the magnitude of the objective function by a different amount), often the algorithm may take a longer time converge or even fail to converge entirely. In MATLAB, the LM algorithm has the option to scale the problem to improve the convergence. The effect of this scaling option is shown in Table 4.7. With "Jacobian" scaling selected the run-time of the algorithm is dramatically reduced.

| No scaling | | | Jacobian scaling | | |
|---|---|---|---|---|---|
| RMS error [mm] | Iterations | Run time [ms] | RMS error [mm] | Iterations | Run time [ms] |
| 2.51 | 41.7 | 82.8 | 2.61 | 15.5 | 44.3 |

Table 4.7: Effect of scaling in the LM algorithm

### 4.4.7. Improved Algorithm

In all of the above tests, the initial solution estimate $\boldsymbol{x}_0$ was chosen to be at the centre of the region of interest. To investigate the worst case scenario for the initial solution, it was set to be the exact opposite of its actual value, *i.e.* the *x, y, z* coordinate was set at the opposite side of the region of interest and the two orientation variables, $\varphi$ and $\theta$, where chosen to point in the opposite direction. For example if the actual solution vector of the sensor was $\{x, y, z, \theta, \varphi\} = \{0.1, 0.1, 0.1, \pi/4, \pi/3\}$ this was instead set to $\{-0.1, -0.1, 0.3, -\pi/4, -\pi/3\}$. This resulted in poor overall performance as generally at each test point the algorithm did not converge to a correct solution as shown in Table 4.8. It was observed that the orientation estimate generally had the largest impact on whether or not the solution would converge. This is in part due to the planar nature of the transmitter which makes the system susceptible to non-convergence.

| Method | Algorithm convergence rate |
|---|---|
| TR | 35.2 % |
| LM (λ=0.001) | 48.1 % |
| LM (λ=0.01) | 50 % |
| LM (λ=0.1) | 40.7 % |
| LM (λ=1) | 44.4 % |
| LM (λ=10) | 42.6 % |

Table 4.8: Algorithm convergence rate for worst case scenario of the initial solution estimate.

To counteract this problem of non-convergence, an additional step was added to the standard least squares algorithms. Firstly, we need to determine if the algorithm has converged to a solution. A simple method to achieve this is to look of the residual of the objective function (*i.e.* the sum of squared errors). If the residual is very large after the algorithm has stopped it is a definite sign that the algorithm has failed. From experimentation it was deduced that a residual greater in magnitude than $1\times10^{-16}$ indicates a failed attempt. Hence if the residual is greater than a certain threshold, we retry the algorithm but with a different initial condition. An unusually large number of iterations also generally indicated a failed attempt. It was found that by adjusting the initial guess of the orientation variables, then on a second attempt the algorithm generally converged to the correct solution. By simply adding $\pi$ radians to each orientation initial guess, *i.e.* $\varphi'_0 = \varphi_0 + \pi$ and $\theta'_0 = \theta_0 + \pi$ , the algorithm was found to converge in almost all cases. Table 4.9 shows a comparison between the TR and LM algorithm with the improved algorithm. All test points converged to a solution in this case. We see that the TR method now gives improved accuracy over the LM method. As expected, the run-time has increased as the algorithm is sometimes required to be calculated twice to reach convergence.

| TR | | | LM | | |
|---|---|---|---|---|---|
| RMS error [mm] | Iterations | Run time [ms] | RMS error [mm] | Iterations | Run time [ms] |
| 2.03 | 6.7 | 44.1 | 2.57 | 11.4 | 44.3 |

Table 4.9: Comparing LM and TR with improved algorithm

### 4.4.8. Final Parameter Choice

After considering all of the above results, the TR solver was chosen as it was seen to give better performance when using the improved algorithm and also has less input parameters to consider, simplifying its implementation. Function tolerance was set to $1\times10^{-17}$ and the step-size tolerance set to $1\times10^{-6}$.

## 4.5. Magnetic Field Testing

### 4.5.1. Single Coil Tests

Extensive testing was carried out to verify the accuracy and validity of the magnetic field models of the coil array. Modelling errors directly affect the system's accuracy and hence accurate models are critical. It was observed experimentally that if errors of greater than approximately 2-3 % exist in the magnetic field models, accuracy significantly decreases. The first tests were carried out on a single coil, verifying its accuracy along its central axis. The results of this test are shown in Figure 4.12, while Figure 4.13 plots the absolute value of the error. The mean percentage error in this case is 1.6 %.

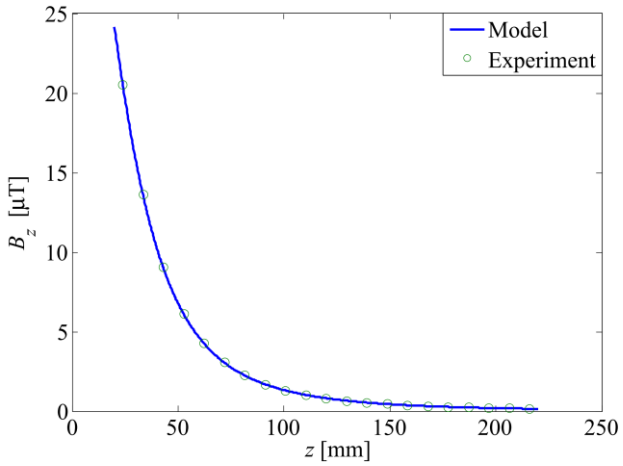



Figure 4.12: Comparing filament model with experimental data along the central axis of a single coil.

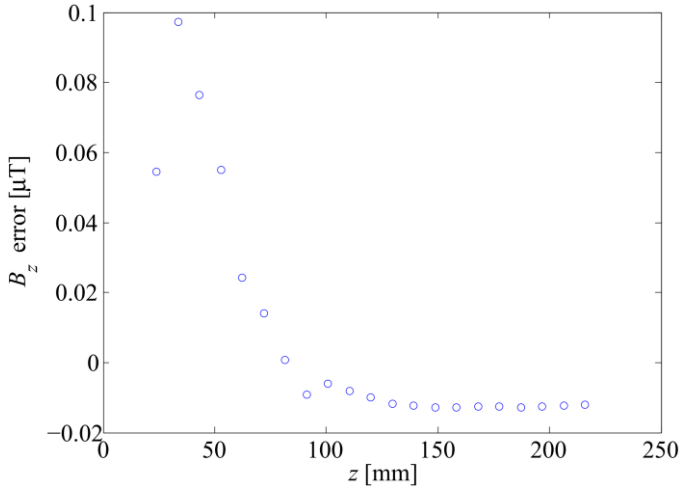



Figure 4.13: Error plot between model and experimental data along the central axis of a single coil.

### 4.5.2. Transmitter Array Testing

This test was expanded to include the entire coil array. Here, a set of test points was gathered along the central axis of the entire coil array and the resulting magnetic fields were recorded. In this test, the mean magnetic field error recorded after calibration was 0.7 %. Figure 4.14

shows the arrangement of each coil in the array, and Figure 4.15 shows a graph the magnetic field contribution from each coil.

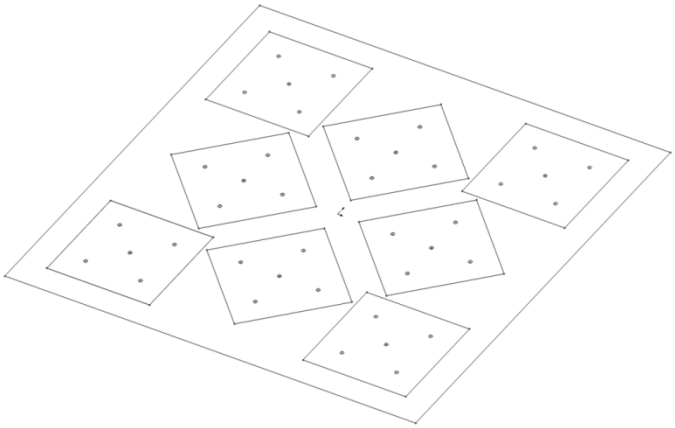


Figure 4.14: Coil array layout. All 8 coils are mounted on a Perspex sheet with a sheet side length of 30 cm. Simulation indicated this particular arrangement is optimum in comparison to other arrangements (see Chapter 3).

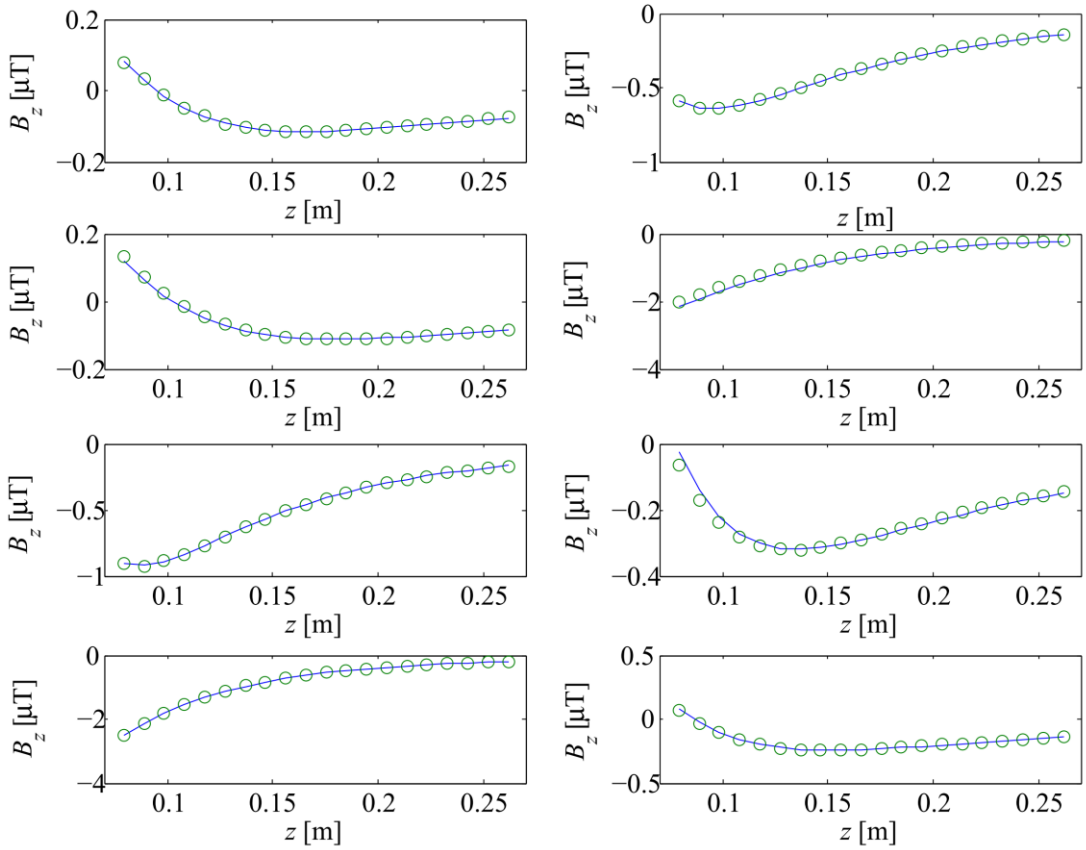



Figure 4.15: Magnetic field along the central axis of the transmitter array ($x = 0$, $y = 0$) comparing the theoretical and experimental result for each of the eight coils.

For a 3D distribution test, 2D 7 × 7 grid of 49 points was gathered over the coil array. The magnetic field from a single coil is plotted in Figure 4.16. The overall mean error in the field measurements was calculated as 3.6 %. For certain flux measurements that are close to a zero crossing such as when the sensor is nearly perpendicular to he applied field, the percentage errors calculated can be much larger, giving the impression that the overall error

is worse than the percentage error would seem to indicate. For example, if the expected value was 1 nT, and the measured value was 2 nT, the error would be 100 %, although an error of 1 nT is relatively small compared to the typical measurements which are normally on the order of 100 nT.

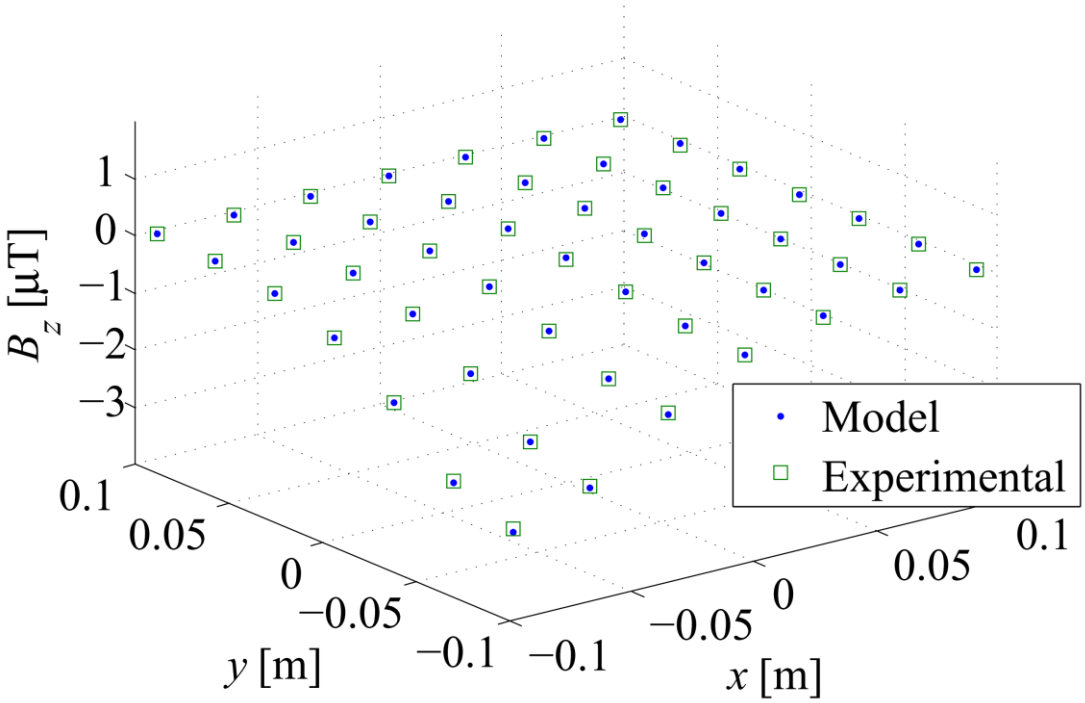



Figure 4.16: 3D scatter plot showing the magnetic field of a single coil in the array.

### 4.5.3. Magnetic Noise Measurements

Magnetic noise levels were measured as variations in detected fields directly affect the overall system accuracy. To investigate magnetic noise, the sensor was placed in the centre of the operating region above the coils and the magnetic fields from each coil were recorded for 15 s. The mean of each magnetic field measurement was then subtracted leaving only the noise component. For each test point, a sample rate of 100 kHz was used with 5000 samples per acquisition. Figure 4.17 shows the noise measured on each coil, the standard deviation of the noise was calculated and this is shown in Table 4.10. This table also shows the same measurement without the transmitter array engaged while Figure 4.18 shows the corresponding noise signals. It is clear that there is more noise when the coil arrays are engaged; this is due to interference from neighbouring coils, as well as small variations in the coil current. Quantisation noise also becomes a factor at very small amplitudes due to the finite step size of the ADC. Noise in each measurement directly effects P&O accuracy, in particular when the sensor is far from the transmitter and is one of the main limiting factors on the useful operating volume of the system

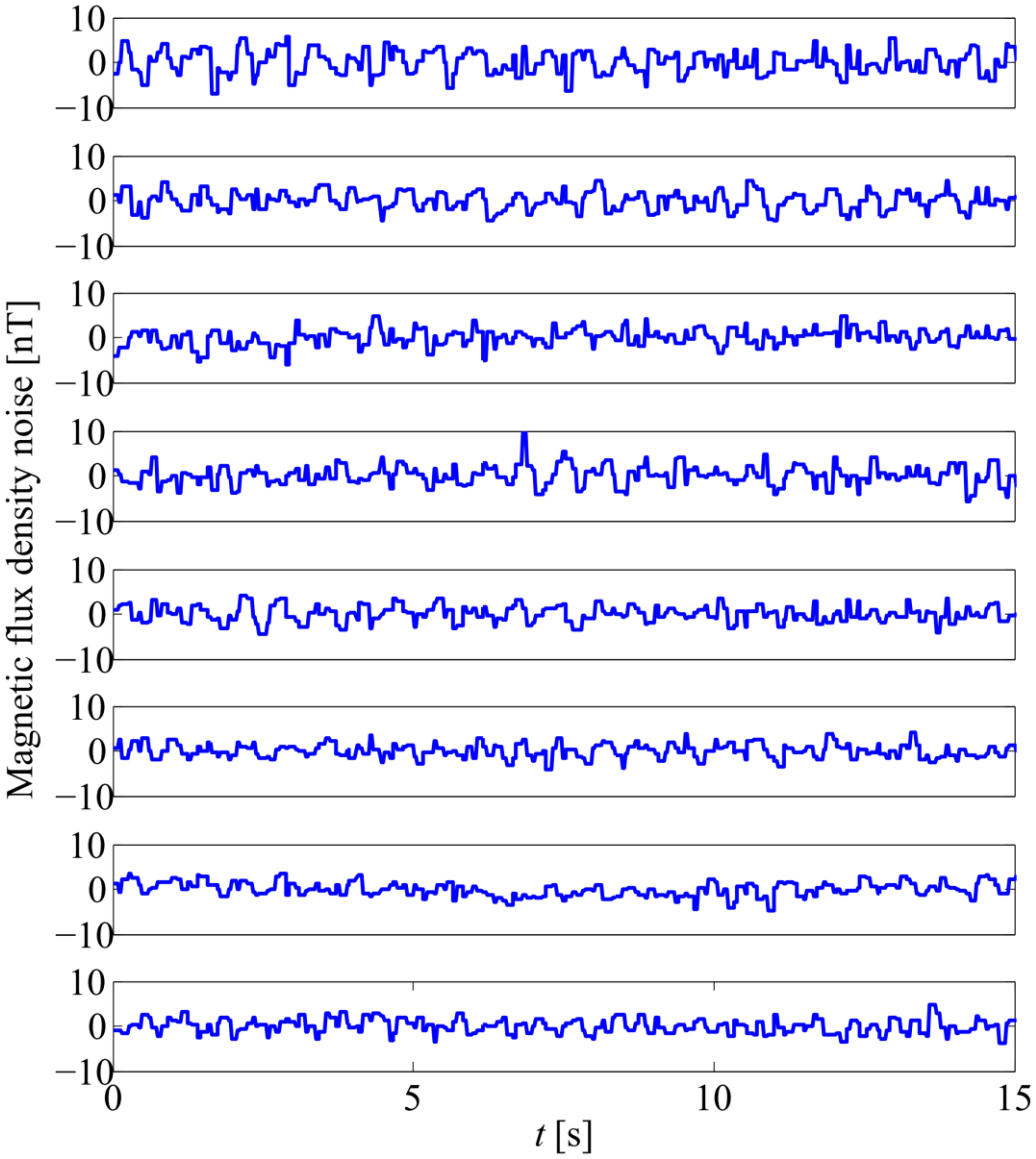



Figure 4.17: Magnetic field noise from each of the 8 coils.

| | Transmitter | $B_1$ | $B_2$ | $B_3$ | $B_4$ | $B_5$ | $B_6$ | $B_7$ | $B_8$ |
|---|---|---|---|---|---|---|---|---|---|
| B RMS | On | 2.66 | 2.11 | 1.92 | 2.21 | 1.81 | 1.57 | 1.63 | 1.61 |
| [nT] | Off | 0.16 | 0.15 | 0.14 | 0.14 | 0.12 | 0.13 | 0.12 | .012 |

Table 4.10: Magnetic field noise at each carrier frequency with and without the transmitter. “On” refers to when the transmitter is fully engaged and powered on; “Off” refers to when it is fully powered down.

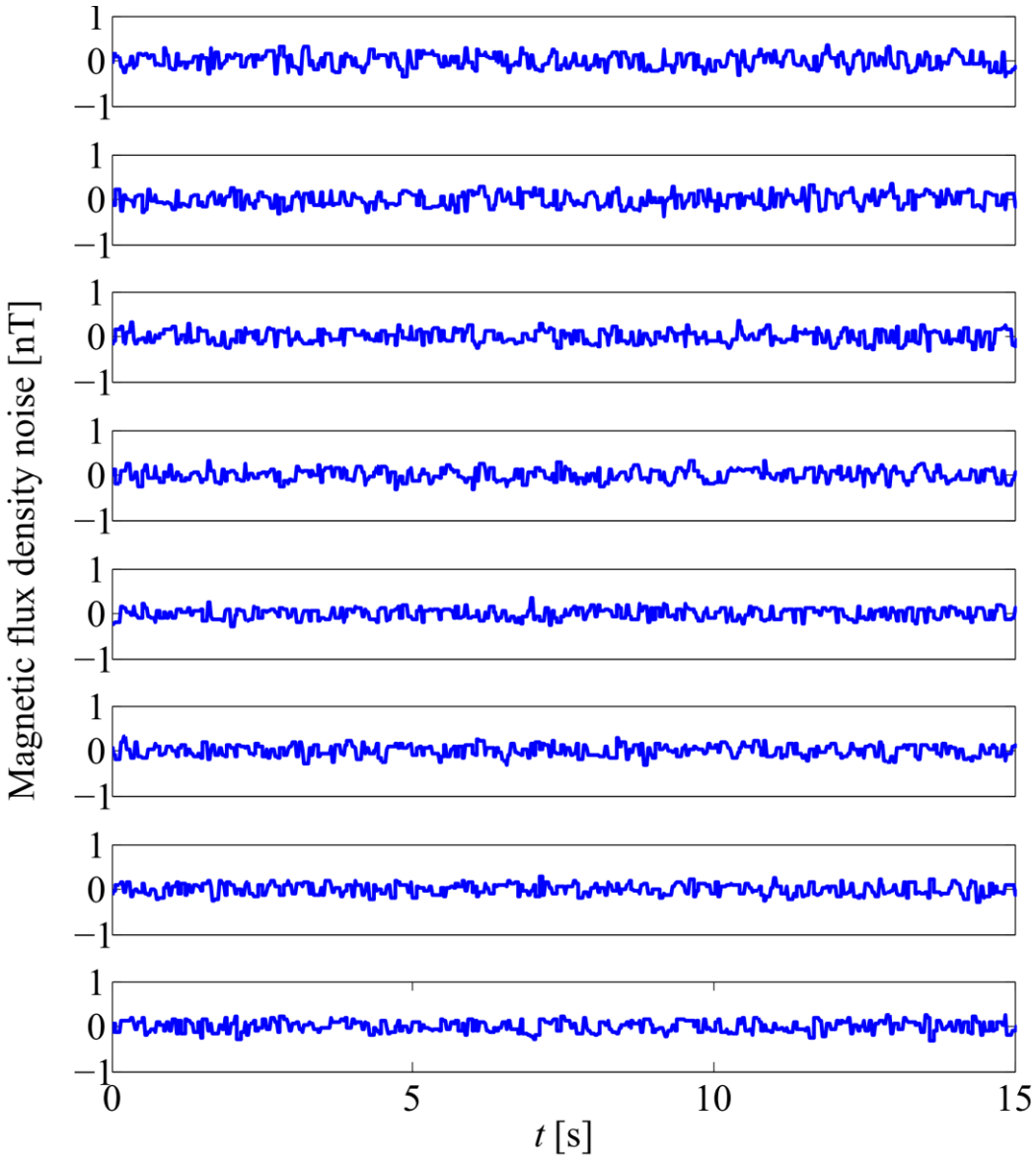



Figure 4.18: Magnetic field noise at each of the carrier frequencies with the transmitter disabled.

### 4.5.4. Safety Limits

Human exposure to alternating magnetic fields must be considered when designing a system of this type which, when in operation, will be constantly exposing its users. The ICNIRP has strict guidelines in this regard [109]. In the range of 3 kHz to 100 kHz, the maximum occupational exposure is set to 100 μT RMS [109]. For multiple frequency exposure, the magnitudes of the each magnetic field source must be summed together. Figure 4.19 illustrates the minimum safe distance away from the coil board at an operating current of 250 mA. For this current, typical of the system's output current during the operation, the minimum safe distance is 12 mm.

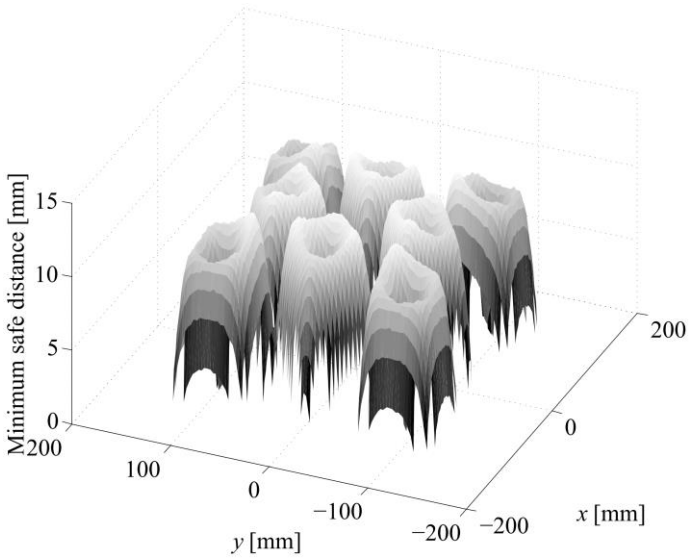



Figure 4.19: Minimum safe distance simulation based on each coil carrying 250 mA in the range 3 kHz to 100 kHz as stipulated by the ICNIRP guidelines. The simulation is centred over the coil array. The contour plot indicates the minimum distance (in mm) from the coils to be within the occupational safety limits. For safe human exposure, a patient must not be exposed to the regions shown.

## 4.6. Position and Orientation Accuracy Testing

This section details the primary results demonstrating the overall accuracy and performance of the system. These results were calculated with the Phase 1 system implementation.

### 4.6.1. Static Position Tests

The first set of tests involved taking a 6 × 6 × 6 matrix of test points in a volume of 190.5 mm × 190.5 mm × 172.8 mm. At each test point, the sensor was aligned in three different orientations that align with directions, (*x*, *y*, *z*), as defined by Figure 3.1 which resulted in 648 points in total. The results are shown in Table 4.11. Figure 4.20 and Figure 4.21 show the position and orientation error for this test plotted versus distance from the centre of the coil array. Figure 4.22 shows the *x*, *y* and *z* positions for a trajectory covering two planes with 72 points in total, here the sensor was placed manually in each position.

| Direction | $e_p$ [mm] | $\sigma_{e_p}$ [mm] | $e_o$ [Deg] | $\sigma_{e_o}$ [Deg] |
|---|---|---|---|---|
| *x* | 1.5 | 0.6 | 1.8 | 0.6 |
| *y* | 1.2 | 0.8 | 1.0 | 0.4 |
| *z* | 0.8 | 0.4 | 0.9 | 0.3 |
| All | 1.2 | 0.7 | 1 | 0.8 |

Table 4.11: Position and orientation accuracy of the shielded sensor.

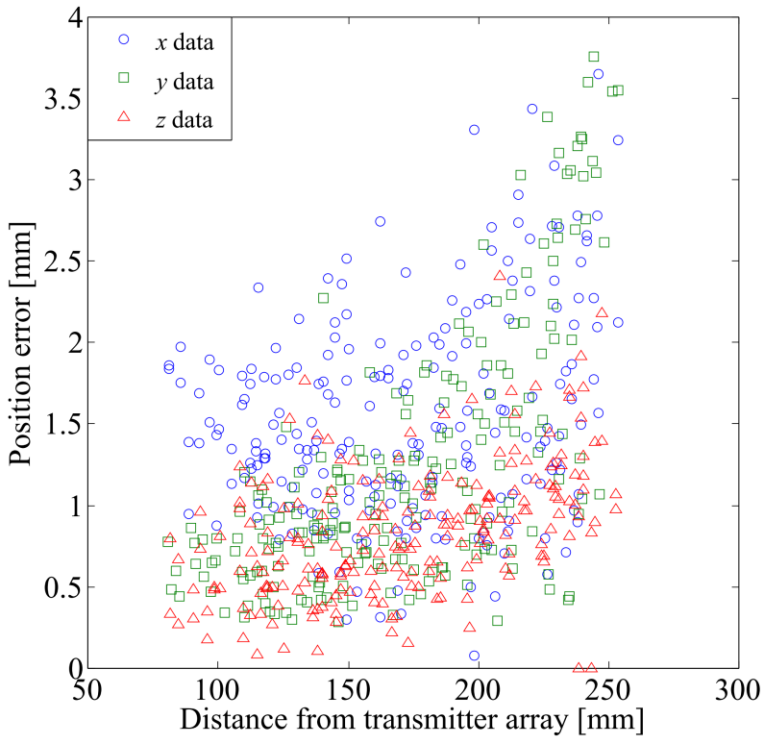



Figure 4.20: Graph showing the RMS accuracy of the system for determining position of the sensor. Three tests were carried out with the sensor rigidly secured in different directions. 216 points were taken in each orientation.

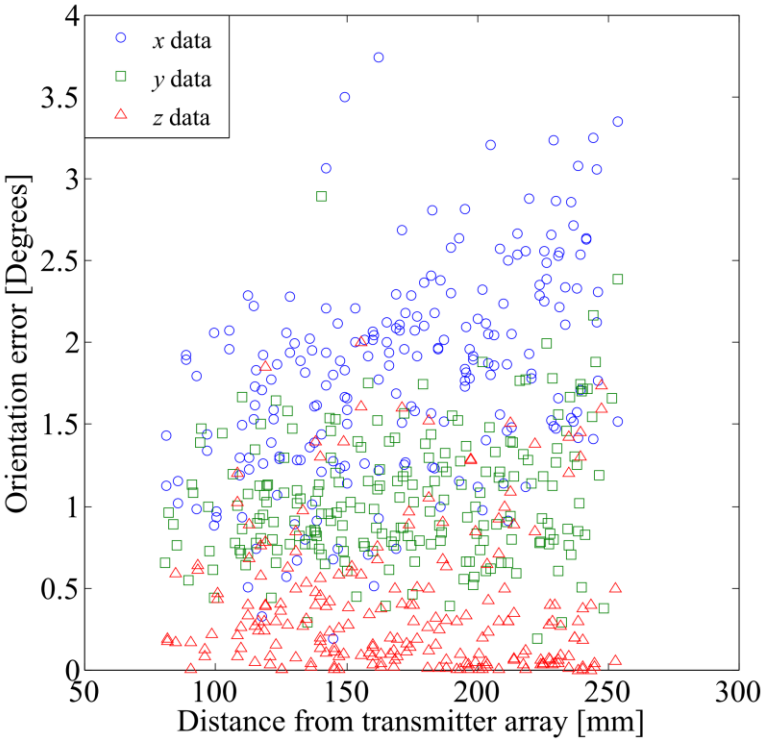



Figure 4.21: Graph showing the RMS accuracy of the system for determining the orientation of the sensor. Three tests were carried out with the sensor rigidly secured in different directions. 216 points were taken in each orientation.

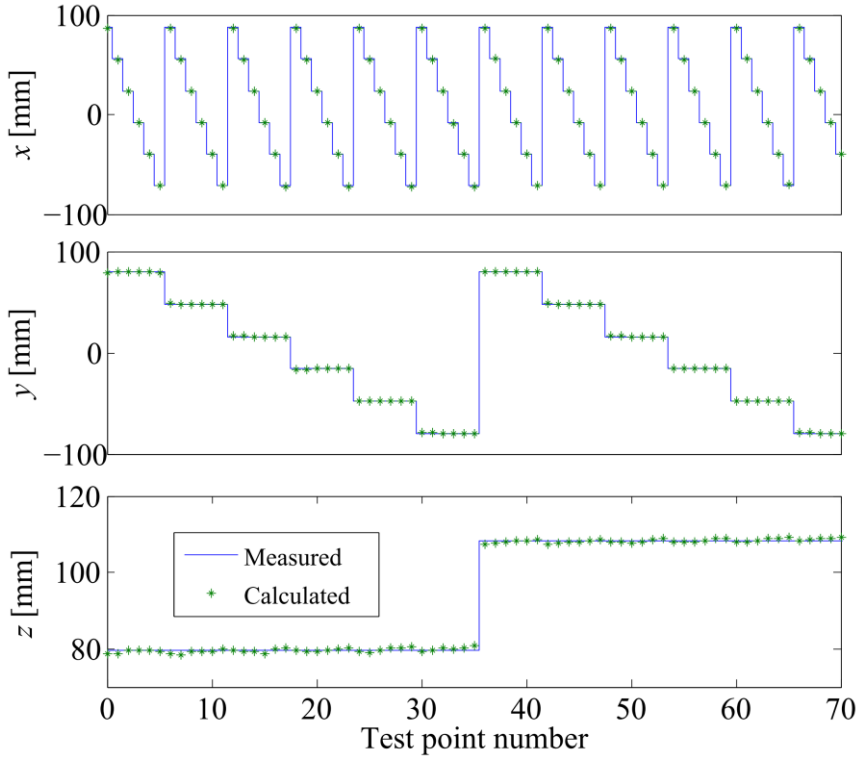



Figure 4.22: A trajectory showing the performance of the *x*, *y* and *z* coordinate errors for 72 points over two planes. The sensor was orientated along the *z* axis.

A further test was carried out to investigate the performance of different types of sensor, in particular to compare between shielded and unshielded probes. 6 probes were tested in total, on a $3 \times 4 \times 4$ grid of test points in a volume of 16 cm × 24 cm × 17 cm, with three orientations at each point yielding 144 points per sensor. The results of this test are shown in Table 4.12. The errors in the 11 mm shielded sensors are possibly due to calibration errors or non-convergence of one of the test points. In general the shielded sensor gave the best performance when both the position and orientation are considered; the unshielded sensors are more sensitive to noise pickup and hence are less reliable. The main trade-off between the two types of sensor is cost and size; the shielded sensors are several times more expensive and are much larger. Overall the tests indicated that the useful operating region of the system is a cylindrical region, 30 cm in height above the coil array and 25 cm in diameter, outside this volume, errors dramatically increase.

| Probe | $e_p$ [mm] | $\sigma_{e_p}$ [mm] | $e_o$ [Deg] | $\sigma_{e_o}$ [Deg] |
|---|---|---|---|---|
| 12 mm shielded 1 | 1.9 | 1 | 0.8 | 0.7 |
| 12 mm shielded 2 | 1.6 | 1 | 0.6 | 0.8 |
| 11 mm unshielded 1 | 1.9 | 1.3 | 1.3 | 1 |
| 11 mm unshielded 2 | 3.5 | 2 | 2.5 | 2.3 |
| 8 mm unshielded 1 | 1.7 | 1 | 2.0 | 1.6 |
| 8 mm unshielded 2 | 1.5 | 0.9 | 1.5 | 1.2 |

Table 4.12: Comparison of probe types.

### 4.6.2. Scribble Tests

Figure 4.23 shows all data points calculated from the dynamic scribble tests. Figure 4.24 illustrates the results from the *–x* direction test (i.e. the sensor was approximately directed in the *–x* direction). Here we can clearly see the four test planes and the associated errors. When all the data from the scribble tests are considered (8000 test points), the mean *z* error was found to be 0.8 mm with a standard deviation of 1.3 mm. However if we consider only values within the 95$^{th}$ percentile, this error decreases to 0.6 mm with a standard deviation of 0.6 mm.

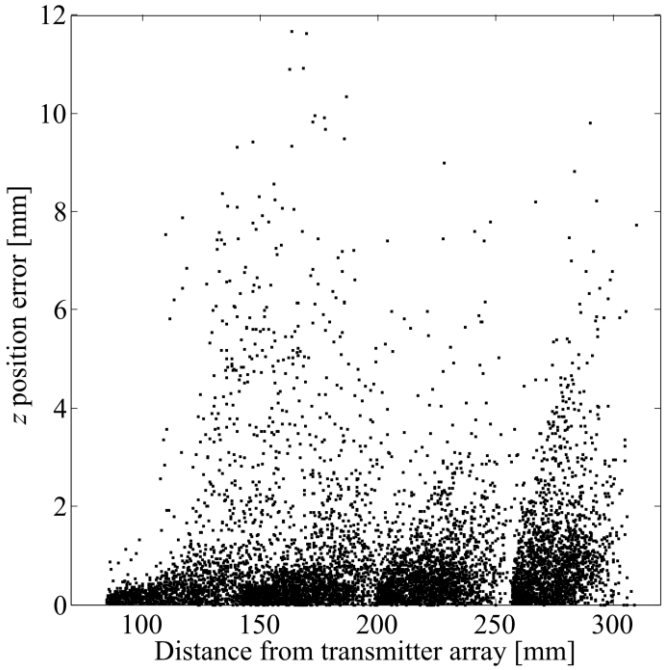



Figure 4.23: All 8000 scribble test points data plotted for an *–x* orientated sensor. Each point was arranged in increasing distance from the magnetic source. The mean *z* error is 0.8 mm with a standard deviation of 1.3 mm. If we consider only values within the 95$^{th}$ percentile, this error decreases to 0.6 mm with a standard deviation of 0.6 mm.

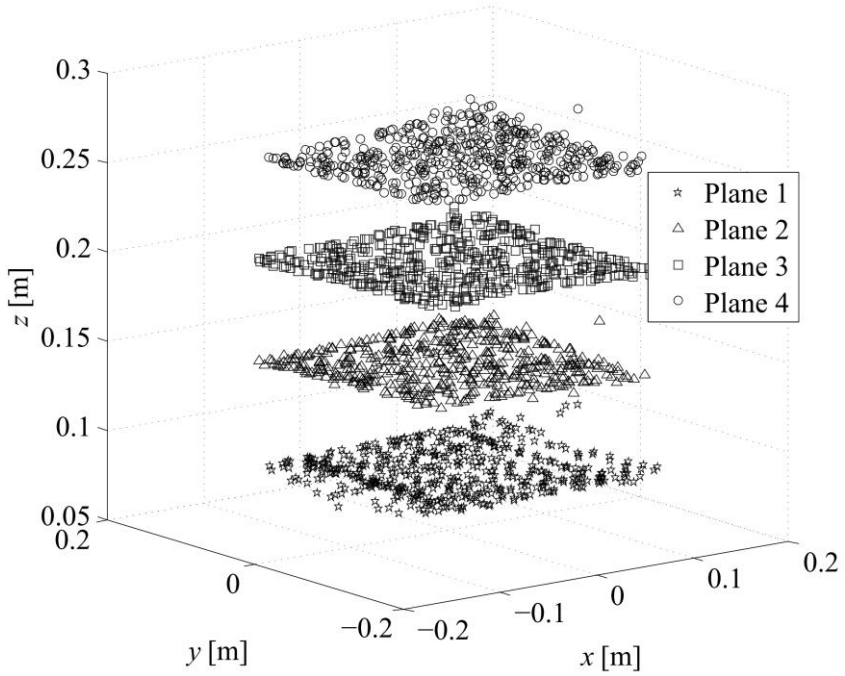



Figure 4.24: Results of scribble test for the *–x* orientation test on 4 planes. Ideally all points are located on each of the 4 planes. Off plane points indicate errors.

### 4.6.3. Dynamic Performance

In order to demonstrate the dynamic performance of the system, an experiment to track the position of simple pendulum was carried out. In this test, the sensor was attached to a small weight and left to hang by its connecting wire from a fixed point above the transmitter array. The pendulum was released from a small displacement above its resting point. During the subsequent motion, the sensor position is recorded. Figure 4.25 shows a picture of the test setup. The period of pendulum motion was found to be approximately 2 seconds. Figure 4.26 shows all the points gathered during the motion of the pendulum, the displacement of pendulum along the *x* axis of the transmitter is shown in Figure 4.27. The resulting displacement resembles that of a damped sinusoid as is expected from a non-ideal pendulum. The average sample rate is 22.6 Hz, and during the tracking period no significant errors are apparent, (*i.e.* the system tracks the pendulum motion without having convergence issues or gross inaccuracies).



Figure 4.25: Test setup for the sensor attached to pendulum.

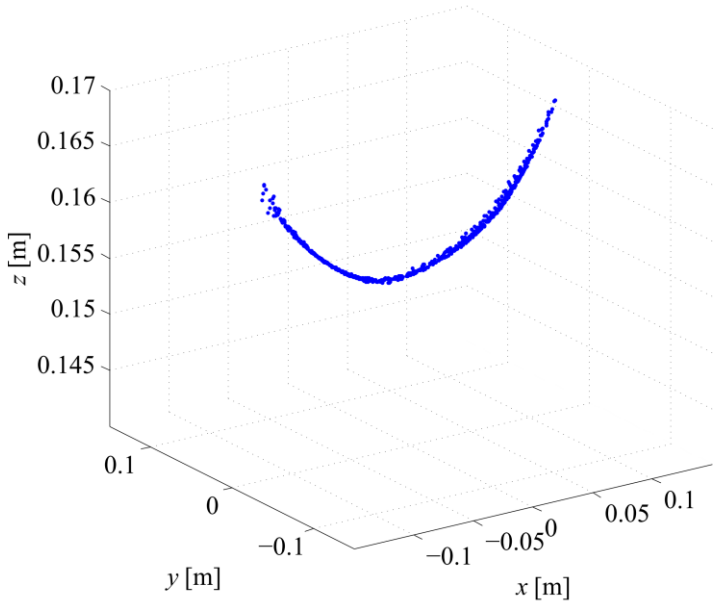



Figure 4.26: Plot of every point gathered during the recorded pendulum motion.

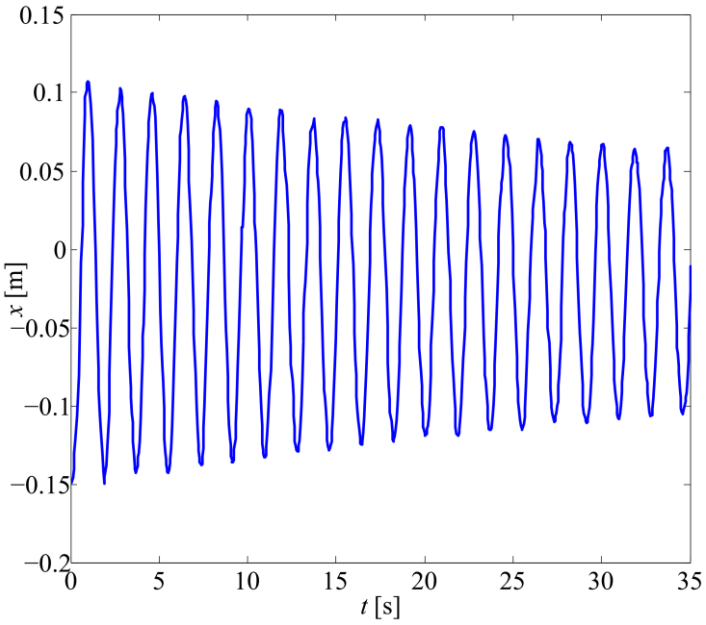



Figure 4.27: *x* axis displacement of the pendulum with time. An average sample rate of 22.6 Hz was used.

The primary limitation on the sample rate in the above experiment is the time taken for the P&O algorithm to run. For applications where real time tracking is not required, much faster samples rates can be used to carry out the magnetic field measurements and then calculate the positions afterwards in an offline fashion. The pendulum experiment was repeated in this manner with a an increased sample rate of 64.1 Hz. The displacement graph for this test is shown in Figure 4.28. This test was also repeated but with the pendulum set to move in a circular pattern and the trajectory of this motion is seen in Figure 4.29.

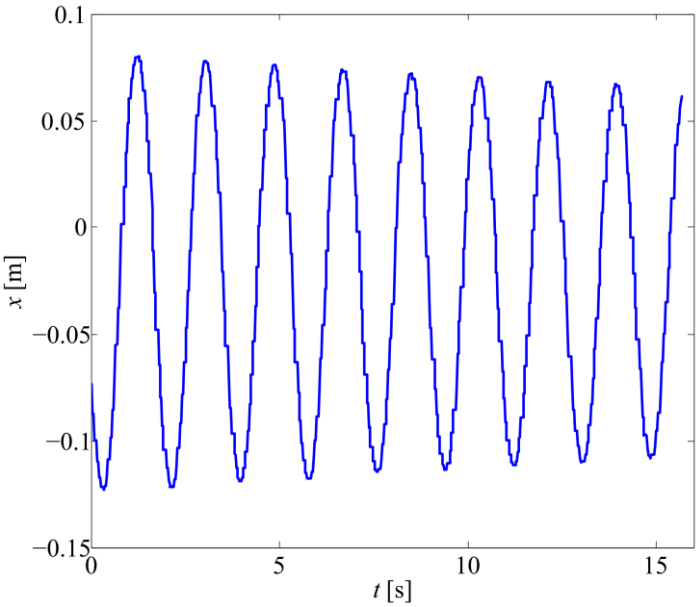



Figure 4.28: Pendulum time displacement with offline measurement with higher sample rate of 64.1 Hz.

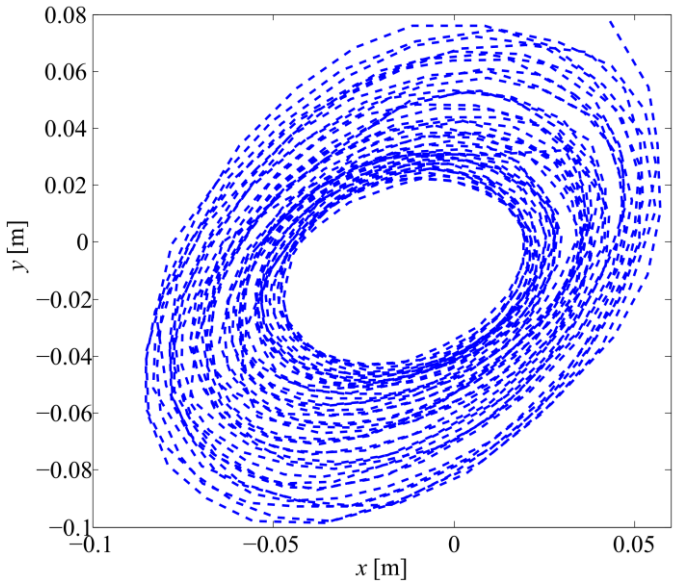



Figure 4.29: *x* and *y* trajectory of the pendulum when moving in a circular motion.

### 4.6.4. Position and Orientation Noise

Due to the inherent noise present in the magnetic field measurements, there is generally a small noise component on the calculated position and orientation. To investigate its effect, the sensor was placed at a static position at the centre of the transmitter operating region and the position was repeatedly calculated. Its displacement was calculated and the mean was subtracted to leave only the position noise component. This test was repeated with an increased number of samples to investigate the effect of a narrower filter band. An increased sample rate was also tested. The results of this test are shown in Figure 4.30. The calculated standard deviation for the first case was 0.107 mm, although with the increased number of samples this reduced to 0.0654 mm. When the sample rate was increased, this result remained largely unchanged as the deviation was found to be 0.0638 mm. Overall, these displacements due to magnetic field noise are quite small and can generally be ignored except at large distances from the transmitter.

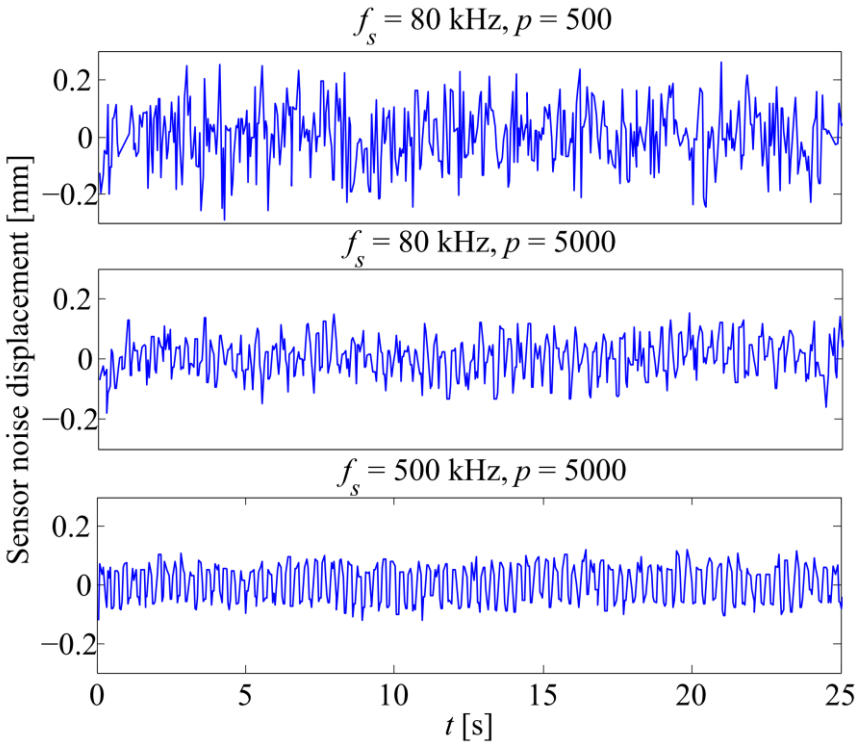



Figure 4.30: Sensor noise displacement for (a) 500 samples, (b) 5000 samples and (c) 5000 samples with an increased sample rate.

## 4.7. System Noise Analysis

To evaluate and quantify the levels of electrical noise in the system, a series of tests were carried out on the sensor and amplifier subsystem. First, the noise power from low frequencies up to 100 kHz was analysed. A $2^{20}$ point FFT was used to sample the data in each case. The DAQ card itself was examined by shorting one of its input channels and recording the measured voltage. The sensor amplifier was then analysed with the input grounded. Finally the sensor was connected and the output voltage measured with and without the coil array engaged. The resulting FFT was then smoothed using a moving average filter to clearly see the overall noise trend. The results of this test are shown in Figure 4.31. Figure 4.32 shows the same data but with a linear scale on the $x$-axis. We see here that the DAQ noise floor is very small and can be neglected. The amplifier with and without the sensor are shown to have similar noise levels, hence the sensor does not directly contribute excessive noise without the transmitter. When the transmitter is enabled however, the overall noise spectrum changes considerably. As well as the carrier frequencies, the transmitter also generates wideband noise which increases with frequency. If we consider the coil current frequency response, shown in Figure 4.33, we see that the coil current has a relatively flat noise distribution except at the carrier frequencies. The induced voltage in the sensor is a differentiated version of this waveform; hence this noise increases linearly with frequency.

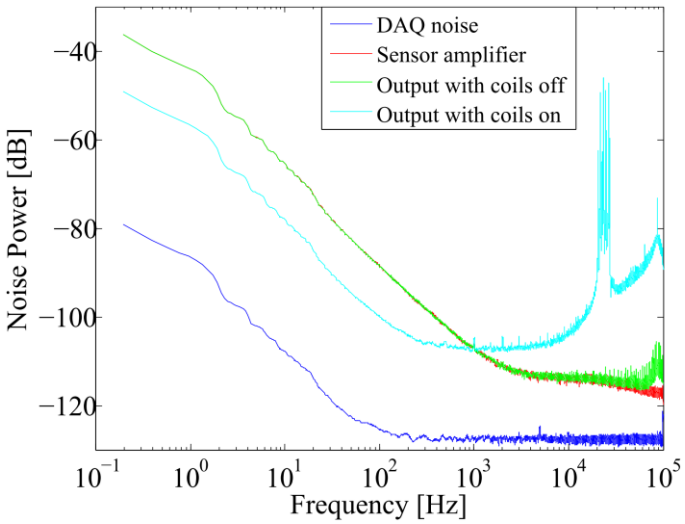



Figure 4.31: Noise power of the sensor subsystem with a moving average applied to smooth the data.

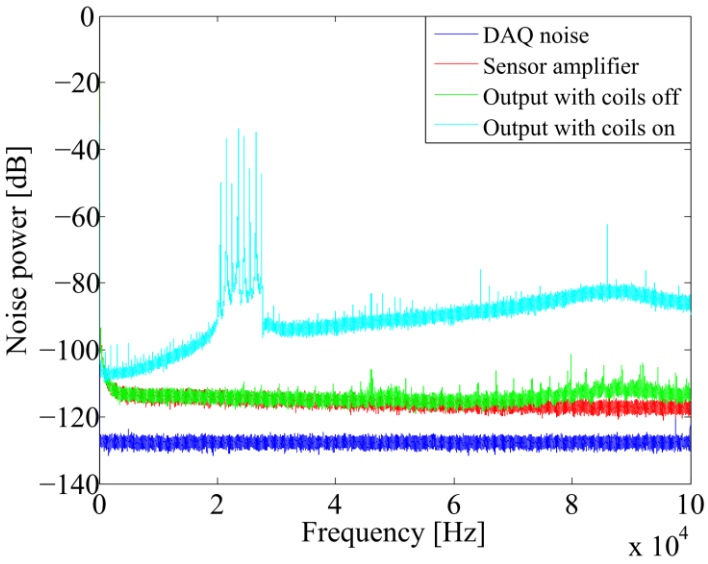



Figure 4.32: Linear *x* scale noise power distribution.

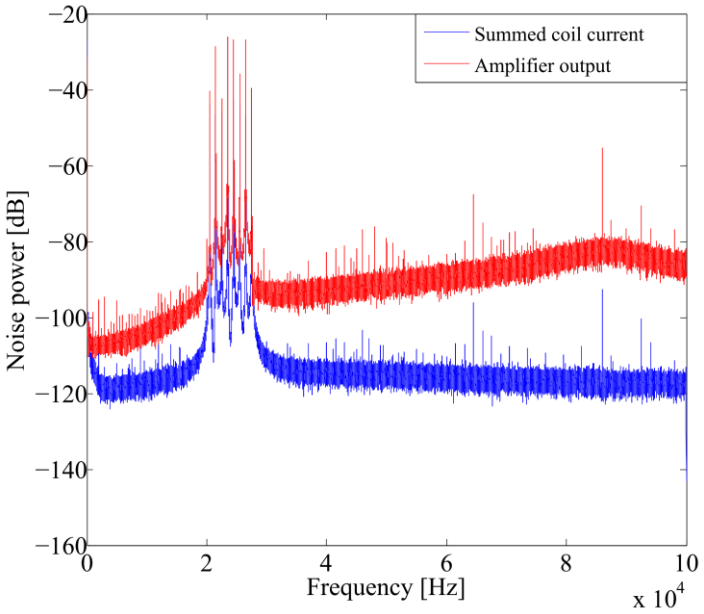



Figure 4.33: Comparing the transmitter current noise and the resulting magnetic field noise.

To calculate an approximate noise figure in the region of interest between 10 - 30 kHz, the mean of the noise power and average noise voltage density was calculated in this range. The results of these noise calculations are shown in Table 4.13. For comparison, the noise was also measured using a precision digital multimeter. A HP 34401A was used. The AC RMS bandwidth of the multimeter is approximately 300 kHz and the noise voltage density was determined by scaling the RMS voltage measurement with the bandwidth as required[††]. We see that the main contributor to the noise is the transmitter and the other noise contributions are small in comparison. If we consider the bandwidth of the systems filter to be 25 Hz, the resulting noise is of the order of 200 μV, which, in general, is far less than the typical signal amplitude.

| Noise Source | Noise Density μV/√Hz | |
|---|---|---|
| | NI PCI 6259 | HP 34401A |
| Sampling noise floor | 0.75 | 0.008 |
| Sensor amplifier | 2.16 | 2.217 |
| Sensor (Coils off) | 2.15 | 1.12 |
| Sensor and amplifier (Coils off) | 3.05 | 2.48 |
| Sensor and amplifier (Coils on) | 40.6 | n/a |

Table 4.13: Approximate noise voltage densities for each stage of the sensor subsystem.

A further test was carried that directly uses the demodulator subsystem to perform a frequency sweep over the spectrum of interest. The demodulator was swept in 1 Hz steps from 10 kHz to 30 kHz, with and without the transmitter engaged. 100,000 points were gathered and the demodulator filter bandwidth was 0.22 Hz. The equivalent noise power bandwidth was calculated at 3.05 Hz. The results of this test are shown in Figure 4.34. We can clearly see that there are a number of spurious frequency components across this range. This is more clearly shown in Figure 4.35. The choice of carrier frequency should be such that these frequencies are avoided. These frequency components could be a result of other sources of magnetic interference such as switch-mode power supplies or lighting fixtures.

[††] The noise of the system with the coils enabled was not calculated using this method as the induced voltage from the coils would give an erroneous reading.

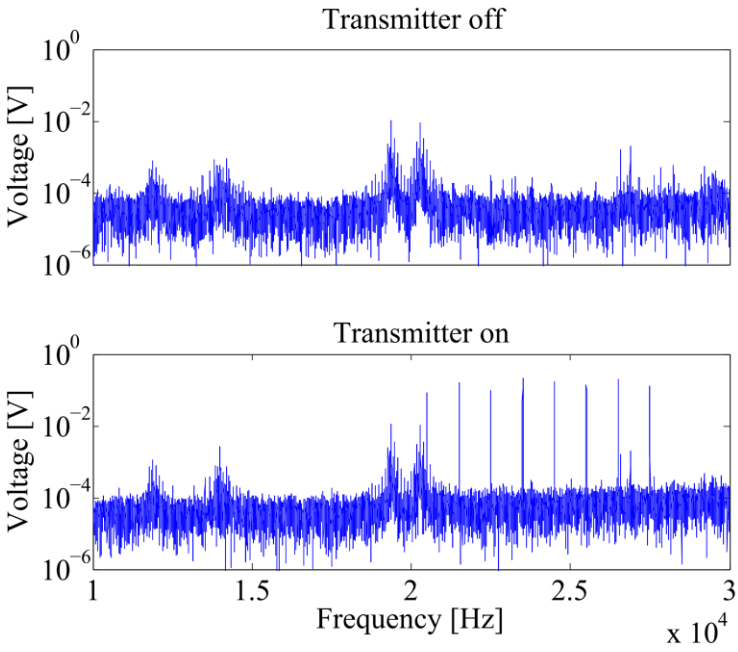



Figure 4.34: Swept demodulator output in 1 Hz steps over the operating frequency range.

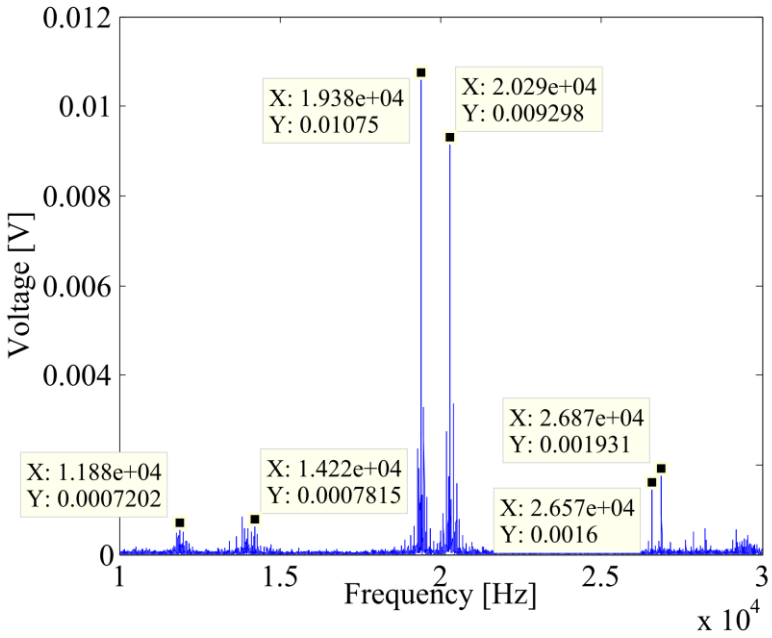



Figure 4.35: Spurious frequency components in the operating frequency range.

## 4.8. Transmitter Current Driver Performance

### 4.8.1. Current Source Stability

To verify the stability of the coil driver system, the current in one of the coils was measured in fixed intervals of 5 minutes for 24 hours. The mean value of the current was found to be 159.6 mA with a standard deviation of 38.2 µA, or 0.024 % of the mean value. Hence the generated magnetic fields also had the same variability. A further test was carried out in three other coils, each varied with a standard deviation of 90.7 µA, 50.9 µA and 45.9 µA or

0.0219 %, 0.0113 % and 0.0099 % of their mean value. The average standard deviation from these tests was 62.5 µA or 0.014 %. Figure 4.36 shows the results of these tests.

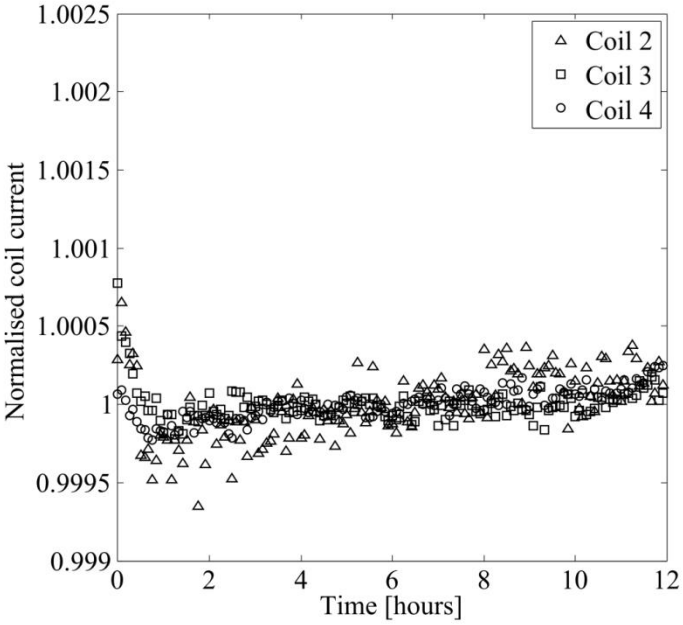



Figure 4.36: Results of 12 hour currents tests in 3 arbitrary coils. Each current is normalized to its mean value. Coil 2 varied with a standard deviation of 0.0219 %, coil 3 was 0.0113 % and coil 4 was 0.0099 %.

### 4.8.2. Induced Crosstalk Reduction

The induced crosstalk in each channel was measured by calculating the FFT of the current waveform and measuring the peaks at each of the carrier frequencies. Each channel was sampled at 150 kHz and an FFT length of $2^{20}$ was used in order to get a suitable frequency resolution. Two configurations were tested; closed loop and open loop. For the open loop measurements, a single channel was left open loop while leaving the remaining channels in their closed loop configuration. Having measured the peaks, the total RMS induced current was calculated using (4.14).

$$i_{Total} = \sqrt{i_1^2 + i_2^2 \ldots i_n^2} \tag{4.14}$$

The induced current per channel is shown for the open loop and closed loop currents in Table 4.14. The mean closed loop current which results is 69 µA in comparison to the open loop result of 1.14 mA. Table 4.15 shows the attenuation per channel gained by using the closed loop system. We see that the attenuation various from each coil considerably, this is because some of the induced currents were small and close to the systems noise floor, so the full impact of its attenuation is difficult to quantify. The largest induced components resulted in the largest corresponding attenuation, for examples for coil 1, the closest coils are number 2 and 4, both of which had the greatest mutual inductance and we see they experienced large attenuations of -19 dB and -25 dB respectively. The average attenuation was found to be -16.5 dB.

| Channel | 1 | 2 | 3 | 4 | 5 | 6 | 7 | 8 | Mean |
|---|---|---|---|---|---|---|---|---|---|
| Closed loop [mA] | .093 | .157 | .052 | .039 | .048 | .051 | .061 | .055 | .069 |
| Open loop [mA] | .771 | 1.18 | .792 | 1.34 | 1.14 | 1.11 | 1.71 | 1.11 | 1.14 |
| Attenuation [dB] | -18.4 | -17.5 | -23.7 | -30.7 | -27.5 | -26.8 | -28.9 | -26.1 | -24.4 |

Table 4.14: Comparison between induced currents resulting from the closed loop and open loop configurations.

| | | Crosstalk attenuation in dBs | | | | | | | |
|---|---|---|---|---|---|---|---|---|---|
| Freq [kHz] | | 20.5 | 21.5 | 22.5 | 23.5 | 24.5 | 25.5 | 26.5 | 27.5 |
| Measured Channel | 1 | 0 | -19 | -1 | -25 | -8 | -8 | -8 | -3 |
| | 2 | -14 | 0 | -17 | -22 | -17 | -6 | -12 | -8 |
| | 3 | -8 | -27 | 0 | -13 | -29 | -7 | -14 | -13 |
| | 4 | -30 | -32 | -18 | 0 | -27 | -33 | -32 | -18 |
| | 5 | -1 | -4 | -11 | -2 | 0 | -8 | -8 | -11 |
| | 6 | -5 | -9 | -9 | -30 | -21 | 0 | -35 | -17 |
| | 7 | -4 | -15 | -11 | -28 | -34 | -36 | 0 | -28 |
| | 8 | 0 | -10 | -14 | -13 | -33 | -17 | -30 | 0 |

Table 4.15: Attenuation of induced currents in each coil when using closed loop current control.

## 4.9. Microcontroller Implementation Results

Here we present the performance of the Phase 2 implementation of the system. For this setup, the NI DAQ card was replaced with a low cost Arduino Due microcontroller which was also used to implement the demodulation process [141]. A novel undersampling method was used which allowed more time between samples for the demodulation calculations.

### 4.9.1. Undersampling Examples

To demonstrate the operation of the undersampling technique, a test signal was sampled using a sample rate of 8 kHz and 160 kHz for reference. An FFT was calculated and this is shown in Figure 4.37. The input waveform consists of the following frequencies:

$$f_i = [20.25\ 21.25\ 22.25\ 23.25\ 24.25\ 25.25\ 26.25\ 27.25]\text{kHz}$$

In this figure we see how the frequencies have been shifted from their correct positions to a smaller frequency band between 0 and 4 kHz ( $f_s / 2$ ). The order of the components has also been changed.

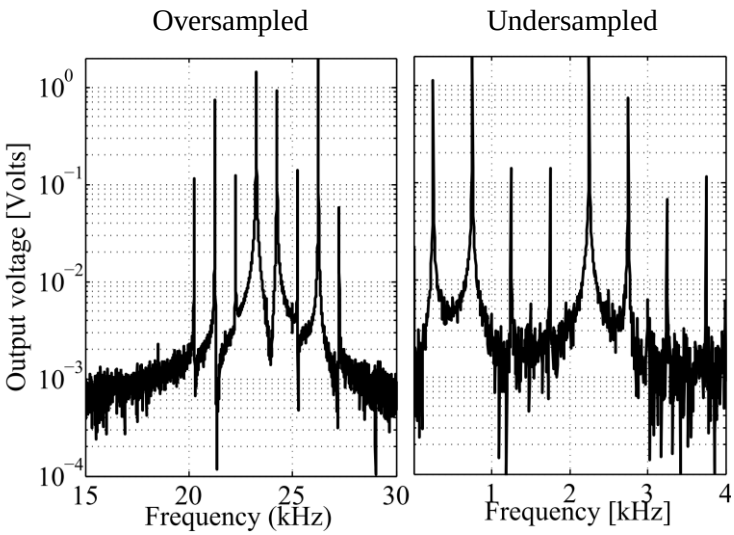



Figure 4.37: Comparing the frequency spectrum of an oversampled and undersampled signal. The first figure uses a sample rate of 160 kHz, while the second is sampled at 8 kHz. Note how the frequency of each signal component have been shifted to a band between 0 and 4 kHz. The new order of the components is now: [24.25, 23.25, 25.25, 22.25, 26.25, 21.25, 27.25, 20.25] kHz which appear from left to right on the undersampled waveform.

### 4.9.2. Asynchronous Demodulator Performance

To verify the performance of the demodulator system, voltage signals were directly applied to the ADC. A National Instruments 6259 DAQ card was used to generate test waveforms that were then demodulated using the Arduino microcontroller. The signal consisted of two frequencies components at 20.25 kHz and 21.25 kHz, where the 20.25 kHz signal was demodulated for these tests. Firstly the accuracy and time response for a variety of input amplitudes signals was analysed. These results can be seen in Figure 4.38. Table 4.16 shows the comparison of the DC value of the settled waveform and the input amplitude. A further test to verify the linearity of the demodulator was also carried out. Here a range of input amplitudes was tested and compared against the demodulator output. A best-fit line was calculated and matches closely to the data giving an $R^2$ value of 0.999. A small offset of 0.31 mV is also observed from the best fit line. The results of this test are shown in Figure 4.39. This offset is related to noise in the frequency range around the carrier frequency, which is shifted down to a DC value by the demodulator, as well as the effect of neighbouring frequency components.

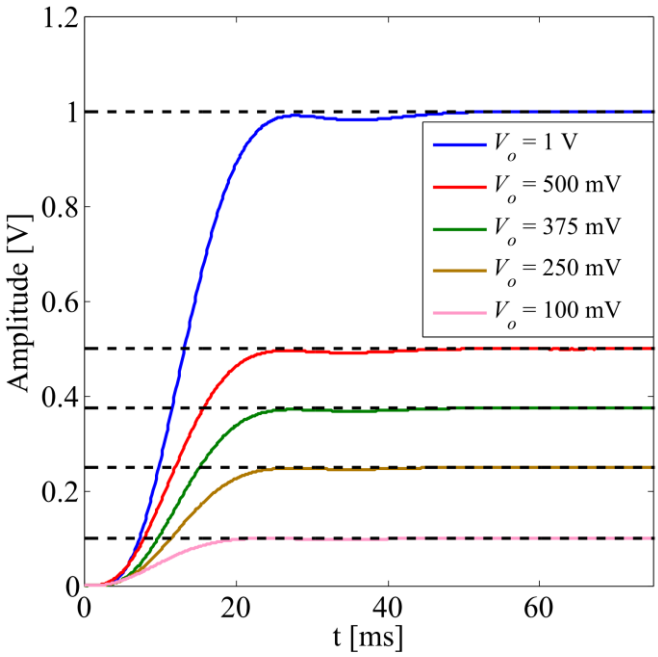



Figure 4.38: Time response of the demodulator for a series of input amplitudes. A 20.25 kHz sinusoid signal is measured in the presence of a second signal at 21.25 kHz. A sample rate of 125 µs is used. Five different amplitudes ranging from 100 mV to 1 V are shown. The filter takes approximately 60 ms to settle.

| $V_{in}$ [mV] | 100 | 250 | 375 | 500 | 1000 |
|---|---|---|---|---|---|
| $V_{out}$ [mV] | 99 | 248 | 373 | 498 | 998 |

Table 4.16: Demodulator performance.

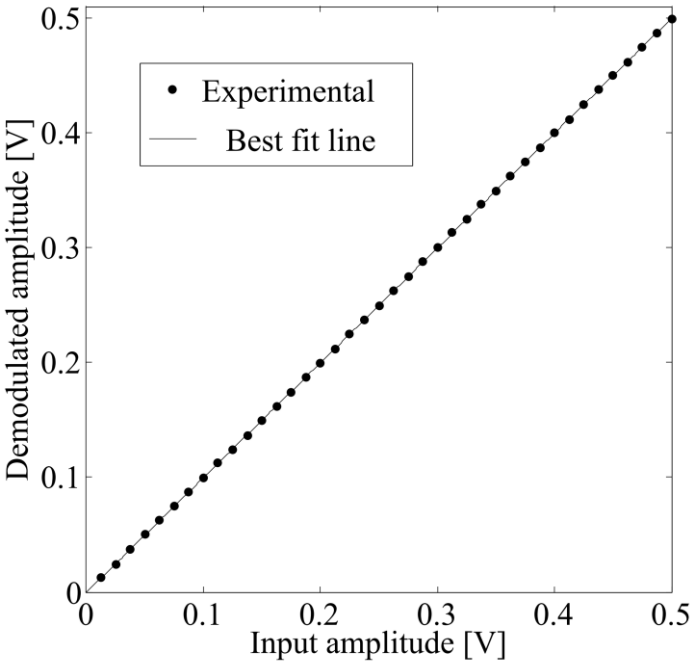



Figure 4.39: Linearity of demodulator system. A signal at 20.25 kHz was applied to the ADC and its amplitude varied from 12.5 mV to 500 mV. A 0.31 mV offset is observed when a best fit line is calculated.

### 4.9.3. Effect of Frequency Mismatch

As discussed in Chapter 3, the reference signal for each magnetic field component need not necessarily be at the exact excitation frequency. The size of this allowable frequency mismatch is dependent on the bandwidth of the filter and the type of filter used. Figure 4.40 shows the demodulator output for a range of frequency mismatches, for an input signal with amplitude of 100 mV and a varying input frequency. We see that the demodulator has a flat output for a range of approximately ±15 Hz. The bandwidth frequency range is directly proportional to the bandwidth of the lowpass filter used to remove the other frequency components. A Butterworth filter has the advantage that it has a flat passband, meaning that there is little variation over the passband of the amplitude. Figure 4.41 shows the frequency response of the IIR filter used in this case.

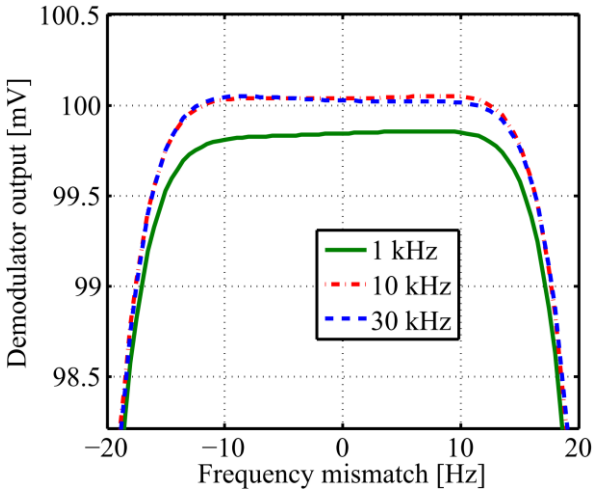



Figure 4.40: Effect of frequency mismatch of the demodulator when sampling at 8 kHz. Three signals at 1 kHz, 10 kHz, and 30 kHz were tested. The flat response of the Butterworth filter can clearly be seen here.

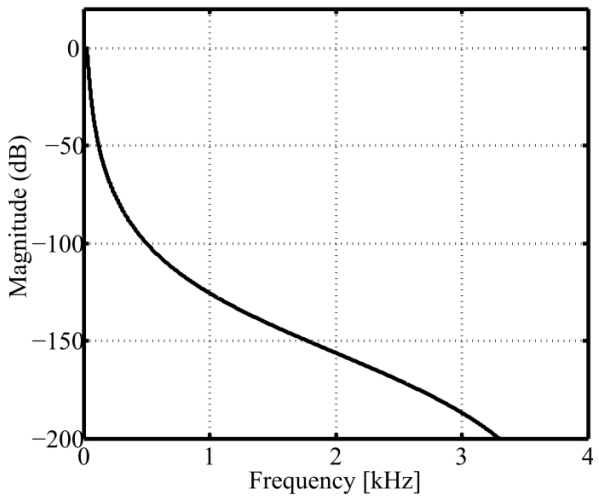



Figure 4.41: Frequency response of the IIR filter.

### 4.9.4. Undersampling Noise Tests

Figure 4.42 shows the results of a test to investigate the level of noise in the system and the increasing noise when sampling with different sample rates. The output of the sensor amplifier was sampled without an applied magnetic signal and an FFT was calculated. Each FFT contains 16384 points. The resulting FFT amplitude is normalised by the bandwidth of each frequency bin to give the noise voltage as a density. Table 4.17 shows the average noise density across the full frequency span. We see here that as the sample rate decreases, the noise generally increases. This is related to the noise folding back onto the sampled spectrum.

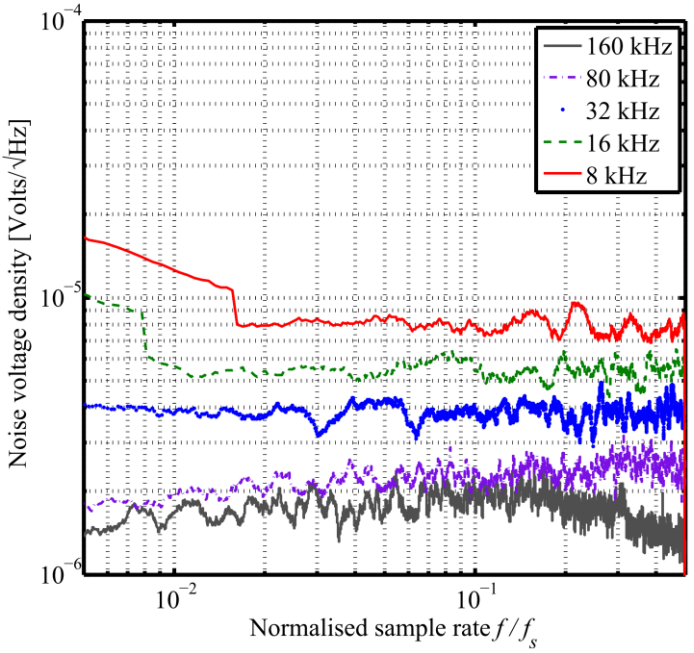



Figure 4.42: Noise spectrum of the analog front end with different sample rates. At lower sample rates higher frequency noise is folded back onto the lower frequencies, hence increasing the noise density.

| $f_s$ [kHz] | 8 | 16 | 32 | 80 | 160 |
|---|---|---|---|---|---|
| $V_n$ [μV/$\sqrt{Hz}$ ] | 8.1 | 5.6 | 3.9 | 2.4 | 1.7 |

Table 4.17: Background noise voltage density.

### 4.9.5. Scribble Tests

The results from each scribble test using the low cost Phase 2 implementation are shown in Table 4.18. The mean and standard deviation of each plane's dataset along each orientation was calculated from 500 test points as described in Section 4.2.2. The data was truncated to the errors within the 95$^{th}$ percentile to remove spurious results. This dramatically improves the calculated accuracy as it removes points resulting from errors during the acquisition process and any non-convergence of the tracking algorithm. A set of points from the tests are plotted in Figure 4.43.

| Plane No. | All $e_p$ [mm] | All $\sigma_{e_p}$ [mm] | 95% $e_p$ [mm] | 95% $\sigma_{e_p}$ [mm] |
|---|---|---|---|---|
| 1 | .9 | 1.7 | .7 | .5 |
| 2 | 1.2 | 2.6 | 0.8 | 0.7 |
| 3 | 1.3 | 2.2 | 1 | 0.9 |
| 4 | 1.5 | 1.6 | 1.2 | 1 |

Table 4.18: Scribble test results.

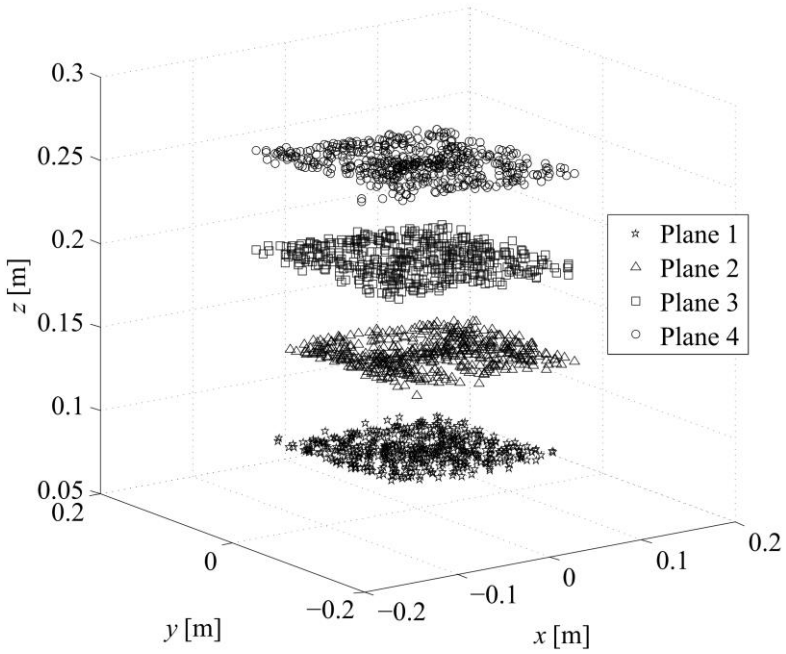



Figure 4.43: Results of scribble test on 4 planes. Ideally all points are located on each of the 4 planes, off plane points indicate errors. The average error was 1.2 mm away from the plane.

Considering the entire dataset of 6000 points, the mean error was 1.2 mm with a standard deviation of 2.7 mm. This improves to 0.9 mm and a standard deviation of 0.7 mm if we only consider points within the 95$^{th}$ percentile. If we take each plane in turn we see that the average error per plane increases as we move away from the emitter: 0.9 mm, 1.2 mm, 1.3 mm and 1.5 mm for planes at 6.5 cm, 12.5 cm, 18.5 cm and 24.5 cm from the transmitter respectively. Figure 4.44 shows a scatter plot of the errors of each test points. Clearly, the majority of the test points have an error of less than 2 mm. The increasing error with distance is also quite evident and expected.

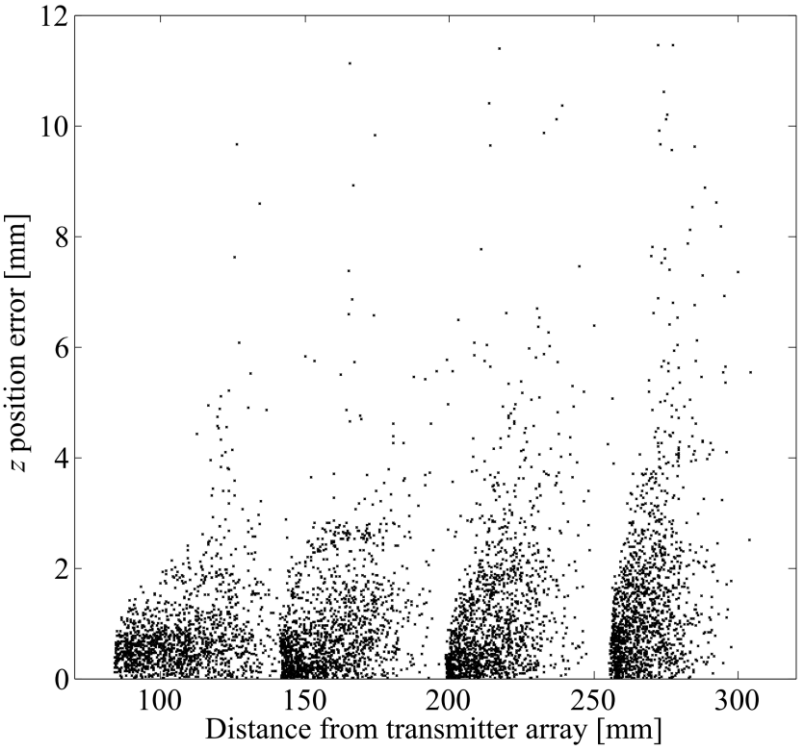



Figure 4.44: Scribble test data scatter plot. All 6000 points all plotted against the distance from the centre of the emitter array.

### 4.9.6. Static Position Tests

A second test, with the sensor rigidly positioned at a series of test points, was also carried out as detailed for the Phase 1 implementation in Section 4.2.1. This test was required as the scribble test method does not allow accurate testing of the orientation or RMS error of the system. 64 points were taken within a volume of approximately 20 cm × 20 cm × 20 cm, and results of this test are shown in Figure 4.45. Fewer points were taken as this process is far more time consuming to obtain the test points than the scribble tests as it involves manually moving the sensor to precise positions. The average RMS error was found to be 0.9 mm with a standard deviation of 0.6 mm. The orientation error resulted as 0.6° with a standard deviation of 0.4°.

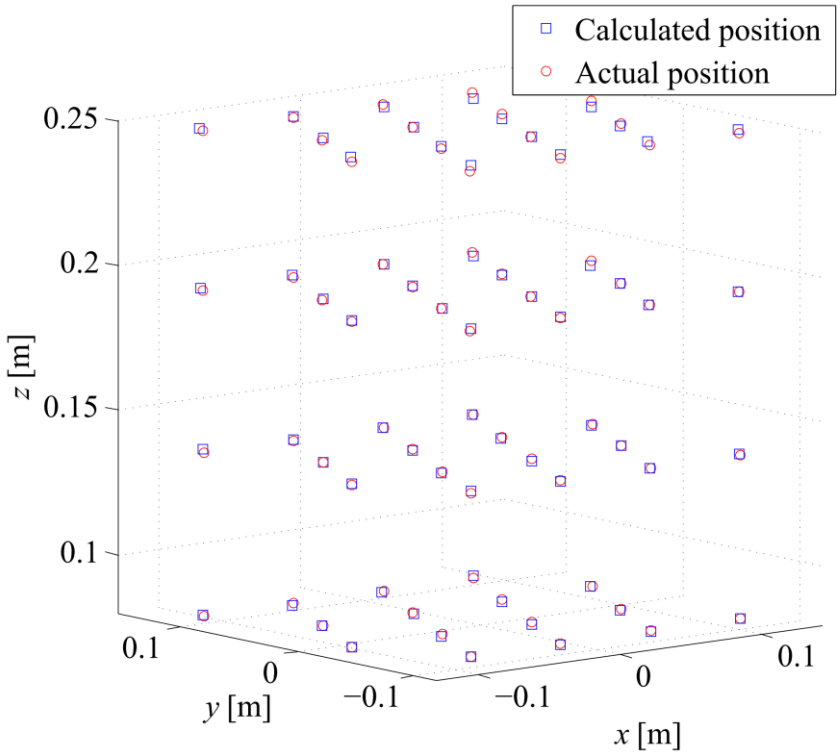



Figure 4.45: Results of a 64 point test. The sensor is statically positioned at a number of points in the operating region. The resulting RMS error is 0.99 mm.

## 4.10. Effect of Coil Size and Field Gradient

### 4.10.1. Experimental Tests

From the results of the position accuracy of the system, it was seen that position errors increase with distance from the transmitter, and beyond a certain distance the system effectively ceased to operate. The magnetic field gradient decreases with distance, and the smaller the gradient the more difficult to discern a position change as the magnetic field changes become progressively smaller. The gradient of a coil is dependent on the physical dimensions. In order to directly investigate the effects of the physical size of the transmitter coils and the associated magnetic field gradient, a PCB was manufactured with 9 coils of increasing size. Each coil was square with 25 turns each, with a side-length that varied from 40 mm up to 280 mm. The main aim of this test was to investigate if larger coils can allow increased range and accuracy for EM tracking. Figure 4.46 shows the PCB with each coil. Table 4.19 shows the electrical characteristics of each coil. Note that the 70 mm coil is identical to the coils used for the first 3 iterations of the EM tracking system.

To characterise the performance of each coil, a Thurlby Thandor TG1010A function generator was used to apply a 30 kHz sine wave excitation signal. The sensor was embedded in a Duplo block and moved in fixed steps away from the central axis of the coil board. The output of the sensor was amplified using a Texas Instruments INA129 instrumentation amplifier. A Powertek GP-102 gain phase analyser was used to measure both the current in

each coil and the induced voltage in the sensor after amplification. The current for each coil was adjusted until the induced voltage at the first test point was approximately same. This was to emphasise the effect of the gradient on the roll-off of the magnetic field, where the larger the coil, the slower its magnetic field decreases with distance.

The resulting measurements were processed in MATLAB. A least-squares algorithm was used to calibrate the recorded data to the magnetic field models of each coil. Figure 4.47 shows the recorded magnetic fields after calibration, while Figure 4.48 shows the magnetic field gradient for each test point. Figure 4.49 shows the percentage error of each test point in comparison to the theoretical model. Using the calibrated data, the position error from each measurement and coil was determined using a non-linear equation solver in MATLAB. The result of this test is shown in Figure 4.50 and this result is summarised for each coil in Table 4.20.

From the results it is seen that there is not a significant change in accuracy between each coil size. The resulting errors are quite low due to the prior calibration of the magnetic field models. Since the resulting errors are quite close the manufacturing tolerances of the Duplo blocks, the majority of the error is thought to be due to the experimental method and not related to the magnetic gradients. The standard deviation of the error is seen to increase with the size of the coils. The smallest coil is seen to have a larger error in comparison to the other coils (except the last coil), which may indicate that smaller coils are more prone to errors. However, it is important to consider that the smaller coils had a lower amplitude due to the faster roll-off of its field strength. The errors are also lower than that of the full 5-DOF system as the test was only along a single axis, hence there is less chance of errors due to the simplicity of the arrangement. Although there is not a major improvement in accuracy, the larger the coil, the more uniform the amplitude of the magnetic field over the region of interest. A lower input current or a frequency can be used as the magnetic fields do not degrade as significantly with distance. A lower dynamic range is also required by the system's ADC.

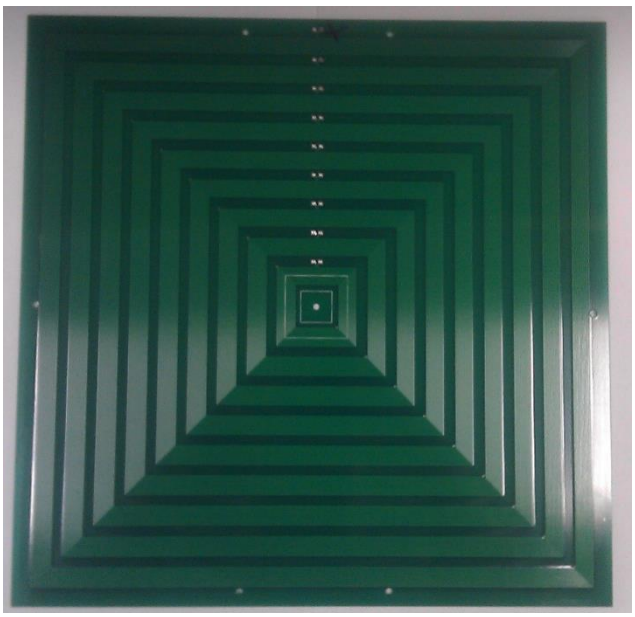


Figure 4.46: Multi-coil board for gradient tests.

| Side length [mm] | 40 | 70 | 100 | 130 | 160 | 190 | 220 | 250 | 280 |
|---|---|---|---|---|---|---|---|---|---|
| Resistance [Ω] | 1.83 | 3.56 | 5.16 | 6.84 | 8.44 | 9.97 | 11.47 | 12.89 | 13.87 |
| Inductance [μH] | 26.5 | 74.42 | 128.7 | 188.3 | 251.4 | 317.4 | 386.3 | 456.8 | 529.4 |

Table 4.19: Electrical characteristics of each coil used to investigate the effect of coil size.

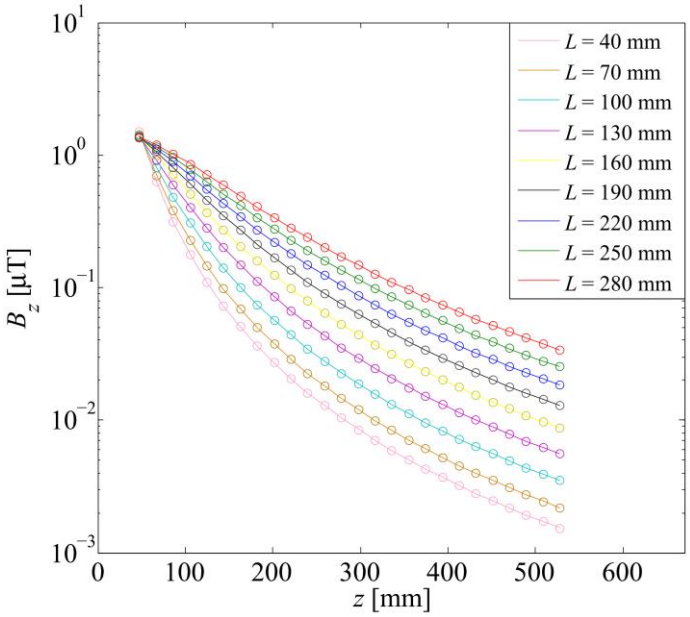



Figure 4.47: Magnetic field plots for each coil size showing the experimental data (circles) and the theoretical modelling (continuous lines) after calibration.

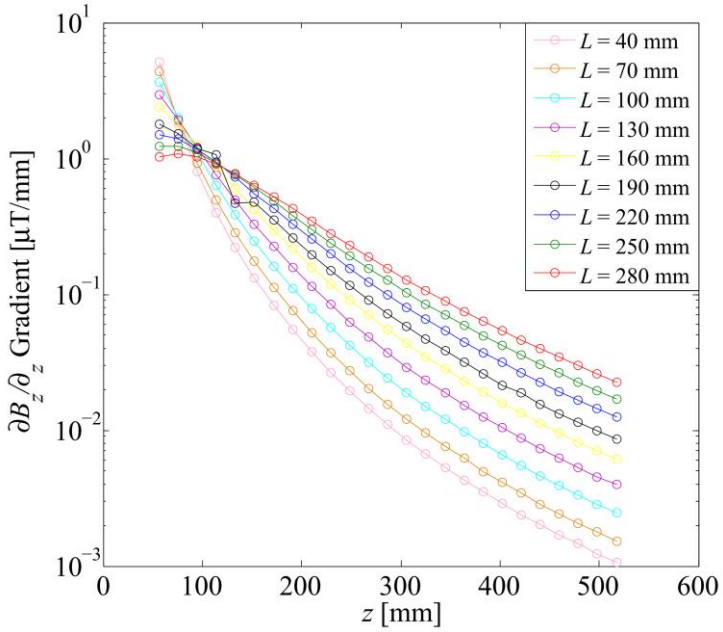



Figure 4.48: Experimental gradient of each coil.

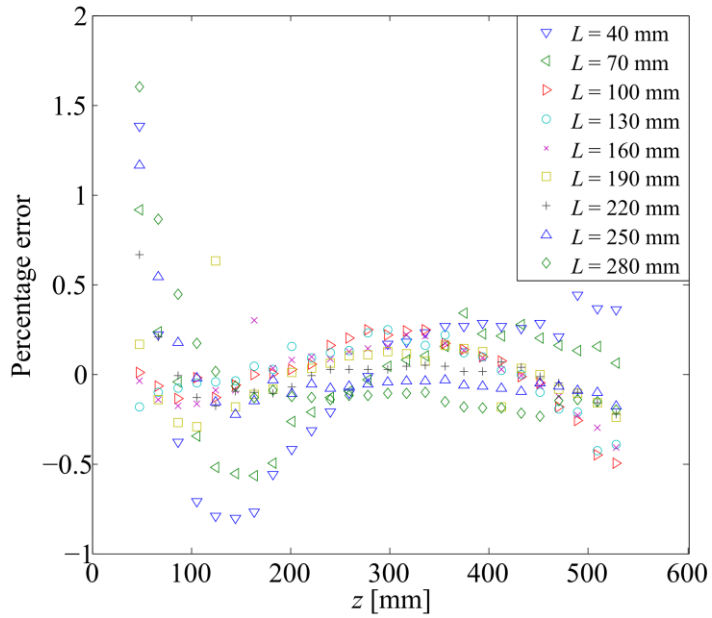



Figure 4.49: Percentage error between the experimental data and the model data for each coil size.

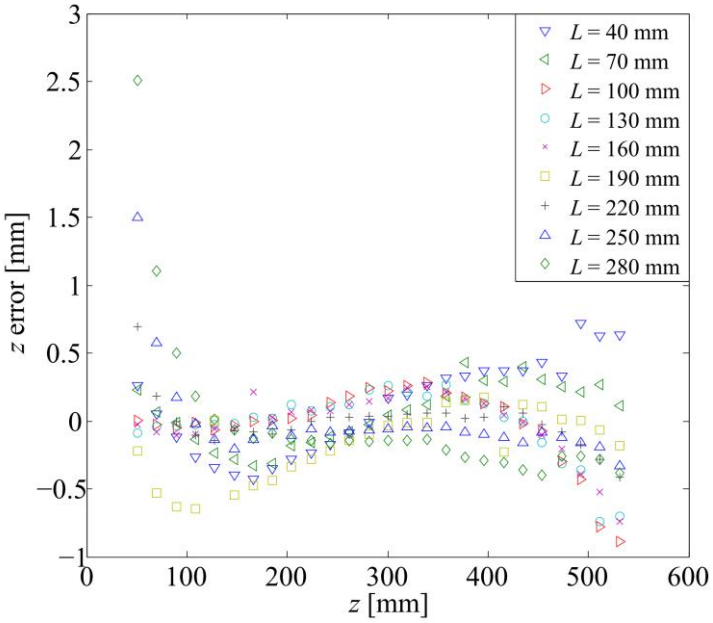



Figure 4.50: Position error in the z direction for each coil size.

| L [mm] | 40 | 70 | 100 | 130 | 160 | 190 | 220 | 250 | 280 |
|---|---|---|---|---|---|---|---|---|---|
| B error % | 0.39 | 0.25 | 0.14 | 0.14 | 0.14 | 0.14 | 0.09 | 0.14 | 0.24 |
| B STD % | 0.29 | 0.21 | 0.13 | 0.11 | 0.09 | 0.12 | 0.13 | 0.23 | 0.32 |
| z error [mm] | 0.31 | 0.19 | 0.18 | 0.17 | 0.17 | 0.22 | 0.11 | 0.18 | 0.34 |
| z STD [mm] | 0.17 | 0.11 | 0.22 | 0.19 | 0.16 | 0.20 | 0.15 | 0.29 | 0.49 |

Table 4.20: Table showing the percentage error of the magnetic field models and the resulting position error for each coil size.

### 4.10.2. Simulation Results

The experimental results shown in the previous section were carried using individual coils. In order to investigate the effects on the eight coil array used in our system, a simulation in MATLAB was carried out. Firstly, the effect of the coil size on the position accuracy when a constant 2 % error is applied to each simulated measurement was determined. The results of this test is shown in Figure 4.51. We see that for each coil size, the error increases with distance from the coil array, as was observed in all experimental results with the full system. Although here we see that the larger coil actually results in a larger error overall, the difference is not overly significant.

A common problem in EM tracking system is systematic errors resulting from detecting secondary magnetic field components through the connecting wires to the sensor and direct induction through the amplification circuitry, as well as spurious noise sources. To investigate these effects, a constant 100 pT offset was added to each simulated measurement. The results of this test are shown in Figure 4.52. In this case, we see that the larger the coil, the less effect a small offset has on the accuracy. This is as a result of the overall larger magnetic field over the operating region; hence a small offset has less of an impact on accuracy.

In conclusion, the larger coils perform better in terms of SNR. However they have worse performance when calibration errors are present. Assuming that the system is well calibrated, larger coils give better performance overall.

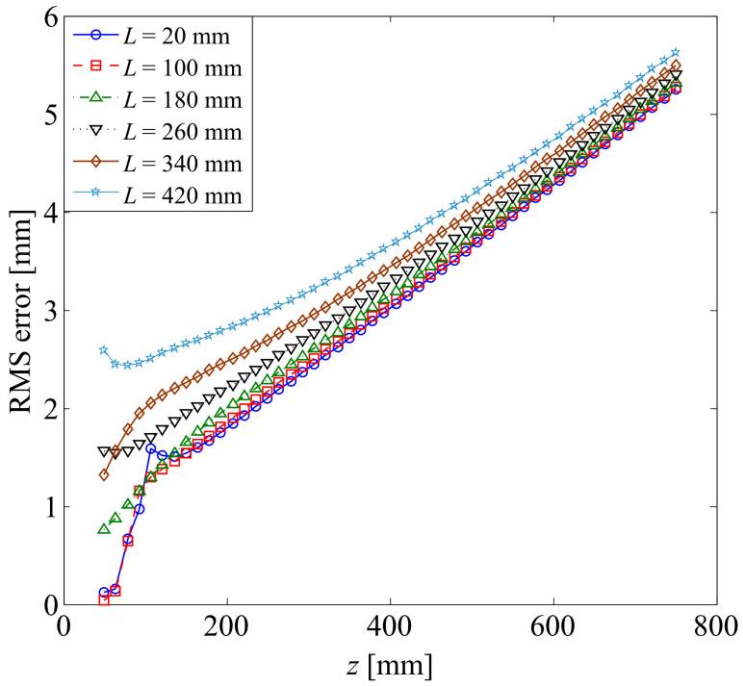



Figure 4.51: Simulated position accuracy with full coil array with different size coils.

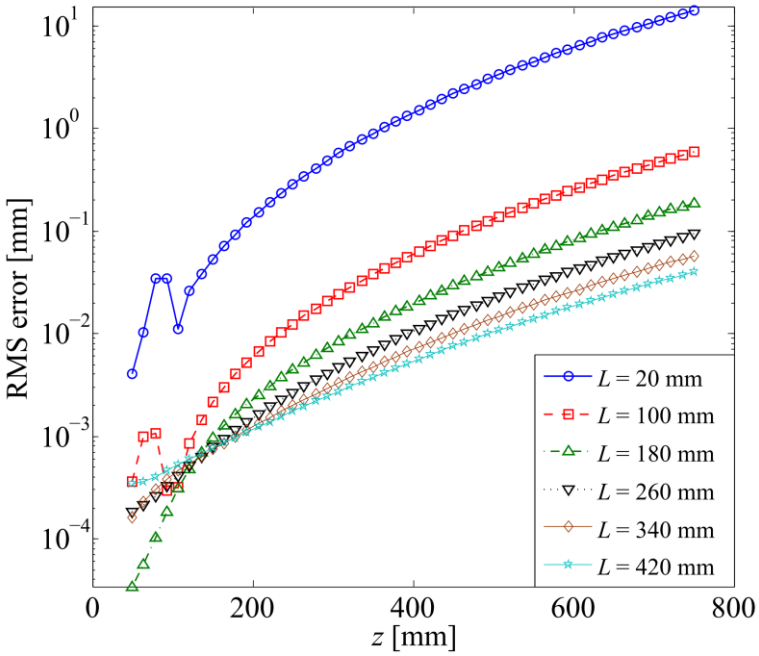



Figure 4.52: Simulated coil array error with constant field offset of 100 pT with different size coils.

## 4.11. Discussion: Phase 1 Implementation

### 4.11.1. System Accuracy

If we compare the results from the two accuracy testing methodologies, the static position

tests and the scribble tests, we see that scribble tests indicate improved accuracy. The error is reduced as only errors in *z* are considered, hence systematic errors due to stacking and tilting of the Duplo blocks is reduced. In the fixed position tests, the manufacturing tolerances of the Duplo blocks and small misalignment of the stacks of blocks contributes to errors in *x*, *y* and *z*. If we consider the deviation of each block to be approximately 200 µm, stacks of blocks can rapidly build up significant errors especially when considering errors in 3 dimensions.

If we consider the errors shown in Table 4.11, it is clear that the *z* directed sensors had a lower error. This is due to the fact that when the sensors are perpendicular to the coil board, the magnetic field in that direction is generally larger than in *x* or *y*. A larger SNR results, which increases the accuracy.

In Figure 4.20 and Figure 4.23, it can be seen that, in general, the position error increases with distance from the array. This is due to the roll-off in the field strength as the sensor moves away from the coils which again reduces the SNR and increases the error. A further reason for this increased error is the decrease of the gradient in the magnetic field, as small changes in the magnetic field are more difficult to resolve. It was observed that when the sensor is moved more than 35 cm from the coil array, the algorithm failed to find the correct position even when the measured magnetic fields matched with those predicted by the model to a high degree of accuracy.

The accuracy of our system is well in line with the accuracy of commercially available systems. The accuracy of the NDI's Aurora system is quoted as 1.1 mm RMS in a dome volume [88] while Ascension trakSTAR's system is 1.4 mm RMS [87]. This compares with our result of 1.2 mm as seen in Table 4.11. Table 4.21 shows a comparison between the accuracy of our system and those quoted in other research systems, our Phase 1 system is well within the norms of accuracy.

| Author | $e_p$ [mm] | $e_o$ [Deg] | Ref |
|---|---|---|---|
| UCC | 1.2 | 1 | |
| Schilstra et al | 1 | .5 | [72] |
| Hu et al | .6 | .26 | [73] |
| Song et al | 0.7 | 2.4 | [142] |
| Plotkin et al | 1 | .6 | [66] |
| Roetenberg et al | 8 | 5 | [61] |
| Hu et al | 1.8 | 1.54 | [99] |
| Hashi et al | .5-2 | n/a | [67] |
| Seiler et al | 1-2 | .5-1 | [107] |

Table 4.21: Comparison of quoted accuracy of research EM systems.

This level of accuracy is suitable for pulmonary navigation with the aim to steer devices to the outer reaches of the lung for cancerous lesions which are typically a few centimetres in

size [143]. Positioning in the lung is also simplified by the restrictive nature of the lung, i.e. the narrowing of the lung walls makes positioning easier as there are less possible sensor locations than in other surgeries.

### 4.11.2. System Stability

It has been shown that the constant current design results in a stable current through the coils. This in turn ensures that the associated magnetic fields are also stable. This gives the advantage that constant monitoring of the current is unnecessary and reduces the need for recalibration of the circuit over time. Even small variations in the field strength can dramatically affect the position accuracy. Hence a stable current improves the overall accuracy of the system.

### 4.11.3. Crosstalk Reduction

The cross talk interference seen present in the open loop system adds correlated noise to the sensor output which can be difficult and complex to account for. The average induced current of 1.01 mA can generate a significant amount of magnetic field interference considering that the desired coil current is approximately 160 mA (0.63% of the expected current). While this may seem small, every source of interference degrades the system performance. The inclusion of the closed loop current feedback dramatically reduces this interference making it negligible.

### 4.11.4. Dynamic Performance

It was shown that the system was able to sample at 22.6 Hz in a dynamic test, tracking the position of a pendulum. With improvements to the algorithm code and the magnetic field models, this sample rate could be increased. However, an update rate of above 20 Hz is more than sufficient for many tracking applications. As a comparison, the NDI Aurora system has a quoted update rate of 40 Hz [88]. Table 4.22 shows a comparison with the reported update rates of a number of research systems for similar medical applications. For pulmonary navigation however, generally the instrument motion is relatively slow and gradual, hence our update rate is quite sufficient.

| Author | Update rate [Hz] | Ref |
|---|---|---|
| UCC | 22.6 | n/a |
| Paperno at al | 50 | [66] |
| Hu et al | 3-10 | [99] |
| Ge at al | 7 | [105] |
| Huo et al | 13 | [144] |
| Schlageter | 50 | [119] |
| Li et al | 35 | [126] |

Table 4.22: Comparison of update rates of research based EM tracking systems.

## 4.12. Discussion: Phase 2 Implementation

### 4.12.1. Undersampling

It is clear from the position accuracy of the system that undersampling is an effective method for detecting amplitude modulated signals. The major advantage of the present approach is that signals of much higher frequencies can be detected with relatively low sample rates. While for our system the signals of interest are less than 30 kHz, this methodology can easily be used with much higher carrier frequencies, well into the 100s of kHz, limited primarily by the analog bandwidth of the ADC. There are disadvantages to undersampling, most notably the increase in noise due to noise folding [145]. As the input bandwidth is folded back onto itself, the noise in and around the frequency of interest increases. From Table 4.17 we see that by increasing the sample rate from 160 kHz to 8 kHz, the noise increases by almost by a factor of 5. This in turn degrades the SNR by around 13.5 dB. The noise can be reduced with appropriate band limiting filters, but, in general, the noise increases as the sampling rate decreases. There is also an increased chance that a spurious signal can be shifted into the bandwidth of the signal of interest due to the nature of the frequency folding.

### 4.12.2. System Accuracy

From both the scribble tests and static positioning tests, we see excellent accuracy (<1 mm) in our system. In comparison with the Phase 1 system, the mean accuracy of the Phase 2 scribble tests has fallen from 0.6 mm (with a standard deviation of 0.6 mm) to 0.9 mm (with standard deviation of 0.9 mm) [146]. This degradation resulted from replacing our demodulation method from a precision DAQ card to a low cost ADC and microcontroller and the associated increase in noise due to the low sample rate used. Even with this reduction in performance, the accuracy of our system is well in line with the accuracy of commercially available systems as noted for the Phase 1 results. Considering the calculated standard deviation, the resulting worst case error is still close to that of these commercial systems.

### 4.12.3. Benefit of External ADCs

The use of dedicated ADCs typically has the advantage of higher resolution and precision compared to those often found embedded within MCUs. Many modern MCUs use digital averaging to increase the resolution. For example the Cortex M4 uses 12-bit ADCs but uses averaging to increase this to 16-bit [147]. This approach introduces increased noise compared to true 16-bit ADCs [148]. The external ADC also has the advantage that there is better isolation from the high frequency clock noise of the processor. MCU ADCs are generally limited to unipolar operation. Had a bipolar ADC been used for this application, the need for the DC biasing and input attenuator could have been removed.

### 4.12.4. System Cost

Table 4.23 shows an approximate breakdown of the hardware costs for implementing our Phase 2 system, which totals to approximately € 660. This figure includes once off costs involved in low volume production of PCBs. Large scale manufacture would see a dramatic decrease in the system cost as the majority of system costs are related to PCB manufacture which makes up approximately € 500 of system cost. This could easily be reduced to below € 100 when manufacturing in large volumes. The emitter board forms a large amount of the overall cost due to the closed loop current control topology used. This has the advantage of stable current levels and cross talk reduction in comparison to resonant circuit approaches which offer less reliable operation [146]. The PCB is also a 4 layer board which adds to the cost.

| | |
|---|---|
| Emitter coil manufacture | € 100 |
| Arduino Due microcontroller | € 40 |
| Analog front-end | € 100 |
| NDI 5-DOF sensor | € 20 |
| Emitter driver board | € 400 |
| Total | € 660 |

Table 4.23: System cost breakdown.

## 4.13. Summary

In this chapter we have summarised the accuracy of the EM tracking system for Phase 1 and Phase 2 of the systems development. The position error from both systems was found to be less than 2 mm, and with reducing the cost of the demodulation and processing (Phase 1 to Phase 2), there is not a major degradation in the system performance. The system accuracy has been shown to be comparable to both commercial and research tracking systems, and this level of accuracy is well suited for its application in virtual bronchoscopy.

Other primary results include:

- Magnetic field modelling errors found to be less than 5 %
- Novel calibration procedure which minimises errors
- Optimum choice of solver parameters to ensure convergence and minimise calculation time
- Magnetic field stability over periods of 24 hours
- Adherence to ICNIRP regulations at distances greater than 12 mm from the transmitter
- Dynamic performance has been demonstrated with a simple pendulum experiment with an update rate of 22.6 Hz which can be increased to 64.1 Hz for offline data collection
- The transmitter was found to contribute noise to the system, however the overall noise voltage density is small enough as to not have a significant impact on the system performance
- Undersampling does not significantly degrade system accuracy while allowing for extended computation time between samples with lower sample rates
- Noise density increases with decreasing sample rates but does not adversely affect accuracy to a great extent
- Relatively low cost of implementation in comparison to commercial systems
- Coil size and gradient effects showed that the larger the coil, the more uniform the amplitude of the magnetic field over the region of interest. This reduces errors from noise sources and systematic magnetic field offsets.

# Chapter 5
# Pre-clinical EM Tracking Evaluation[‡‡]

## 5.1. Overview

In this chapter, the testing of the system in a pre-clinical setting is evaluated. This serves as a precursor for future clinical work through animal and, eventually, human trials. The EM tracking system is tested in a breathing lung model to verify its performance in a realistic setting. This chapter details the operation of the breathing lung model, registration of the tracking coordinate system to the lung model and the results of navigation through the airways.

The following summarises the main results:

- Using a landmark based registration algorithm, a mean registration error of 2.9 mm resulted.
- Using a novel hybrid registration algorithm, the registration error was found to be 4.1 mm.
- During navigation of the primary airways after registration, 94.3 % of the test points were found to be within the airway model.
- The primary source of errors in the system is misalignment between the lung model and the CT scan of the lung. This can be easily mitigated by scanning the model directly before the experiments to minimise changes in the physical position of the lungs.
- As expected, breathing motion causes larger errors in the position. Displacements of up to 10 mm are typical with a standard breathing cycle.

## 5.2. Clinical Background

Lung cancer accounts for the largest portion of deaths arising due to cancer with over one

[‡‡]This chapter is based on K. O'Donoghue, A. Corvó, P. Nardelli, C. O'Shea, K. A. Khan, M. Kennedy and P. Cantillon-Murphy, "Evaluation of a novel tracking system in a breathing lung model", *36th Annual International Conference of the IEEE Engineering in Medicine and Biology Society*, Chicago, Illinois, USA, August 26-30, 2014.

million people dying worldwide from the various forms of lung cancer each year [15]. The main cause of lung cancer is smoking. However other contributing factors including exposure to asbestos, family history, high levels of air pollution and radon gas to name but a few [149]. There are two common forms of lung cancer, non-small cell lung cancer (NSCLC), which is the most common making up around 80 % of reported cases, and small cell lung cancer [150].

There are a range of methods used for detecting lung cancer, most notably CT scans, chest x-ray, and positron emission tomography (PET) [151]. CT however is the most common method as it gives good resolution and cancer nodules can easily be identified.

In order to diagnose lung cancer, a biopsy is typically carried out. The gold standard for lung biopsy of suspected cancerous peripheral (hard to reach) nodules is the CT-guided biopsy [152]. The procedure has relatively high complication rates (*e.g.*, 5 - 40 % pneumothorax) [153], patient radiation exposure and higher cost compared to endoscopic biopsy. Commercial platforms such as Broncus and SuperDimension offer virtual reality systems combining CT data with GPS-like tracking technology for visualisation and guidance during endoscopic biopsy [108], [154]. However these systems (i) have not displaced CT-guided biopsy in the case of peripheral nodules and (ii) suffer from the spatial limits of mechanically-driven (*i.e.*, cable) navigation in narrow (*e.g.*, 2 mm) bronchi [155].

Currently, the least invasive method of accessing suspect nodules for biopsy is flexible bronchoscopy. This procedure is carried out on a patient under conscious sedation and involves the entry of a flexible bronchoscope into the trachea via the mouth or nose, guidance is achieved using cables. However this method is of limited use when applied to peripheral lung nodules, as bronchoscopes are typically too large and as result visualisation is limited [13]. Flexible bronchoscopy is noted for having very low sensitivity when the peripheral legions are less than 2 cm in diameter [156]. The rate of successful diagnosis from standard nonsurgical techniques available for peripheral lung nodules is less than 30 % [108]. By providing EM tracking and 3D virtual display of instrument position, peripheral regions become more accessible.

Other more invasive methods for lung biopsy include needle biopsy, where a needle is inserted through the chest wall to sample tissue. Typically this approach is used if the tumour is located near the outside of the chest. Open biopsy is where the surgeon makes an incision between the ribs and directly samples lung tissue while video assisted thorascopic surgery (VATS) is where a scope is manoeuvred through a small incision in the chest to sample suspect tissue [157].

By creating an alternative, minimally invasive approach for lung biopsy and cancer diagnoses, there are considerable benefits to patients in terms of early diagnosis and reduced trauma resulting from invasive procedures. In particular, navigation to peripheral lung regions, where many early stage cancers develop, using standard methods have limited

success [158].

## 5.3. Portable EM Tracking System

To facilitate the pre-clinical testing, the EM tracking system was reconfigured into a more portable setup. This version of the system is referred to as Phase 3. The main change from Phase 2 is that the data acquisition system now utilised a NI USB DAQ card instead of the custom ADC and MCU unit that made up the Phase 2 system. The demodulation is now also completely implemented in MATLAB using a more efficient demodulation scheme as described in Chapter 3. The USB DAQ allowed the use of a laptop computer for collecting the relevant data, which helped with the portability of the system. The USB DAQ was used to simplify the implementation in place of the MCU undersampled demodulator. This was to simplify the system in case any quick changes were required to the demodulation scheme.
The transmitter was also now mounted into a Perspex enclosure that measured 2 cm thick. This allowed the transmitter to be positioned below the region of interest and not interfere with the workspace. For calibration, a Lego Duplo baseplate can be directly mounted onto the transmitter which allows for test points to be easily gathered in an accurate fashion. The new transmitter is shown in Figure 5.1. All the electronics, as well as the DAQ system were placed in a single enclosure to make moving the system easier. This enclosure is shown in Figure 5.2 and Figure 5.3. The full system can be seen in Figure 5.4.

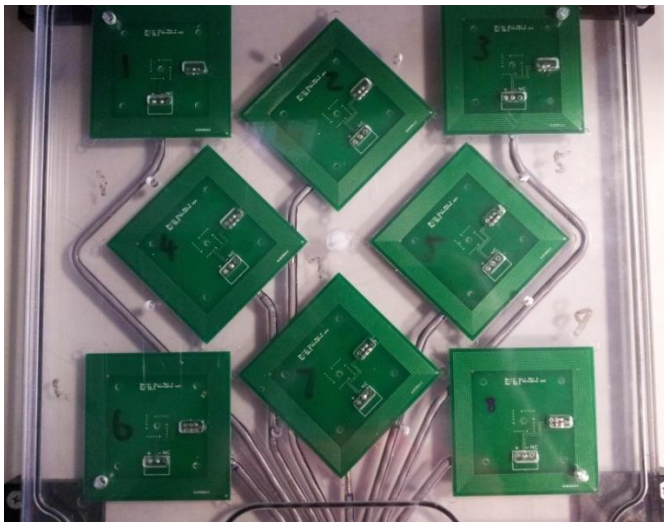


Figure 5.1: Perspex enclosure for the transmitter which measures 2 cm × 30 cm× 30 cm.

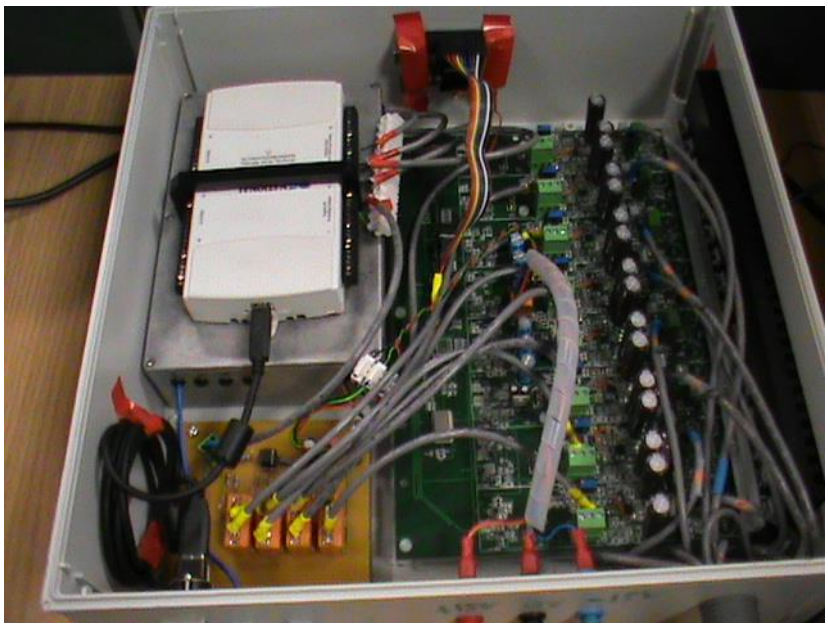


Figure 5.2: Electronics enclosure for the system which houses the coil driver circuit, current waveform summing circuit, sensor amplifier and USB DAQ.

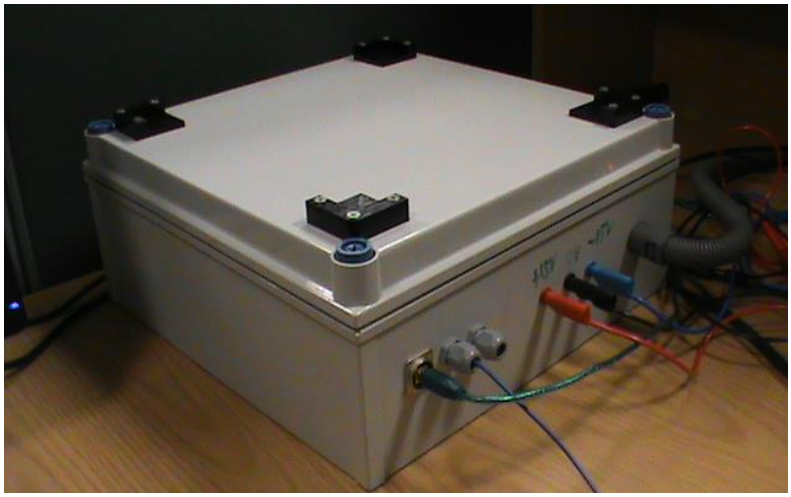


Figure 5.3: Electronics enclosure with sensor, power, transmitter and USB ports.

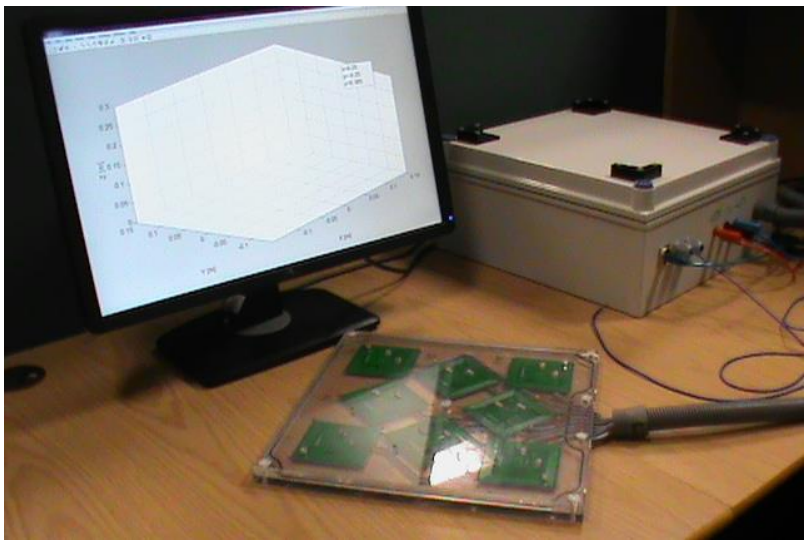


Figure 5.4: Full system showing the electronics enclosure, transmitter and display (connected to a laptop).

## 5.4. Inflatable Lung Model

A BioQuest Inflatable Lung kit (Nasco, Fort Atkinson, WI) was used as a phantom for evaluating the EM tracking system. These kits comprise of plasticised pig lungs and can be inflated to various levels as required. The lungs are placed in a vacuum chamber, with the trachea connected to atmospheric pressure. When the chamber is evacuated, the pressure differential between the outside and the inside of the lungs causes them to inflate. Venting the chamber to the atmosphere equalises the pressure which causes the lungs to collapse to an uninflated equilibrium form (see Figure 5.5 and Figure 5.6). The lungs were made to inflate and deflate in a programmable way to simulate standard breathing patterns. An Arduino Uno microcontroller was used to enable a set of solenoid valves (AD612 by CS Fluid Power) to control the lung inflation level. One valve connects the vacuum pump, while another is used for venting the chamber as seen in Figure 5.5. To set the breathing cycle, two dials are connected to the microcontroller. One sets the overall period of the cycle while a second sets the inflation time as a percentage of the period. This simple and low cost solution proved very effective in simulating the human breathing pattern. A vacuum sensor was attached to the vacuum chamber for recording the exact pressure used during inflation.

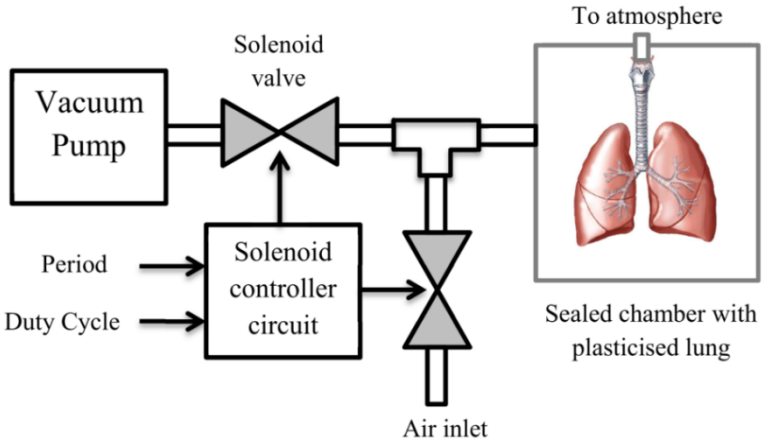



Figure 5.5: Lung breathing apparatus. A set of solenoid valves are used to control the pressure in a sealed vessel. A transistor circuit controlled by a microcontroller is used to enable each valve in sequence to replicate the human breathing cycle.

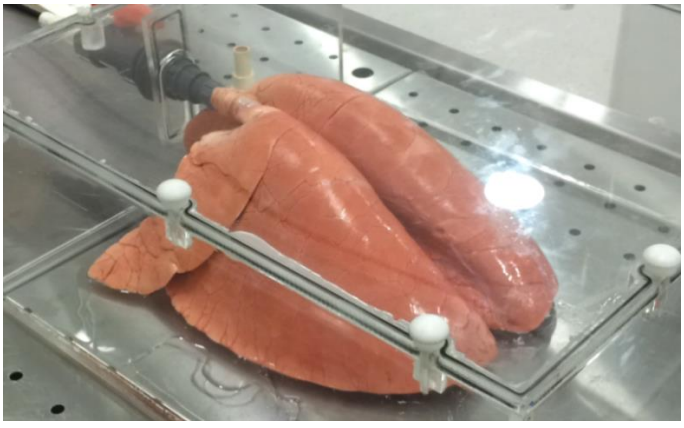


Figure 5.6: Plasticised pig lung when fully inflated.

## 5.5. 3D CT Lung Models

A CT scan (0.65 mm resolution) of the lungs in the inflated state was used to generate a 3D model [159] of the main airways which was then used to visualise the sensor's position in 3D.

A GE Discovery CT750 CT Scanner was used to scan the inflated lung model inside its vacuum chamber. The scanner used can be seen in Figure 5.7. To reduce artefacts in the scan, the lungs were raised away from the high density Perspex housing using a low density packing foam.

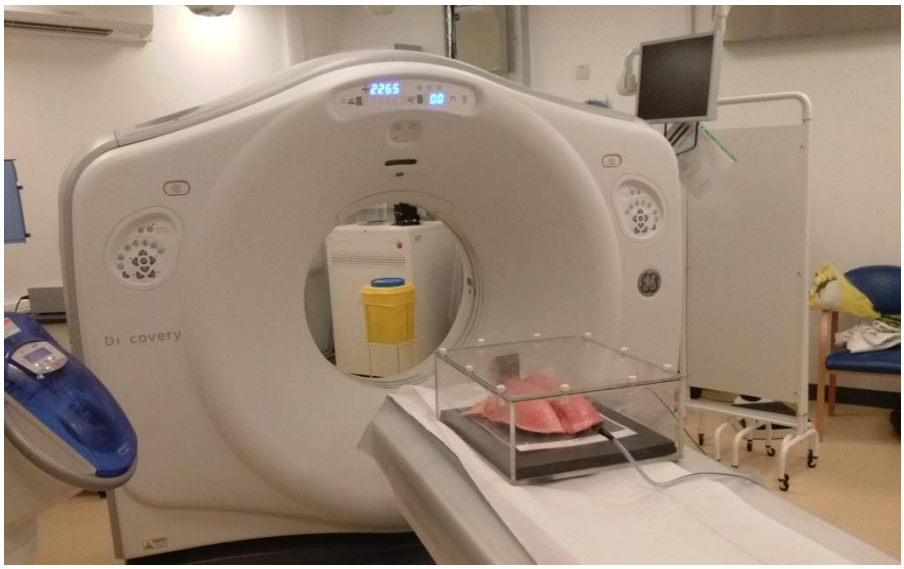



Figure 5.7: GE Discovery CT750 CT scanner and the inflated lungs within the vacuum chamber. A scan resolution of 0.65 mm was used for the scan.

To ensure that the lung model matches the CT scan as much as possible, a photograph of the lungs in their uninflated position was taken. This image was then printed to scale, laminated and placed at the base of the vacuum chamber. Every time the lungs were placed in the chamber, the uninflated lungs were positioned to match the position of the picture. By maintaining the same pressure as recorded during the scan, the lungs should nominally be in the same position, although over time the lung's will change due to wear and tear. To reduce errors, the CT scan should be taken as close to the experiment time as possible. Ideally the experiment would take place directly after the scan, without moving the lungs. Figure 5.8 shows the vacuum chamber with the lungs before the CT scan in both the inflated and deflated state. Below the lungs, the laminated figure can be seen.

(a) (b)

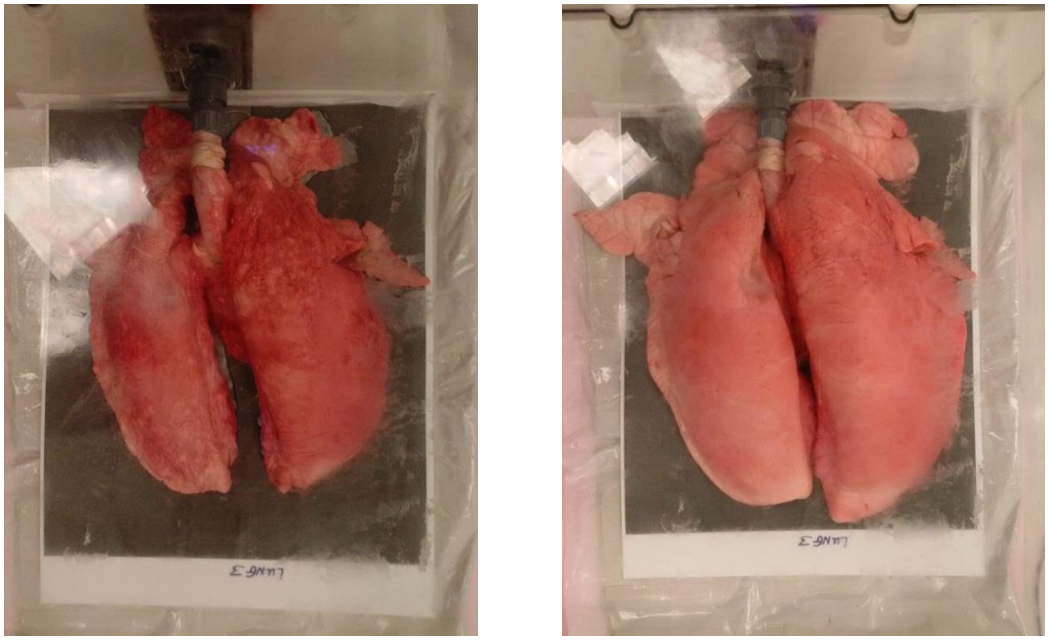


Figure 5.8: The inflatable lung model setup for the CT scan when (a) inflated and (b) deflated. Below each lung there is a laminated scaled image of the deflated lungs used for lining up the model in a repeatable manner.

A custom segmentation algorithm was used to generate the 3D model. This algorithm takes the CT scan data and calculates the 3D reconstruction. This was implemented using a combination of 3DSlicer and Python [159]. Figure 5.9 shows an example of a 3D model of the pig lung using this segmentation algorithm.

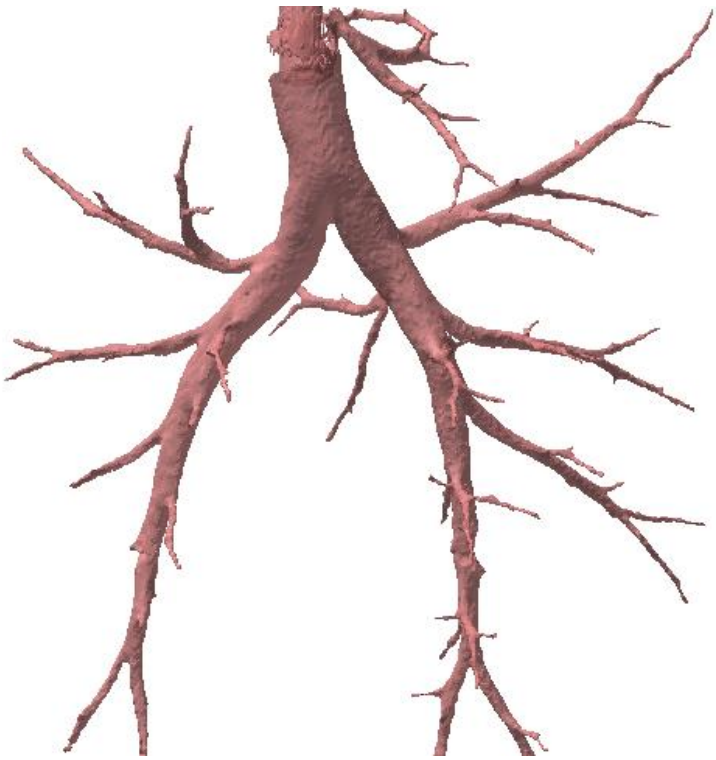


Figure 5.9: Segmented model of the breathing lung model.

## 5.6. Registration

### 5.6.1. Overview

Registration refers to the process of transforming a set of points in one coordinate frame of reference to another. In our application, this involves taking the position and orientation data from the EM tracking and system and transforming this data to the frame of a model for the navigation region. The navigation region in this case is the breathing lung model. For registration we determine a rotation matrix, translation vector and if required a scaling factor to transform between the EM tracking frame to the lung model frame. Once the points have been transformed, the position relative to the lung may be displayed in real-time to aid in navigation.

Numerous methods exist for registration of the coordinate frame of a tracking system and that of the underlying 3D models including basic point based approaches where natural landmarks or fiducials inside the real model are visually identified [160]. This method is also known as rigid registration and is typically appropriate when the imaged object is also rigid such as within the brain [161]. For bronchoscopic navigation, the video signal can be used to provide information to determine the required registration by matching the visual signal with 3D CT data [162],[163]. This method is also used in commercial systems such as the Broncus Lungpoint virtual bronchoscopy system [154]. Landmark-based registration often has the disadvantage of errors arising due to difficulty in accurately obtaining the registration data and it has also been shown that fiducial free schemes provide better accuracy [164].

In this section, we discuss two different registration methods that were used for registration of the breathing lung phantom, one based on a rigid landmark registration and a second hybrid algorithm that combines two fiducial free methods.

### 5.6.2. Rigid Landmark Registration Method

For registration using a landmark-based approach, the aim is to determine a transformation matrix which transforms a set of points in one frame of reference to another. In this case, a set of coordinates of easily identifiable locations in the lung are used to register the coordinate frame of the EM tracking system to that of the lung model.

This problem, which is sometimes referred to as Wahba's Problem [165], can be solved using Single Value Decomposition (SVD), which is a form of matrix factorisation, in a method known as the Kabsch algorithm [166]. If we consider two sets of data points given by **A** and **B** which are both in different coordinate frames, the aim of the algorithm is to find a translation vector $\boldsymbol{t}$ and a rotation matrix **R** such that (5.1) is satisfied.

$$\mathbf{B} = \mathbf{RA} + \boldsymbol{t} \tag{5.1}$$

**R** is a 3 × 3 matrix representing the 3 rotation variables and $\boldsymbol{t}$ is a column vector defined by (5.2) which represents translations in the *x*, *y* and *z* direction.

$$\boldsymbol{t} = \begin{bmatrix} t_x \\ t_y \\ t_z \end{bmatrix} \tag{5.2}$$

If we consider each point in **A** and **B** to be denoted by $\boldsymbol{a}_i$ and $\boldsymbol{b}_i$, then the cost function to be minimised can be represented by (5.2) where *M* is the number of test points in each dataset.

$$J(\mathbf{R},\boldsymbol{t}) = \sum_{i=1}^{M} \left\| \boldsymbol{b}_i - \mathbf{R}\boldsymbol{a}_i - \boldsymbol{t} \right\|^2 \tag{5.3}$$

The first step in the Kabsch algorithm is to subtract the centroid of each dataset, which results in (5.4).

$$\boldsymbol{a}'_i = \boldsymbol{a}_i - \frac{1}{M}\sum_{j=1}^{M} \boldsymbol{a}_j \qquad \boldsymbol{b}'_i = \boldsymbol{b}_i - \frac{1}{M}\sum_{j=1}^{M} \boldsymbol{b}_j \tag{5.4}$$

A covariance matrix, **H,** is then calculated using

$$\mathbf{H} = \sum_{i=1}^{M} \left(\boldsymbol{a}'_i\right)\left(\boldsymbol{b}'_i\right)^T \tag{5.5}$$

Using SVD, the covariance matrix **H** can be factorised into 3 matrices given by (5.6).

$$\mathbf{H} = \mathbf{USV} \tag{5.6}$$

The rotation matrix can then be calculated using (5.7) where **M** is given by (5.8).

$$\mathbf{R} = \mathbf{VMU}^T \tag{5.7}$$

$$\mathbf{M} = \begin{pmatrix} 1 & 0 & 0 \\ 0 & 1 & 0 \\ 0 & 0 & |\boldsymbol{U}||\boldsymbol{V}| \end{pmatrix} \tag{5.8}$$

Finally, the translation is calculated using (5.9) where $\boldsymbol{c}_A$ and $\boldsymbol{c}_B$ are the centroids of the datasets **A** and **B** respectively.

$$\boldsymbol{t} = \boldsymbol{c}_B - \mathbf{R}\boldsymbol{c}_A \tag{5.9}$$

The transformation matrix is then found using (5.10).

$$\mathbf{T} = \begin{pmatrix} \mathbf{R} & \mathbf{t} \\ 0 & 1 \end{pmatrix} \tag{5.10}$$

### 5.6.3. Landmark Registration Example

To demonstrate this algorithm, consider a set of 5 points in frame A and a corresponding 5 points in frame B. The algorithm finds the transformation matrix that minimised the distance between the two sets of points. The 5 points in frame A are distorted with noise to simulate errors in recording the points. Figure 5.10 shows both sets of points from frame A and B along with the noisy points in frame A that have now been shifted to frame B. This calculation took approximately 3.1 ms to calculate using MATLAB.

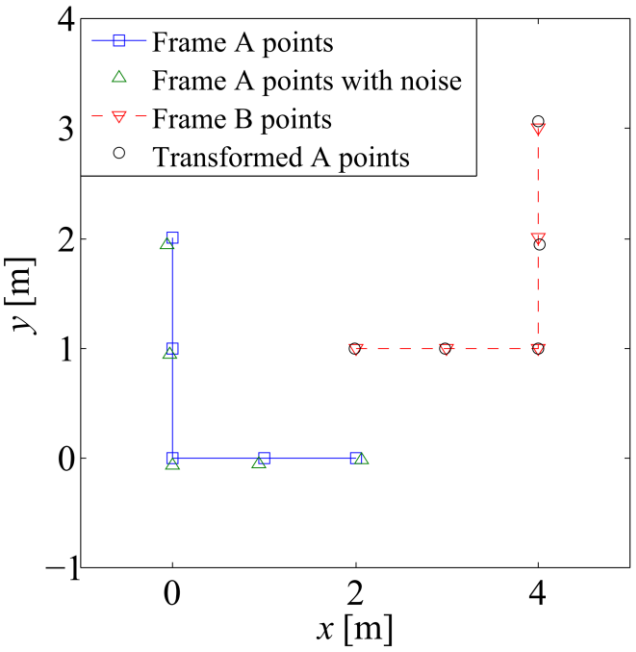



Figure 5.10: Example of landmark registration method in 2D.

### 5.6.4. Hybrid Registration Method

A second registration method was also investigated with our system. This algorithm is a hybrid between the iterative closest point (ICP) algorithm [167] and the in-volume maximization (IVM) algorithm [164]. ICP minimizes the distance between a number of test points inside the model to the centre line of the model. IVM attempts to minimize the number of points that are outside the model (i.e., those which are located outside the bounds of the airway).

In our system, the coordinate frame of the EM tracker is denoted by $\mathbf{T}_e$ and the 3D model frame $\mathbf{T}_m$. The aim of this algorithm is to find the transformation matrix $\mathbf{T}_m^e$ which minimizes the distance between a cloud of test points denoted by **A** (in the EM tracker frame) distributed along the airway and a vector function ***f*(B)** that contains the points **B** (in the lung model frame) that form the centre line of the airway. The number of points outside the airway model, $M_{out}$, must also be minimised. By forming an objective function given by (5.11), which is based on the mean Euclidean distance between each point in **A**, denoted by $\boldsymbol{a}_i$, and the centreline ***f*(B)**, as a function of a transformation matrix **T**, a non-linear 6 variable equation results (3 each for rotation and translation) is generated. **T** is comprised of a rotation matrix **R** which is a function of the three rotation variables shown in (5.13), and a translation vector ***t***, given by (5.14). The input vector to the objective function is given by (5.15).

$$J(\mathbf{T}) = \frac{1}{M}\sum_{i=1}^{M}\min(\left\|\mathbf{T}\boldsymbol{a}_i - \boldsymbol{f}(\mathbf{B})\right\|^2) \tag{5.11}$$

$$\mathbf{T} = \begin{bmatrix} \mathbf{R} & \boldsymbol{t} \\ 0 & 1 \end{bmatrix} \tag{5.12}$$

$$\mathbf{R} = \mathbf{R}_z\mathbf{R}_y\mathbf{R}_x = \begin{bmatrix} 1 & 0 & 0 \\ 0 & \cos\gamma & -\sin\gamma \\ 0 & \sin\gamma & \cos\gamma \end{bmatrix}\begin{bmatrix} \cos\beta & 0 & \sin\beta \\ 0 & 1 & 0 \\ -\sin\beta & 0 & \cos\beta \end{bmatrix}\begin{bmatrix} \cos\alpha & -\sin\alpha & 0 \\ \sin\alpha & \cos\alpha & 0 \\ 0 & 0 & 1 \end{bmatrix} \tag{5.13}$$

$$\boldsymbol{t} = \begin{bmatrix} x_t \\ y_t \\ z_t \end{bmatrix} \tag{5.14}$$

$$\boldsymbol{x} = (x_t, y_t, z_t, \alpha, \beta, \gamma) \tag{5.15}$$

This function has numerous local minima. To determine which solution is correct, the number of points outside the model is considered. If a high percentage of test points are found to be outside the 3D model, the equation solver is reset to a different starting point until the global minimum is found. To help the algorithm to converge faster, an initial registration can be carried out using the method described earlier in Section 5.6.2. This acts as a starting point for the algorithm. This algorithm was implemented in MATLAB using the *fminunc* function (which finds the minimum of an unconstrained multivariable function) and typical runtime was 1-2 minutes depending on the number of test points and the accuracy of the initial registration.

The advantage of this method is that rigid landmarks are not required for the registration. The required data can be gathered by simply navigating through the airways and gathering points. The larger the number of points gathered and more complex the path traversed, the more accurate the resulting registration will be.

### 5.6.5. Hybrid Method Example

Figure 5.11 shows an example of the hybrid registration algorithm in operation. A set of test points were randomly generated within the airway and transformed out of the airway to simulate incorrect registration. The mean distance to the centreline in this case is 7.98 mm with 57/174 points inside the airway. After applying the registration algorithm detailed in the previous section, the mean distance to the centreline decreases to 3.67 mm with 173/174 points now within the airway.

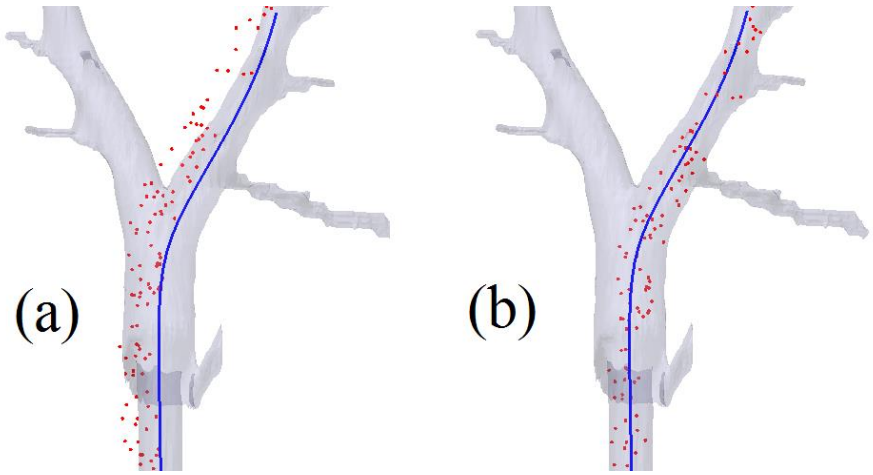



Figure 5.11: Simulated performance of the registration algorithm when applied to a 3D segmented lung model. The algorithm minimises the distance between each test point and the centre line as seen in the figure. (a) shows the point alignment before applying the algorithm and (b) shows the resulting transformed data set.

## 5.7. Experimental Setup

### 5.7.1. Bronchoscope

An Olympus 1T160 bronchoscope was used for the breathing lung tests. The unit has a 6 mm OD with an instrument channel diameter of 2.8 mm. The position tracking probe was inserted through the bronchoscopes instrument channel for the tests that follow.

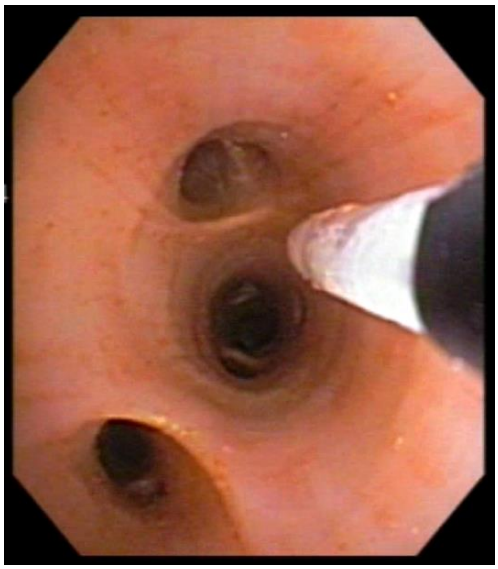


Figure 5.12: View from the bronchoscope inside the phantom with the sensor extended out from the distal end of the instrument port.

### 5.7.2. Real Time Display

The segmented CT model was imported into MATLAB and used to display the sensors position with real time updates after the registration algorithm has been applied. Figure 5.13 shows this display in MATLAB.

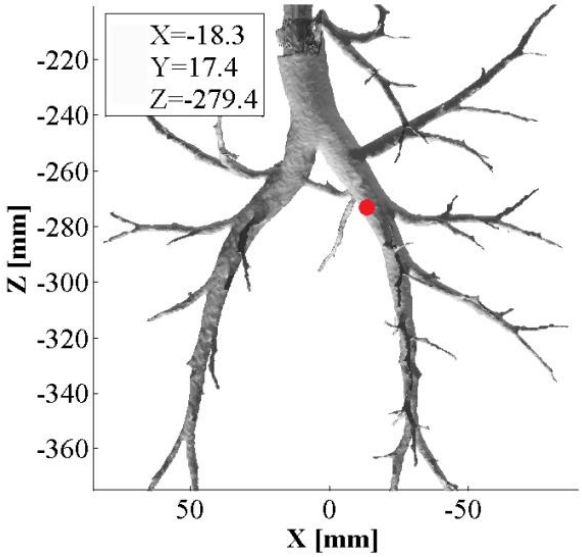



Figure 5.13: MATLAB display showing the 3d lung model and the calculated position (indicated with a red dot).

### 5.7.3. EM Tracker

The transmitter was mounted directly below the lung vacuum chamber during the tests. The transmitter was rigidly aligned with the vacuum chamber to reduce errors after registration due to relative motion between the chamber and the transmitter. Once in place, the transmitter and sensors were first calibrated and then the registration was implemented. Figure 5.14 shows the vacuum chamber positioned over the transmitter array.

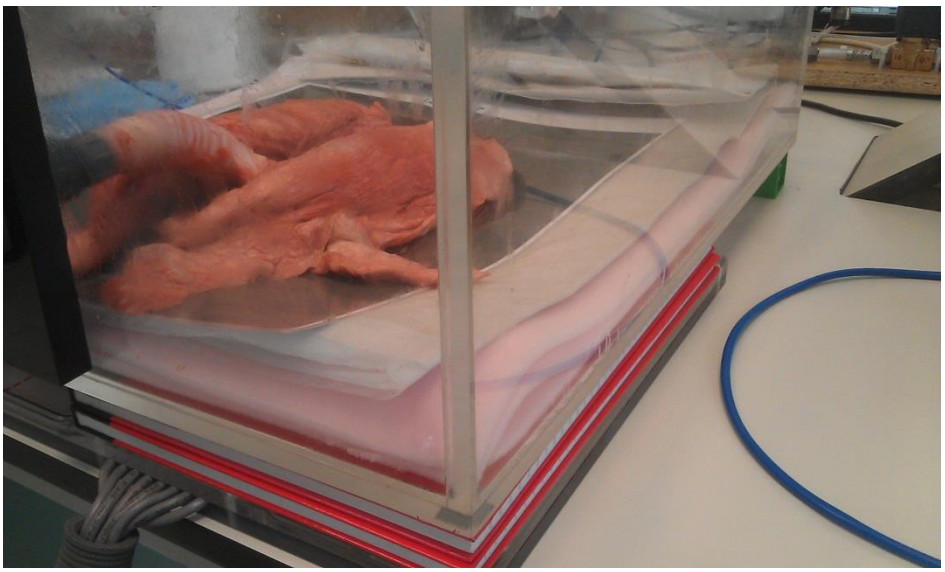


Figure 5.14: Lung chamber placed above the transmitter array. Additional spacers are added between the transmitter and the chamber to avoid saturation of the sensor.

### 5.7.4. Breathing Lung Model

For the majority of the tests, the lung was kept at a static inflation level. A vacuum sensor attached to the chamber was used as an indicator of the vacuum level. The pressure was

adjusted until it matched the levels recorded during the CT scan of the lung. A vacuum pressure of 1.1 kPa was used to fully inflate the lung. For the final test, cyclic breathing was enabled. The breathing cycle period was set to 5.3s, where simulated inhalation was enabled for 27% of the period, and exhalation occupied the remaining time.

## 5.8. Results

### 5.8.1. Landmark Registration

The first test carried out was to gather registration data for the landmark-based method. Eleven points inside the lung were identified as easily identifiable and hence were used as target points for the registration algorithm. Each point is a carina or branch point along the primary airway. A total of 11 points were gathered which included the main carina at the base of the trachea and 5 on each side of the lungs. Figure 5.15 shows the target points and the recorded points after registration. An overall registration error of 2.9 mm was calculated with a standard deviation of 1.5 mm.

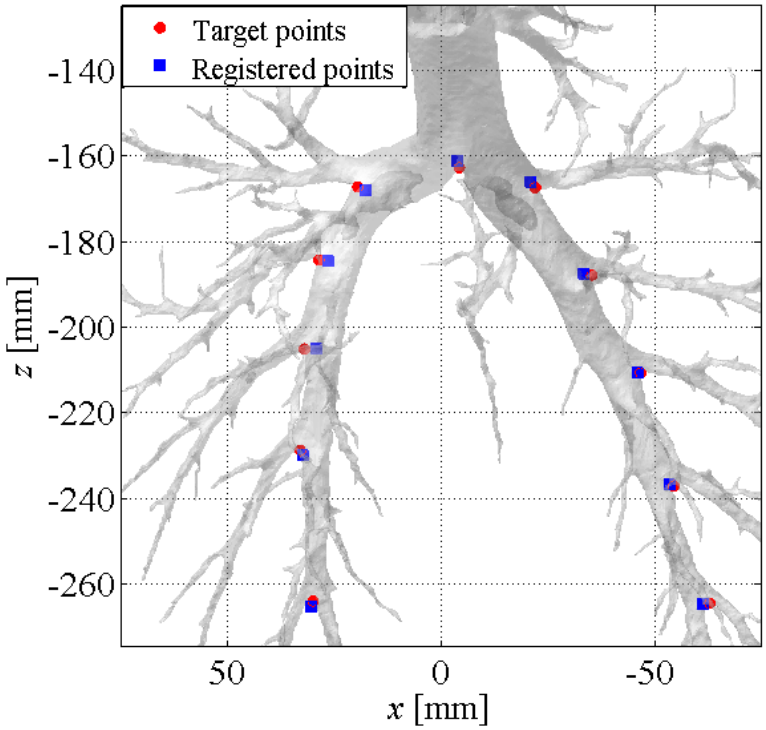



Figure 5.15: Landmark registration of the branch points away from the central airway. Overall registration error of 2.9 mm was recorded.

### 5.8.2. Navigation Accuracy

After registration, the airways of the lung were navigated and numerous test points gathered with the lung in its fully inflated position. Figure 5.16 shows the results of a navigation along the central airways. We see that the majority of points here are found to be within the airway

model. However accuracy decreases as the airways decrease in size. The primary source of error in these tests is misalignment of the lung model with the CT scan model. This is due to the difficulty in exactly matching the lung position with its position during the CT scan of the lung. To mitigate these errors, the tests inside the lung should be taken directly after the CT scan. Figure 5.17 shows the results when the sensor is navigated through the smaller airways. We see that, as before, along the central axis accuracy is maintained, but along the smaller airways, more and more points are found to be outside the airway model.

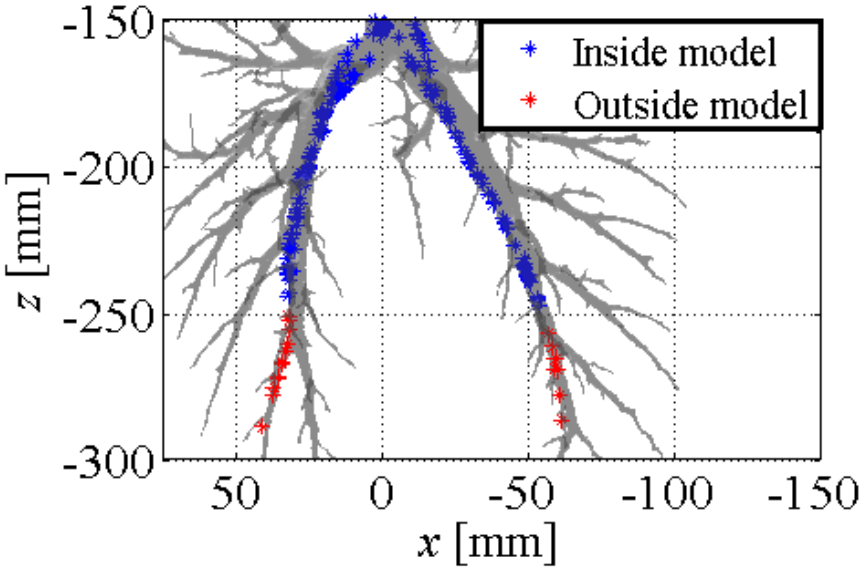



Figure 5.16: Overlay of points gathered during navigation of the main airway after registration. Erroneous points outside the model are generally due to positioning errors of the inflated lung model relative to the CT scan data. In this test, 94.3% of the 246 test points were found to be inside the airway.

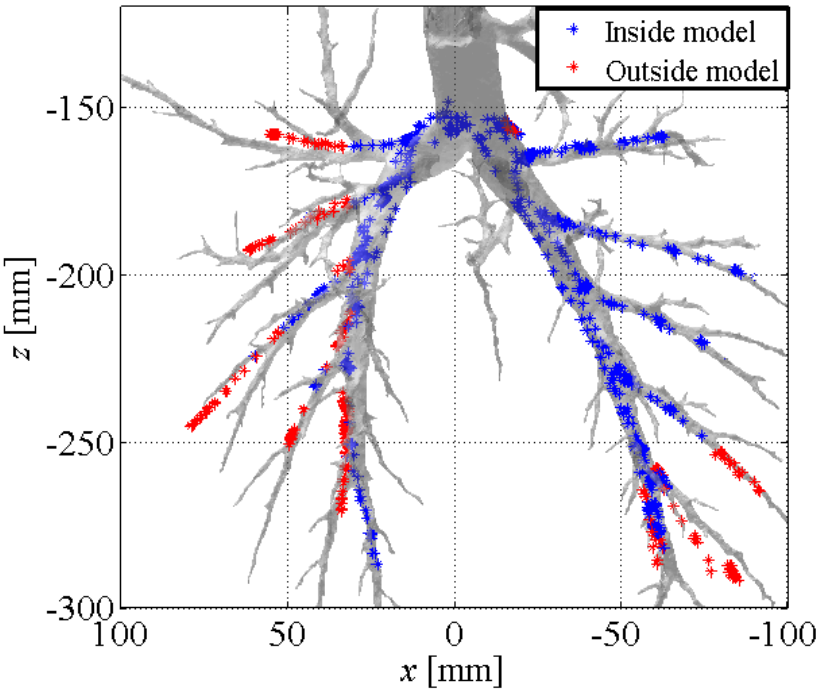



Figure 5.17: Results of a navigation of numerous airways. Accuracy decreases away from the main airways due to misalignment of the lung model with the CT scan model.

### 5.8.3. Hybrid Algorithm Registration

The sensor position data gathered along the main airway as shown in the previous section was used as the input point cloud for our hybrid registration algorithm. Using the previously calculated transformation matrix determined with the landmark registration method as an initial condition, the algorithm converged to a result in 192.3 s. Using this new transformation matrix, the registration error was again calculated which resulted in 4.1 mm mean error. When applied to the data gathered along the main airway, the resulting mean distance to the centreline was calculated as 2.7 mm, with a total of 83.2 % of the dataset found to be within the airway. Figure 5.18 shows the results for the algorithm with the centreline displayed along with the set of registered points. Hence, the hybrid algorithm, while taking a relatively long time to compute, gives similar performance to the landmark-based approach without the need for a specific registration protocol or touch-points during the registration.

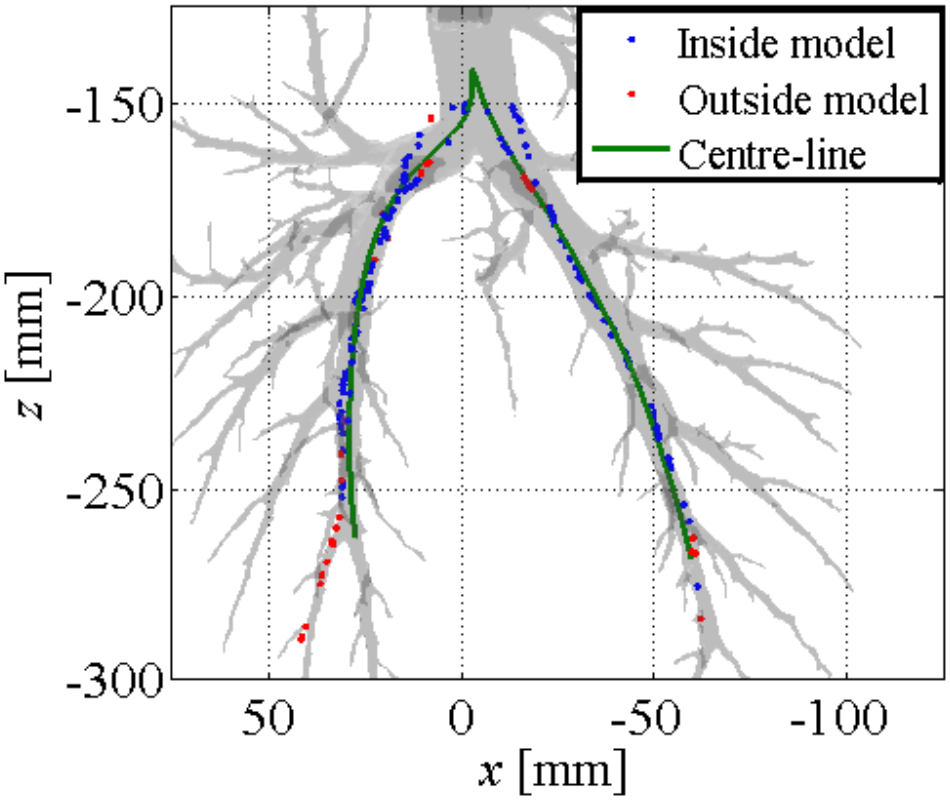



Figure 5.18: Results of the hybrid registration algorithm showing the centreline and the registered dataset. 83.4 % of the points were found to be within the airways.

### 5.8.4. Reaching the Target

The performance of the system in navigating to a particular target was evaluated. Two targets along a peripheral airway off the main airway was chosen. Figure 5.19 shows the overall trajectory of the sensor during this navigation and the two targets are also indicated.

The final sensor position was found to be within 2.6 mm of the first target and 3.2 mm from the second target. Figure 5.20 shows the motion of the sensor in *x*, *y* and *z* with respect to time and Figure 5.21 shows a screenshot of the system during this experiment where we can see the MATLAB real-time display and the bronchoscope view.

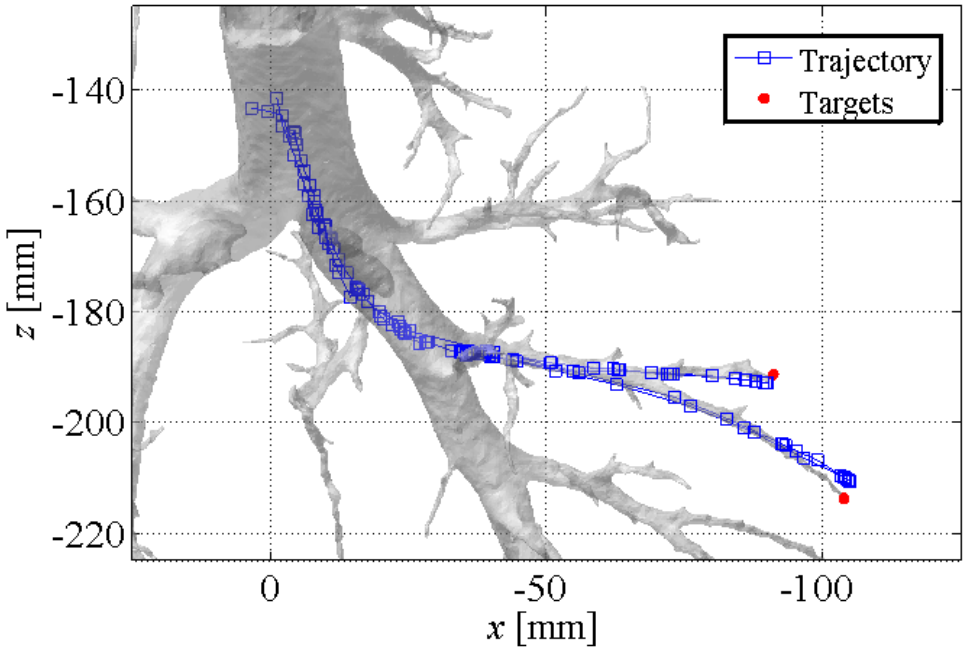



Figure 5.19: Shows the trajectory of a navigation between the trachea and the two target points. The sensor was calculated as being within 2.6 mm from the first target and 3.2 mm from the second target.

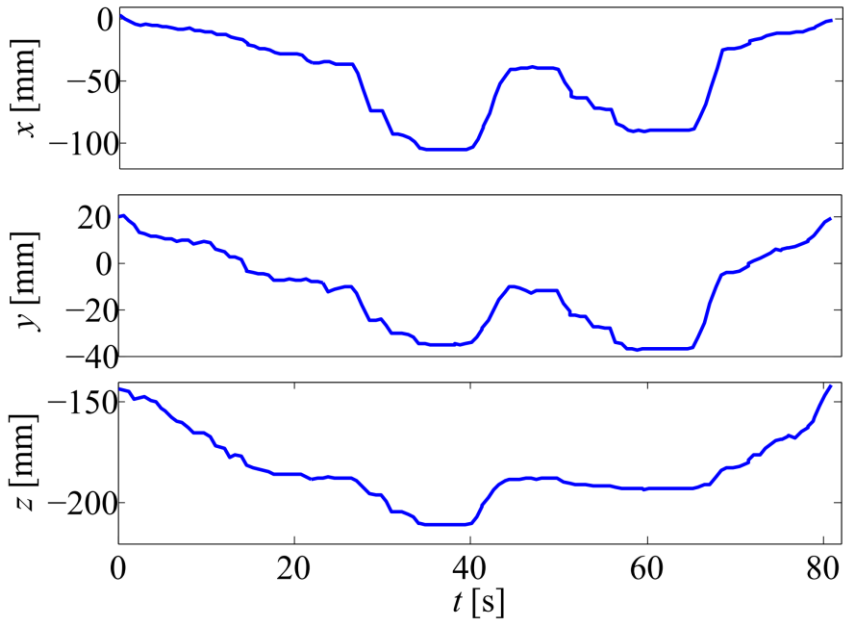



Figure 5.20: Motion of the sensor towards the targets in *x*, *y* and *z* with respect to time.

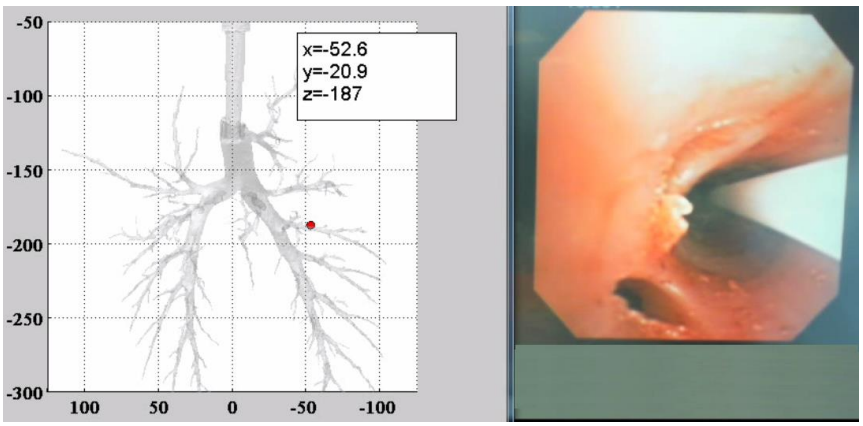



Figure 5.21: Screenshot of the navigation along this airway during the experiment.

### 5.8.5. Breathing Motion

Figure 5.22 demonstrates position tracker displacement experienced at various points within the lung when a standard breathing cycle is implemented. As expected, the amplitude of displacement varies depending on the position of the lung. Maximum displacement was observed at points more central to the lung model, while distal points and smaller airways experienced less. The amplitude of the displacement recorded was found to range from a few mm to less than 10 mm. This is in line with clinical test data from patients reported elsewhere [168], [169]. Figure 5.23 shows each vector component of the displacement versus time. We can see that the maximum displacement is observed in the *z* direction, which represents a vertical motion. This result is expected as when the lungs inflate they expand up and outwards.

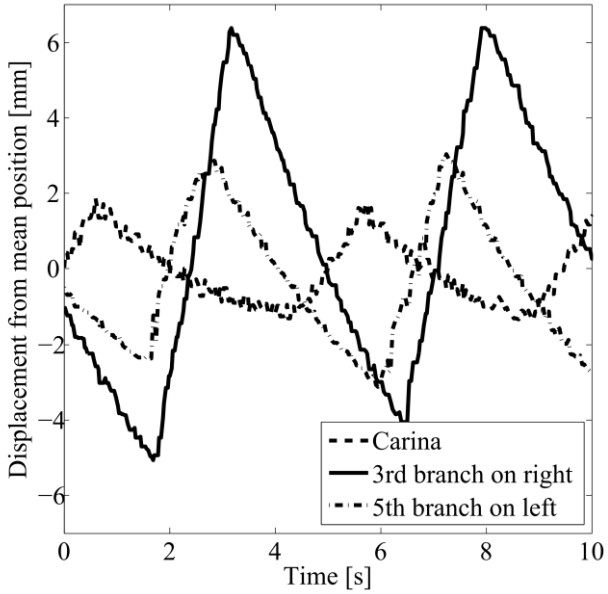



Figure 5.22: Displacement of sensor with time due to breathing cycle. The sensor was positioned in three positions, one at the carina, a second at a central location in the lung and finally at a distal branch. The maximum amplitude of displacement was observed in the centre of the lung.

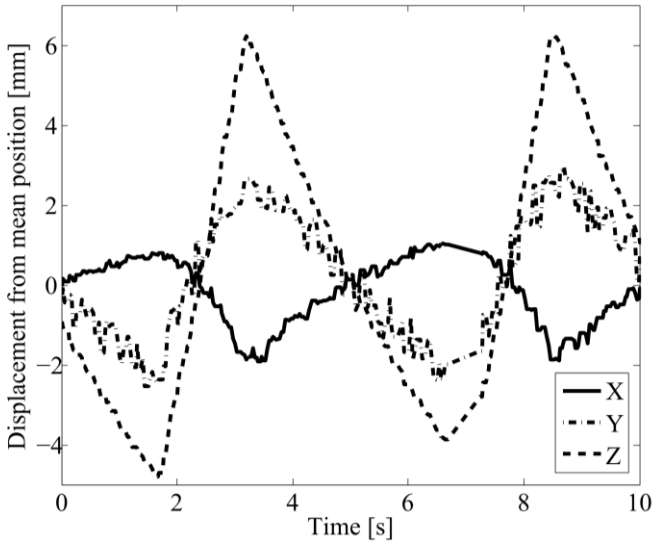



Figure 5.23: Individual vector component displacement of senor with time when positioned at a central location in the lung. Maximum displacement is observed in the *z* direction, which in this case is vertical.

Figure 5.24 shows the relationship between the displacement of the sensor and the logic control signal for the breathing valves. A value of 1 (or logic high) indicates that the lung is inflating, while a value of 0 (or logic low) indicates that the lung deflating. We see that the response of the lung is exponential in form resembling that of a first order differential equation. The use of a simple adaptive time domain model of the lung motion could lead to a possible method for accounting for the displacement of the lung position. Figure 5.25 shows the same response but with each *x*, *y* and *z* component. A similar response is observed in each direction.

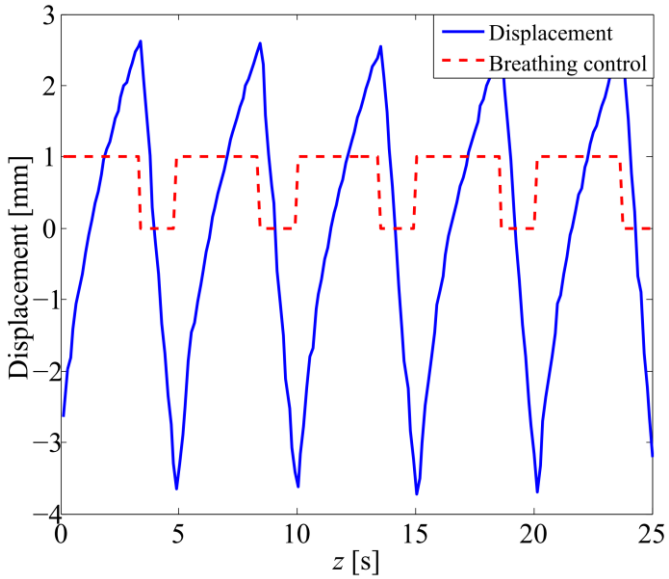



Figure 5.24: Displacement of the sensor with breathing enabled also showing the logic control signal for the breathing valves. A value of 1 indicates inhalation and 0 indicates exhalation.

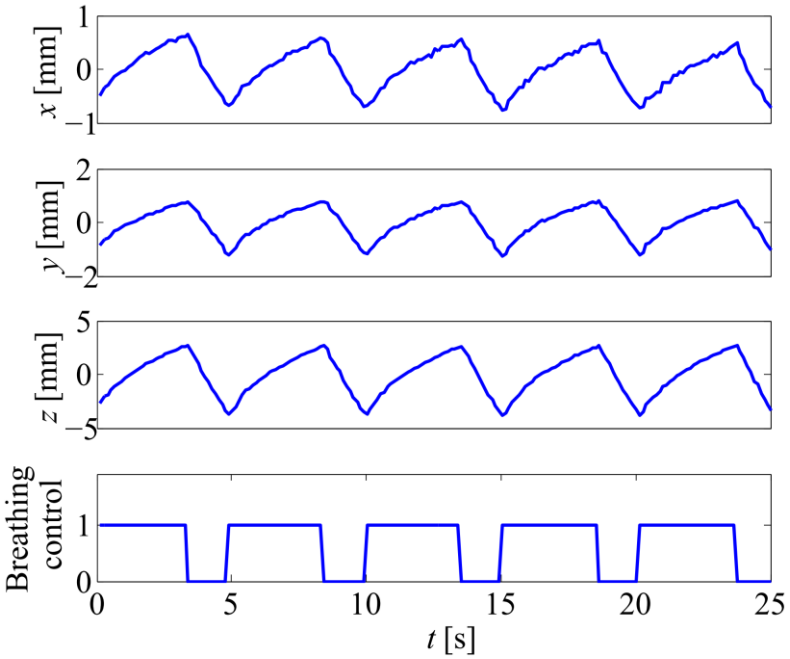



Figure 5.25: Displacement of the sensor in *x*, *y* and *z* along with the breathing logic control signal.

Next, the sensor was placed at a number of different locations throughout the lung and the displacement over a 25 s period was recorded. Figure 5.26 shows an overlay of each set of points gathered. A surprisingly small displacement is seen at each point. The maximum displacement at each point is listed in Table 5.1. Here we can clearly see that the displacement varies considerably between different lung locations.

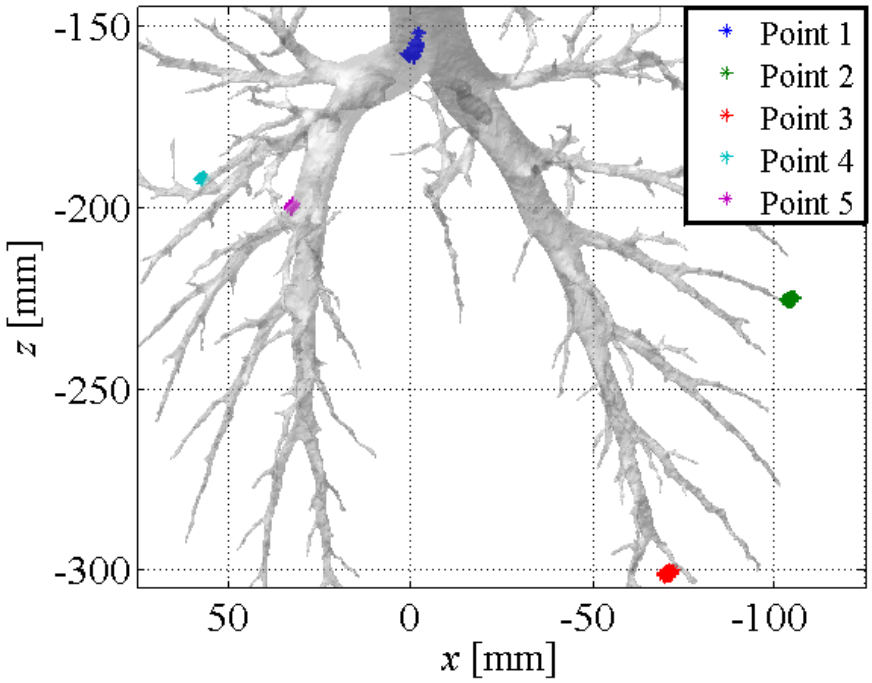



Figure 5.26: Displacement of the sensor for a range of positions over a 25 s breathing period.

| Location | Displacement [mm] |
|---|---|
| Point 1 | 5.6 |
| Point 2 | 2.8 |
| Point 3 | 3.1 |
| Point 4 | 3.5 |
| Point 5 | 6.4 |

Table 5.1: Maximum displacement at experienced at each test point.

Finally, the sensor was navigated along the main airways with breathing enabled. The results are shown in Figure 5.27. Here we can see that during the breathing motion, the sensor is seen to move out of the lung model. Hence measures must be taken to account for the movement of the lung to ensure accurate navigation.

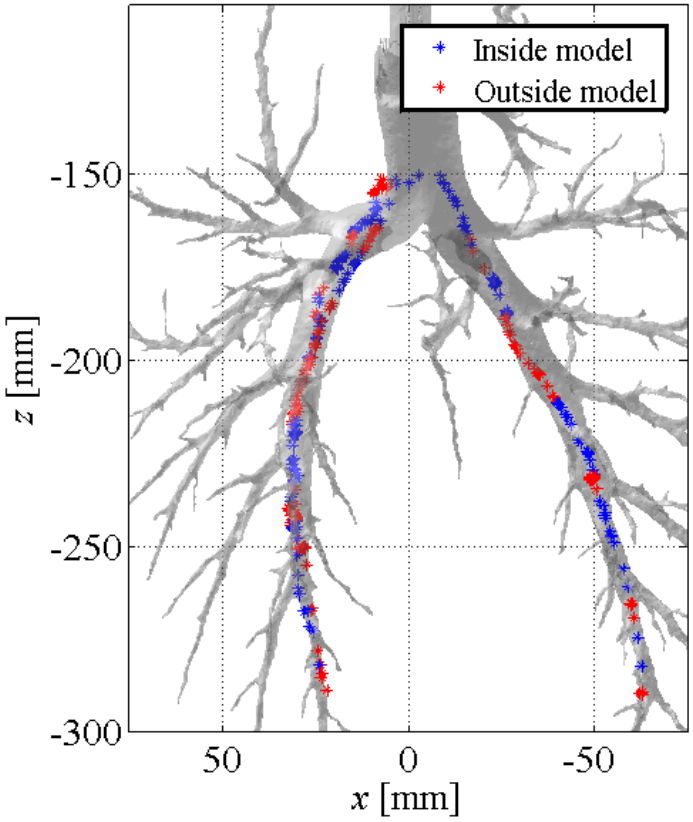



Figure 5.27: Navigation of the main airways with breathing enabled. Breathing motion causes a larger number of the points to be outside the airways during navigation. 52.9% of all test points were found to be within the airway.

Methods exist for counteracting the effect of breathing displacements in position data [168] and future work will attempt to implement modelled displacements to account for these variations. This is required, as typically only a static 3D model is available and breathing artefacts can affect registration and overall system accuracy. Other methods also exist that model the mechanical motion of the lung [170], [171] and these could be incorporated into our system to reduce the effects of breathing motion.

## 5.9. Discussion

From the results presented, it is clear the EM tracking system performs well in aiding navigation within the lung. With the landmark based registration, a low registration error was observed which gives the user a high level of confidence that the sensor is where the registered system indicates and not lost in a different airway. We saw that along the primary airway, the majority of points recorded were within the segmented model after registration, further confirming the quality of the registration. For the airways branching off from the main airway however we saw that most points recorded were found to be outside the model. If we assume that the tracking errors are small (experimentally shown to be $< 2$ mm in Chapter 4) then the primary source of errors is changes in the physical shape and position of the lung between the scan and the experiment. The experiment was not carried out directly after the procedure and it is very difficult to match the lung and the CT model up even with the precautions taken by using a laminated image template as a guide for positioning the lungs. In a real application such as in a human or animal study, this is not expected to be such a problem as typically the lung's position will not change significantly in a short time.

In terms of the registration algorithm used, both have their advantages. The landmark based approach proved to be more accurate. However it was time consuming and difficult to acquire the data accurately although the calculation time is quite short. Using the hybrid method is easy to gather the required data although it was found to be less accurate and quite time consuming to calculate, although improvements may be possible to the code implementation to increase speed.

The effect of the breathing motion on the sensors position indicates that the breathing motion must be taken into account in some fashion to reduce errors. Significant errors were demonstrated as a direct result of the breathing motion.

The next stage in the evaluation of this system will be with animal and eventually clinical trials. This initial evaluation demonstrates the performance of the system and the challenges that may arise in implementation. Accurate registration is critical to make the system useful and the methods shown here should be easily implementable in live trials although other registration methods may also prove of use.

# Chapter 6

# Planar Magnetic Shielding for use with EM Tracking Systems[§§]

## 6.1. Overview

This chapter evaluates planar magnetic shielding for use in EM tracking systems to prevent field distortion from ferromagnetic objects below a magnetic field transmitter. A comparison between the shielding performance of MuMetal, ferrite, aluminium and steel is presented over a frequency range of 1 Hz to 1 MHz. Both simulation and experimental results show the merits of each shield material. MuMetal and ferrite are found to give excellent shielding performance over a wide frequency range. The use of a ferrite and MuMetal shield is also demonstrated in a full 5 degree of freedom (DOF) EM tracking system and is shown to successfully operate with position errors of 1.8 mm and 2.3 mm respectively in a volume of 25 cm × 25 cm × 25 cm. This compares with a mean position error 67.3 mm without shielding. The orientation error for each shield was found to be 1.9° and 2.1° for the ferrite and MuMetal respectively, in comparison to an error of 115.1° without shielding [172].

## 6.2. Introduction

This chapter describes the evaluation of planar magnetic shields for use with EM tracking systems, in particular for use in medical environments. EM tracking systems have become a major component in many medical procedures in particular minimally invasive surgeries where accurate positioning of medical tools and devices is critical [60], [108], [173]. Typical operating rooms contain various sources of metallic distortion such as C-arms, surgical instruments, equipment racks and most significantly the operating table [58], [174]. Most operating tables are made from various grades of stainless steel and present a problem from

[§§] This chapter is based on K. O'Donoghue and P. Cantillon-Murphy, "Planar magnetic shielding for use with electromagnetic tracking systems", *IEEE Transactions on Magnetics*, doi: 10.1109/TMAG.2014.2352344, Aug 2014.

both induced eddy currents and field distortion due to their ferromagnetic properties [174].

Most commercial EM tracking systems use either a table top generator or a planar generator that can be placed below the patient [174]. These planar generators typically contain magnetic shielding. However these designs are proprietary [175]. As a result, there is very little information on the design considerations required for the development of these types of magnetic shields. This chapter examines a number of different shield materials, comparing their properties and demonstrating their performance in the presence of a large ferromagnetic distorter placed below the shield.

There are numerous works analysing the effectiveness of different magnetic materials for attenuation and absorption [133], [176]. At lower frequencies, it is often more effective to divert unwanted flux lines around a volume to be shielded rather than absorb or reflect the magnetic energy [177], [178]. This method is sometimes called "flux shunting". At higher frequencies, conductive materials such as copper can provide improved attenuation over high permeability materials in standard shielding applications [133]. In this application, the low frequency approach of flux redirection is used to stop a magnetic transmitter from experiencing any magnetic distorter below the transmitter. This approach has the added benefit of increasing the field strength in the region of interest, hence increasing the signal to noise ratio (SNR) of the system and reducing position and orientation (P&O) errors.

The different shielding materials are analysed over a frequency range from 1 Hz up to 1 MHz as well as with increasing distance from the transmitter. The performance of the shield is tested for its ability to block the effect of a large ferromagnetic plate placed below a magnetic field source. The large frequency range is chosen as EM tracking systems operate at very different frequencies depending on the application. An operating frequency comparison of typical research systems is found in Table 6.1.

| Author | Frequency Range | Ref |
|---|---|---|
| O'Donoghue et al | 20.5-27.5 kHz | [146] |
| Plotkin et al | 6.25-25 kHz | [9] |
| Li et al | 1 kHz | [126] |
| Barandiaran et al | 157-440 kHz | [77] |

Table 6.1: EM tracking operating frequency comparison.

## 6.3. Background Theory

### 6.3.1. Method of Images

In the ideal shielding case, the shield may be considered as an semi-infinite planar slab of relative magnetic permeability $\mu_r$ and zero conductivity. In this case, it is well known that a current carrying conductor with a spatial current density distribution, $\boldsymbol{J}(x,y,z)$, will generate a mirror image $\boldsymbol{J}'$ within the slab given by (6.1) where $J_{\parallel}$ is the current density parallel to the slab and $J_{\perp}$ is the perpendicular component [179].

$$\boldsymbol{J}_{\parallel}^{'} = \frac{\mu_r - 1}{\mu_r + 1}\boldsymbol{J}_{\parallel}(x, y, -z) \qquad \boldsymbol{J}_{\perp}^{'} = -\frac{\mu_r - 1}{\mu_r + 1}\boldsymbol{J}_{\perp}(x, y, -z) \tag{6.1}$$

If the coil is parallel to the slab, the perpendicular component is zero. For the parallel current density, the positive sign indicates that this current density is additive to the source current, *i.e.* it will add magnetic flux in the region of interest hence increasing the field strength. For a planar coil carrying a current *I* placed a distance $z_0$ from the slab, a mirror image is found at $-z_0$.

For slabs of finite thickness and low permeability, the situation is more complex. In addition to the additive current contribution, there is also an infinite number of smaller mirror images that tend to reduce the flux increase in the region of interest [180]. If we consider the scalar quantity, α, given by:

$$\alpha = \frac{\mu_r - 1}{\mu_r + 1} \tag{6.2}$$

and a slab with thickness, $w$, each additional mirror coil will carry a current $\alpha^{2n-3}(1-\alpha^2)I$ where $n \geq 2$ and $n \in \mathbb{Z}$. Each of these mirror coils will be found at a distance $z = -(2nw + z_0)$ below the shield. This situation is shown in Figure 6.1. If the permeability is very high (*i.e.* greater than 1000), higher order terms can be neglected.

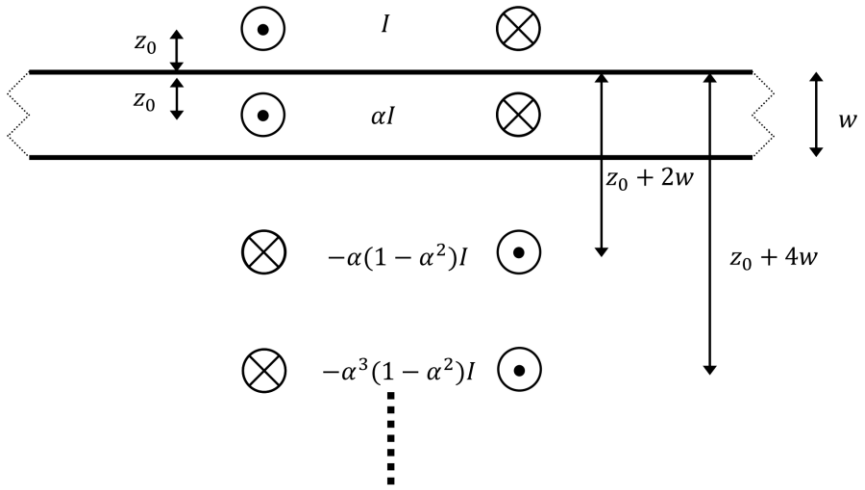



Figure 6.1: Method of images for shields of finite thickness. The coil placed above the shield at $z_0$ carrying current *I* is mirrored below the surface by an infinite number of identical coils carrying a current dependent on the permeability of the shield.

This mirror effect is also true for magnetic dipoles over magnetic slabs. If we consider the dipole to be positioned at $(x, y, z)$ with a magnetic dipole moment of $\boldsymbol{m} = (m_x, m_y, m_z)$, as before a mirror image will be formed at $(x, y, -z)$ with a dipole moment of $\boldsymbol{m} = (-\alpha m_x, -\alpha m_y, \alpha m_z)$ where $\alpha$ is normally $\sim 1$ [181]. In the AC case with conductive as well as magnetic materials, the method of images is still valid. However it is a more complicated situation as induced eddy currents are also present.

### 6.3.2. Eddy Current Distortion and Higher Frequency Effects

A large source of magnetic field errors in AC EM tracking systems is the induced eddy currents in conductive materials, which in turn generate secondary fields in the region of interest [129], [182]. The magnitude of these eddy currents is proportional the applied field strength, the conductivity of the material and the applied frequency. The relative permeability also has an effect as it affects the skin depth of the material. The skin depth for conductive media is given by:

$$\delta = \sqrt{\frac{2\rho}{\omega\mu_0\mu_r}} \tag{6.3}$$

where $\rho$ is the resistivity of the material in units of Ω·m and $\omega$ is the angular frequency in rad/s. Eddy current effects are lower in high permeability materials as the effective resistance of the material is higher, which results in lower induced current levels [183].

The method of images can be expanded to model the effects eddy currents [184], [185]. The resulting formulations are complicated and vary depending on model parameters. For EM tracking applications, minimising calculation time is also a key concern as this directly effects the update time of the system.

A further complication in the design of magnetic shielding is the non-linear nature of ferromagnetic materials in relation to applied field, temperature, frequency and geometry [30]. Changes in frequency have the most dramatic effect, as the permeability of all materials has a frequency dependence [30]. As frequency increases, the permeability decreases. Typically, the higher the DC permeability of a material, the faster its permeability rolls off with increasing frequency [133]. The resistivity of certain materials is also frequency dependant and separate to skin effects and proximity effects [186]. MnZn ferrite for example can vary from 1 Ω·m to 0.001 Ω·m at high frequencies.

## 6.4. Simulations

### 6.4.1. Finite Element Modelling

In order to predict the behaviour of the shields which were tested, finite element analysis (FEA) was used. FEMM, an open source axisymmetric finite element software package, was used for this purpose [187]. Figure 6.2 shows a schematic representation of the arrangement used for the FEA. The transmitter coil consists of 25 turns of 50 mA while the receiver sensor coil has 1000 turns. For the conductive material simulation, a fine mesh with a maximum triangular side length of 25 μm was used to ensure accurate modelling of the skin effect. The distorter was modelled as a disk with radius of 325 mm and a thickness of 15 mm. Its relative permeability was set to 500, with a conductivity of 5.8 MS/m.

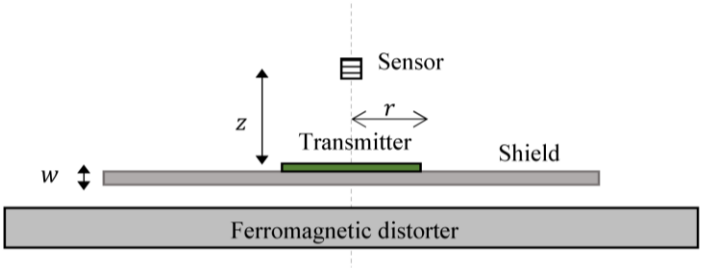



Figure 6.2: Experimental setup for axial testing of the shielding performance. The distance $z$, measured from the centre of the sensor, indicates the distance of the sensor from the transmitter and $r$ indicates radial displacement. For the finite element simulations, an identical layout and notation is used.

### 6.4.2. Shielding Performance

Figure 4 shows a comparison of the simulated flux patterns resulting from the presence of the shield. In this simulation, the shield is made of ferrite with a relative permeability of 1500. The simulation frequency is set to 10 Hz. We see that the shield redirects the flux patterns so they do not reach the area below the shield. In the absence of the shield, the flux lines reach the distorter and hence alter the magnetic field in the region of interest. Ideally the ferromagnetic distorter would not have any impact on the magnetic field of the transmitter.

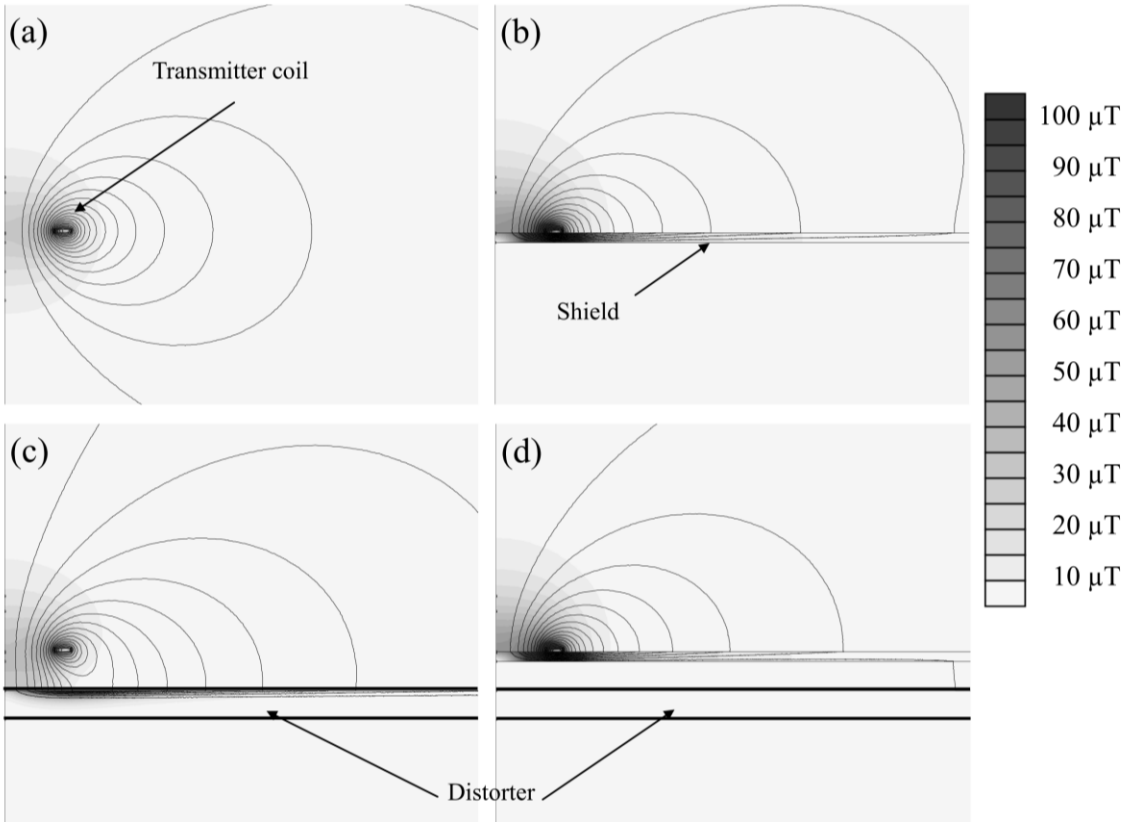



Figure 6.3: Finite element simulations showing the flux patterns of the transmitter coils in the following cases: (a) no shield or distorter, (b) with shield no distorter, (c) no shield with distorter, (d) shield with distorter. The shield effectively blocks flux lines from reaching the distorter hence minimizing its impact on the flux above the shield.

The performance of a range of materials over a frequency range of 1 Hz up to 1 MHz was

simulated and this is shown in Figure 6.4 and Figure 6.5. Figure 6.4 shows the increase in the induced sensor voltage due to shielding. A summary of the properties of the shields used is shown in Table 6.2. Figure 6.5 shows the field errors resulting from the addition of the distorter.

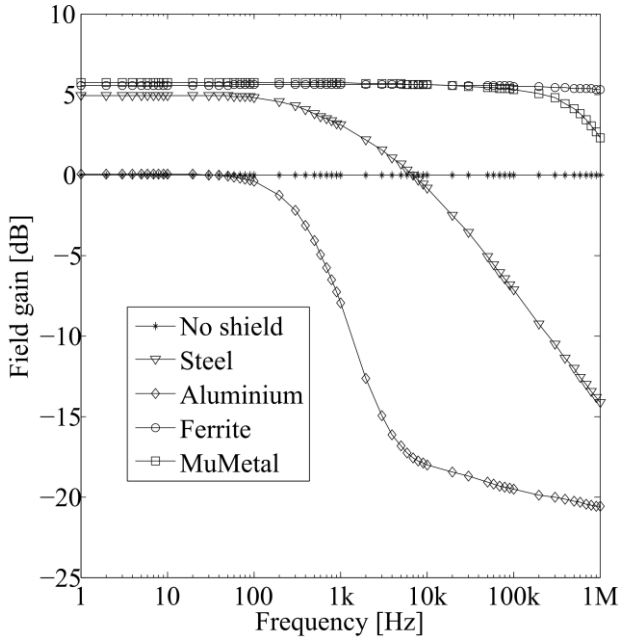



Figure 6.4: Simulations results for the signal gain associated with each shield material.

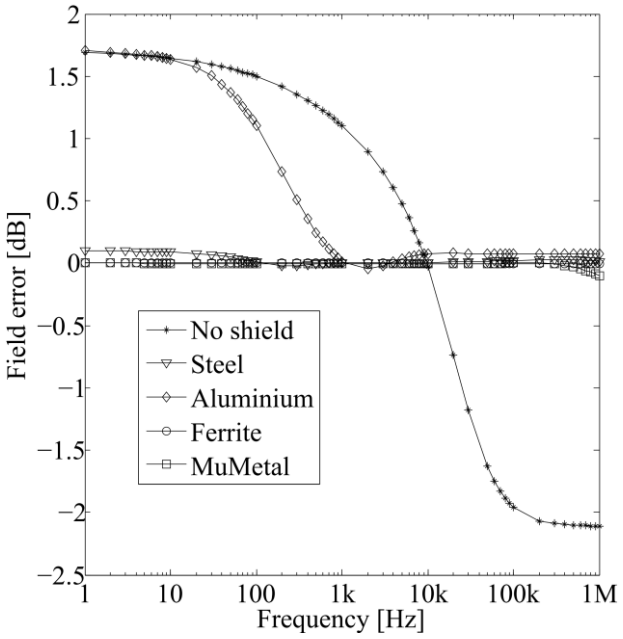



Figure 6.5: Simulations results for the field errors due to a large ferromagnetic plate placed below the shield.

| Material | $\mu_r$ | $\sigma$[MS/m] | $r[mm]$ | $w$[mm] |
|---|---|---|---|---|
| Mild steel | 500 | 5.8 | 250 | 2 |
| Aluminium | 1 | 35 | 250 | 0.9 |
| MnZn Ferrite | 1500 | 0.001 | 340 | 5 |
| MuMetal | 100,000 | 1.8 | 250 | 0.5 |

Table 6.2: Shield simulation parameters.

To investigate the effects of the distorter on the field above the shield, the magnetic field in this region was recorded for the case with and without the distorter. By calculating the percentage error, the contour plot in Figure 6.6 was created. Here it is seen that as we approach the edge of the shield ($r$ = 250 mm), fringing effects from the distorter cause large errors. The error also tends to increase with $z$ displacement from the shield.

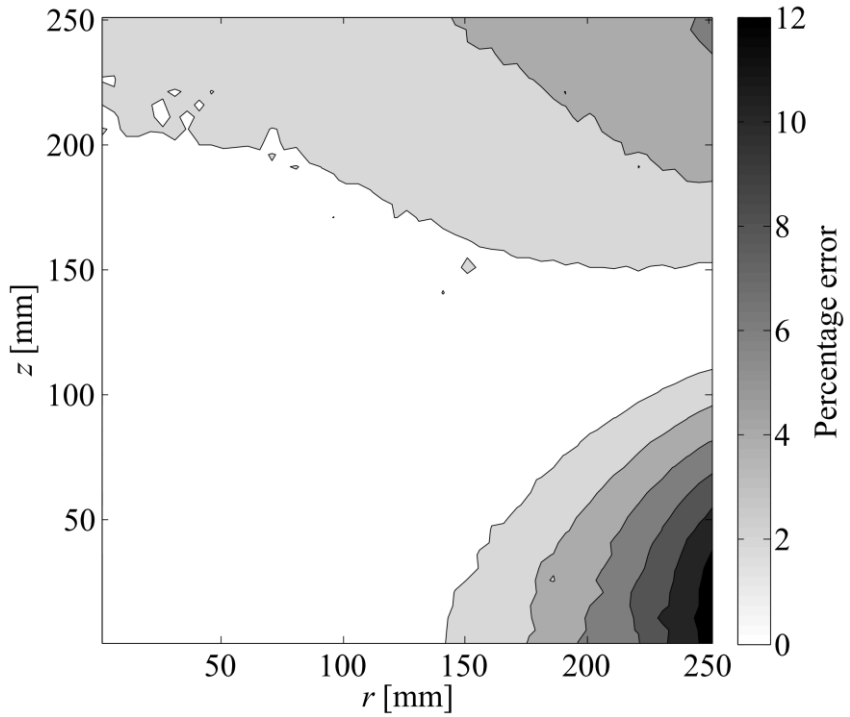



Figure 6.6: Error contour plot showing the region directly over the shield where fringing effects of the distorter cause larger errors. The errors increase with distance from the centre of the shield and as the shield edge is approached

## 6.5. Experimental Setup and Methods

### 6.5.1. Magnetic Measurement Circuit

In order to measure the AC magnetic field components over a wide frequency range, a trans-impedance op-amp circuit was used to ensure a flat sensor response over a wide frequency range. The circuit used is shown in Figure 6.7 [188]. The virtual ground of the non-inverting input effectively shunts the effect of any parallel capacitance in the sensor, hence avoiding resonance [115]. The choice of capacitor $C$ as well as $R$ and $R_f$ is chosen to extend the flat frequency response to lower frequencies. Figure 6.8 shows the frequency response of the sensor and amplifier to an applied magnetic field over the range of interest (1 Hz to 1 MHz). At higher frequencies, the finite bandwidth of the amplifier causes the flat response to degrade. A Powertek GP-12 gain-phase analyser was used to characterize the frequency response and to record the experimental data for the shielding tests. The frequency response of Figure 6.8 shows the response between the current flowing in the transmitter to the output voltage of the amplifier. The gain at higher frequencies is seen to increase as the circuit has a

resonant point at approximately 4 MHz, after which point the gain rolls off as expected.

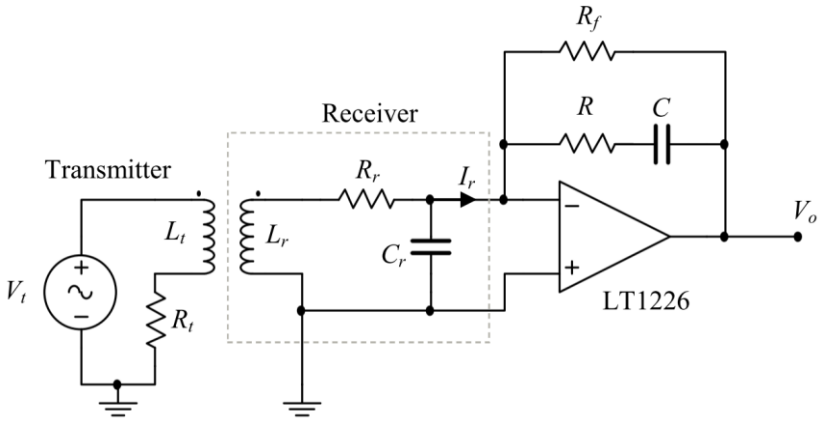



Figure 6.7: Circuit diagram used for the measuring magnetic field output from the sensor. The basic topology is a trans-impedance amplifier which converts the induced current $I_r$ in the receiver coil into a voltage. This reduces the effect of the parasitic capacitance $C_r$ of the receiver and the compensation network of $R$ and $C$ improve the low frequency response.

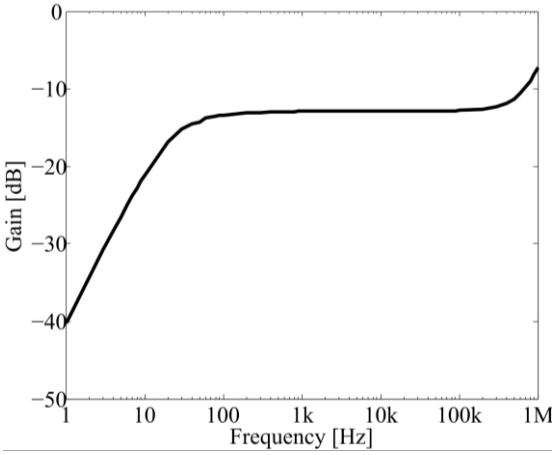



Figure 6.8: Frequency response of the magnetic amplifier circuit. This response is the gain between the output voltage on the receiver amplifier and the applied transmitter current. A flat response is observed between 100 Hz and 200 kHz, with a deviation of less than 0.5dB in this range.

### 6.5.2. Shielding Tests

In contrast to investigations which record shielding effectiveness of planar sheets, where typically a transmitter and receiver are placed on opposite sides of a shield [189], we place both on the same side of the shield, *i.e.* in the area of interest. The key parameter is the effectiveness of the shield in blocking field distortion from metallic materials below the shield.

Figure 6.9 (b) shows the experimental setup of the schematic in Figure 6.2. A planar PCB coil is used as the transmitter, while the receiver sensor is moved in fixed positions along its axis. Lego bricks are used to move the sensor in fixed steps of 9.6 mm.

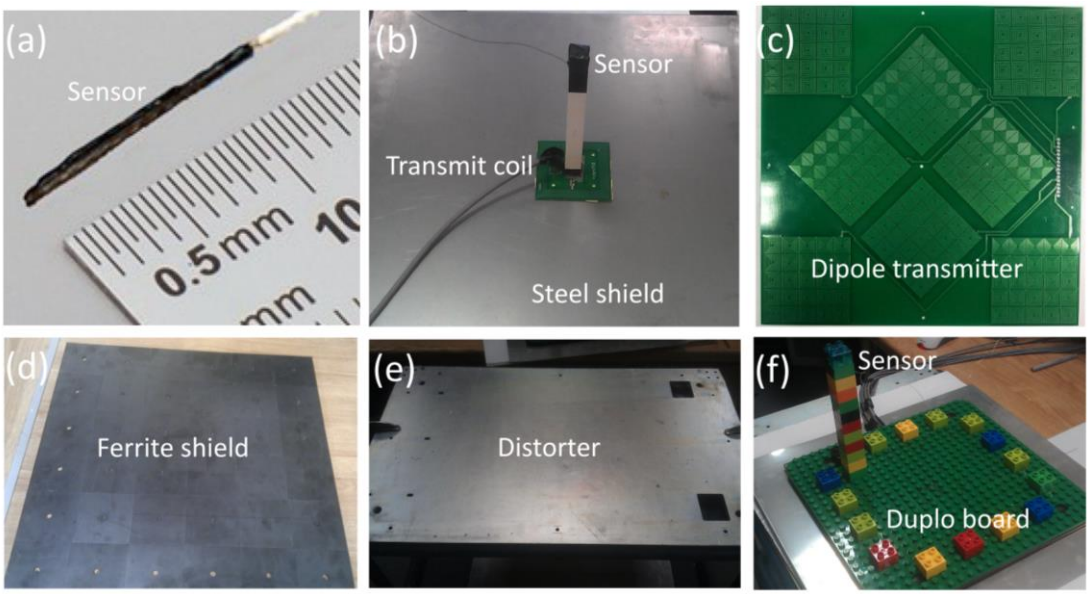



Figure 6.9: (a) Shielded search coil manufactured by NDI for their Aurora tracking system. ( b) Setup for axial single transmitter tests. (c) Single PCB multi-dipole transmitter, which consists of 8 groups of 25 coils. Each group transmits at a different frequency. (d) Ferrite shield comprised of multiple ferrite tiles. (e) Ferromagnetic distorter used for the tests. The steel sheet measures 80 cm × 50 cm × 1 cm and has a relative permeability of approximately 500. (f) Test setup for 5-DOF system.

Two main tests were undertaken to investigate (i) the field gain of the shields (*i.e.* the increase in the field strength with the shield) and (ii) the shielding effectiveness in blocking distortion effects of a large ferromagnetic object placed below the shield.

Effects of frequency and sensor position are investigated. For frequency tests, three sensors positions are used, at 24 mm, 120 mm, and 216 mm from the transmitter. A range of frequencies from 1 Hz up to 1 MHz is considered. For the sensor position tests, two frequencies are investigated, 500 Hz and 30 kHz, and 21 test points in 9.6 mm increments are measured.

The distorter used was a large steel sheet which measures 80 cm × 50 cm × 1cm and has a relative permeability, $\mu_r$ , of approximately 500. A 15 mm spacer was inserted between the shield material and the distorter to reduce leakage flux between them.

### 6.5.3. Shielding Materials

Sheets of the following materials were used for a comparison of shielding effectiveness:

- Aluminium
- Cold rolled mild steel
- MnZn Ferrite
- MuMetal

MuMetal is well known for its use in low frequency magnetic shielding applications [176] primarily due to its high permeability. Ferrite is often used for shielding in anechoic chambers up to very high frequencies [190]. It is advantageous in low frequencies applications as it less susceptible to eddy currents due to its high resistivity. Its relatively

high permeability makes it useful for shielding applications, although its brittle nature makes it difficult to machine. It is also expensive as it generally needs to be quite thick to maintain its strength [175]. The material properties of these materials and dimensions of the shields are shown in Table 6.3. The relative permeability of the materials are not exact values as they are difficult to measure accurately and depend on a range of parameters like temperature, manufacturing methods and geometry [30].

| Material | $\mu_r$ | $\sigma$ [MS/m] | $A$ [m$^2$] | $w$ [mm] |
|---|---|---|---|---|
| Mild steel | >500 | 5.8 | 0.25 | 2 |
| Aluminium | 1 | 35 | 0.25 | 0.9 |
| MnZn Ferrite | 1500 | 0.001 | 0.36 | 5 |
| MuMetal | >100,000 | 1.8 | 0.25 | 0.5 |

Table 6.3: Shield parameters.

### 6.5.4. Multi-Dipole Transmitter Board

Our previous work has demonstrated the design and testing of an EM tracking system that used a selection of transmitter coils printed on individual PCBs [146]. In this chapter we have improved this design by manufacturing a single PCB with a multitude of small coils. Each coil is square and measures 15 mm × 15 mm with 13 turns, and hence can be considered a dipole at distances beyond a few centimetres with a magnetic dipole moment of 0.017 Am$^2$ per amp flowing in the coil. This approach allows for simpler modelling over our previous filament based methods [64]. Eight series-connected groups of 25 coils form the board, which measures 30 cm × 30 cm × 1.6 mm. The magnetic field due to each group is calculated using (6.4):

$$\boldsymbol{B}(\boldsymbol{r}) = \frac{\mu_0}{4\pi}\sum_{i=1}^{M}\left(\frac{3\boldsymbol{r}_i(\boldsymbol{m}_i \bullet \boldsymbol{r}_i)}{r_i^5} - \frac{\boldsymbol{m}_i}{r_i^3}\right) \tag{6.4}$$

where $M$ is the number of dipoles in the group, $\boldsymbol{m}_i$ is a vector representing the magnetic dipole moment and $\boldsymbol{r}_i$ is a vector of the distance from the dipole to the sense point [27]. When the shielding is added to the system, the magnetic field of each dipole group is given by (6.5)where $\boldsymbol{r'}_i$ is the distance from the dipole image and the sense point and $\boldsymbol{m'}_i$ is dipole moment image as described in Section 6.3.1.

$$\boldsymbol{B}(\boldsymbol{r}) = \frac{\mu_0}{4\pi}\sum_{i=1}^{M}\left(\frac{3\boldsymbol{r}_i(\boldsymbol{m}_i \bullet \boldsymbol{r}_i)}{r_i^5} - \frac{\boldsymbol{m}_i}{r_i^3}\right) + \left(\frac{3\boldsymbol{r'}_i(\boldsymbol{m'}_i \bullet \boldsymbol{r'}_i)}{r'_i{}^5} - \frac{\boldsymbol{m'}_i}{r'_i{}^3}\right) \tag{6.5}$$

Each coil group is driven by a constant current AC driver amplifier. The planar PCB transmitter array is shown in Figure 6.9 (c). The use of the new dipole transmitter represents Phase 4 of the EM tracking system (see Chapter 3).

### 6.5.5. Single Axis Position Accuracy Tests

For the single axis testing, position accuracy was determined by recording the magnetic fields at each test point in the presence of the ferromagnetic distorter and comparing this measurement to models of the magnetic field. The resulting position error is then calculated by solving (6.6):

$$z_i = \min_z \left| B_{model}(z) - B_i \right| \tag{6.6}$$

where $z_i$ is the calculated $z$ position, $z$ is the variable distance from the emitter, $B_i$ is the measured field at that point and $B_{model}$ is an analytical model of the axial field.

### 6.5.6. 5-DOF Position Accuracy Tests

To test the performance of the shields for a 5 DOF system, a similar setup to our previous work was used [146]. Eight coils formed on a single PCB generate independent magnetic fields ranging from 10 kHz to 17 kHz in steps of 1 kHz. Figure 6.9 (f) shows this setup. Above the transmitter board, a Lego Duplo base plate is mounted. This allows a sensor embedded inside a Duplo brick to be positioned accurately relative to the transmitter in order to collect data. The manufacturing tolerance allows accurate positioning on the order of 100s of microns (although the quoted manufacturing tolerance is 10 microns [191]).
Four different arrangements are used to investigate the shielding performance:

- Transmitter without shield or distorter
- Transmitter without shield with distorter
- Transmitter with ferrite shield and distorter
- Transmitter with MuMetal shield and distorter

In each case, 96 test points are gathered spread over a volume of 25 cm × 25 cm × 25 cm, 6 planes with 16 points on each are used for each test. An analytical dipole model of the transmitter array was first calibrated by calculating a set of scaling factors to match the measurements to the model. Models of the shielded arrangements are also calculated using the method of images discussed in Section 6.3.1, and experimentally calibrated in advance.

## 6.6. Results

### 6.6.1. Frequency Response of Shielding

Figure 6.10 shows the frequency response of each of the materials in the absence of the distorter when the sensor was positioned 24 mm from the transmitter. The gain of the system is calculated in (6.7):

$$G(f) = 20\log_{10}\left(\frac{V_o}{I_t}\right) \tag{6.7}$$

where $V_o$ is the amplifier output voltage and $I_t$ is the transmitter current. $G(f)$ varies depending on position and orientation of the sensor relative to the transmitter as well as the presence of the shielding and distorter materials. Figure 6.11 shows the gain in field strength due to the shielding materials. The field gain is determined by subtracting the gain of the amplifier from the reference gain for the amplifier without any shield materials:

$$G_{field}(f) = G(f) - G_R(f) \tag{6.8}$$

where $G_R(f)$ is the reference gain. $G_R(f)$ is simply the output voltage without any shielding or distorting materials present.

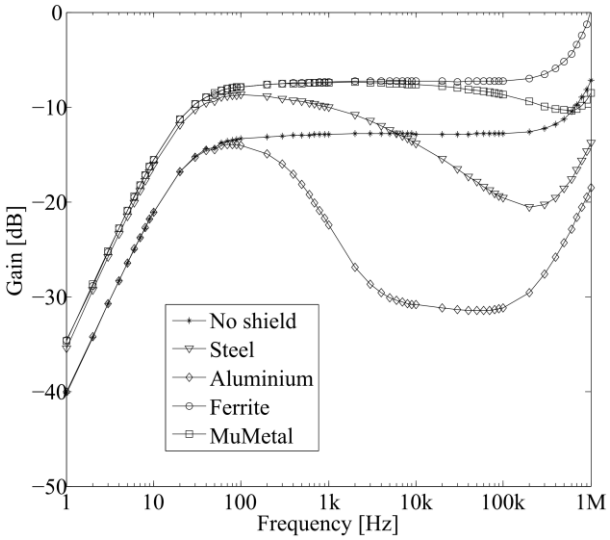



Figure 6.10: Frequency response of the sensor and amplifier in the presence of the shield materials.

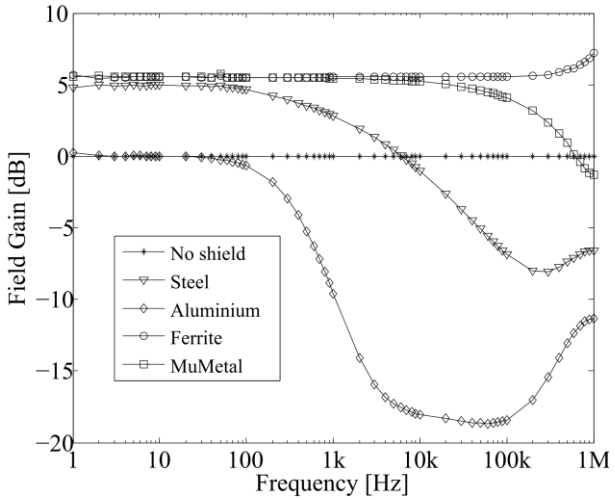


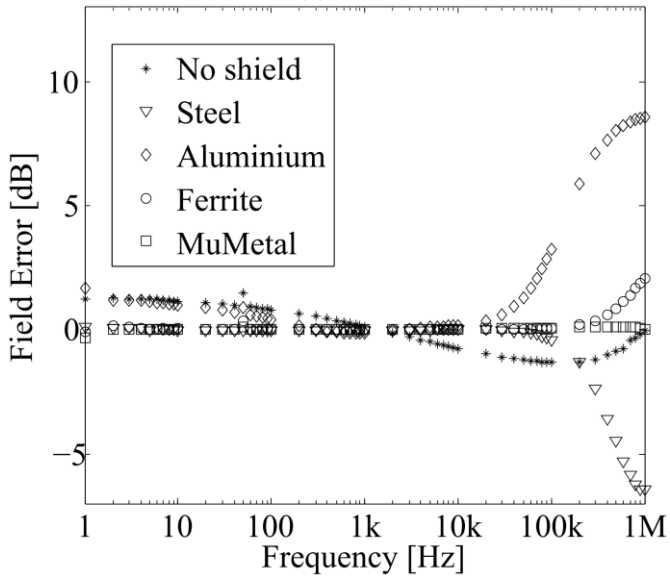

Figure 6.11: Gain in the magnetic field due to the shield materials.

Figure 6.12 shows the change in the sensor output due to the ferromagnetic distorter placed below the shield for the case of three different sensor positions. The field error is determined by calculating the difference in the measured signal due to the distorter:

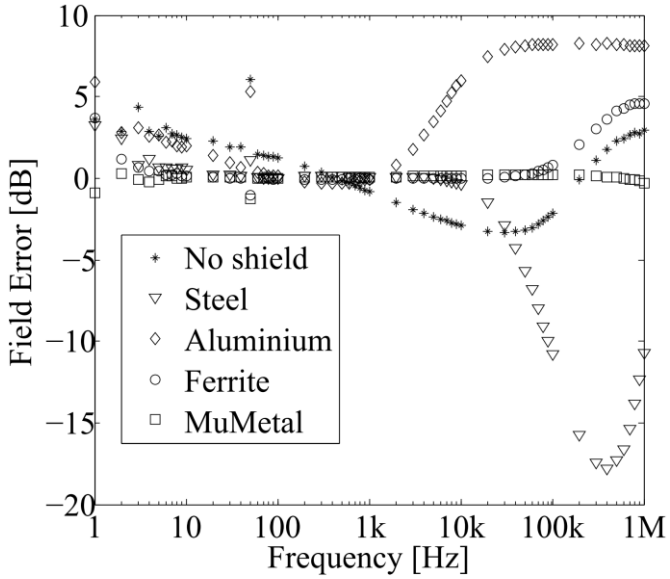
$$G_{error}(f) = G_N(f) - G_D(f) \tag{6.9}$$

where $G_D(f)$ is the gain with the distorter and $G_N(f)$ is the undistorted measurement.

(a) 24 mm




(b) 120 mm




(c) 216 mm

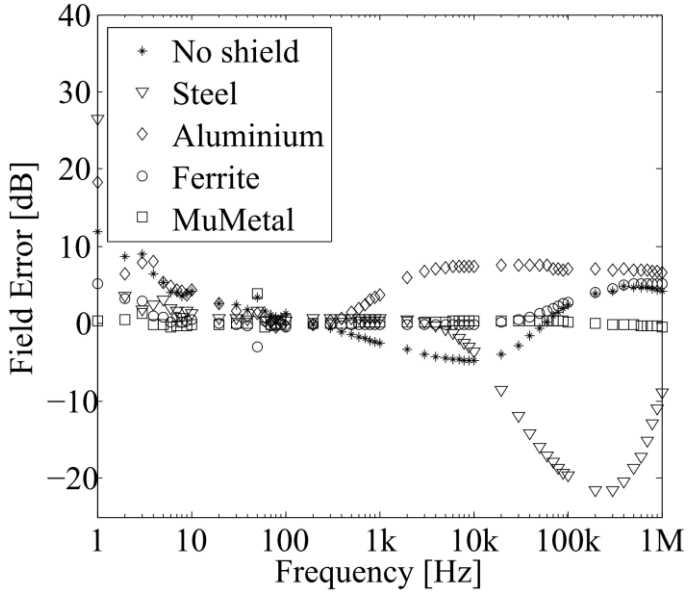



Figure 6.12: Field errors due to the distorter at distances of (a) 24 mm, (b) 120 mm and (c) 216 mm.

### 6.6.2. Shielding Performance with Distance

Figure 6.13 shows the performance of the shield in terms of its rejection of the distorter's effect. This normalised shielding performance is calculated by dividing the sensor output with and without the distorter:

$$V_{norm}(z) = \frac{V_D(z)}{V_o(z)} \tag{6.10}$$

where $V_D$ is the amplifier output with the distorter. Ideally this result is unity at every point. Table 6.4 shows the mean percentage deviation due to the distorter.

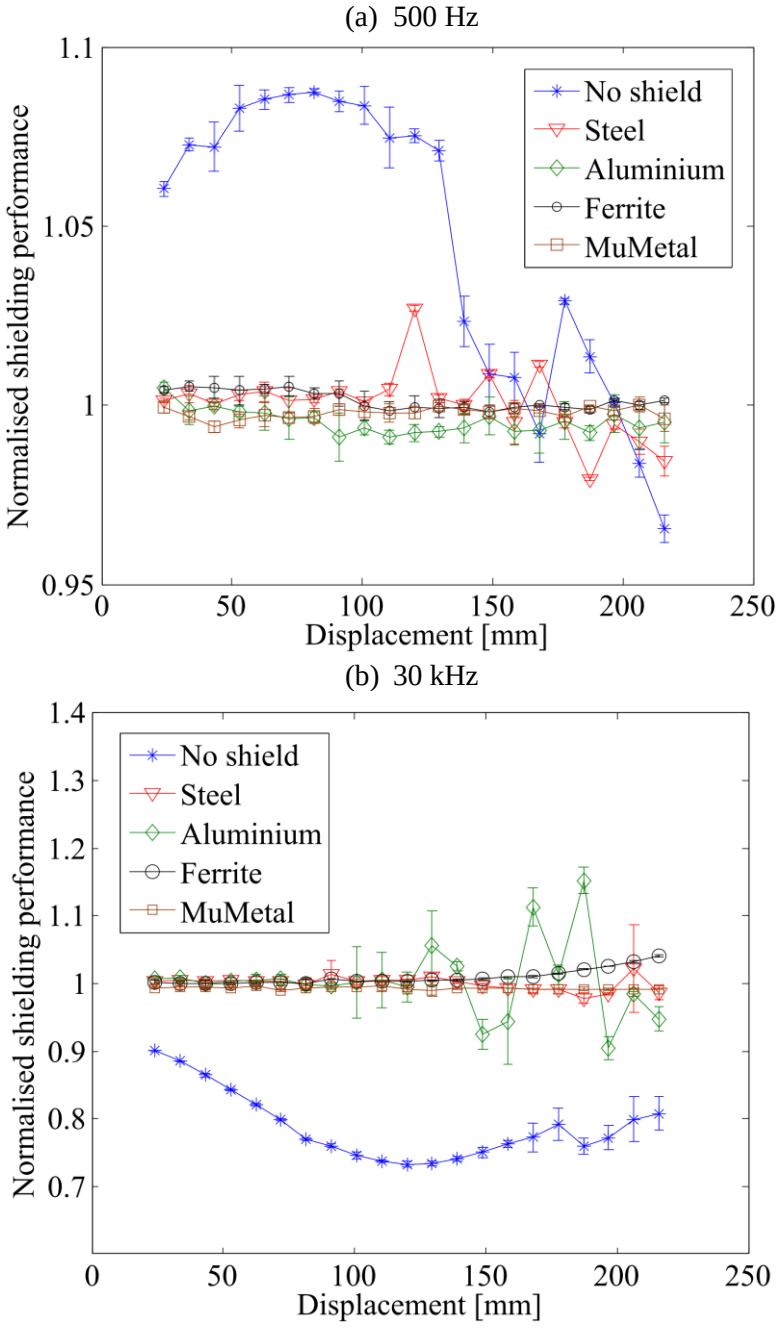



Figure 6.13: Shielding performance with axial displacement from the transmitter at (a) 500 Hz and (b) 30 kHz.

| | Percentage Difference | | Position error [mm] | |
|---|---|---|---|---|
| Shield | 500Hz | 30kHz | 500Hz | 30kHz |
| No Shield | 5.1 | 21.2 | 2 | 12.9 |
| Mild steel | 0.63 | 0.78 | 0.4 | 0.5 |
| Aluminium | 0.51 | 3.35 | 0.3 | 2.6 |
| Ferrite | 0.22 | 0.91 | 0.1 | 0.7 |
| MuMetal | 0.21 | 0.71 | 0.1 | 0.4 |

Table 6.4: Distorter effects with shields.

### 6.6.3. Linearity of Shield Materials

It is well known that most ferromagnetic materials are non-linear in terms of permeability in regards to applied field. To investigate this, the current in the transmitter coil was varied and the resulting receiver voltage was measured when the sensor is placed proximal to the magnetic shield. A linear dependence indicates that the non-linearity is negligible over this field range. Frequencies of 500 Hz and 30 kHz were again used for these tests, with a current range from 100 μA to 50 mA. Figure 6.14 shows the response of the three ferromagnetic materials.

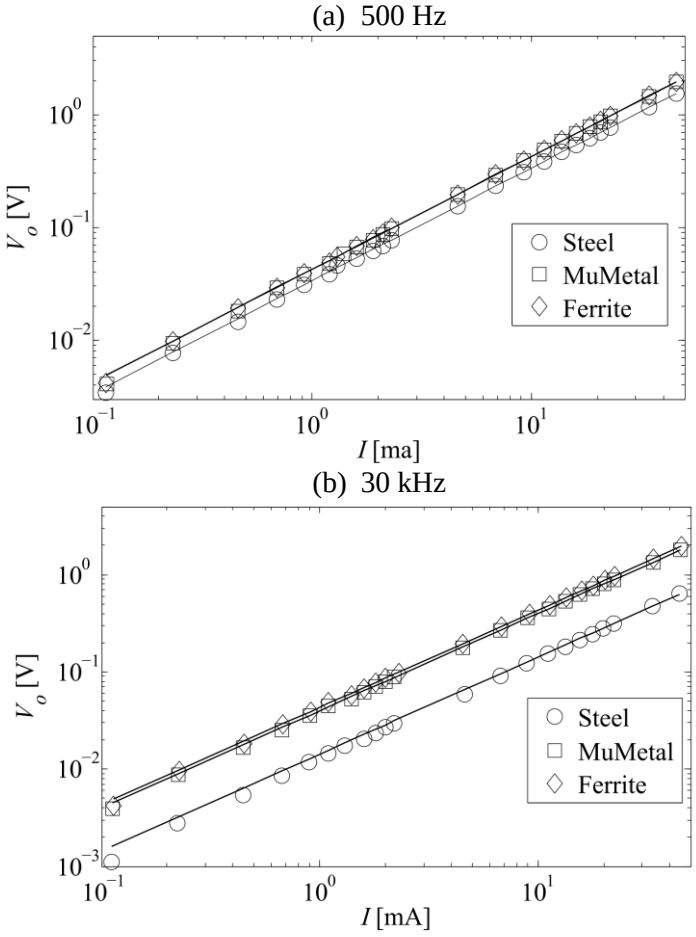



Figure 6.14: Linearity of ferromagnetic shield materials at 500 Hz (a) and 30 kHz (b). Steel is noted for having a higher non-linearity; however due to the small ranges of applied fields this is negligible.

### 6.6.4. Method of Images

The method of images was used to model the fields above the shields. For example with the ferrite shield, the model matches the experimental results with a mean percentage difference of 2.6 %. A single image positioned 1.6 mm behind the shield was simulated. This offset matched the thickness of the PCB coil. The scaling factor, $\alpha$, for the image current was adjusted to 0.96 to give an extrapolated best fit to the data.

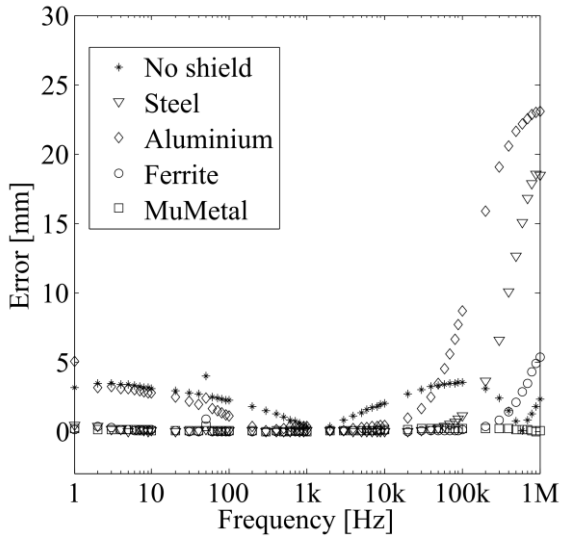
### 6.6.5. Position Accuracy Performance

The results of the axial position error calculations are shown in Figure 6.15 for variability versus frequency while Figure 6.16 shows results at 500 Hz and 30 kHz versus axial displacement. The mean position errors with distance for each test are shown in Table IV. The error, $e_z$, is calculated as follows:

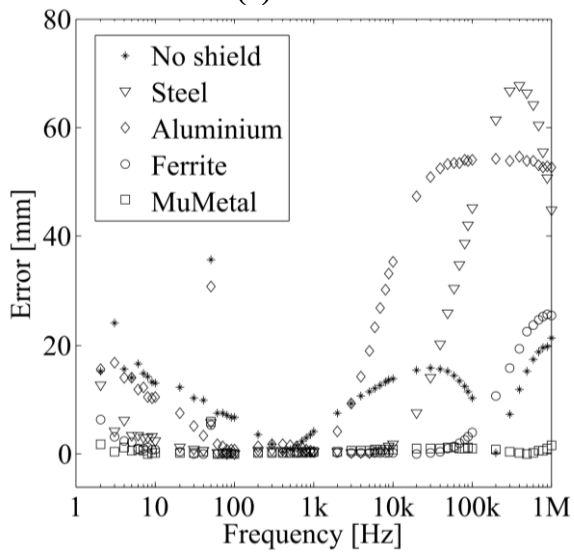
$$e_z = \left| z_a - z_i \right| \tag{6.11}$$

where $z_a$ is the actual $z$ position of the sensor. Only $z$ errors are examined as a single transmitter coil is used for this set of experiments and there is insufficient data to determine all 5 DOF.

(a) 24 mm




(b) 120 mm




(c) 216 mm

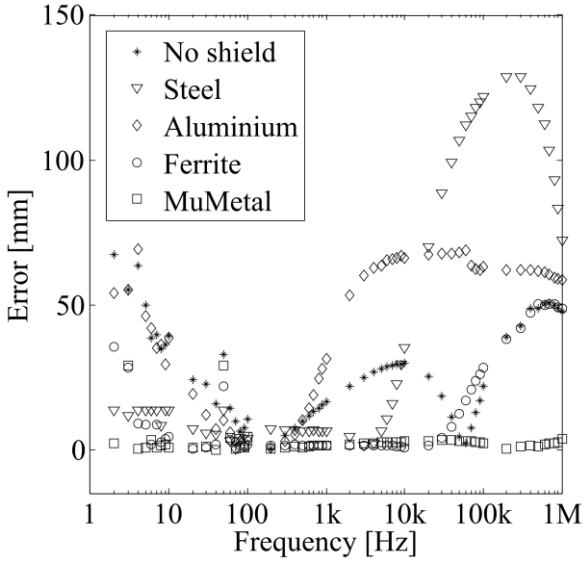



Figure 6.15: Position error frequency dependence of shield materials in the presence of the steel distorter. Three sensor positions perpendicular and along the central axis of the transmitter coil are used: (a) 24 mm, (b) 120 mm and (c) 216 mm.

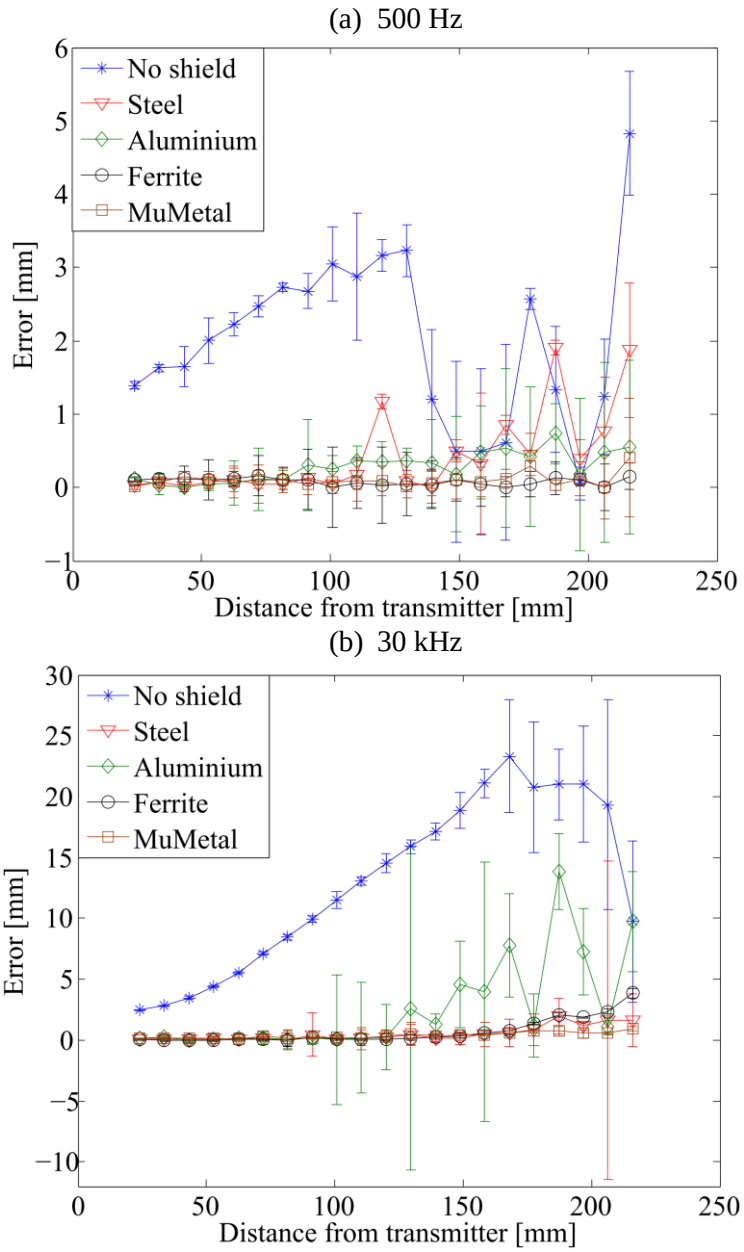



Figure 6.16: Position error with axial displacement from the transmitter at (a) 500 Hz and (b) 30 kHz.

Figure 6.17 shows the RMS position error and Figure 6.18 shows the RMS orientation error for each of the 5-DOF tests described in Section 6.5.6 while Table 6.5 shows the mean results for both along with the standard deviations.

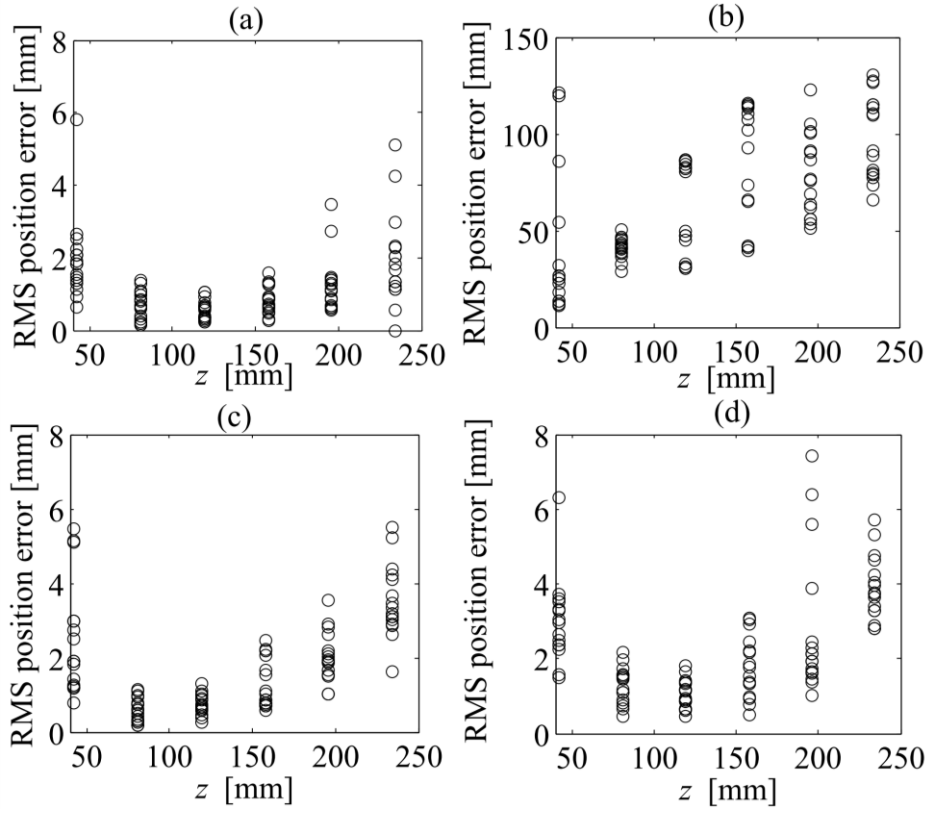



Figure 6.17: Error results of the full 5-DOF tracking test. Each test consists of 96 points spread over a 25 cm × 25 cm × 25 cm volume with the following shield and distorter arrangements: (a) No shield or distorter, (b) No shield with distorter, (c) Ferrite shield with distorter and (d) MuMetal shield and distorter. Each graph shows the error as a function of the *z* displacement from the planar transmitter. The mean RMS position error in each case is (a) 1.2 mm, (b) 67.3 mm, (c) 1.8 mm and (d) 2.3 mm.

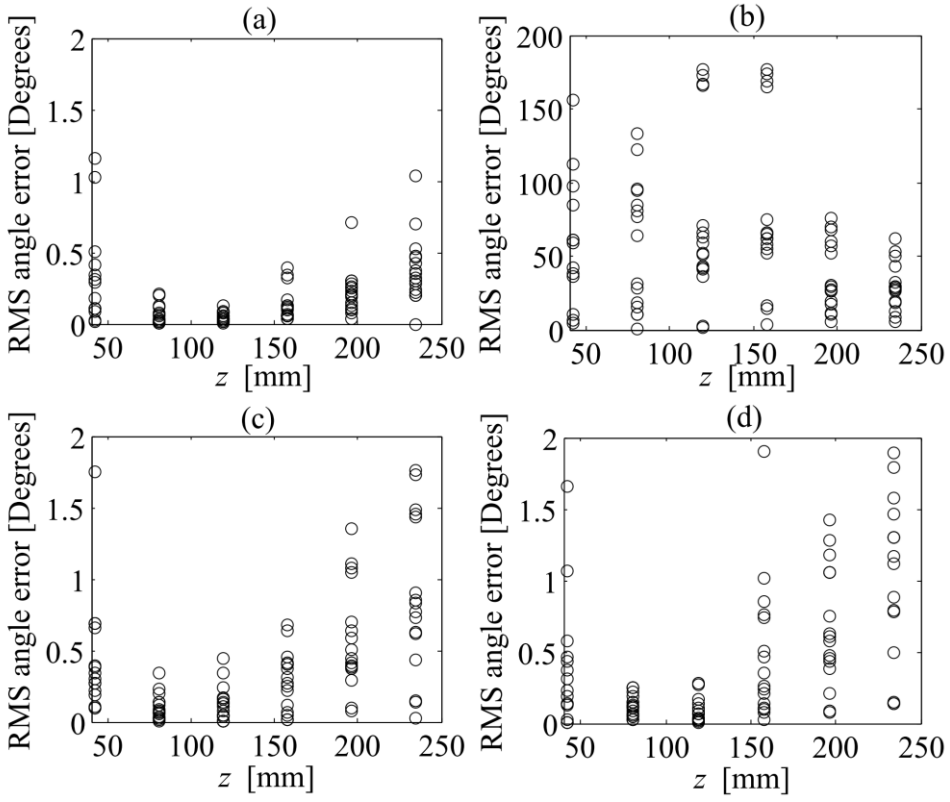



Figure 6.18: Orientation error results of the full 5-DOF tracking test with the following shield and distorter arrangements: (a) No shield or distorter, (b) No shield with distorter, (c) Ferrite shield with distorter and (d) MuMetal shield and distorter. The mean RMS orientation error in each case is (a) 1 °, (b) 115.1 °, (c) 1.9 °, and (d) 2.1 °.

| Case | $e_p$ [mm] | $\sigma_{e_p}$ [mm] | $e_o$ [Deg] | $\sigma_{e_o}$ [Deg] |
|---|---|---|---|---|
| No shield or distorter | 1.2 | 0.9 | 1.5 | 2.7 |
| No shield with distorter | 67.3 | 33.4 | 115.1 | 77.2 |
| Ferrite shield | 1.8 | 1.3 | 1.9 | 3.9 |
| MuMetal shield | 2.3 | 1.4 | 2.1 | 4.4 |

Table 6.5: 5 DOF test results.

## 6.7. Discussion

### 6.7.1. Shielding Performance

From the data presented, it is clear that in the presence of the steel distorter causes a dramatic effect on the field measurements in the region of interest as expected. The MuMetal and Ferrite shields gave similar levels of performance except at higher frequencies where MuMetal gave better rejection of the distorter as seen in Figure 6.12. Data from very low frequencies up to 100 Hz becomes inconsistent as we move away from the transmitter due to the small amplitude of the induced sensor voltage. We also see that the steel performs well up to a few kHz. However beyond this range, its effectiveness diminishes considerably.

In terms of field gain, the use of the ferrite and MuMetal almost double the signal as seen in Figure 6.11, which can give a large boost to the SNR of the system. This may be important for certain applications. The steel also increases the field strength but above 100 Hz, induced eddy currents begin to dominate and reduce the field strength. The very high permeability of the MuMetal reduces the effect of eddy currents as induced fields are confined to the skin depth which is only a few microns thick at 1 MHz. Hence MuMetal has a higher effective AC resistance in comparison to steel although they both have similar conductivities due to the skin effect and the higher permeability of the MuMetal.

As expected, at low frequencies, aluminium has little impact on the field gain. However at higher frequencies, the induced eddy currents dramatically attenuate the signal.

In terms of distance from the transmitter, generally the shielding performance degrades with increased distance. This is clearly seen in Figure 6.13. This is due to degradation of the SNR, as well as fringing effects as the sensor moves away from the shield which was seen in simulation in Figure 6.6.

In general, similar performance was observed in the simulations shown in Figure 6.5 except at frequencies above 100 kHz. This could be related to unmodelled high frequency effects.

### 6.7.2. Positioning Accuracy

From the position accuracy frequency sweep, MuMetal and Ferrite have similar performance

up to approximately 50 kHz where the performance of the ferrite begins to degrade. Steel also performs well at low frequencies, but its effectiveness reduces at larger distances. Interestingly aluminium blocks the effect of the distorter over a small frequency range between 100 Hz and 10 kHz. However this degrades considerably as the sensor is moved away from the shield. This is quite clear in Figure 6.16 where errors for all shields increase with distance. Table 6.4 summaries the mean errors for the displacement tests.

When we examine the results of the 5-DOF system, as seen in Figure 6.17, Figure 6.18 and summarised in Table 6.5, we see that the MuMetal and Ferrite provides a considerable reduction in the effects of the distorter on the position accuracy. However, contrary to the overall trend seen in the axial tests, the Ferrite is seen to give better performance. This is clear if we consider the mean error for Ferrite and MuMetal which was calculated as 1.8 mm and 2.3 mm respectively. The larger area and thickness of the ferrite shield used contributes to this improvement, as well as the reduced eddy current effects due to its high resistivity.

From Figure 6.17 and Figure 6.18, we see that errors are at a minimum between 50 mm and 150 mm from the transmitter. Errors close to the transmitter result from the dipole approximation, which is less valid closer to the source. This effect can be accounted for by using more accurate magnetic field models. Errors increase away from the transmitter as the magnetic gradient in these areas decreases, which makes it more difficult to discern changes in the recorded magnetic field, which, in turn directly affects the position accuracy.

Additional sources of errors include the manufacturing tolerances of the Lego, which contributes an uncertainty to the position and orientation measurements of approximately 250 μm and 1° respectively, both of which were noted to increase with the number of blocks used. The possibility of the Lego blocks slanting to one side is an additional source of error as well as possible small misalignment between the baseplate and the transmitter array.

### 6.7.3. Linearity

From Figure 6.14, we see that all the materials were effectively linear in the region of operation (<200 μT). In general for most EM tracking systems, the applied fields are constant and non-linear shield materials would have little overall effect on its operation. A more important concern is saturation of the shield material, which radically reduces its effectiveness. Saturation effects are more pronounced if we consider the small skin depth of high permeability materials, causing the resulting flux to concentrate into a smaller region. Hence, the saturation flux density may be reached with relatively low levels of applied field. Ensuring the shield is sufficiently thick to avoid saturation can easily counteract this as the flux would extend around the saturated regions and still maintain its effectiveness.

## 6.8. Conclusion

From the analysis of the four shielding materials examined, it is clear that over a wide frequency spectrum both MuMetal and ferrite both provide excellent shielding performance. Aluminium and Steel are both useful in certain arrangements and frequency ranges but not in general. It is seen that shielding performance degrades with distance from the planar shield.
For a full position and orientation system, it was seen while the accuracy was not as high as in the undistorted system; the rejection of the distorter still offers a major improvement compared to the unshielded performance.

# Chapter 7
# Frequency Effects in EM Tracking

## 7.1. Overview

This chapter explores two key sources of errors in EM tracking systems; (i) the effect of conductive materials such as instruments or medical equipment in the operating room, and (ii) the interference of human tissue and organs on the transmitter magnetic field with respect to frequency. It is well known that AC magnetic fields induce eddy currents in conductive materials. The magnitude of these eddy currents tends to increase with frequency as described by Faraday's law. At low frequencies, these effects are often sufficiently small as to be neglected. However as frequency increases the secondary magnetic fields created can become problematic. Higher frequencies are advantageous for EM tracking applications as their use increases the induced signal strength, which, in turn, allows for the use of smaller sensors and increased SNR. However, increased eddy current and capacitive effects begin to reduce the useful operating frequency range. By directly investigating the errors in the induced magnetic field in a sensor due to the presence of both conductive metals and human tissue, practical frequency limits can be deduced.

## 7.2. Frequency Response of Conductive Distorters

### 7.2.1. Introduction

There are many examples of research documenting the effects of conductive objects on EM tracking accuracy [129], [192], [193]. Eddy currents induced in metallic objects generate secondary magnetic fields that linearly superimpose over the source magnetic field [129]. The secondary field is at the same frequency as the source field; hence the two are difficult to separate. Bien et al have demonstrated methods for separating the secondary field. However these methods are quite time consuming [129].

The majority of documented testing on the effect of metallic objects has been carried out

with commercial systems such as NDI Aurora or Ascensions trakSTAR [58], [68], [194], and, as such, an analysis of the frequency response of conductive distorters has not been analysed. Eddy currents are largely dependent on the frequency of excitation and hence a good understanding of their behaviour may lead to an optimum operating frequency for EM tracking systems.

In this section we present both simulated and experimental data which shows the effect of conductive materials on magnetic field measurements in the range of 1 Hz to 1 MHz. Ferromagnetic materials are not tested as they alter the shape of the source magnetic field as well as adding additional eddy current fields. The distortion of ferromagnetic fields can be counteracted using non-linear calibration procedures [194].

### 7.2.2. Modelling

The behaviour of a conductive distorter can be modelled as an inductor and resistor mutually coupled to both the transmitter and the sensor coils. The resistance, inductance and mutual coupling of the distorter are highly dependent on frequency, orientation, geometry and conductivity. Figure 7.1 shows a schematic representing the mutual coupling between the transmitter (*T*), the conductive distorter (*D*) and the sensor (*S*). *R* and *L* denote the resistance and inductance of each component [129]. $M_{TD}$ represents the mutual coupling between the transmitter and distorter, $M_{TS}$ represents the coupling between the transmitter and the sensor, and finally, $M_{DS}$ represents the coupling between the distorter and the sensor. The transmitter in Figure 7.1 is driven by a constant current source, $I_{T,}$ and it is assumed that the transmitter and the distorter both contribute to an induced current in the sensor $I_S$. In the experimental setup, the output terminal in the schematic is connected to a trans-impedance amplifier which effectively grounds the terminal, allowing the current to flow.

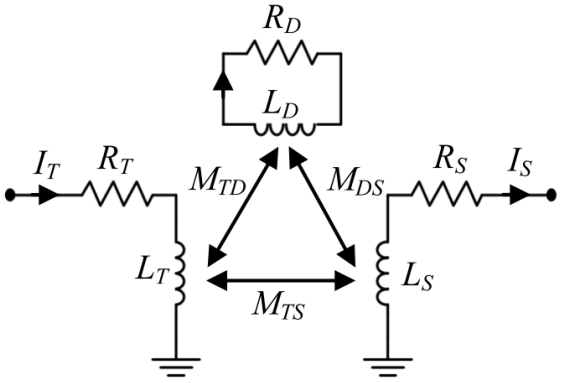



Figure 7.1: Coupling schematic between the transmitter, the distorter and the sensor.

The induced voltage within the conductive distorter is given by (7.1), assuming that the induced current in the sensor does not also induce currents in the distorter due to the small amplitude of the induced sensor current. Equation (7.1) can be represented in the Laplace domain by (7.2).

$$v_D(t) = L_D \frac{di_D}{dt} + i_D R_D + M_{TD} \frac{di_T}{dt} \tag{7.1}$$

$$V_D(s) = L_D s I_D + I_D R_D + M_{TD} s I_T \tag{7.2}$$

By Kirchoff's voltage law, the induced current in the distorter will be given by (7.3).

$$I_D(s) = \frac{-M_{TD} s I_T}{R_D + L_D s} \tag{7.3}$$

If we now consider the voltage induced in the sensor resulting from both the transmitter and the induced current in the distorter, (7.4) results, which can be represented in the Laplace domain by (7.5).

$$v_S(t) = L_S \frac{di_S}{dt} + M_{DS} \frac{di_D}{dt} + M_{TS} \frac{di_D}{dt} + i_S R_S \tag{7.4}$$

$$V_S(s) = L_S s I_S + M_{DS} s I_D + M_{TS} s I_T + I_S R_S \tag{7.5}$$

Assuming the sensor is connected to the virtual ground of a trans-impedance amplifier, the resulting induced current is given by (7.6).

$$I_S(s) = \left( \frac{M_{TD} M_{DS} s^2}{R_D + L_D s} - M_{TS} s \right) \left( \frac{1}{R_S + L_S s} \right) I_T(s) \tag{7.6}$$

Equation (7.7) results if we consider the ratio, $D(s)$, between the induced voltages resulting from the cases with and without the conductive distorter. This expression directly represents the error induced in the sensor due to the presence of the distorter. The expression ideally equals unity when there is no coupling with a distorting element. However, the expression is approximate and only valid over a low frequency range due to the frequency dependence of $R_D$ and $L_D$, as well as other unmodelled high frequency effects due to skin effect, reflections and absorption [189].

$$D(s) = 1 - \frac{M_{DS} M_{TS} s}{(R_D + L_D s) M_{TD}} = \frac{M_{TD} R_D + (M_{TD} L_D - M_{DS} M_{TS}) s}{(R_D + L_D s) M_{TD}} \tag{7.7}$$

Figure 7.2: Simulated field measurement frequency response due to a distorter. Figure 7.2 shows a simulated bode plot of (7.7), with the following parameters: $R_D = 0.01\ \Omega$, $L_D = 1\ \mu H$, $M_{TD} = 0.1\ \mu H$, $M_{TS} = 0.1\ \mu H$ and $M_{DS} = 0.5\ \mu H$. At low frequencies ideally the distorter has limited effect on the detected signal. Attenuation becomes apparent beyond a characteristic cut-off frequency.

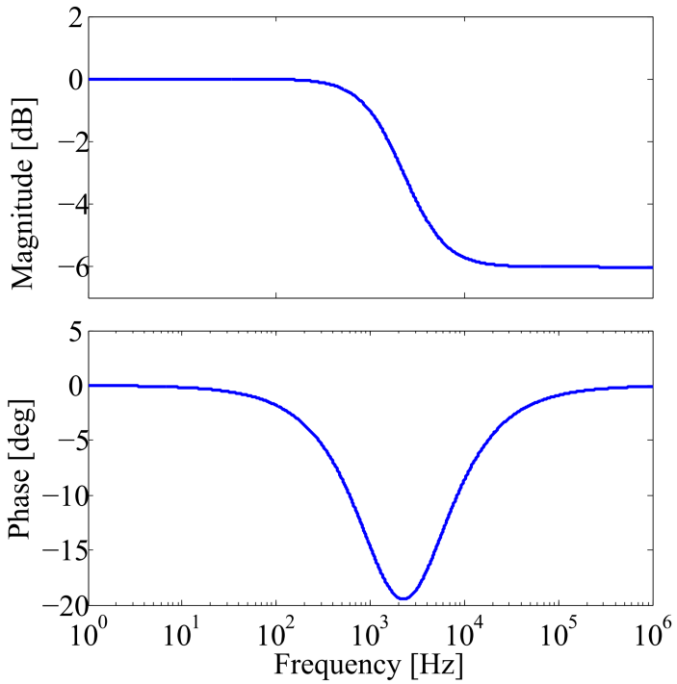



Figure 7.2: Simulated field measurement frequency response, $D(s)$, due to a distorter.

### 7.2.3. Simulation

To investigate the effect of conductive materials, a finite element simulation using FEMM was undertaken (see Chapter 6). In this simulation, a transmitter coil carrying an AC current of amplitude 1 A was simulated and the voltage in a second smaller sensor coil was calculated. The simulation was then repeated with a hollow aluminium disk structure added at various positions relative to the transmitter and sensor. The sensor position was also varied. Figure 7.3 shows a schematic representation of the setup for FEA simulation where $z_S$ represents the height of the sensor relative to the transmitter and $z_D$ represents the height of the conductive aluminium disk.

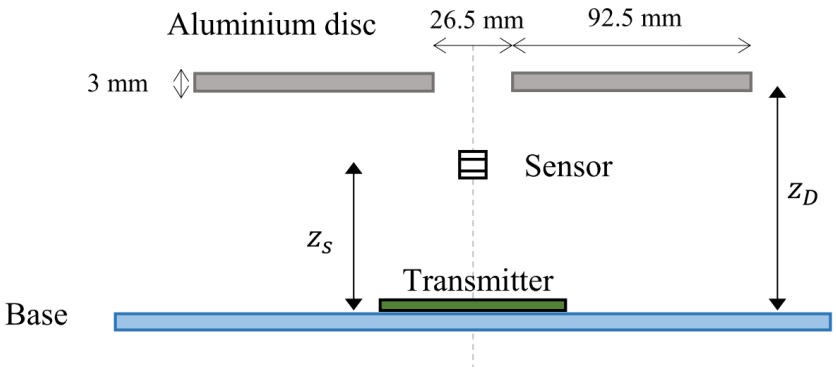



Figure 7.3: Schematic representation of the test setup used for finite element simulation and experimental tests.

For each sensor and distorter position, the frequency response from 1 Hz to 1 MHz was simulated. The gain and phase of the measured voltage relative to the applied current was calculated. The gain and phase error is defined as the difference in system gain between the

applied current and the measured current, with and without the distorter, expressed in dB. Equation (7.8) represents the gain error where $G_{WD}(s)$ is the system gain with the distorter and $G_{ND}(s)$ is the system gain without the distorter.

$$D(s) = \frac{G_{WD}(s)}{G_{ND}(s)} \tag{7.8}$$

Figure 7.4, Figure 7.5 and Figure 7.6 show the simulated frequency response of five sensor locations with the conductive disk placed at 39.9 mm, 135.9 and 212.7 mm respectively. Figure 7.7, Figure 7.8 and Figure 7.9 shows the gain error at different sensor locations for a set of ten different distorter locations. From each of the plots, we see that at very low frequencies the distorter has little impact on the output. However as the frequency goes increase above 100 Hz, the error dramatically increases in certain cases. Typically, if the distorter is closer to the transmitter, the sensor will see a greater error. However if the sensor is closer to the transmitter than the distorter, the error is relatively small.

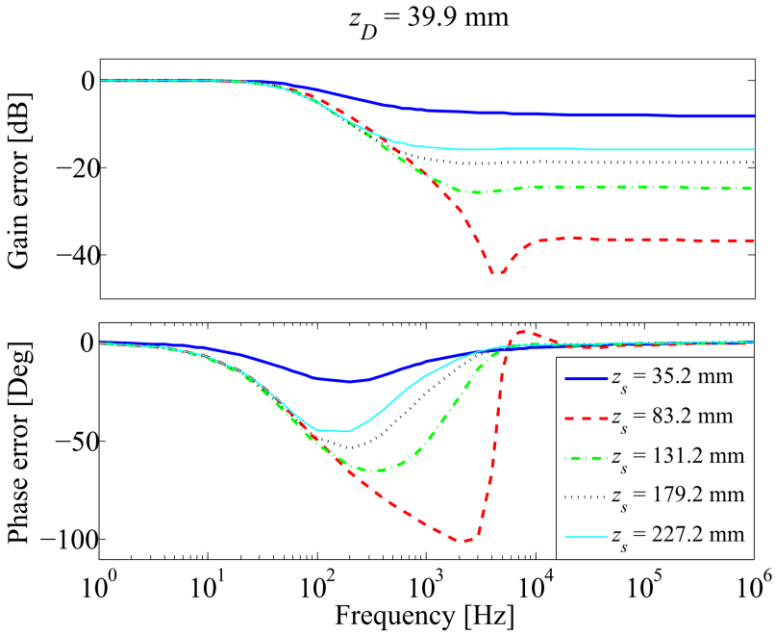



Figure 7.4: Simulated frequency response error, $D(s)$, from five sensor locations with the conductive disk placed at 39.9 mm from the transmitter coil.

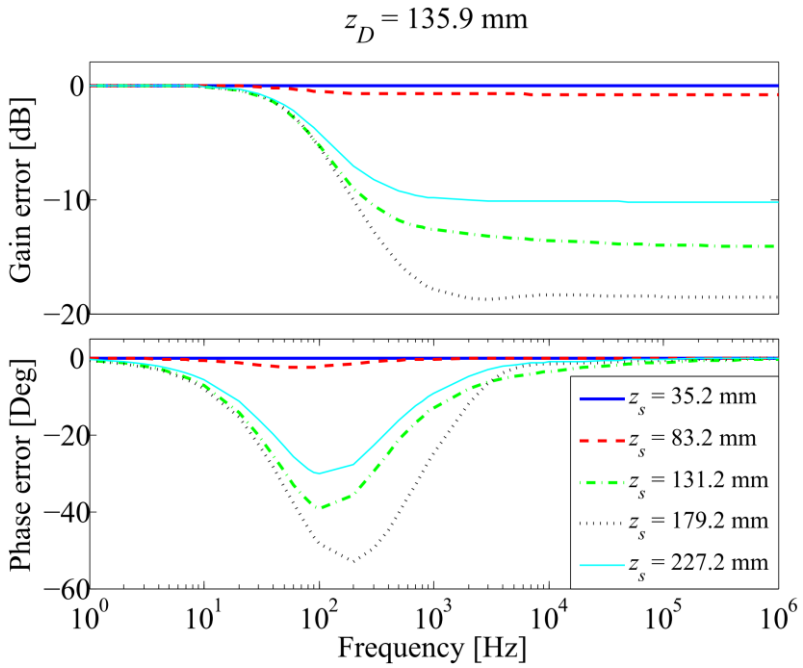



Figure 7.5: Simulated frequency response error, $D(s)$, from five sensor locations with the conductive disk placed at 135.9 mm from the transmitter coil.

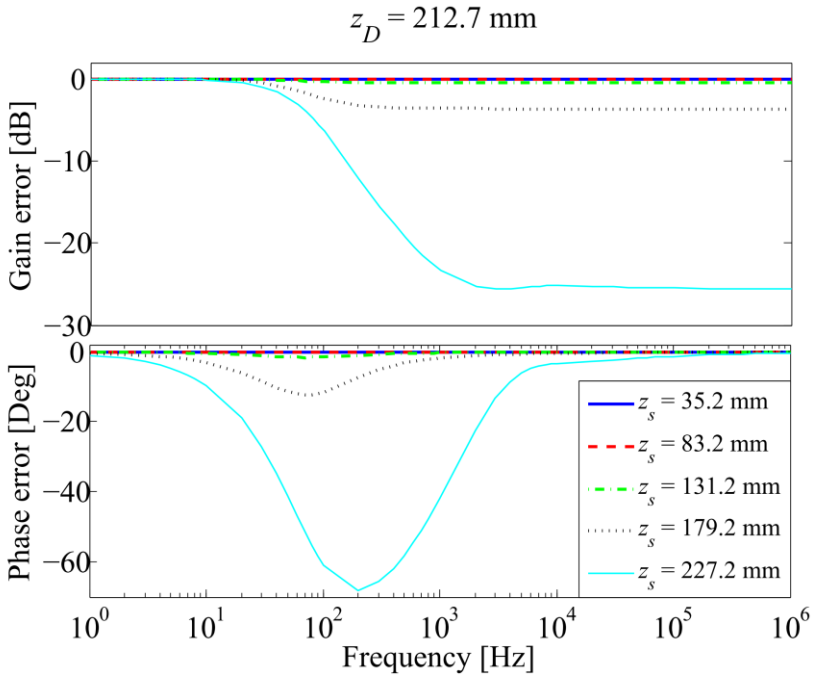



Figure 7.6: Simulated frequency response error, $D(s)$, from five sensor locations with the conductive disk placed at 212.7 mm from the transmitter coil.

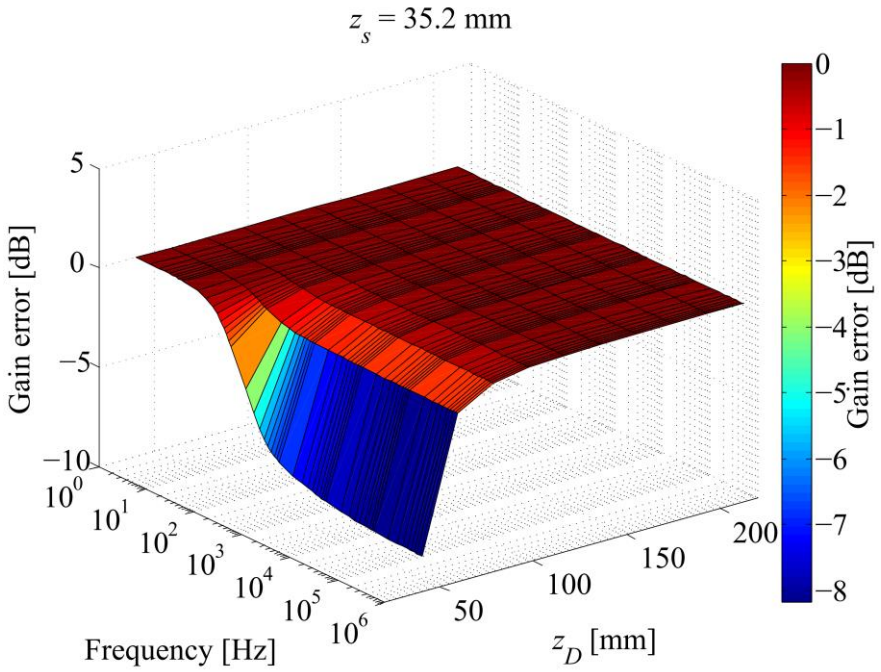



Figure 7.7: Simulated frequency response error, *D*(s), surface plot for ten different disc locations with the sensor coil placed at 35.2 mm from the transmitter coil.

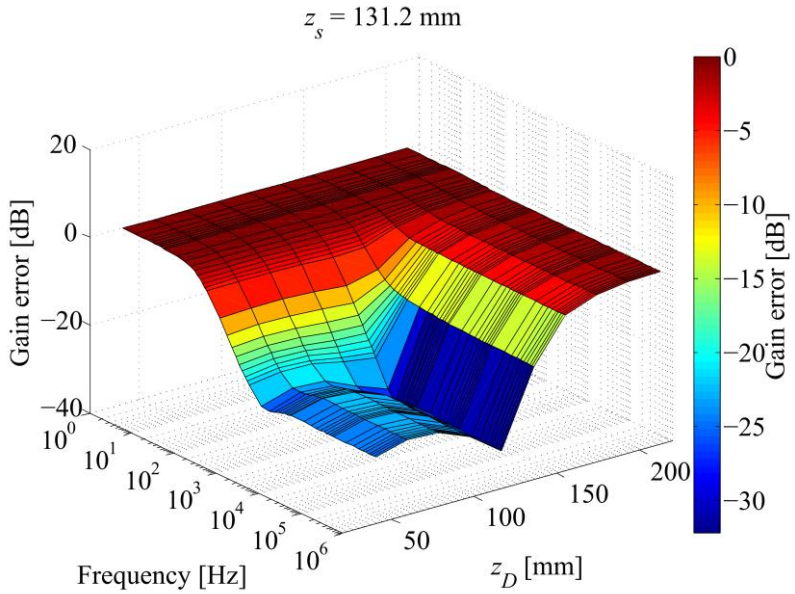



Figure 7.8: Simulated frequency response error, *D*(s), surface plot for ten different disc locations with the sensor coil placed at 131.2 mm from the transmitter coil.

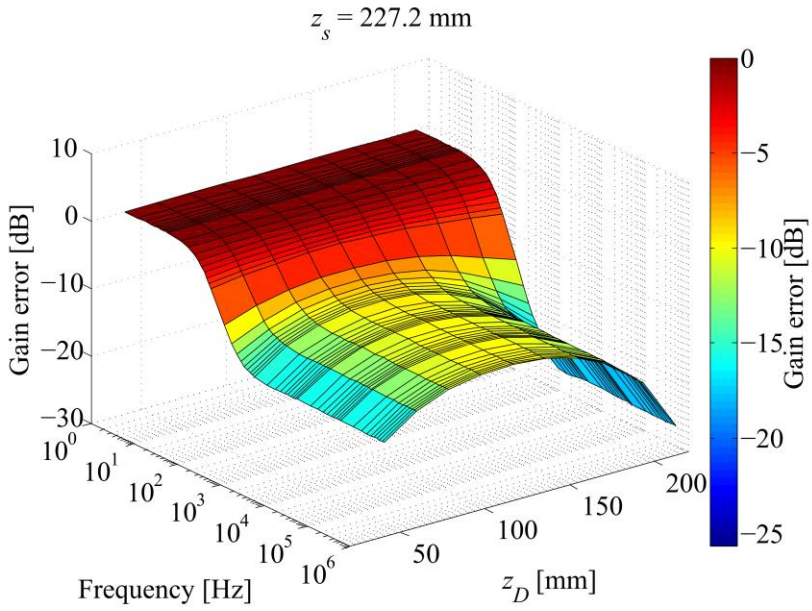



Figure 7.9: Simulated frequency response error, $D(s)$, surface plot for ten different disc locations with the sensor coil placed at 227.2 mm from the transmitter coil.

### 7.2.4. Experimental Setup

To determine the magnetic field measurements and the transmitter current, the circuit described in Section 6.4.1 was used. This circuit facilitated magnetic field measurements over a wide range, between 1 Hz up to 1 MHz. A GP-102 Gain Phase Analyser was used to take the measurements.

For the conductive distorter, a 3 mm thick aluminium disc was used. The disc has an inner radius of 13.25 mm and an outer radius of 105.25 mm. The hole through the centre allowed the sensor to be positioned anywhere along the axis of the transmitter. Figure 7.10 shows this disc. Two Lego Duplo blocks attached to the disc allowed it be raised vertically as required.

The transmitter coil was secured to a Perspex base, and the sensor, which was an NDI Aurora 610057 sensor, was rigidly placed within a Lego block. This arrangement allowed the sensor to be accurately positioned along the central axis of the transmitter coil. Figure 7.11 shows a photograph of the test setup, which is the same as the schematic shown in Figure 7.3.



Figure 7.10: The aluminium disc which was used as the conductive distorter for all tests. The disc is 3 mm thick, with an inner radius of 13.25 mm and an outer radius of 105.25 mm.

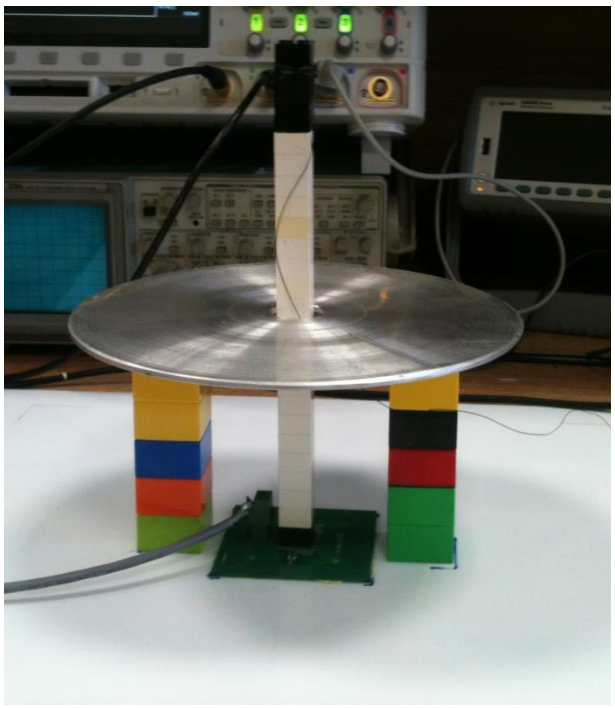


Figure 7.11: Experimental setup used for the testing system distortion. The transmitter coil is fixed on the Perpex base, with the sensor positioned using standard Lego Duplo blocks. The height of the disk is changed by adding Duplo blocks, two of which are rigidly secured to the disc itself.

### 7.2.5. Results

Figure 7.12, Figure 7.13 and Figure 7.14 show the experimental frequency response for five sensor locations with the conductive disk placed at 39.9 mm, 135.9 and 212.7 mm respectively. Figure 7.15, Figure 7.16 and Figure 7.17 show the gain error for different sensor locations for a set of ten different distorter locations. For all the results shown, measurements below 100 Hz are noisy due to the small amplitude of the induced current in the sensor. Results below 100 Hz are considered unreliable, as much larger low frequency

magnetic fields would be required to get reliable results. At these low frequencies, *1/f* or "flicker noise" also contributes to the variation in the measured signal as well as other noise sources, such as 50 Hz mains. In the range from 100 Hz up to approximately 5 kHz, the results are similar to the simulated case. However above 5 kHz, the gain error is seen to decrease, which contradicts both the simulation and theoretical model. The primary reason for this is high frequency effects such as parasitic capacitance which are not modelled.. Reflection and absorption of the aluminium could also be contributing to these differences, as beyond around 10 kHz conductive materials such as aluminium or copper show a dramatic rise in both absorption and reflection losses [195].

The main result here is that it is clear that conductive materials contribute significantly to errors in magnetic field measurements over a wide frequency range. Similar to the simulation case, it was observed that errors are generally much greater if the distorter is closer to the transmitter than the sensor. This is because larger eddy currents are induced in the distorter when it is closer to the transmitter. Hence the resulting secondary field is large in comparison to the field seen by the sensor resulting from the transmitter alone.

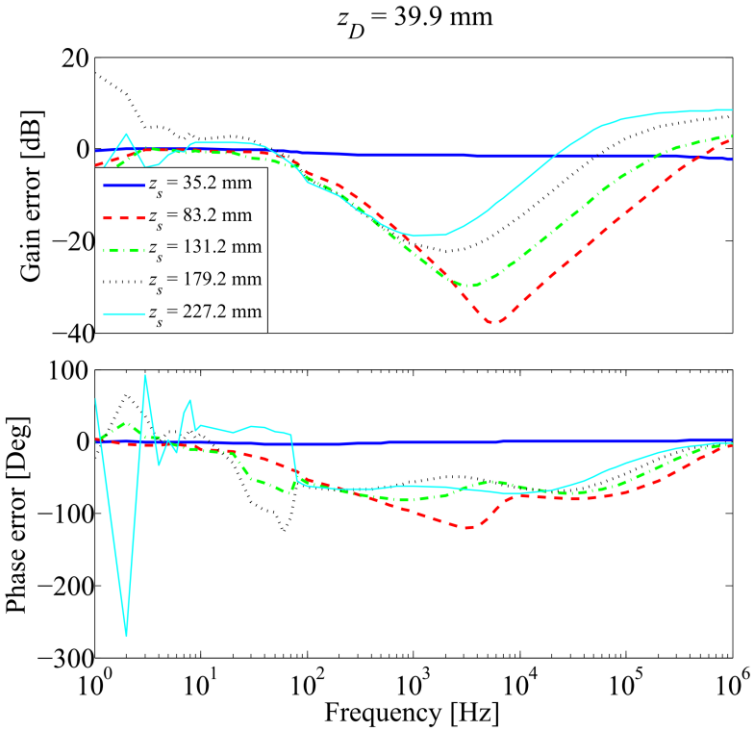



Figure 7.12: Experimental frequency response error, $D(s)$, from five different sensor locations with the conductive disk placed at 39.9 mm from the transmitter coil.

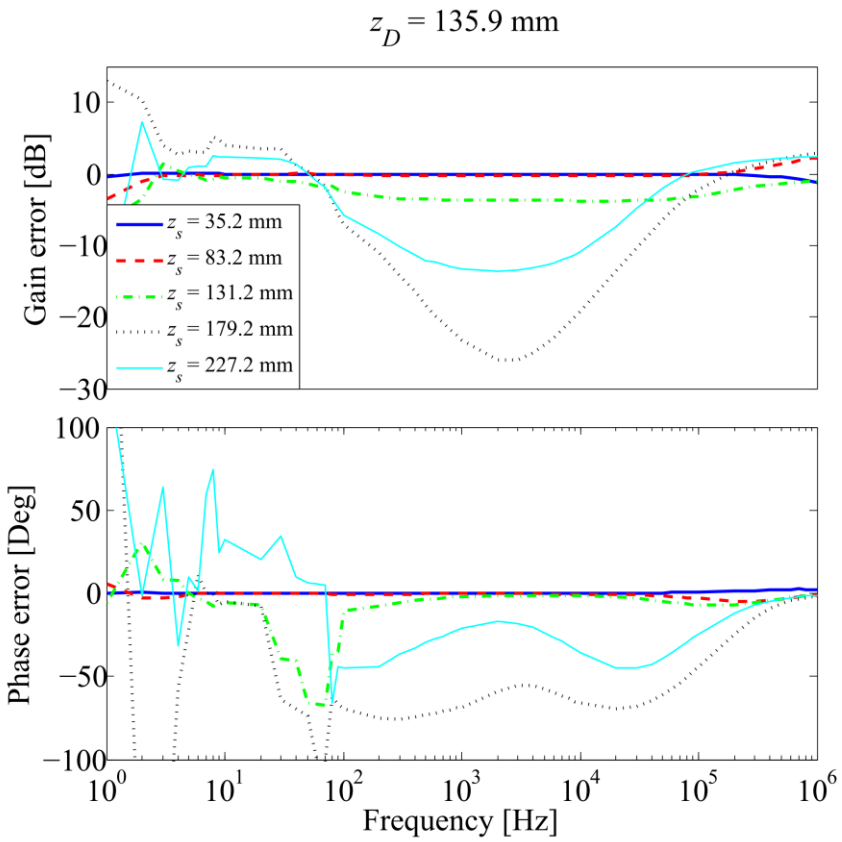



Figure 7.13: Experimental frequency response error, $D(s)$, from five different sensor locations with the conductive disk placed at 135.9 mm from the transmitter coil.

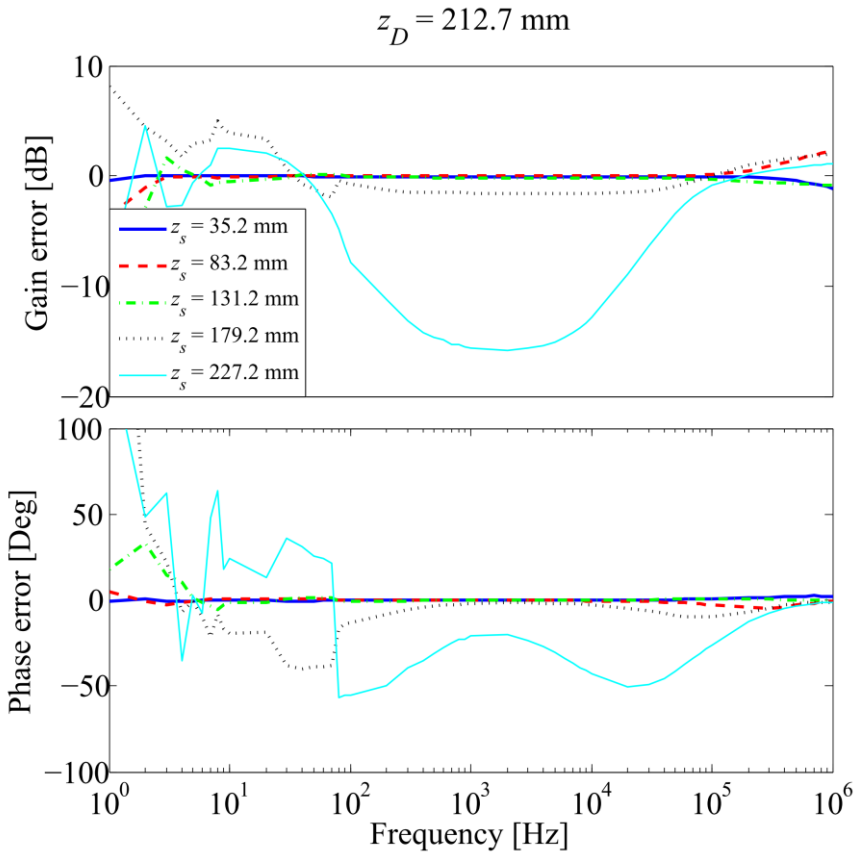



Figure 7.14: Experimental frequency response error, $D(s)$, from five different sensor locations with the conductive disk placed at 212.7 mm from the transmitter coil.

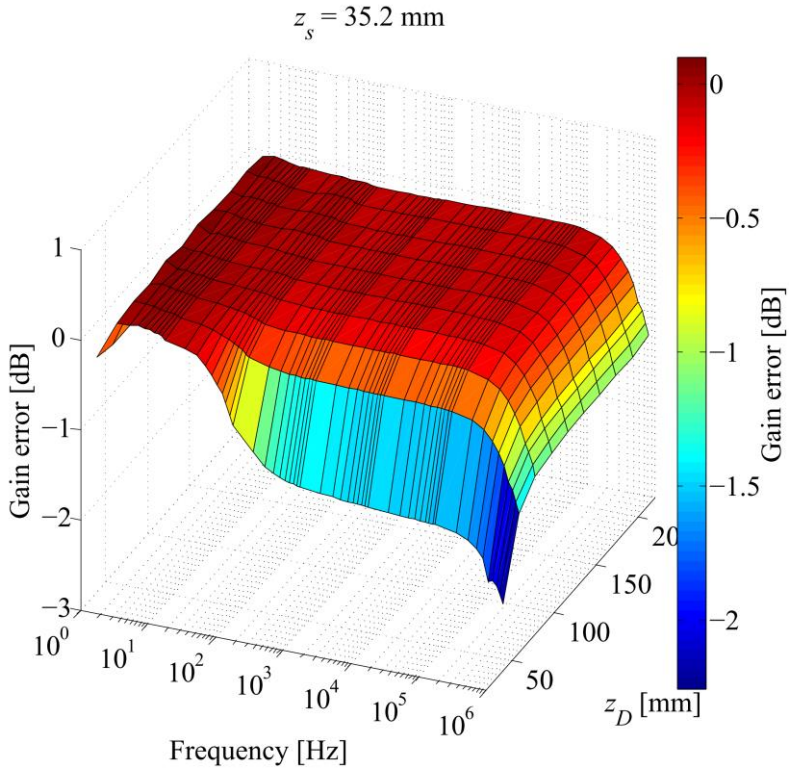



Figure 7.15: Experimental frequency response error, $D(s)$, surface plot from ten different disc locations with the sensor coil placed at 35.2 mm from the transmitter coil.

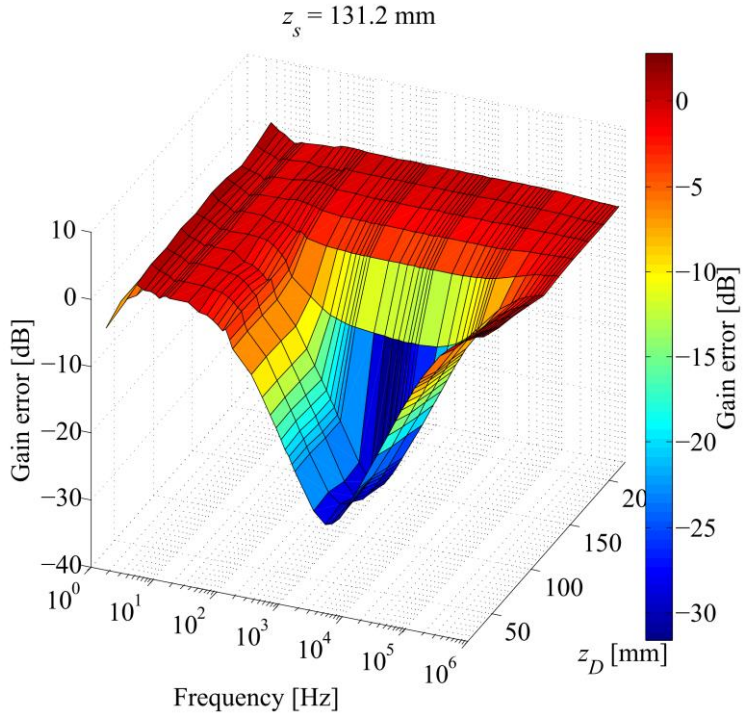



Figure 7.16: Experimental frequency response error, $D(s)$, surface plot from ten different disc locations with the sensor coil placed at 131.2 mm from the transmitter coil.

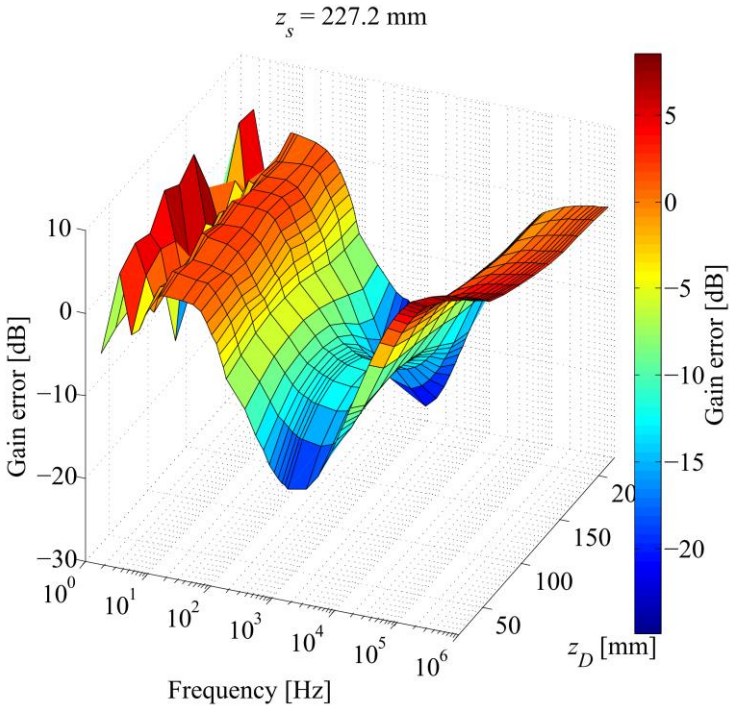



Figure 7.17: Experimental frequency response error, $D(s)$, surface plot from ten different disc locations with the sensor coil placed at 227.2 mm from the transmitter coil.

### 7.2.6. Discussion

From the experimental results, we see that at higher frequencies the basic model presented in theory section does not closely match the recorded data. The primary reason for this is the skin effect. At higher frequencies, the resistance of the distorter begins to sharply increase in proportion to the square root of the applied frequency. This increase in resistance decreases the induced eddy currents and, in turn, reduces the size of the secondary magnetic field which reduces the error at higher frequencies. The skin effect can be modelled into the equations using Bessel functions [196]. However such investigations are considered beyond the scope of this work. The inductance of the distorter is also dependant on frequency, which contributes to the deviation from the model.

From both sets of data it was seen that at low frequencies, attenuation is less pronounced. However it is clear from the experimental data that it is difficult to get a reliable signal measurement due to noise, and the small amplitude of the induced voltage. If a higher amplitude magnetic field was used at lower frequencies, this could mitigate against the effect of eddy current effects. However other disadvantages of this approach are higher power requirements for the transmitter array as well as slower demodulation, since more time would be required to gather sufficient data samples to ensure a reliable measurement.

## 7.3. Frequency Response of Human Tissue

### 7.3.1. Introduction

There are numerous studies which examine the interaction of the human body with electromagnetic fields, ranging from the effects of high voltage power lines [197], to power absorption of RF and microwave EM fields [198]. This area is also relevant to wireless power transmission for powering various implantable medical devices [199]. For EM tracking, a key assumption is that the low frequency magnetic fields used are not perturbed by the human body and can be ignored [88], [174]. However there exists little or no experimental evidence verifying this assumption or investigating the frequency response of the human body over the relevant frequency range. In particular, the cross-over frequency at which the human body begins to noticeably attenuate magnetic fields is not clearly defined. There exists numerous publications examining very high frequency absorption of EM fields, typically greater than 1 MHz [199]–[202], but in the range from DC to 1 MHz, limited information is available. Chen et al demonstrated that significant power attenuation of the order of 2-4 dB was observed in porcine tissue at frequencies between 500 kHz and 2 MHz [203]. Attenuation at this level is more than enough to severely affect EM tracking performance. The use of higher frequencies (e.g., >100 kHz) allows for larger induced voltages for induction sensors which potentially decreases the sensor size required, extends the range and allows for wireless EM tracking [67], [77].

In this section we investigate this low frequency attenuation of the human body by directly measuring the change in magnetic field measurements due to the presence of a human test subject. By determining a cut-off frequency above which significant attenuation is observed, the maximum practical range for a quasi-static EM tracking system can be estimated.

### 7.3.2. FEMM Simulations

To predict the potential effect of induced eddy currents due to the conductivity of human tissue, a simple 2D finite element model was simulated using FEMM. The human test subject was approximated as a homogenous cylinder of 350 mm diameter and 200 mm in height. These dimensions were chosen to roughly approximate the size of the upper torso. For electrical conductivity, a volume-averaged value of 0.1 S/m was chosen based on experimental data presented by Gabriel et al [204]. For the transmitter and sensor, two coils with 25 turns and a radius of 35 mm were simulated at a distance of 250 mm from each other at opposite ends of the cylinder. Figure 7.18 shows the attenuation in the induced signal. Clearly, the level of attenuation is very low for this simple model.

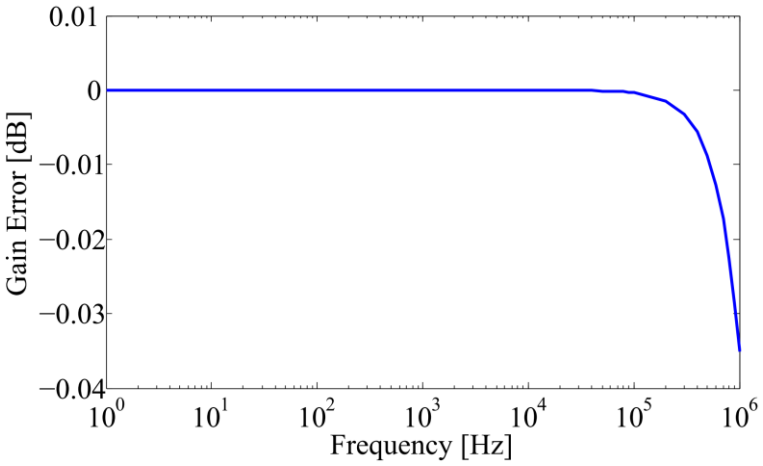



Figure 7.18: Simulated attenuation of a cylindrical body model 350 mm in diameter and 200 mm in height with a conductivity of 0.1 S/m.

FEMM is best suited for low frequency simulations as it does not take displacement currents into account. To investigate whether displacement current needs to be considered, we examine the ratio of induced currents to displacement currents as given by (7.8) [27] where $\sigma$ is the electrical conductivity, $\omega$ is the angular frequency and the electrical permittivity of the material is given by the product of the its relative permittivity and the permittivity of free space as in (7.9). A volume-averaged value of the relative permittivity of 1000 was used in this instance [205]. With these values, at 1 MHz, the ratio of displacement currents to conduction currents, given by (7.8), results as 1.79. This indicates that at 1 MHz, the displacement current is comparable with the induced conduction current and contributes significantly to the total induced current. However, this effect would only result in a small increase in the attenuation shown Figure 7.18.

$$\frac{|J_C|}{|J_D|} = \frac{\sigma}{\omega\varepsilon} \tag{7.8}$$

$$\varepsilon = \varepsilon_0 \varepsilon_r \tag{7.9}$$

### 7.3.3. Experimental Setup

**Transmitter**

A single square PCB coil with 25 turns and a side length of 70 mm was used as the transmitter in this test. This coil has a low self-capacitance and a relatively linear impedance with respect to frequency up to at least 1 MHz. The transmitter was driven with a sinusoidal output signal from a Powertek GP-102 Gain Phase Analyser. A 100 Ω sense resistor was used to measure the current flowing through the transmitter. The sense resistor was also tested to ensure a uniform resistance over the frequency range of interest. The transmitter current was carefully selected to ensure that the test subjects were not exposed to magnetic fields beyond the ICNIRP limits for occupational exposure [109].

**Sensor**

For the sensor, a customised square pick-up coil was wound with a side length of 64 mm and 200 turns to ensure a large SNR. This coil was wound directly onto a group of Lego Duplo blocks, allowing the sensor to be positioned accurately above the test subject and transmitter. The sensor coil was measured to have a series resistance of 16 Ω, an inductance of 1.3 mH and a parallel capacitance of 250 pF.

**Sensor Amplifier**

To amplify the signal from the sensor, a trans-impedance amplifier was used. This converted the induced current in the sensor coil into a voltage. An LT1226 operational amplifier was used for this circuit, with a feedback resistor of 220 kΩ. The induced current in the sensor is calculated using Kirchoff's voltage laws and results in (7.10) where $M$ is the mutual inductance between the transmitter and sensor coil. The output voltage of the trans-impedance amplifier is given by (7.11). The Gain Phase Analyser measures the output voltage of the amplifier. The gain between the output voltage of the amplifier and the input transmitter current is then determined. A change in the gain due to the presence of the test subject indicates attenuation in the detected magnetic field.

$$I_S = \frac{-Ms}{R_S + L_S s} I_T \tag{7.10}$$

$$V_{out} = I_S R_f \tag{7.11}$$

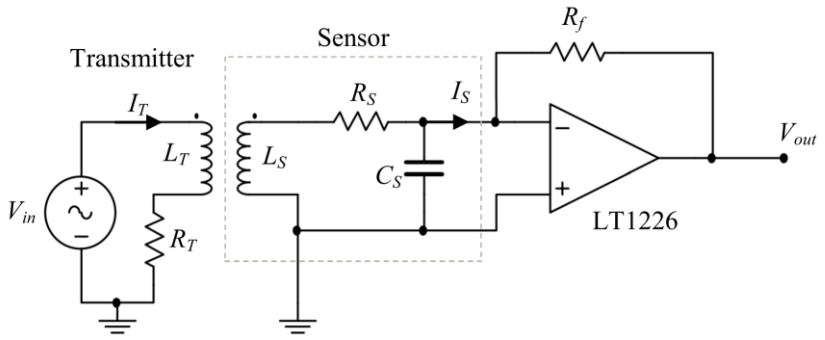



Figure 7.19: Circuit diagram of the transmitter and receiver circuit with trans-impedance amplifier.

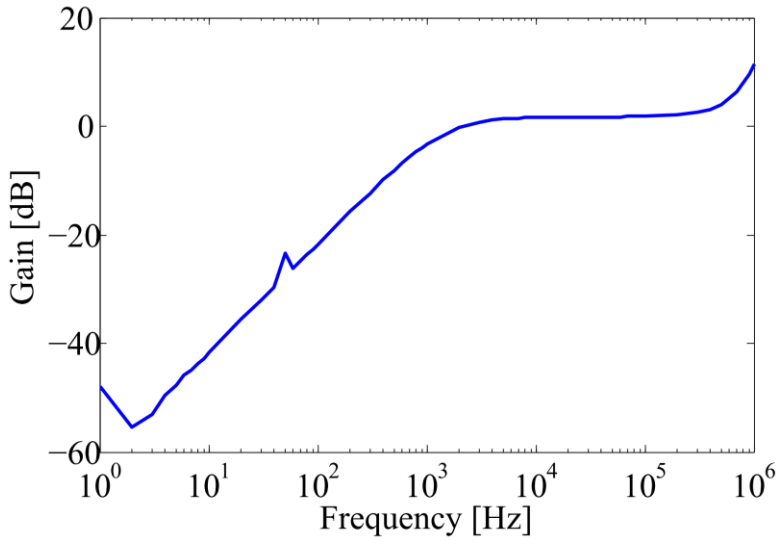
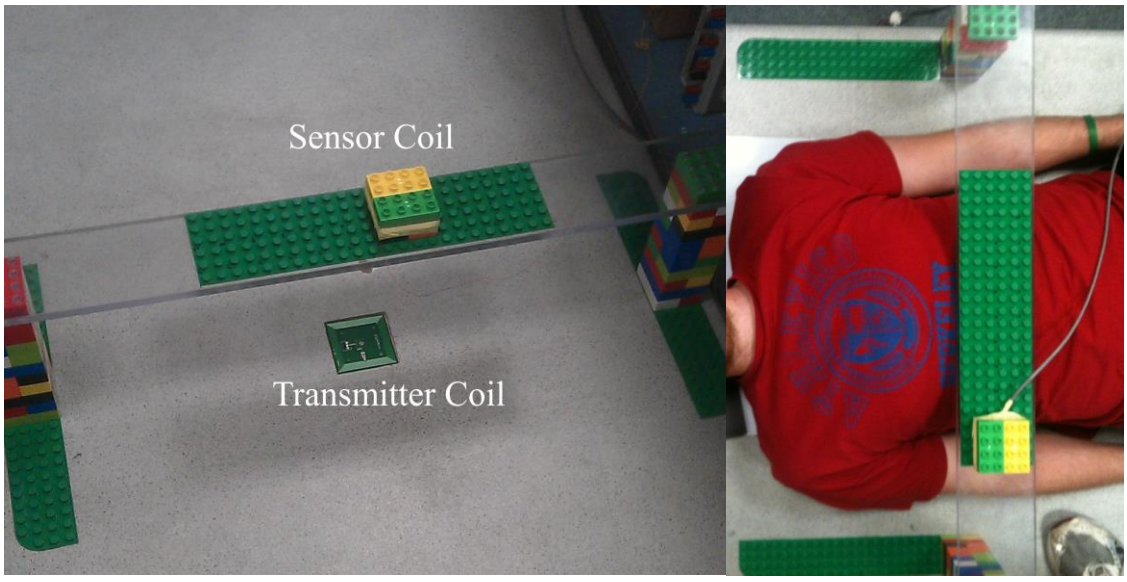



Figure 7.20: Experimental gain between the sensor amplifier output and transmitter input current at an axial displacement of 280 mm.

**Test Bed**

Figure 7.21 shows the test bed for the experiment. The test subject lies on the base board directly over the transmitter coil and below the sensor coil. The sensor can be placed in fixed positions along a Lego Duplo baseplate above the test subject. The height of the board can also be increased depending on the size of the test subject. This allows for repeatable testing. An additional Perspex spacer was added above the transmitter to reduce interference with the transmitting current.




(a) (b)

Figure 7.21: (a) Test rig showing the transmitter and receiver coil along with the Lego Duplo positioning fixture. (b) Photo of a test subject during a test.

### 7.3.4. Results

**Frequency Response Data**

The main tests recorded the gain between the transmitter current and the output of the sensor

amplifier. By calculating the error in the measured signal due to the presence of the human test subject between the transmitter and the sensor, the frequency at which the body begins to affect measurements can be easily determined. Figure 7.22 shows an example of the recorded signal from a test subject plotted as a surface plot with the sensor position as the variable on the *y* axis. The zero position of the sensor refers to when the sensor is co-axial with the transmitter coil. From this figure we see that the measured signal below 100 Hz is noisy and unreliable. Hence, for the remaining results, only measurements above 100 Hz are considered. For each test, the body under test was positioned such that the sensor was directly above the sternum. Figure 7.21(b) shows an example of test setup during an experiment.

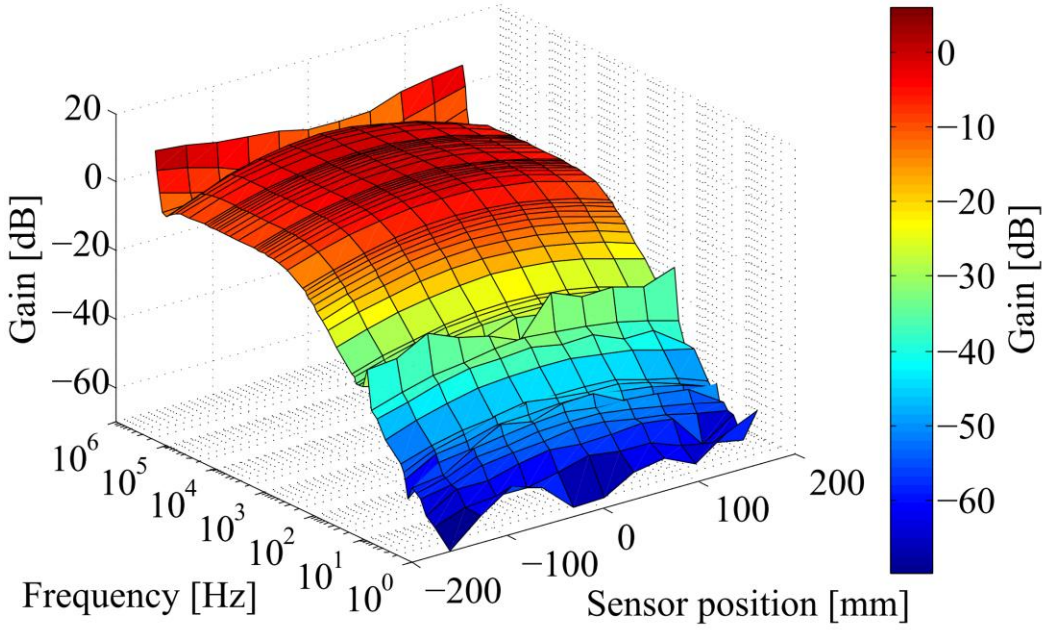



Figure 7.22: Surface plot of the amplifier gain with a test subject between the transmitter and sensor for varying sensor position.

Figure 7.23 shows the frequency response from three different test subjects. The sensor was positioned in eleven different locations across the chest with the zero positon being vertically above the sternum. From each of the tests, very little variation is observed up to approximately 100 kHz. Beyond this frequency, it was observed that the signal was generally attenuated by the test subject. However, at frequencies approaching 1 MHz the signal was seen to increase. This may be due to capacitive coupling between the test subject and the receiver coil as the effect is dependent on position, and some positions show this behaviour more than others. The BMI of each test subject was 27.1, 23.3 and 27.2 respectively. We see that the second test subject had the lowest BMI and experienced the lowest attenuation. Hence, higher BMI would seem to increase the attenuation effects.

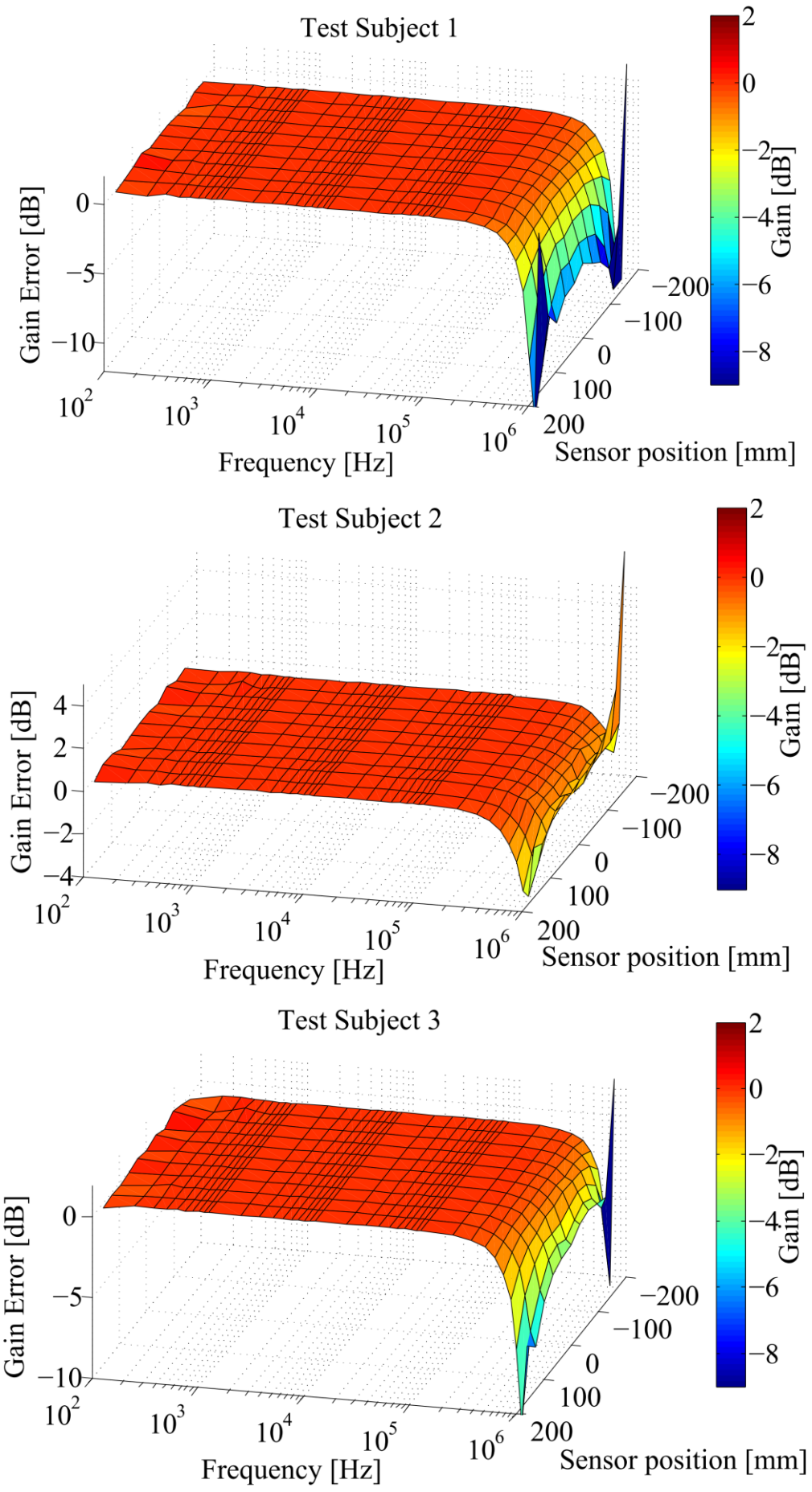



Figure 7.23: Gain error surface plots for three different test subjects.

An additional test was carried out on a single test subject where the sensor was positioned in 121 locations over a square grid measuring 32 cm × 32 cm directly above the torso with the square area centred on the sternum. At each location, the frequency response between 10 kHz and 2 MHz was recorded. Using this result, the -3dB frequency of the gain error was determined using an interpolating spline. The resultant gain error was plotted as a surface shown in Figure 7.24. From Figure 7.24 we see that beyond 500 kHz, every measurement was seen to at least have an error of −3 dB which is equivalent to 29.2 % error. This interpolation was repeated to determine the frequencies above which a 5 % error occurred. The result is shown in Figure 7.25. Above 250 kHz, we see that every position experienced an error greater than 5%.

Figure 7.26 shows the gain error at each location for frequencies of 600 kHz, 800 kHz and 1 MHz. At 600 kHz, attenuation is relatively uniform. However at 800 kHz and 1 MHz, the gain begins to increase on the edges of the test locations, which also correspond to the edges of the body under test. This is thought to be due to capacitive loading effects as will be explored in the next section. From testing of the EM tracking system in Chapter 4, it was observed that errors of greater than 2-3% significantly degraded the accuracy of the system. Hence above 200 kHz EM tracking systems become sensitive to the presence of the body.

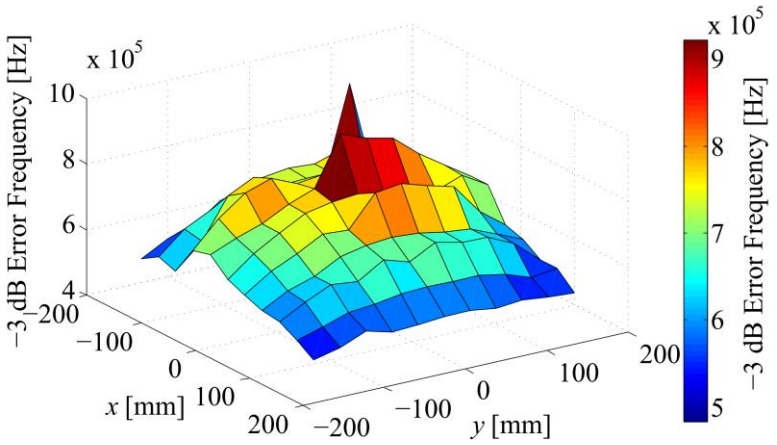



Figure 7.24: Surface plot showing the interpolated -3 dB error point for each test position.

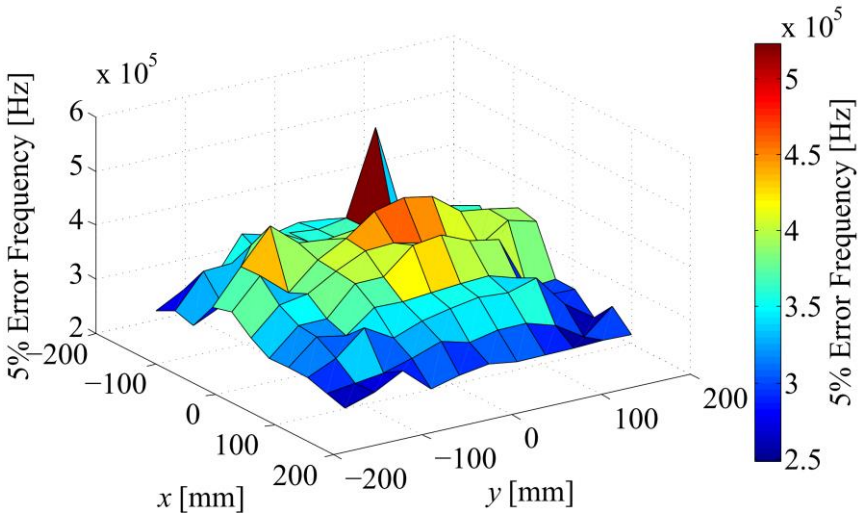



Figure 7.25: Surface plot showing the interpolated 5% error frequency position for each test point.

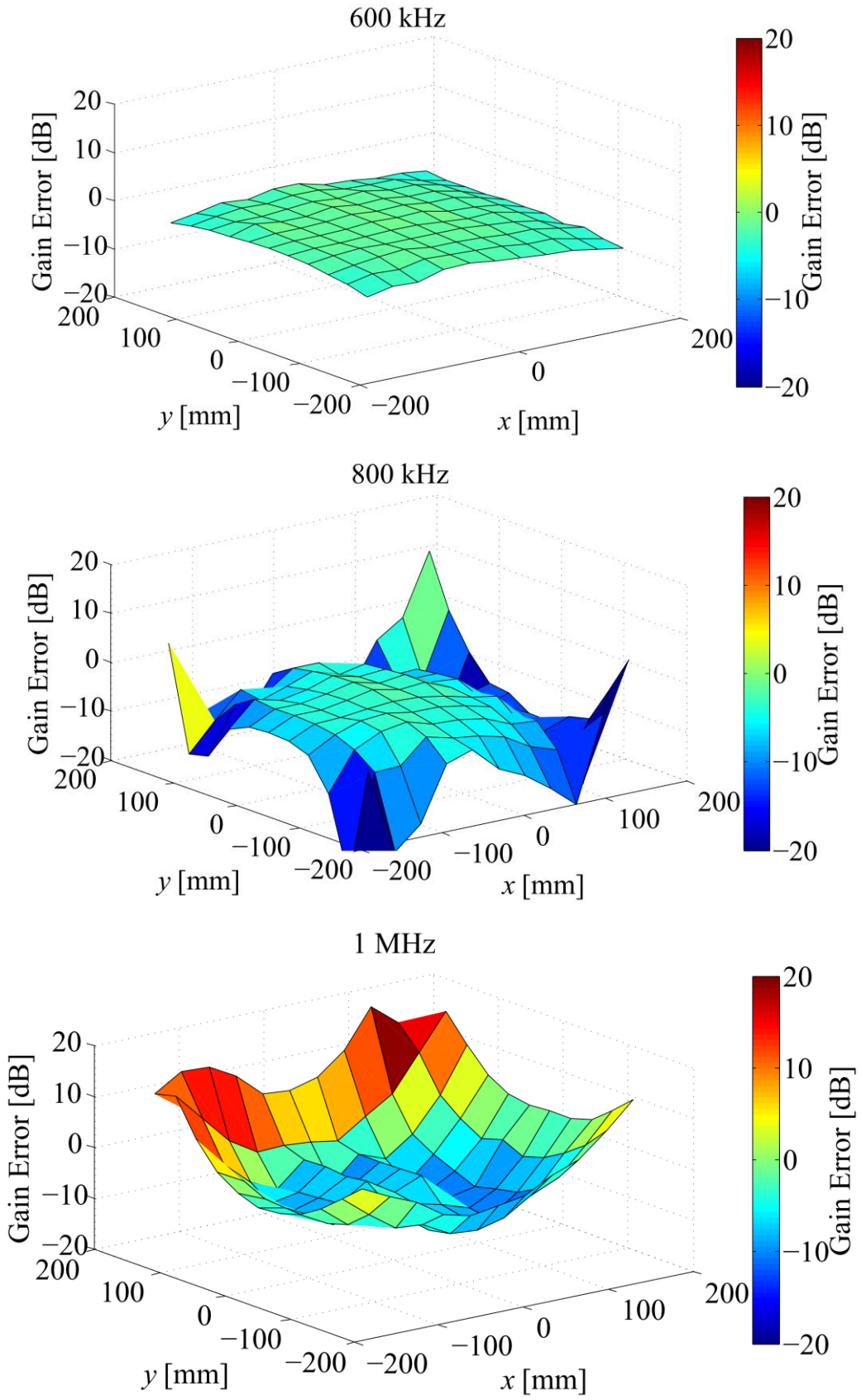



Figure 7.26: Surface error plots showing the gain error at 600 kHz, 800 kHz and 1 MHz.

**Transmitter Capacitive Effects**

One source of attenuation is the transmitter itself and effect of increased parasitic capacitance due to the proximity of the body to the coil. At higher frequencies, the parasitic

capacitance of the coil, the connecting cable and the capacitance between the body and the transmitter coils begins to shunt current flow away from the transmitter coil. Hence, the recorded current in the sense resistor does not directly correspond to the transmitter current. To illustrate this phenomenon, consider the schematic representation shown in Figure 7.27. In this figure, $V_{Source}$ and $R_{Source}$ represent the applied voltage and output impedance of the signal source respectively. $R_{Sense}$ is the resistance of the current sense resistor, $I_{Sense}$ is the current flowing in the sense resistor, $I_C$ is the current flowing through the capacitance, $I_T$ is the transmitter current, $L_T$ is the inductance of the transmitter and $R_T$ is its resistance. The parasitic capacitance $C_P$ is given by (7.12) and comprises the transmitter capacitance, $C_T$, the capacitance of the connecting cables and any additional capacitance $C_{Body}$ added by proximity to the human test subject.

$$C_P = C_T + C_{Cable} + C_{Body} \tag{7.12}$$

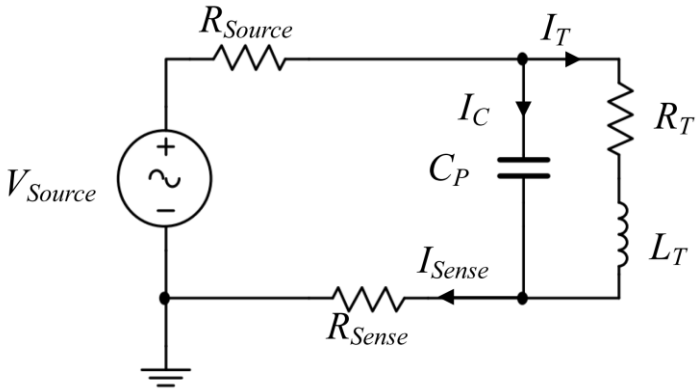



Figure 7.27: High frequency equivalent circuit of the transmitter and test subject.

The current in both the parallel capacitance and the transmitter is represented by (7.13) and (7.14), with the total current represented by (7.15).

$$I_C = \frac{V_{Source}\left(C_P R_T s + C_P L_T s^2\right)}{\left(R_{Source} + R_{Sense}\right)\left(1 + C_P R_T s + C_P L_T s^2\right) + \left(R_T + L_T s\right)} \tag{7.13}$$

$$I_T = \frac{V_{Source}}{\left(R_{Source} + R_{Sense}\right)\left(1 + C_P R_T s + C_P L_T s^2\right) + \left(R_T + L_T s\right)} \tag{7.14}$$

$$I_{Sense} = I_C + I_T \tag{7.15}$$

Changes in the overall capacitance can affect the distribution of current between $I_C$ and $I_T$. Hence the transmitter current may change due to proximity to the test subject. For example, at 1 MHz the measured sense resistor voltage was 765.3 mV, with the test subject over the transmitter. This voltage increased to 801.2 mV which is a change of 4.69 %. Using the model presented here, this corresponds to an additional capacitance of 5.4 pF. By adding a 10 mm Perspex spacer between the transmitter and the test subject, this capacitance change was reduced to 0.9 pF and the change in the sense resistor voltage reduces to 1.56 %.

Figure 7.28 compares the gain error due to a test subject with and without a spacer above the

transmitter. Clearly, the results are less perturbed when there is reduced capacitive coupling between the transmitter and the body.

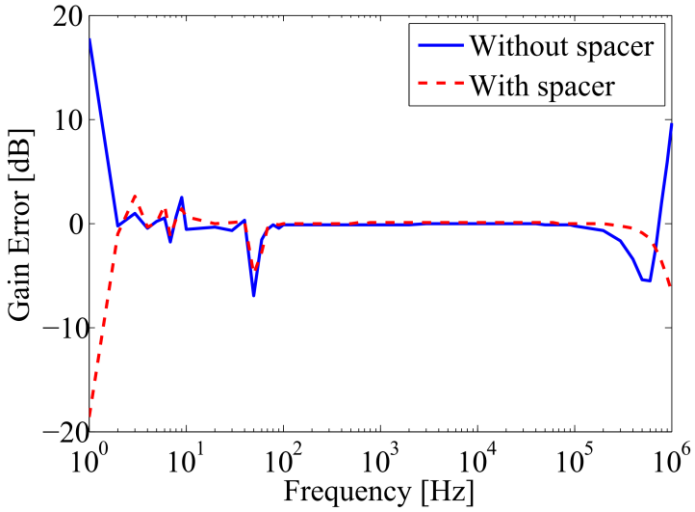



Figure 7.28: Comparing the effect of a Perspex spacer between the test subject and the transmitter.

**Sensor Capacitive Coupling Effects**

A significant factor in the test results was the effect of capacitive coupling between the human test subject and the sensor. It was observed that when the body was in close proximity to the sensor, large changes in detected voltages were observed at frequencies above 200 kHz. To confirm that this effect was capacitive in nature, the sensor coil was wrapped in a copper foil shield. The error due to the test subject was determined for the cases with and without the shield, and with both grounded and ungrounded arrangements. Grounding allows a low impedance path for induced charge such that it reduces the effect on the sensor [133]. Figure 7.29 shows the result of this test for a single sensor location. Above 300 kHz, the grounded shielded case deviates less from expected performance than the case without the ungrounded shield. Hence, the capacitive coupling has been reduced although there still is a significant deviation even with the grounded shield.

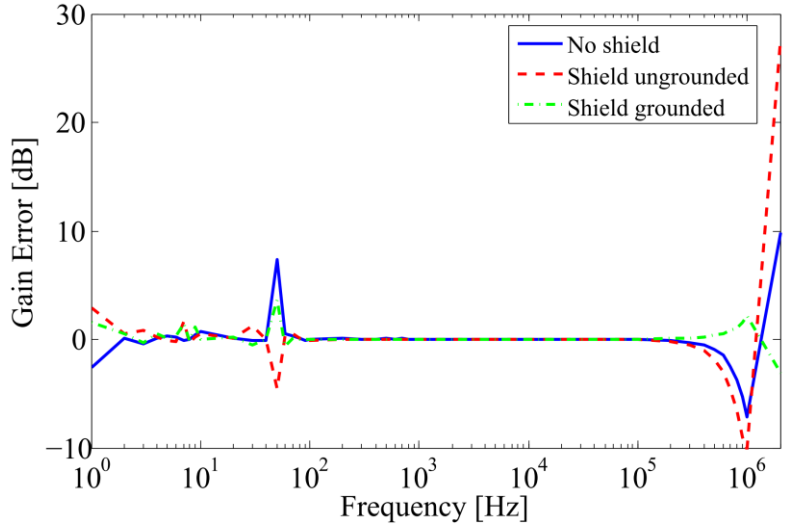



Figure 7.29: Comparing the effect of capacitive coupling between the sensor and the body by adding a copper foil shield.

To account for the effects of parasitic capacitance added to the sensor circuit by the presence of the human test subject, modifications were made to the circuit model of the sensor amplifier. Jonassen has proposed a capacitance model for the human body as a parallel combination of a capacitor and a large value resistor, with this capacitance on the of order between 200-400 pF [206]. It was assumed that a small capacitance coupled this human subject model to the detector circuit as illustrated in Figure 7.30. The body is represented by a resistance $R_B$ and a capacitance value between the body and ground given by $C_{BG}$. The capacitance between the body and sensor was denoted by $C_{BS}$. $M_{TS}$ here represents the mutual inductance between the transmitter and the sensor and $V_{ind}$ represents the induced voltage in the sensor due to the transmitter.

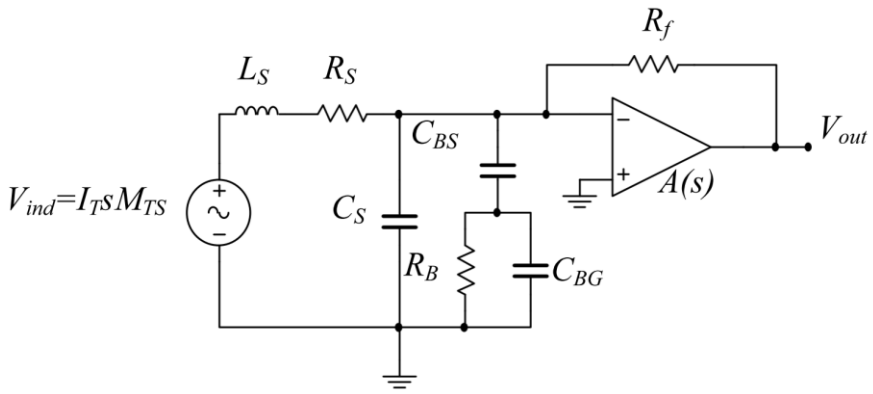



Figure 7.30: Schematic of the sensor amplifier including parasitic capacitance due to the human body.

In order to determine the effects of this coupled capacitance, the output of the amplifier including the non-ideal operational amplifier was determined analytically. A simplified model for the circuit is shown in Figure 7.31. The output of the amplifier is given by (7.16) where $Z_1$, $Z_2$ and the amplifier gain $A(s)$ are defined by (7.17), (7.18) and (7.19) respectively. The model was simulated using the parameters given in Table 7.1.

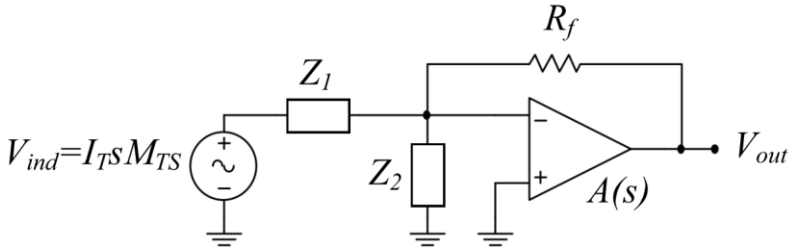



Figure 7.31: Simplified schematic used to determine the analytical output of the amplifier.

$$\frac{V_{out}}{I_T} = \frac{-A(s)R_f Z_2 M_{TS} s}{Z_1 R_f + Z_2 R_f + Z_1 Z_2 + A(s) Z_1 Z_2} \tag{7.16}$$

$$Z_1 = R_T + L_T s \tag{7.17}$$

$$Z_2 = \frac{1 + sR_B\left(C_{BG} + C_{BS}\right)}{s\left(C_{BS} + C_S + sR_B\left(C_{BG}C_{BS} + C_S C_{BG} + C_S C_{BS}\right)\right)} \tag{7.18}$$

$$A(s) = \frac{K}{1 + s\tau} \tag{7.19}$$

| Variable | Value |
|---|---|
| $R_S$ | 16 Ω |
| $R_f$ | 200 kΩ |
| $R_B$ | 100 GΩ |
| $L_S$ | 1.35 mH |
| $M_{TS}$ | 5.5 nH |
| $C_S$ | 250 pF |
| $C_{BG}$ | 200 pF |
| $C_{BS}$ | 20 pF |
| $K$ | 50,000 |
| $\tau$ | 25 µs |

Table 7.1: Parameters used for the simulation of the effects of parasitic capacitance changes.

Figure 7.32 shows the results of a MATLAB simulation of the model presented in Figure 7.31. Close to 1 MHz, the gain error sharply rises. This is similar to behaviour seen in certain positions in Figure 7.23. The sharp rise in gain error is also seen in Figure 7.29. Hence, it may be concluded that a certain amount of the deviation, particularly at 1 MHz and beyond, corresponds to capacitance model presented in (7.16). The increase in gain, changes the resonant point of the sensor circuit. Ideally, the trans-impedance amplifier shorts out the parallel capacitances due to the virtual ground of the inverting input. However, at higher frequencies when the op-amp gain reduces, it can no longer effectively maintain the virtual ground and the capacitance begins to take effect. This behaviour would also be seen in other amplifier topologies, and may have an even greater effect on instrumentation amplifier designs which do nothing to counteract parallel capacitance effects.

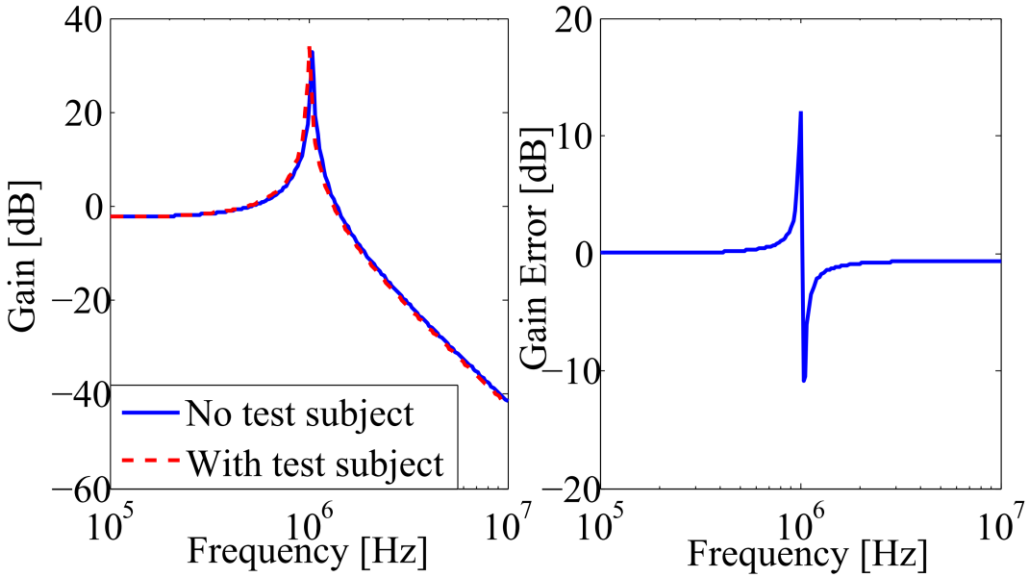



Figure 7.32: Simulated effect of parasitic capacitance on the gain error in the receiver.

One further effect already noted is the effect of induced voltages in the body which are

capacitively coupled through the same mechanism as capacitance loading. The changing magnetic field caused by the sensor induces electric fields in the body, which, as a result, generates a potential difference due to the dielectric behaviour of the human body [205]. An induced voltage such as this could easily be coupled to the receiver as shown in Figure 7.33, where $V_C$ represents an induced voltage which is capacitively coupled to the amplifier. Depending on the phase of this voltage, it may add or subtract from the induced sensor voltage which may account for the reduced gain seen in Figure 7.23 and Figure 7.29 before the capacitive effects shown in Figure 7.32 take effect. The analysis is not considered here but complex numerical methods could be used to predict the induced voltage $V_C$ by using Maxwell's equations to determine the induced potential difference in the body.

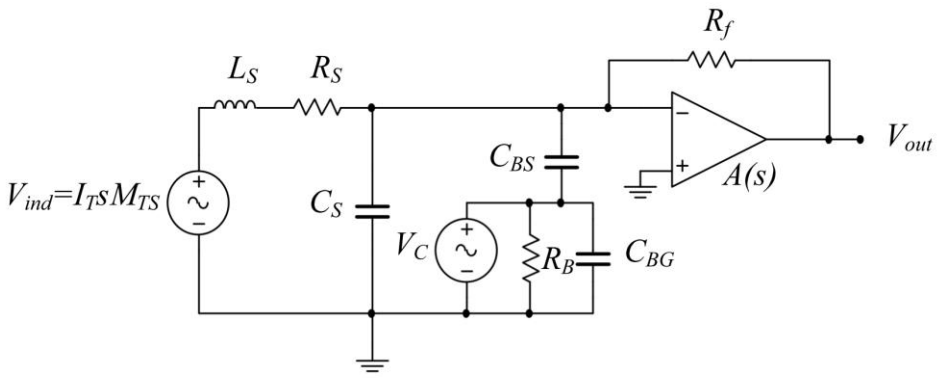



Figure 7.33: Revised schematic showing a capacitively-coupled voltage into the system from the test subject.

### 7.3.5. Discussion

**Frequency Response Data**

From the results presented, it is clear that beyond 100–200 kHz, magnetic field measurements in proximity to human tissue become unreliable. This is due to a number of factors, most notably induced eddy currents in the body, and capacitive coupling between both the subject with the transmitter, and the subject with the sensor. Subject variation resulted in inconsistencies between test subjects, as some subjects were seen to cause larger attenuation than others.

Between 100 Hz and 100 kHz, a mostly flat response is observed as expected. At lower frequencies, the effects of capacitive coupling and induced eddy currents are very small and can be neglected. At higher frequencies are required, careful attention is required to avoid capacitive effects. However the unpredictability of the measurements in a clinical setting makes operating in this range undesirable. For other applications such as tracking of objects in outdoor areas over large distances, higher frequencies may be used and have been shown to work well [207].

**Transmitter Capacitive Results**

At higher frequencies it was shown that a large portion of the sensed current begins to flow through the parallel capacitance of the transmitter and the connecting cables. The additional capacitance of the body is also shown to alter the transmitter current. The distance between the transmitter and the test subject should be minimised to reduce the effects of capacitive loading of the transmitter as well as the effect of coupling signals into the test subject which can then be capacitive coupled into the sensor. For EM tracking systems that use resonant circuits for the transmitter source [9], [77], additional capacitance may change the resonant frequency of the transmitter which may cause significant errors.

**Receiver Capacitive Results**

The main source of errors in the measurements at higher frequencies seems to be the effect of capacitive coupling between the test subject and the sensor. It is well known that the human body can often act as an antenna even for low frequency signals such as 50/60 Hz mains. From our experiments, above 100 kHz considerable attenuation was observed by simply placing a hand close to the sensor. In this frequency range, test subjects and people close to the test setup began acting as antennas due to the induced electric fields. These induced electric fields then easily interfered with the sensor through capacitive coupling between the body and the receiver circuit.

Through the use of a simple copper foil shield, the effect of the capacitive coupling was seen to reduce attenuation of the measured signal although it was not eliminated entirely. For the case where the sensor is positioned inside the test subject or patient, the effect of coupling may be even more pronounced. Further investigations would be necessary to fully quantify coupling effects due to *in vivo* attenuation.

## 7.4. Conclusion

We have investigated the potential magnetic field measurements associated with conductive materials and the human body. From the tests, it was seen that conductive materials severely affect the measured sensor signal, particularly in the case where the distorting element was closer to the transmitter that the sensor. This effect was shown by simulation to be small at low frequencies. However the small SNR at lower frequencies makes operation at these frequencies less useful. Complex methods must be employed when excessive conductive material is expected in the operating region [129].

No direct investigation into the effect of human tissue on EM tracking systems has been found in the literature. Experiments with human test subjects showed that below 100 kHz that there was negligible attenuation observed due to the presence of the test subject. However, above 100 kHz, the cumulative effect of the capacitive coupling, induced eddy currents (both conduction and displacement currents) and other unmodelled effects caused

the measurements to become unreliable. Hence, for reliable operation, EM tracking systems should use transmit frequencies of below 100 kHz to minimise the effect of the human body on overall tracking accuracy.

# Chapter 8
# Summary and Future Work

## 8.1. Summary of Thesis Contributions

This thesis represents an analysis of the use of magnetic fields in the steering and tracking of catheter devices. A detailed examination into magnetic steering has been presented. A complete 5-DOF EM tracking system has been developed, constructed, tested and evaluated in the pre-clinical setting. Finally, shielding for use in EM tracking systems has been examined and the performance benefits have been established. The novel contributions of this thesis are summarised here.

- The use of external electromagnets to steer permanently magnetised catheter tips has been shown to be impractical (Chapter 2). Large and very high power electromagnets would be required to generate a reasonable force for steering, primarily due to the limited volume of permanent magnetic material which can be attached to a low profile catheter and the considerable attenuation of magnetic field strength with distance.
- A unique demonstration of the use of electromagnetic fields to simultaneously steer and track the position of a permanent magnet has been presented (Chapter 2). The use of a simple closed-loop control system showed the control attainable with this type of arrangement. Through the use of a custom air-core sensor, the EM tracking system has been shown to operate in the presence of considerable external magnetic fields which may have application in MRI or clinical environments.
- A detailed mathematical analysis of the deflection mechanics of chains of permanently magnetised spheres has been presented (Chapter 2). Magnetic spheres in chain formations have been shown to give much larger deflections in comparison to other arrangements and the mathematical model presented here can be used to accurately predict these deflections.
- The design of our EM tracking system has been presented in detail and the relevant theory explored (Chapter 3). Novel improvements over other designs include the

PCB construction of the transmitter array, closed-loop current control and the demodulation schemes presented. The PCB transmitter allows for low cost manufacture and reproducibility as each coil can now be effectively assumed identical. The closed loop control of the transmitter current maintains a stable magnetic field over long time durations and effectively decouples each coil from each other, reducing cross-coupling effects. The efficient matrix based demodulation scheme allows for rapid demodulation of the multiple frequency components in the magnetic field waveform.

- The novel undersampling method for demodulation allows for a reduced sampling rate with which to acquire the magnetic field data (Chapter 3). This gives more time between samples for processing of each magnetic field component in real time. This, in turn, allows the use of low cost MCU and ADC hardware to detect the magnetic fields without a significant reduction in accuracy.
- Extensive testing of the EM tracking system using both the undersampling asynchronous demodulation method and the standard synchronous demodulation method has been demonstrated (Chapter 4). Position errors of $< 2$ mm are reported with orientation error of $< 1°$. A novel, least-squares calibration method for minimising errors in the magnetic field models is also presented.
- The use of the EM tracking system in a pre-clinical setting has been evaluated and the airways of a breathing lung phantom have been successfully navigated (Chapter 5). Registration was achieved using two methods; a rigid landmark-based method and a method fiducial-free approach. Both methods gave good registration although landmark registration gave better accuracy. The effect of breathing motion was demonstrated to contribute a significant displacement of the sensor which must be taken into consideration in future work.
- The testing and analysis of planar magnetic shielding materials for EM tracking systems was presented (Chapter 6). The use of MuMetal and ferrite was shown to give good performance, both successfully reducing errors resulting from a large ferromagnetic distorter placed below the transmitter.
- Finally, an investigation into the effect of conductive materials and the human body has on magnetic field measurements over a wide frequency range (Chapter 7). It was shown that conductive materials considerably effect magnetic field measurements and overall EM tracking accuracy over a large frequency range. The human body was seen to considerably effect measurements above 100 kHz.

## 8.2. Proposals for Future Work

### 8.2.1. Optimised Transmitter Configuration

The transmitter array has the largest impact on the performance of the EM tracking system. The convergence of P&O algorithm is directly affected by the position of each transmitter, with certain configurations giving improved performance. Due to the massive number of variables and permutations in the arrangement, optimisation is a difficult and complex process. Various optimisation techniques could be implemented to find the optimum configuration such as Monte-Carlo simulations or genetic algorithms to name but a few.
The number of transmit coils also has a considerable impact as there is more information available. However this increases the complexity of the model which may reduce the update rate albeit with a gain in overall accuracy. Reducing the operating frequency of excitation could also reduce errors from induced eddy currents in conductive materials in the region of operation. Improved modelling of the magnetic fields from each coil taking into account experimental data may also be investigated to reduce systematic modelling errors.

### 8.2.2. Consolidation of Circuit Subsystems

In Chapter 3, each subsystem of the EM tracker was presented in detail. Many of these subsystems are circuits and systems that are implemented separately. Consolidating all the hardware components into a single unit, possibly on a single PCB, would considerably decrease cost and improve reliability. The transmitter driver could also be optimised for increased efficiency as the Class B topology used is inherently inefficient in comparison to modern, high efficiency amplifier designs such as a Class D topology. In terms of DSP, an integrated processer, either MCU or FPGA for example, could be used for generating the control reference signals and demodulating the magnetic field components at high speed. With a consolidated system, the production costs, even for small scale manufacture, would be considerably lower than commercial alternatives.

### 8.2.3. Commercialisation and Medical Device Classification

The technology presented in this thesis could be potentially commercialised and sold as a medical device. Like all medical devices, it must adhere to the strict guidelines of the counties that it is sold in. For the greatest commercial opportunities the device would need to be certified for use in both the USA and the EU, both of which have different standards for classification of medical devices.
In the USA, the EM tracking system would be a Class 2 device due to its relatively low level of invasiveness and would fall under the 21 CFR 892.1750 (Computed Tomography X-ray

System) regulation number, similar to both Veran Medical's SPINDrive and superDimension's iLogic systems. Due to the fact that similar devices exist on the market, a Premarket Notification 510(k) procedure can be used to quickly get the device certified, as previous testing of existing systems can be referenced [208].

For classification in Europe, the device must meet European Directive 93/42/EEC [209]. According to this directive, the device would be a Class IIa device due to its low level of invasiveness and risk to the patient. Similar to the FDAs 510(k) procedure, for sale of a device similar to that already on the market in the EU, the device must be CE marked. To get this certification the device and its manufacturing must be clearly documented as stipulated by Annex VII of the 93/42/EEC Directive. Following an audit of these documents and the manufacturing process by a certified institution, the device may be CE marked and sold within the EU.

### 8.2.4. Miniature Transmitter with External Sensor Array

A fundamental limitation of many EM tracking systems, both commercial and research based systems, is the size of the tracking sensors. Typically these sensors are single axis sensors for 5-DOF tracking, or two axis for 6-DOF. As a result, typically iterative non-linear least squares algorithms such as Levenberg Marquardt must be used since only flux measurements are available and not full magnetic field measurements. When sensing all three components of the magnetic field, non-iterative methods can be used to determine position and orientation [86], [120]. These calculations can be determined at speeds which are orders of magnitude greater than those achievable with iterative methods. However, to maintain the miniature size of the overall device, typically 3-axis sensors are impractical.

In order to make use of these linear algorithms, one approach would be to invert the tracking system, *i.e.* transmit a signal internally and use a sensor array externally to record the magnetic fields. Typical induction coil sensors can easily be used as transmitters instead of receivers by driving them with an AC current source. The advantage of this approach is that the external sensors are not limited by size, and the size and number of turns on an induction sensor dictate the sensitivity. Hence, much larger sensors can be used to detect the very small signal generated by a small internal coil. By constructing high sensitivity 3-axis sensors [116], each component of the magnetic field can be detected and a non-iterative algorithm could be used. A non-iterative algorithm could also be processed on an embedded processor removing the need for a PC to calculate the position.

### 8.2.5. Breathing Motion Compensation

In Chapter 5, it was seen that breathing motion contributed significant errors to the registration accuracy during navigations of the breathing lung model. Further work is

required to take these breathing displacements into account and determine the true position of the sensor in the airway models. Possible solutions include non-linear, time dependant transformation matrices which take the breathing pattern into account and using the sensor's position to given an estimate of the displaced position on the CT scan. Other methods include using principal component analysis and the wavelet transform as well as adaptive modelling schemes which have been shown to successfully account for breathing motion [210],[168]. Integrating methods such as these would increase the usefulness of the system in a real clinical setting.

# Bibliography


[1] C. Jackson, “A Bullet in the Lung,” *J. Am. Med. Assoc.*, vol. 90, no. 16, p. 1272, Apr. 1928.

[2] M. Equen, “Magnetic influence in bronchoscopy,” *Laryngoscope*, vol. 58, no. 7, pp. 726–734, Jul. 1948.

[3] M. Schiemann, R. Killmann, M. Kleen, N. Abolmaali, J. Finney, and T. J. Vogl, “Vascular guide wire navigation with a magnetic guidance system: experimental results in a phantom.,” *Radiology*, vol. 232, no. 2, pp. 475–81, Aug. 2004.

[4] D. M. Pham and S. M. Aziz, “A real-time localization system for an endoscopic capsule,” in *2014 IEEE Ninth International Conference on Intelligent Sensors, Sensor Networks and Information Processing (ISSNIP), Singapore*, 2014, pp. 1–6.

[5] R. Guignet, G. Bergonzelli, V. Schlageter, M. Turini, and P. Kucera, “Magnet Tracking: a new tool for in vivo studies of the rat gastrointestinal motility,” *Neurogastroenterol. Motil.*, vol. 18, no. 6, pp. 472–478, 2006.

[6] M. S. Grady, M. A. Howard, J. A. Molloy, R. C. Ritter, E. G. Quate, and G. T. Gillies, “Nonlinear magnetic stereotaxis: three-dimensional, in vivo remote magnetic manipulation of a small object in canine brain,” *Med. Phys.*, vol. 17, no. 3, pp. 405–15, 1990.

[7] E. G. Ashcraft, “Variable differential transformer,” U.S. Patent No. 2,459,2101949.

[8] H. P. Kalmus, “A new guiding and tracking system,” *RE Trans. Aeronaut. Navig. Electron.*, vol. ANE-9, no. 1, pp. 7–10, 1961.

[9] A. Plotkin, O. Shafrir, E. Paperno, and D. M. Kaplan, “Magnetic eye tracking: a new approach employing a planar transmitter,” *IEEE Trans. Biomed. Eng.*, vol. 57, no. 5, pp. 1209–15, May 2010.

[10] T. S. Weiser, K. Hyman, J. Yun, V. Litle, C. Chin, and S. J. Swanson, “Electromagnetic navigational bronchoscopy: a surgeon’s perspective,” *Ann. Thorac. Surg.*, vol. 85, no. 2, pp. S797–S801, 2008.

[11] J. Krücker, S. Xu, N. Glossop, A. Viswanathan, J. Borgert, H. Schulz, and B. J. Wood, “Electromagnetic Tracking for Thermal Ablation and Biopsy Guidance: Clinical Evaluation of Spatial Accuracy,” *J. Vasc. Interv. Radiol.*, vol. 18, no. 9, pp. 1141–1150, 2007.

[12] M. D. Comparetti, A. Vaccarella, D. D. Lorenzo, G. Ferrigno, and E. D. Momi, “Multi-robotic approach for keyhole neurosurgery: the ROBOCAST project,” in *SCATh Joint Workshop on New Technologies for Computer/Robot Assisted Surgery, Graz, Austria*, 2011, pp. 1–4.

[13] F. J. F. Herth, R. Eberhardt, and A. Ernst, “The future of bronchoscopy in diagnosing, staging and treatment of lung cancer,” *Respiration.*, vol. 73, no. 4, pp. 399–409, Jan. 2006.

[14] C. Gilbert, J. Akulian, R. Ortiz, H. Lee, and L. Yarmus, “Novel bronchoscopic strategies for the diagnosis of peripheral lung lesions: present techniques and future directions.,” *Respirology*, vol. 19, no. 5, pp. 636–44, Jul. 2014.

[15] World Health Organization, “Cancer Factsheet,” 2012. [Online]. Available: http://globocan.iarc.fr/Pages/fact_sheets_cancer.aspx. [Accessed: 15-Aug-2014].

[16] D. Makris, A. Scherpereel, S. Leroy, B. Bouchindhomme, J.-B. Faivre, J. Remy, P. Ramon, and C.-H. Marquette, “Electromagnetic navigation diagnostic bronchoscopy for small peripheral lung lesions,” *Eur. Respir. J.*, vol. 29, no. 6, pp. 1187–92, Jul. 2007.

[17] F. M. Creighton, R. C. Ritter, and P. Werp, “Focused magnetic navigation using optimized magnets for medical therapies,” in *Digests of the IEEE International Magnetics Conference, Nagoya, Japan*, 2005, pp. 1253–1254.

[18] F. M. Creighton, “Optimal distribution of magnetic material for catheter and guidewire cardiology therapies,” in *Digests of the IEEE International Magnetics*

*Conference, San Diego, California*, 2006, p. 111.
[19] Y. Fu, H. Liu, W. Huang, S. Wang, and Z. Liang, "Steerable catheters in minimally invasive vascular surgery," *Int. J. Med. Robot. Comput. Assist. Surg. MRCAS*, vol. 5, no. 4, pp. 381–91, Dec. 2009.
[20] K. B. Yesin, K. Vollmers, and B. J. Nelson, "Modeling and control of untethered biomicrorobots in a fluidic environment using electromagnetic fields," *Int. J. Rob. Res.*, vol. 25, no. 5–6, pp. 527–536, 2006.
[21] K. Ishiyama, M. Sendoh, A. Yamazaki, and K. I. Arai, "Swimming micro-machine driven by magnetic torque," *Sensors Actuators A Phys.*, vol. 91, no. 1, pp. 141–144, 2001.
[22] K. Ishiyama, M. Sendoh, and K. I. Arai, "Magnetic micromachines for medical applications," *J. Magn. Magn. Mater.*, vol. 242, pp. 41–46, 2002.
[23] T. P. L. Roberts, W. V Hassenzahl, S. W. Hetts, and R. L. Arenson, "Remote control of catheter tip deflection: an opportunity for interventional MRI," *Magn. Reson. Med.*, vol. 48, no. 6, pp. 1091–1095, 2002.
[24] V. Lalande, F. P. Gosselin, and S. Martel, "Catheter steering using a Magnetic Resonance Imaging system," in *Conference of the IEEE Engineering in Medicine and Biology Society, Buenos Aires, Argentina*, 2010, pp. 1874–7.
[25] J.-B. Mathieu and S. Martel, "Magnetic microparticle steering within the constraints of an MRI system: proof of concept of a novel targeting approach," *Biomed. Microdevices*, vol. 9, no. 6, pp. 801–8, Dec. 2007.
[26] S. Tamaz, R. Gourdeau, A. Chanu, J.-B. Mathieu, and S. Martel, "Real-time MRI-based control of a ferromagnetic core for endovascular navigation," *Biomed. Eng. IEEE Trans.*, vol. 55, no. 7, pp. 1854–1863, 2008.
[27] D. J. Griffiths, *Introduction to Electrodynamics*. New Jersey: Pearson Education, Limited, 2012, p. 624.
[28] A. Senyei, K. Widder, and G. Czerlinski, "Magnetic guidance of drug-carrying microspheres," *J. Appl. Phys.*, vol. 49, no. 6, p. 3578, Aug. 1978.
[29] S. Hosseini and M. B. Khamesee, "Design and control of a magnetically driven capsule-robot for endoscopy and drug delivery," in *2009 IEEE International Conference Science and Technology for Humanity (TIC-STH), Torono, Canada*, 2009, pp. 697–702.
[30] R. M. Bozorth, *Ferromagnetism*. New York: Wiley-VCH, 1993.
[31] T. Zickler, "Basic design and engineering of normal-conducting, iron-dominated electromagnets," Geneva, Accelerator Physics, Mar. 2011.
[32] A. K. Bhowmick and H. Stephens, *Handbook of elastomers*. New Jersey: CRC Press, 2000.
[33] Pebax, "Mechanical Properties." [Online]. Available: http://www.pebax.com/en/properties/mechanical-properties/. [Accessed: 18-Aug-2014].
[34] S. Fakirov, *Handbook of condensation thermoplastic elastomers*. New York: John Wiley & Sons, 2006.
[35] K. O'Donoghue and P. Cantillon-Murphy, "Deflection modeling of permanent magnet spherical chains in the presence of external magnetic fields," *J. Magn. Magn. Mater.*, vol. 343, pp. 251–256, 2013.
[36] S. Ernst, F. Ouyang, and C. Linder, "Initial experience with remote catheter ablation using a novel magnetic navigation system. Magnetic remote catheter ablation," *ACC Curr. J. Rev.*, vol. 13, no. 6, pp. 51–52, Jun. 2004.
[37] M. Vonthron, V. Lalande, and S. Martel, "A MRI-based platform for catheter navigation," in *Conference of the IEEE Engineering in Medicine and Biology Society, Boston, MA*, 2011, pp. 5392–5.
[38] F. P. Gosselin, V. Lalande, and S. Martel, "Characterization of the deflections of a catheter steered using a magnetic resonance imaging system," *Med. Phys.*, vol. 38, no. 9, pp. 4994–5002, Sep. 2011.
[39] H. C. Corben and P. Stehle, *Classical Mechanics*. New York: Courier Dover Publications, 1994, p. 389.
[40] J. Stambaugh, D. P. Lathrop, E. Ott, and W. Losert, "Pattern formation in a

monolayer of magnetic spheres," *Phys. Rev. E. Stat. Nonlin. Soft Matter Phys.*, vol. 68, no. 2, pp. 206–207, Aug. 2003.
[41] B. Y. Kim, I.-B. Shim, O. L. A. Monti, and J. Pyun, "Magnetic self-assembly of gold nanoparticle chains using dipolar core-shell colloids," *Chem. Commun. (Camb).*, vol. 47, no. 3, pp. 890–2, Jan. 2011.
[42] Y. Sahoo, M. Cheon, S. Wang, H. Luo, E. P. Furlani, and P. N. Prasad, "Field-Directed Self-Assembly of Magnetic Nanoparticles," *J. Phys. Chem. B*, vol. 108, no. 11, pp. 3380–3383, Mar. 2004.
[43] M. Tanase, L. A. Bauer, A. Hultgren, D. M. Silevitch, L. Sun, D. H. Reich, P. C. Searson, and G. J. Meyer, "Magnetic Alignment of Fluorescent Nanowires," *Nano Lett.*, vol. 1, no. 3, pp. 155–158, Mar. 2001.
[44] P. A. Deymier, C. Jung, and S. Raghavan, "Molecular dynamics of magnetic particulate dispersions," *J. Appl. Phys.*, vol. 75, no. 10, p. 5571, 1994.
[45] K.-P. Schneider and J. Keller, "Computer simulation of the orientation of lipid headgroups," *Chem. Phys. Lett.*, vol. 275, no. 1–2, pp. 63–69, Aug. 1997.
[46] H. Zhang and M. Widom, "Field-induced forces in colloidal particle chains," *Phys. Rev. E. Stat. Nonlin. Soft Matter Phys.*, vol. 51, no. 3, pp. 2099–2103, Mar. 1995.
[47] J. M. D. Coey, "Permanent magnet applications," *J. Magn. Magn. Mater.*, vol. 248, no. 3, pp. 441–456, Aug. 2002.
[48] F. J. Sierra-Valdez, F. Pacheco-Vázquez, O. Carvente, F. Malloggi, J. Cruz-Damas, R. Rechtman, and J. C. Ruiz-Suárez, "Acoustic gaps in a chain of magnetic spheres," *Phys. Rev. E. Stat. Nonlin. Soft Matter Phys.*, vol. 81, no. 1, pp. 113–115, Jan. 2010.
[49] M. Beleggia and M. De Graef, "General magnetostatic shape–shape interactions," *J. Magn. Magn. Mater.*, vol. 285, no. 1–2, pp. L1–L10, Jan. 2005.
[50] M. Beleggia, S. Tandon, Y. Zhu, and M. De Graef, "On the magnetostatic interactions between nanoparticles of arbitrary shape," *J. Magn. Magn. Mater.*, vol. 278, no. 1–2, pp. 270–284, Jul. 2004.
[51] D. Vokoun, M. Beleggia, L. Heller, and P. Šittner, "Magnetostatic interactions and forces between cylindrical permanent magnets," *J. Magn. Magn. Mater.*, vol. 321, no. 22, pp. 3758–3763, Nov. 2009.
[52] E. P. Furlani, *Permanent Magnet and Electromechanical Devices: Materials, Analysis, and Applications*. New York: Academic Press, 2001, p. 518.
[53] J. J. Moré, "The Levenberg-Marquardt algorithm: implementation and theory," in *Numerical analysis*, New York: Springer, 1978, pp. 105–116.
[54] J. M. Hammersley and D. C. Handscomb, *Monte Carlo Methods*. New York: Wiley, 1964, p. 178.
[55] R. H. Byrd, R. B. Schnabel, and G. A. Shultz, "A Trust Region Algorithm for Nonlinearly Constrained Optimization," *SIAM J. Numer. Anal.*, vol. 24, no. 5, pp. 1152–1170, Oct. 1987.
[56] M. R. Celis, J. E. Dennis, and R. A. Tapia, "A trust region strategy for nonlinear equality constrained optimization," *Numer. Optim.*, vol. 1984, pp. 71–82, 1985.
[57] J. Wang, S. She, and S. Zhang, "An improved Helmholtz coil and analysis of its magnetic field homogeneity," *Rev. Sci. Instrum.*, vol. 73, no. 5, p. 2175, Apr. 2002.
[58] J. B. Hummel, M. R. Bax, M. L. Figl, Y. Kang, C. Maurer, W. W. Birkfellner, H. Bergmann, and R. Shahidi, "Design and application of an assessment protocol for electromagnetic tracking systems.," *Med. Phys.*, vol. 32, no. 7, pp. 2371–9, Jul. 2005.
[59] C. J. Banker, P. C. Pedersen, and T. L. Szabo, "Interactive Training System for Medical Ultrasound," in *2008 IEEE Ultrasonics Symposium*, 2008, pp. 1350–1354.
[60] E. Wilson, Z. Yaniv, D. Lindisch, and K. Cleary, "A buyer's guide to electromagnetic tracking systems for clinical applications," in *Medical Imaging*, 2008, p. 69182B–69182B–12.
[61] D. Roetenberg, P. Slycke, A. Ventevogel, and P. H. Veltink, "A portable magnetic position and orientation tracker," *Sensors Actuators A Phys.*, vol. 135, no. 2, pp. 426–432, Apr. 2007.
[62] A. Zikmund and P. Ripka, "A magnetic distance sensor with high precision," *Sensors Actuators A Phys.*, vol. 186, pp. 137–142, Oct. 2012.
[63] E. Paperno and A. Plotkin, "Cylindrical induction coil to accurately imitate the ideal

magnetic dipole," *Sensors Actuators A Phys.*, vol. 112, no. 2–3, pp. 248–252, May 2004.

[64] C. L. W. Sonntag, M. Sprée, E. A. Lomonova, J. L. Duarte, and A. J. A. Vandenput, "Accurate Magnetic Field Intensity Calculations for Contactless Energy Transfer Coils," in *Proceedings of the 16th International Conference on the Computation of Electromagnetic Fields, Achen, Germany*, 2007.

[65] A. Plotkin, E. Paperno, G. Vasserman, and R. Segev, "Magnetic Tracking of Eye Motion in Small, Fast-Moving Animals," *IEEE Trans. Magn.*, vol. 44, no. 11, pp. 4492–4495, Nov. 2008.

[66] A. Plotkin and E. Paperno, "3-D magnetic tracking of a single subminiature coil with a large 2-D array of uniaxial transmitters," *IEEE Trans. Magn.*, vol. 39, no. 5, pp. 3295–3297, Sep. 2003.

[67] S. Hashi, S. Yabukami, H. Kanetaka, K. Ishiyama, and K. I. Arai, "Wireless Magnetic Position-Sensing System Using Optimized Pickup Coils for Higher Accuracy," *IEEE Trans. Magn.*, vol. 47, no. 10, pp. 3542–3545, Oct. 2011.

[68] C. Nafis, V. Jensen, and R. Von Jako, "Method for evaluating compatibility of commercial Electromagnetic ( EM ) micro sensor tracking systems with surgical and imaging tables," *Proc. SPIE, San Diego, March 17th*, vol. 6918, 2008.

[69] J. Heikkinen, P. Salonen, and M. Kivikoski, "Planar rectennas for 2.45 GHz wireless power transfer," in *IEEE Radio and Wireless Conference, Colorado*, 2000, pp. 63–66.

[70] L. Lizzi, F. Viani, and a. Massa, "Dual-Band Spline-Shaped PCB Antenna for Wi-Fi Applications," *IEEE Antennas Wirel. Propag. Lett.*, vol. 8, pp. 616–619, 2009.

[71] C. Peters and Y. Manoli, "Inductance calculation of planar multi-layer and multi-wire coils: An analytical approach," *Sensors Actuators A Phys.*, vol. 145–146, pp. 394–404, Jul. 2008.

[72] C. Schilstra and J. H. van Hateren, "Using miniature sensor coils for simultaneous measurement of orientation and position of small, fast-moving animals," *J. Neurosci. Methods*, vol. 83, no. 2, pp. 125–31, Sep. 1998.

[73] C. Hu, S. Song, X. Wang, M. Q.-H. Meng, and B. Li, "A Novel Positioning and Orientation System Based on Three-Axis Magnetic Coils," *IEEE Trans. Magn.*, vol. 48, no. 7, pp. 2211–2219, Jul. 2012.

[74] A. Mariscotti, "A Magnetic Field Probe With MHz Bandwidth and 7-Decade Dynamic Range," *IEEE Trans. Instrum. Meas.*, vol. 58, no. 8, pp. 2643–2652, Aug. 2009.

[75] A. Sheinker, B. Ginzburg, N. Salomonski, L. Frumkis, and B.-Z. Kaplan, "Localization in 3-D Using Beacons of Low Frequency Magnetic Field," *IEEE Trans. Instrum. Meas.*, vol. 62, no. 12, pp. 3194–3201, Dec. 2013.

[76] H. G. Ramos and P. S. Girao, "Measurement of low level DC magnetic fields using a synchronous demodulation technique," *IEEE Trans. Instrum. Meas.*, vol. 42, no. 2, pp. 544–546, Apr. 1993.

[77] J. M. Barandiaran, S. Hashi, M. Toyoda, S. Yabukami, K. Ishiyama, Y. Okazaki, K. I. Arai, and H. Kanetaka, "Wireless magnetic motion capture system using multiple LC resonant magnetic markers with high accuracy," *Sensors Actuators A Phys.*, vol. 142, no. 2, pp. 520–527, 2008.

[78] M. L. Meade, "Advances in lock-in amplifiers," *J. Phys. E.*, vol. 15, no. 4, pp. 395–403, Apr. 1982.

[79] M. Habibi and S. M. Sayedi, "Asynchronous demodulation technique for use in vision sensor image classification and segmentation," *Int. J. Circuit Theory Appl.*, vol. 39, no. 1, pp. 17–30, Jan. 2011.

[80] C. Nader, W. Van Moer, N. Bjorsell, K. Barbe, and P. Handel, "Reducing the Analog and Digital Bandwidth Requirements of RF Receivers for Measuring Periodic Sparse Waveforms," *IEEE Trans. Instrum. Meas.*, vol. 61, no. 11, pp. 2960–2971, Nov. 2012.

[81] P. Petrovic, "New Digital Multimeter for Accurate Measurement of Synchronously Sampled AC Signals," *IEEE Trans. Instrum. Meas.*, vol. 53, no. 3, pp. 716–725, Jun. 2004.

[82] B. Aschenbrenner and B. G. Zagar, “DSP based read out system for contactless high – frequency inductive position sensors,” in *XX IMEKO World Congress Metrology for Green Growth, Busan, Korea*, 2012, pp. 1–6.
[83] S. C. Saxena and S. B. L. Seksena, “A self-compensated smart LVDT transducer,” *IEEE Trans. Instrum. Meas.*, vol. 38, no. 3, pp. 748–753, Jun. 1989.
[84] H. P. Kalmus, “A New Guiding and Tracking System,” *IRE Trans. Aeronaut. Navig. Electron.*, vol. ANE-9, no. 1, pp. 7–10, Mar. 1962.
[85] F. Raab, E. Blood, T. Steiner, and H. Jones, “Magnetic Position and Orientation Tracking System,” *IEEE Trans. Aerosp. Electron. Syst.*, vol. AES-15, no. 5, pp. 709–718, Sep. 1979.
[86] C. Hu, M. Li, S. Song, W. Yang, R. Zhang, and M. Q.-H. Meng, “A Cubic 3-Axis Magnetic Sensor Array for Wirelessly Tracking Magnet Position and Orientation,” *IEEE Sens. J.*, vol. 10, no. 5, pp. 903–913, May 2010.
[87] “3D Guidance trakSTAR,” 2013. [Online]. Available: http://www.ascension-tech.com/medical/pdf/trakSTAR_SpecSheet.pdf. [Accessed: 18-Aug-2014].
[88] “NDI Aurora EM Tracking System,” 2013. [Online]. Available: http://www.ndigital.com/medical/documents/aurora/aurora-brochure.pdf. [Accessed: 18-Aug-2014].
[89] W. Wang, C. Hu, W. Lin, and J. Bao, “An improved PSO-based algorithm for extracting week coupling AC signal in electromagnetic localization system, Zhengzhou,” in *Automation and Logistics (ICAL)*, 2012, pp. 623–627.
[90] J. E. Dennis and R. B. Schnabel, *Numerical Methods for Unconstrained Optimization and Nonlinear Equations*. SIAM, 1983, p. 378.
[91] “Magnetic position sensing using Levenberg-Marquardt - File Exchange - MATLAB Central.” [Online]. Available: http://www.mathworks.com/matlabcentral/fileexchange/43395. [Accessed: 08-Oct-2013].
[92] Varian Medical Systems, “Calypso System Overview.” [Online]. Available: http://www.varian.com/euen/oncology/imaging_solutions/calypso/. [Accessed: 16-Aug-2014].
[93] Medical Physics, “Prostate localization: maximizing precision.” [Online]. Available: http://medicalphysicsweb.org/cws/article/research/42294. [Accessed: 16-Aug-2014].
[94] Y. Schwarz, J. Greif, H. D. Becker, A. Ernst, and A. Mehta, “Real-Time Electromagnetic Navigation Bronchoscopy to Peripheral Lung Lesions Using Overlaid CT Images The First Human Study,” *Chest J.*, vol. 129, no. 4, pp. 988–994, 2006.
[95] Y. Schwarz, J. Greif, H. D. Becker, A. Ernst, and A. Mehta, “Real-Time Electromagnetic Navigation Bronchoscopy to Peripheral Lung Lesions Using Overlaid CT Images The First Human Study,” *Chest J.*, vol. 129, no. 4, pp. 988–994, 2006.
[96] S. Leong, H. Ju, H. Marshall, R. Bowman, I. Yang, A.-M. Ree, C. Saxon, and K. M. Fong, “Electromagnetic navigation bronchoscopy: A descriptive analysis,” *Journal of Thoracic Disease*, vol. 4, no. 2. pp. 173–185, 2012.
[97] R. S. Santos, A. Gupta, M. I. Ebright, M. DeSimone, G. Steiner, M.-J. Estrada, B. Daly, and H. C. Fernando, “Electromagnetic navigation to aid radiofrequency ablation and biopsy of lung tumors,” *Ann. Thorac. Surg.*, vol. 89, no. 1, pp. 265–268, 2010.
[98] Veran Medical, “SPINDrive 2.0.” [Online]. Available: http://www.veranmedical.com/healthcare-professionals/products/spin-drive. [Accessed: 16-Aug-2014].
[99] C. Hu, M. Li, S. Song, W. Yang, R. Zhang, and M. Q.-H. Meng, “A Cubic 3-Axis Magnetic Sensor Array for Wirelessly Tracking Magnet Position and Orientation,” *IEEE Sens. J.*, vol. 10, no. 5, pp. 903–913, May 2010.
[100] C. Schilstra and J. H. van Hateren, “Using miniature sensor coils for simultaneous measurement of orientation and position of small, fast-moving animals.,” *J. Neurosci. Methodseuroscience methods*, vol. 83, no. 2, pp. 125–31, Sep. 1998.
[101] E. Paperno and P. Keisar, “Three-dimensional magnetic tracking of biaxial sensors,”

*IEEE Trans. Magn.*, vol. 40, no. 3, pp. 1530–1536, 2004.
[102] M. Heinig, R. Bruder, A. Schlaefer, and A. Schweikard, "3D Localization of a Thin Steel Rod Using Magnetic Field Sensors: Feasibility and Preliminary Results," in *Bioinformatics and Biomedical Engineering (iCBBE), 2010 4th International Conference, Chengdu, China*, 2010, pp. 1–4.
[103] S. Yabukami, H. Kikuchi, M. Yamaguchi, K. I. Arai, K. Takahashi, A. Itagaki, and N. Wako, "Motion capture system of magnetic markers using three-axial magnetic field sensor," *IEEE Trans. Magn.*, vol. 36, no. 5, pp. 3646–3648, 2000.
[104] M. Q.-H. Meng and M. Mandal, "A Linear Algorithm for Tracing Magnet Position and Orientation by Using Three-Axis Magnetic Sensors," *IEEE Trans. Magn.*, vol. 43, no. 12, pp. 4096–4101, Dec. 2007.
[105] X. Ge, Y. Wang, N. Ding, X. Wu, Y. Wang, and Z. Fang, "An Electromagnetic Tracking Method Using Rotating Orthogonal Coils," *IEEE Trans. Magn.*, vol. 48, no. 12, pp. 4802–4810, Dec. 2012.
[106] E. Paperno and P. Keisar, "Three-dimensional magnetic tracking of biaxial sensors," *IEEE Trans. Magn.*, vol. 40, no. 3, pp. 1530–1536, 2004.
[107] P. G. Seiler, H. Blattmann, S. Kirsch, R. K. Muench, and C. Schilling, "A novel tracking technique for the continuous precise measurement of tumour positions in conformal radiotherapy," *Phys. Med. Biol.*, vol. 45, no. 9, pp. N103–N110, Sep. 2000.
[108] R. Eberhardt, D. Anantham, F. Herth, D. Feller-Kopman, and A. Ernst, "Electromagnetic navigation diagnostic bronchoscopy in peripheral lung lesions," *Chest*, vol. 131, no. 6, pp. 1800–5, Jun. 2007.
[109] "Guidelines for limiting exposure to time-varying electric and magnetic fields (1 Hz to 100 kHz)," *Health Phys.*, vol. 99, no. 6, pp. 818–36, Dec. 2010.
[110] C. T. Robertson, *Printed circuit board designer's reference: basics*. Prentice Hall Professional, 2004.
[111] S. S. Mohan, M. del Mar Hershenson, S. P. Boyd, and T. H. Lee, "Simple accurate expressions for planar spiral inductances," *IEEE J. Solid-State Circuits*, vol. 34, no. 10, pp. 1419–1424, 1999.
[112] D. K. C. MacDonald, "Magneto-resistance in metals," *Philos. Mag.*, vol. 2, no. 13, pp. 97–104, 1957.
[113] E. Ramsden, *Hall-effect sensors: theory and application*. Oxford: Newnes, 2011.
[114] P. Ripka, *Magnetic sensors and magnetometers*. Prague: Artech House on Demand, 2001.
[115] C. C. and P. Leroy, *Magnetic Sensors - Principles and Applications*. New York: InTech, 2012.
[116] S. Tumanski, "Induction coil sensors—a review," *Meas. Sci. Technol.*, vol. 18, no. 3, pp. R31–R46, Mar. 2007.
[117] C. Hu, M.-H. Meng, M. Mandal, and X. Wang, "3-Axis Magnetic Sensor Array System for Tracking Magnet's Position and Orientation," in *The Sixth World Congress on Intelligent Control and Automation, 2006. Dalian, China*, 2006, vol. 2, pp. 5304–5308.
[118] M. Heinig, R. Bruder, A. Schlaefer, and A. Schweikard, "3D Localization of a Thin Steel Rod Using Magnetic Field Sensors: Feasibility and Preliminary Results," in *Bioinformatics and Biomedical Engineering (iCBBE), 2010 4th International Conference on*, 2010, pp. 1–4.
[119] V. Schlageter, P. Drljaca, R. S. Popovic, and P. Kucera, "A Magnetic Tracking System based on Highly Sensitive Integrated Hall Sensors.," *JSME Int. J. Ser. C*, vol. 45, no. 4, pp. 967–973, 2002.
[120] E. Paperno, I. Sasada, and E. Leonovich, "A new method for magnetic position and orientation tracking," *IEEE Trans. Magn.*, vol. 37, no. 4, pp. 1938–1940, 2001.
[121] "Helmholtz Coil." [Online]. Available: http://en.wikipedia.org/wiki/Helmholtz_coil. [Accessed: 16-Aug-2014].
[122] L. W. Hopkins, *Development of a Highly Accurate Synchronous Demodulator*. Glasgow: CRC Press, 1949, p. 110.
[123] S. Frasca, "Basic tool for periodic signal detection," 1998. [Online]. Available:

http://grwavsf.roma1.infn.it/dadps/LastVersion/dad_per_basic.pdf. [Accessed: 16-Aug-2014].
[124] D. Ganyun and Z. Rong, "Spectrum Estimation of Harmonics and Interharmonics Based on Prony Algorithm [J]," *Trans. China Electrotech. Soc.*, vol. 10, p. 18, 2005.
[125] H. V. Sorensen and C. S. Burrus, "Efficient computation of the DFT with only a subset of input or output points," *IEEE Trans. Signal Process.*, vol. 41, no. 3, pp. 1184–1200, Mar. 1993.
[126] T. B. Mengfei Li, "FPGA based electromagnetic tracking system for fast catheter navigation," *Int. J. Sci. Eng. Res.*, vol. 4, no. 9, pp. 2566 – 2570, 2013.
[127] J. Dunlop and D. G. Smith, *Telecommunications Engineering, 3rd Edition*. Glasgow: CRC Press, 1994, p. 593.
[128] D. Stranneby, *Digital Signal Processing: DSP and Applications: DSP and Applications*. Stockholm: Newnes, 2001, p. 229.
[129] T. Bien, M. Li, Z. Salah, and G. Rose, "Electromagnetic tracking system with reduced distortion using quadratic excitation.," *Int. J. Comput. Assist. Radiol. Surg.*, vol. 9, no. 2, pp. 323–332, Aug. 2013.
[130] L. R. Rabiner and B. Gold, *Theory and application of digital signal processing*, vol. 1. Englewood Cliffs, NJ: Prentice-Hall, 1975.
[131] J. Vankka and K. A. I. Halonen, *Direct Digital Synthesizers: Theory, Design and Applications*. New York: Springer, 2001, p. 193.
[132] Texas Instruments, "INA128." [Online]. Available: http://www.ti.com/product/ina128.
[133] H. W. Ott, *Noise reduction techniques in electronic systems*. New York: Wiley, 1988.
[134] H. Nyquist, "Certain Topics in Telegraph Transmission Theory," *Trans. Am. Inst. Electr. Eng.*, vol. 47, no. 2, pp. 617–644, Apr. 1928.
[135] P. Pérez and A. Santos, "Undersampling to acquire nuclear magnetic resonance images," *Med. Eng. Phys.*, vol. 26, no. 6, pp. 523–9, Jul. 2004.
[136] S. Dasgupta, "Control over bandlimited communication channels: limitations to stabilizability," in *42nd IEEE International Conference on Decision and Control, Maui*, vol. 1, pp. 176–181.
[137] K. Kubo, "Under-sampling technique for sine wave frequency estimation," in *SICE 2001. Proceedings of the 40th SICE Annual Conference. International Session Papers, Japan*, 2001, pp. 380–385.
[138] R. H. Hosking, "Putting Undersampling to Work," 2006. [Online]. Available: http://www.eetimes.com/document.asp?doc_id=1275354. [Accessed: 19-Dec-2013].
[139] "Arduino Due." [Online]. Available: http://www.arduino.cc/. [Accessed: 16-Aug-2014].
[140] F. Vanden Berghen, "Levenberg-Marquardt algorithms vs Trust Region algorithms," 2004. [Online]. Available: http://www.applied-mathematics.net/LMvsTR/LMvsTR.pdf. [Accessed: 18-Aug-2014].
[141] K. O'Donoghue and P. Cantillon-Murphy, "Low Cost Super-Nyquist Asynchronous Demodulation for Use in EM Tracking Systems," *IEEE Trans. Instrum. Meas.*, 2014.
[142] S. Song, C. Hu, B. Li, X. Li, and M. Q.-H. Meng, "An Electromagnetic Localization and Orientation Method Based on Rotating Magnetic Dipole," *IEEE Trans. Magn.*, vol. 49, no. 3, pp. 1274–1277, Mar. 2013.
[143] K. N. Jeon, K. Bae, M. J. Park, H. C. Choi, H. S. Shin, S. Shin, H. C. Kim, and C. Y. Ha, "US-guided transthoracic biopsy of peripheral lung lesions: pleural contact length influences diagnostic yield," *Acta Radiol.*, vol. 217, Aug. 2013.
[144] X. Huo, J. Wang, and M. Ghovanloo, "A magneto-inductive sensor based wireless tongue-computer interface," *IEEE Trans. Neural Syst. Rehabil. Eng.*, vol. 16, no. 5, pp. 497–504, Oct. 2008.
[145] P. Pérez, A. Santos, and J. J. Vaquero, "Potential use of the undersampling technique in the acquisition of nuclear magnetic resonance signals," *Magn. Reson. Mater. Physics, Biol. Med.*, vol. 13, no. 2, pp. 109–17, Oct. 2001.
[146] K. O'Donoghue, P. Cantillon Murphy, D. Eustace, J. Griffiths, H. Mansfield, T. Power, and M. O'Shea, "Catheter position tracking system using planar magnetics and closed loop current control," *IEEE Trans. Magn.*, vol. 50, no. 7, 2014.

[147] Atmel Corporation, “32-bit Cortex M4 Microcontroller SAM4E Datasheet,” 2013. [Online]. Available: http://www.atmel.com/Images/Atmel_11157_32-bit-Cortex-M4-Microcontroller_SAM4E_Datasheet.pdf. [Accessed: 18-Aug-2014].
[148] Microchip Technology Inc., “Analog-to-Digital converter design guide,” 2005. [Online]. Available: http://www.microchip.com/stellent/groups/analog_sg/documents/market_communication/en022326.pdf. [Accessed: 18-Aug-2014].
[149] J. G. Ford and J. M. Samet, “Epidemiology of Lung Cancer ACCP Evidence-Based Clinical Practice Guidelines,” *Chest*, vol. 132, no. 3, 2007.
[150] S. A. Kenfield, E. K. Wei, M. J. Stampfer, B. A. Rosner, and G. A. Colditz, “Comparison of aspects of smoking among the four histological types of lung cancer,” *Tob. Control*, vol. 17, no. 3, pp. 198–204, 2008.
[151] E. F. Patz Jr, P. C. Goodman, and G. Bepler, “Screening for lung cancer,” *N. Engl. J. Med.*, vol. 343, no. 22, pp. 1627–1633, 2000.
[152] J. M. Anderson, J. Murchison, and D. Patel, “CT-guided lung biopsy: factors influencing diagnostic yield and complication rate.,” *Clin. Radiol.*, vol. 58, no. 10, pp. 791–7, Oct. 2003.
[153] L. B. Haramati and G. Aviram, “What constitutes effective management of pneumothorax after CT-guided needle biopsy of the lung?,” *Chest*, vol. 121, no. 4, pp. 1013–5, Apr. 2002.
[154] R. Eberhardt, N. Kahn, D. Gompelmann, M. Schumann, C. P. Heussel, and F. J. F. Herth, “LungPoint--a new approach to peripheral lesions.,” *J. Thorac. Oncol.*, vol. 5, no. 10, pp. 1559–63, Oct. 2010.
[155] Y. Schwarz, A. C. Mehta, A. Ernst, F. Herth, A. Engel, D. Besser, and H. D. Becker, “Electromagnetic navigation during flexible bronchoscopy,” *Respiration.*, vol. 70, no. 5, pp. 516–22.
[156] G. Schreiber and D. C. McCrory, “Performance characteristics of different modalities for diagnosis of suspected lung cancer: summary of published evidence.,” *Chest*, vol. 123, no. 1 Suppl, p. 115S–128S, Jan. 2003.
[157] “Lung Biopsy.” [Online]. Available: http://www.webmd.com/lung/lung-biopsy. [Accessed: 15-Aug-2014].
[158] P. Mazzone, P. Jain, A. C. Arroliga, and R. A. Matthay, “Bronchoscopy and needle biopsy techniques for diagnosis and staging of lung cancer.,” *Clin. Chest Med.*, vol. 23, no. 1, pp. 137–158, 2002.
[159] P. Nardelli, R. San Jose Estepar, and P. Cantillon-Murphy, “Semi-automated Airway Segmentation for Lung CT Datasets,” in *27th International Congress and Exhibition in Computer Assisted Radiology and Surgery (CARS)*, 2013.
[160] S. B. Solomon, P. White, C. M. Wiener, J. B. Orens, and K. P. Wang, “Three-dimensional CT-guided bronchoscopy with a real-time electromagnetic position sensor: a comparison of two image registration methods.,” *Chest*, vol. 118, no. 6, pp. 1783–7, Dec. 2000.
[161] J. M. Fitzpatrick, J. B. West, and C. R. Maurer Jr, “Predicting error in rigid-body point-based registration,” *IEEE Trans. Med. Imaging*, vol. 17, no. 5, pp. 694–702, 1998.
[162] D. Deguchi, M. Feuerstein, T. Kitasaka, Y. Suenaga, I. Ide, H. Murase, K. Imaizumi, Y. Hasegawa, and K. Mori, “Real-time marker-free patient registration for electromagnetic navigated bronchoscopy: a phantom study,” *Int. J. Comput. Assist. Radiol. Surg.*, vol. 7, no. 3, pp. 359–369, 2012.
[163] S. X. Liu, L. F. Gutiérrez, and D. Stanton, “Quantitative evaluation for accumulative calibration error and video-CT registration errors in electromagnetic-tracked endoscopy.,” *Int. J. Comput. Assist. Radiol. Surg.*, vol. 6, no. 3, pp. 407–19, May 2011.
[164] T. Klein, J. Traub, H. Hautmann, A. Ahmadian, and N. Navab, “Fiducial-free registration procedure for navigated bronchoscopy.,” *Med. Image Comput. Comput. Assist. Interv.*, vol. 10, no. Pt 1, pp. 475–82, Jan. 2007.
[165] F. L. Markley, “Attitude Determination using Vector Observations and the Singular Value Decomposition,” *J. Astronaut. Sci.*, vol. 38, pp. 245–258, 1988.

[166] W. Kabsch, “A solution for the best rotation to relate two sets of vectors,” *Acta Crystallogr.*, vol. 32, p. 922, 1976.
[167] D. Deguchi, K. Ishitani, T. Kitasaka, K. Mori, Y. Suenaga, H. Takabatake, M. Mori, and H. Natori, “A method for bronchoscope tracking using position sensor without fiducial markers,” in *Medical Imaging*, 2007, p. 65110N–65110N–12.
[168] D. Ruan, J. A. Fessler, and J. M. Balter, “Mean position tracking of respiratory motion,” *Med. Phys.*, vol. 35, no. 2, pp. 782–92, Feb. 2008.
[169] Y. Seppenwoolde, H. Shirato, K. Kitamura, S. Shimizu, M. van Herk, J. V. Lebesque, and K. Miyasaka, “Precise and real-time measurement of 3D tumor motion in lung due to breathing and heartbeat, measured during radiotherapy,” *Int. J. Radiat. Oncol.*, vol. 53, no. 4, pp. 822–834, Jul. 2002.
[170] T. A. Sundaram and J. C. Gee, “Towards a model of lung biomechanics: pulmonary kinematics via registration of serial lung images.,” *Med. Image Anal.*, vol. 9, no. 6, pp. 524–37, Dec. 2005.
[171] R. Werner, J. Ehrhardt, R. Schmidt, and H. Handels, “Patient-specific finite element modeling of respiratory lung motion using 4D CT image data,” *Med. Phys.*, vol. 36, no. 5, p. 1500, Apr. 2009.
[172] K. O’Donoghue and P. Cantillon Murphy, “Planar magnetic shielding for use with EM tracking systems,” *IEEE Trans. Magn.*, 2014.
[173] H. Zhang, F. Banovac, R. Lin, N. Glossop, B. J. Wood, D. Lindisch, E. Levy, and K. Cleary, “Electromagnetic tracking for abdominal interventions in computer aided surgery.,” *Comput. Aided Surg.*, vol. 11, no. 3, pp. 127–36, May 2006.
[174] C. Nafis, V. Jensen, R. Von Jako, and R. von Jako, “Method for evaluating compatibility of commercial Electromagnetic ( EM ) micro sensor tracking systems with surgical and imaging tables,” *Proc. SPIE*, vol. 6918, Mar. 2008.
[175] W. Ashe, “Magnetic field permeable barrier for magnetic position measurement system,” US 624623112-Jun-2001.
[176] R. Schulz, “ELF and VLF Shielding Effectiveness of High-Permeability Materials,” *IEEE Trans. Electromagn. Compat.*, vol. EMC-10, no. 1, pp. 95–100, Mar. 1968.
[177] R. G. Olsen and P. Moreno, “Some observations about shielding extremely low-frequency magnetic fields by finite width shields,” *IEEE Trans. Electromagn. Compat.*, vol. 38, no. 3, pp. 460–468, 1996.
[178] J. F. Hoburg, “Principles of quasistatic magnetic shielding with cylindrical and spherical shields,” *IEEE Trans. Electromagn. Compat.*, vol. 37, no. 4, pp. 574–579, 1995.
[179] W. A. Roshen and D. E. Turcotte, “Planar inductors on magnetic substrates,” *IEEE Trans. Magn.*, vol. 24, no. 6, pp. 3213–3216, 1988.
[180] W. A. Roshen, “Effect of finite thickness of magnetic substrate on planar inductors,” *IEEE Trans. Magn.*, vol. 26, no. 1, pp. 270–275, 1990.
[181] O. Talcoth and T. Rylander, “Optimization of sensor positions in magnetic tracking: Technical report,” Goteborg, 2011.
[182] T. Theodoulidis, “Developments in Calculating the Transient Eddy-Current Response From a Conductive Plate,” *IEEE Trans. Magn.*, vol. 44, no. 7, pp. 1894–1896, Jul. 2008.
[183] F. de Leon and A. Semlyen, “Time domain modeling of eddy current effects for transformer transients,” *Power Deliv. IEEE Trans.*, vol. 8, no. 1, pp. 271–280, 1993.
[184] A. H. Salemi and S. H. H. Sadeghi, “Electromagnetic field distributions around conducting slabs, produced by eddy-current probes with arbitrary shape current-carrying excitation loops,” *IEE Proc. - Sci. Meas. Technol.*, vol. 148, no. 4, pp. 187–192, Jul. 2001.
[185] F. Fu and J. Bowler, “Transient Eddy-Current Driver Pickup Probe Response Due to a Conductive Plate,” *IEEE Trans. Magn.*, vol. 42, no. 8, pp. 2029–2037, Aug. 2006.
[186] W. G. Hurley and W. H. Wölfle, *Transformers and Inductors for Power Electronics: Theory, Design and Applications*. John Wiley & Sons, 2013.
[187] D. Meeker, “Finite Element Method Magnetics 4.2,” 2013. [Online]. Available: http://www.femm.info. [Accessed: 16-Sep-2014].
[188] R. J. Prance, T. D. Clark, and H. Prance, “Ultra low noise induction magnetometer

for variable temperature operation," *Sensors Actuators A Phys.*, vol. 85, no. 1–3, pp. 361–364, Aug. 2000.
[189] P. Bannister, "New Theoretical Expressions for Predicting Shielding Effectiveness for the Plane Shield Case," *IEEE Trans. Electromagn. Compat.*, vol. EMC-10, no. 1, pp. 2–7, Mar. 1968.
[190] C. L. Holloway, R. R. DeLyser, R. F. German, P. McKenna, and M. Kanda, "Comparison of electromagnetic absorber used in anechoic and semi-anechoic chambers for emissions and immunity testing of digital devices," *IEEE Trans. Electromagn. Compat.*, vol. 39, no. 1, pp. 33–47, 1997.
[191] The Lego Group, "Company Profile: An Introduction to the LEGO Group," 2010.
[192] F. Stevens, M. A. Conditt, N. Kulkarni, S. K. Ismaily, P. C. Noble, and D. R. Lionberger, "Minimizing electromagnetic interference from surgical instruments on electromagnetic surgical navigation.," *Clin. Orthop. Relat. Res.*, vol. 468, no. 8, pp. 2244–50, Aug. 2010.
[193] C. Nafis, V. Jensen, L. Beauregard, and P. Anderson, "Method for estimating dynamic EM tracking accuracy of surgical navigation tools," in *Proceeddings of SPIE, Medical Imaging, San Diego, CA*, 2006.
[194] W. Birkfellner, F. Watzinger, F. Wanschitz, R. Ewers, and H. Bergmann, "Calibration of tracking systems in a surgical environment.," *IEEE Trans. Med. Imaging*, vol. 17, no. 5, pp. 737–42, Oct. 1998.
[195] C. R. Paul, *Introduction to electromagnetic compatibility*, vol. 184. New York: John Wiley & Sons, 2006.
[196] S. Mei, C. Amin, and Y. I. Ismail, "Efficient model order reduction including skin effect," in *Proceedings of the 40th annual Design Automation Conference*, 2003, pp. 232–237.
[197] A. Legros, M. Corbacio, A. Beuter, J. Modolo, D. Goulet, F. S. Prato, and A. W. Thomas, "Neurophysiological and behavioral effects of a 60 Hz, 1,800 μT magnetic field in humans," *Eur. J. Appl. Physiol.*, vol. 112, no. 5, pp. 1751–1762, 2012.
[198] P. J. Dimbylow, "FDTD calculations of the whole-body averaged SAR in an anatomically realistic voxel model of the human body from 1 MHz to 1 GHz," *Phys. Med. Biol.*, vol. 42, no. 3, pp. 479–490, Mar. 1997.
[199] A. Christ, M. Douglas, J. Nadakuduti, and N. Kuster, "Assessing Human Exposure to Electromagnetic Fields From Wireless Power Transmission Systems," *Proc. IEEE*, vol. 101, no. 6, pp. 1482–1493, Jun. 2013.
[200] P. J. Dimbylow, "FDTD calculations of the whole-body averaged SAR in an anatomically realistic voxel model of the human body from 1 MHz to 1 GHz," *Phys. Med. Biol.*, vol. 42, no. 3, p. 479, 1997.
[201] P. Röschmann, "Radiofrequency penetration and absorption in the human body: Limitations to high-field whole-body nuclear magnetic resonance imaging," *Med. Phys.*, vol. 14, no. 6, pp. 922–931, 1987.
[202] N. Kuster and Q. Balzano, "Energy absorption mechanism by biological bodies in the near field of dipole antennas above 300 MHz," *Veh. Technol. IEEE Trans.*, vol. 41, no. 1, pp. 17–23, 1992.
[203] H.-Z. T. Chen and A. S. L. Lou, "A Study of RF Power Attenuation in Bio-tissues," *J. Med. Biol. Eng.*, vol. 24, pp. 141–146, 2004.
[204] C. Gabriel, S. Gabriel, and E. Corthout, "The dielectric properties of biological tissues: I. Literature survey," *Phys. Med. Biol.*, vol. 41, no. 11, p. 2231, 1996.
[205] C. Gabriel, S. Gabriel, and E. Corthout, "The dielectric properties of biological tissues: I. Literature survey," *Phys. Med. Biol.*, vol. 41, no. 11, p. 2231, 1996.
[206] N. Jonassen, "Human body capacitance: static or dynamic concept? [ESD]," in *Electrical Overstress/ Electrostatic Discharge Symposium Proceedings. 1998 (Cat. No.98TH8347)*, 1998, pp. 111–117.
[207] D. D. Arumugam, J. D. Griffin, D. D. Stancil, and D. S. Ricketts, "Magneto-Quasistatic Tracking of an American Football: A Goal-Line Measurement," *IEEE Antennas Propag. Mag.*, vol. 55, no. 1, pp. 138–146, 2013.
[208] "U.S. Food and Drug Administration." [Online]. Available: http://www.fda.gov/. [Accessed: 12-Nov-2014].

[209] "EU Medical Devices." [Online]. Available: http://ec.europa.eu/enterprise/policies/european-standards/harmonised-standards/medical-devices/index_en.htm. [Accessed: 12-Nov-2014].

[210] F. Deligianni, A. Chung, and G.-Z. Yang, "Decoupling of respiratory motion with wavelet and principal component analysis," in *Medical Image Understanding and Analysis (MIUA04), London, UK*, 2004, vol. 5.